

Spin resonance in novel environments

Alexander R Barbaro

St Catherine's College, Oxford

Prof. Andrew Briggs & Dr. Jan Mol

Thesis submitted in fulfilment of the requirements for the degree of Doctor of Philosophy at the University of Oxford

Michaelmas Term, 2017





Dedication

For my mentors. You know who you are.

Acknowledgements

Despite having a single author, a thesis results from the support of many, who give the author the opportunity to devote themselves wholly to a research project.

First and foremost, I must thank those that made my DPhil possible. *The General Sir John Monash Foundation* and St. Catherine's College both supported me through the DPhil experience.

My supervisors, Prof. Andrew Briggs and Dr. Jan Mol, were remarkable. Their dedication, support, guidance and scientific insight matched the distinguished University they work at. Andrew, I never felt more ready, organised and enthused than after our meetings. Thank you for your sound advice, wealth of knowledge, your enthusiasms and encouragement. Jan, your perceptive ability to extract scientifically relevant information amongst the metaphorical noise never ceased to amaze me. Your devotion to your DPhil students must be acknowledged. Thank you for your sound advice.

I had the opportunity to meet and discuss my research with many esteemed researchers, whom I admire. These were Prof. Martin Brandt, Dr. Hans Huebl and David Franke (Technische Universität München), Prof. Michelle Simmons and Dr. Dane McCamey (University of New South Wales), who also hosted me, Prof. John Morton (University College London), Prof. Mike Thewalt (Simon Fraser University), and Radka Chakalova, Dr. Simon Cassidy and Dr. Simon Clarke (University of Oxford). Your experience and insight saved me from reinventing the wheel and sent my research on the right trajectory.

My collaborators were Prof. Sven Rogge, Dr. Joost van der Heijden (University of New South Wales), Dr. Cheuk Lo (University College London) and Prof. Henry Snaith, Prof. Arzhang Ardavan and Dr. Amir-Abbas Haghighirad (University of Oxford). You are exceptional. Dr. Junjie Liu (University of Oxford) gets a special mention; I learnt

so much working with you. Dr. Will Myers too, your ongoing support was invaluable. You are a treasure to CAESR. A special thanks must also go to members of my research group: Natalia, Pascal, Aaron, Greg, Matthias, Felix, Paweł and Rubin. As postdocs and peers you provided unique advice (and laughs) as you were enjoying the same research journey with me.

I was privileged to use multi-gate transistors designed and fabricated by partners of the Towards Low Power (TOLOP) ICT project. The results of the experiments on these samples are in chapter 2. I was similarly privileged to use samples fabricated by Dr. Cheuk Chi Lo at the University of California, Berkeley. The results of the experiments on these samples are in chapters 4 and 5.

Oxford provides a vibrant community for its students. Although the history, buildings and artefacts are dazzling, its the people that are the lifeblood of the University. I could not possibly list all of the friends I have made throughout my DPhil but some people get a special mention because you enriched my life the most. In no particular order: Zubin, Faye, Mark and Maddie, Pete, Anna, John, Renee, James, Jerome, Sarah, Jenny, Nina, Julian and Carla. You lot got me through to the end! Most of these friendship began through my connections with St. Catherine's College, the Oxford University Triathlon Club or St. Catherine's College Boat Club. These clubs delivered some of my fondest memories from my four years in Oxford. It was a unique experience I am thankful for and will treasure. It was also heart warming to know some of my best friends back in Australia had me in their thoughts. Tom, Fili, Shaun and Sam; at least we will be on the same continent in the coming years.

Living so far from my family was made infinitely easier by my 'English family', the Siganporias. Ruby, Nauser, Zarina and of course Zubin (again), thank you for your love and support.

Dr. Richard Bailey, thanks for the enjoyable and useful discussion about research. It was refreshing to discuss research approaches with someone outside my field.

Finally, thank you to my family, who provided love and support that cannot be replaced or matched, nor can its positive influence on me be sufficiently articulated. You are the greatest.

Several figure is this thesis were generated by others. Dr. Mol generated figure 2.4, Dr. Liu generated figure 2.10 and Dr. Haghighirad generated figure B.1.

Abstract

In this thesis I experimentally investigate semiconductor defects in novel environments. I do this by exploiting the unpaired defect-bound electrons that can be measured through electron paramagnetic resonance (EPR) effects. I extend my analysis to electrically detected magnetic resonance (EDMR) as it characterises the influence of paramagnetic recombination centre on a sample's conductivity, which is important for typical applications like optoelectronics, complementary metal oxide semiconductor devices and donor spin quantum information processing.

My experimentation can be divided into three parts. I firstly investigated rectification effects in nanoscale tri-gate transistors setup for EDMR measurements. An understanding of rectification currents is a stepping stone to effective EDMR measurements of non-linear devices in the future. By using a two-dimensional Taylor series, I accurately model rectification currents through a tri-gate nanoscale transistor situated in a microwave cavity. My model requires minimal coupling to exist between the gate and bias terminals. I show that the phase difference between the AC voltage on the gate and bias terminals is critical in determining the magnitude and direction of the rectification current. I then demonstrate that rectification currents can be used to my advantage in broadband microwave detection. By operating my device in a non-linear mode under the influence of microwave fields it becomes sensitive to small changes in the cavity's field. Microwave absorption by foreign paramagnetic materials in the sample space can then be measured by a change in the rectification current. This I demonstrated through the detection of 2,2-diphenyl-1-picrylhydrazyl at X-band frequencies and oxygen at D-band frequencies. My experiment demonstrates a novel way with which to perform EPR experiments in a small sample space, without the need to isolate high frequency D-band detection circuitry from the static field.

I secondly investigated EDMR in naturally occurring silicon ion-implanted with ^{33}S and ^{75}As. My aim was to observe spin-dependent recombination (SDR) of electron-hole pairs mediated by the shallow donor ^{75}As in a neutral charge state and the deep donor ^{33}S in the charge state S^+. Continuous wave-EDMR (cwEDMR) measurements revealed the spin signature of ^{75}As, a plethora of P_{b0}, P_{b1} and E' interface defects and residual ^{31}P. In each sample, the EDMR spectra gave no definitive indication of electrically active ^{33}S, ^{33}S clusters or ^{33}S complexes. I attribute this to the photoneutralisation of the paramagnetic S^+ state. I also detected amorphisation of the silicon crystal from ion-implantation, which recrystalised for longer anneal durations as expected. My results gave an indication of the interface-like defects created during amorphisation and the effect these have on hindering charge transport. Pulsed-EDMR was used to investigate the charge carrier interactions leading to the cwEDMR spectra. The decrease in current upon microwave excitation indicated SDR of electron-holes pairs across all resonances. An unremarkable 2 μs coherence time was determined for ^{75}As-bound electrons and a 4.5 μs electronic transition time, which is comparable to published data involving shallow donors and interface charge traps. Electrically detected electron double resonance experiments demonstrated the formation of spin-pairs between ^{75}As and the amorphisation defects, which led to electron-hole recombination.

Finally, EPR was used to investigate UV-irradiated PbI_2 and $MAPbBr_3$/$MAPbI_3$ crystals, which had previously shown paramagnetism. Intrinsic defects are believed to be the cause of their long electron-hole diffusion lengths in organic-inorganic hybrid perovskite. In my measurements, the materials all appeared EPR-silent, which is attributed to the high purity of the lead halide precursor.

List of Publications

Published manuscripts during DPhil

Barbaro, A.R., "A literature review on Quantum read-out of spin resonance in a silicon transistor", *Journal of Material Science and Technology* 32.8, (2016), pp. 823-845.

Manuscripts in preparation/submitted

1. *EPR detection via rectification*
2. *Spin-dependent recombination via arsenic and ion-implantation induced defects in silicon*
3. *Charge dynamics in polydimethylsiloxane*

Conference presentations and posters

Presentation

Impurity Spins for Quantum Information and Technologies, 2017 September 13-15, Okinawa Institute for Science and Technology Graduate University, Okinawa, Japan

Posters

The 50th Annual International Meeting of the ESR Spectroscopy Group of the Royal Society of Chemistry, 2nd April – 6th April 2017, University of Oxford, United Kingdom

Silicon Quantum Information Processing 2015: Scaling up, 11 Sep 2015, Murray Edwards College, University of Cambridge, United Kingdom

Contents

Page

Dedication i

Acknowledgements ii

Abstract v

List of Publications vii

Contents xii

Abbreviations xvi

1 Introduction 1

2 The theory of spin-dependent recombination 6

2.1 Electron paramagnetic resonance 6

2.1.1 Spin angular momentum and magnetic moment 6

2.1.2 Single spin Hamiltonian 8

2.1.3 Spin populations 9

2.2 Recombination 12

2.2.1 Lepine's SRH-based spin polarisation model 12

2.2.2 Kaplan, Solomon and Mott's 'spin-pair' model 13

2.2.2.1 Variations to Lepine's and the KSM model 14

2.3 Spin-pair Hamiltonian 18

2.3.1 Mathematical description of the current transient resulting from a microwave pulse 20

3 Rectification in nanostructures 24

3.1 Introduction . . . 25

3.1.1 Electric and magnetic field coupling typical in EDMR measurements 25

3.1.2 Rectification in a three terminal device . . . 28

3.1.3 Rectification in EDMR measurements of non-linear devices . . . 31

3.2 TOLOP tri-gate transistors . . . 32

3.3 Rectification model . . . 34

3.4 Multi-frequency EPR detected by rectification effects . . . 41

3.4.1 Detection of DPPH in the rectification current at X-band microwave excitation . . . 41

3.4.2 Detection of O_2 molecules in the rectification current at D-band microwave excitation . . . 44

3.5 Conclusion . . . 47

4 Identification of electrically active spin species in arsenic and sulfur doped silicon 49

4.1 Introduction . . . 50

4.1.1 Sulfur doping in photodetectors . . . 51

4.1.2 Sulfur doping in photodiodes . . . 51

4.1.3 Sulfur doping in photovoltaics . . . 52

4.1.4 Chalcogen doping for quantum information . . . 52

4.1.4.1 Chalcogens as donor spin qubits . . . 52

4.1.4.2 Chalcogens for qubit coupling . . . 53

4.1.5 Sulfur doping for quantum readout of donor spin qubits using spin-dependent recombination . . . 55

4.1.6 Properties of sulfur in silicon . . . 56

4.1.6.1 Hole capture . . . 57

4.1.6.2 Spin characteristics of sulfur donors . . . 59

4.1.7 Electrical observation of deep donor state . . . 60

4.1.7.1 Compensation of double donor's D^0 state with background acceptor doping . . . 61
4.2 Experimental setup . . . 63
4.2.1 Thermal treatment experimental setup . . . 64
4.2.2 Light source . . . 66
4.3 Device design . . . 67
4.3.1 Donor concentration profile . . . 68
4.3.1.1 Annealing . . . 69
4.3.2 Electrode design and the metal semiconductor contact . . . 75
4.3.2.1 Patterning of electrodes . . . 78
4.3.2.2 H-passivation and oxide reduction . . . 79
4.4 Current-voltage response . . . 79
4.5 Spin-dependent recombination in arsenic and sulfur doped crystalline silicon 82
4.5.1 Ion implantation damage . . . 82
4.5.2 Spin species identities . . . 85
4.5.3 Thermal treatment effects on activation . . . 88
4.5.4 Absence of As-S spin-pairs . . . 90
4.6 Conclusions . . . 92

5 Characterisation of spin-dependent processes in arsenic and sulfur doped silicon 94

5.1 Introduction . . . 95
5.1.1 Alternative spin-state readout techniques . . . 96
5.2 Experimental setup . . . 97
5.3 Current transient analysis . . . 98
5.4 Spin-to-charge conversion . . . 102
5.4.1 Spin echo electrical detection . . . 105
5.5 Coherent spin manipulation . . . 107
5.5.1 Coherent spin oscillations . . . 108
5.5.2 Spin coherence measurements . . . 108

5.6 Recombination and generation rates . . . 114
5.7 Identification of spin-dependent recombination mechanism . . . 116
5.8 Electrically detected echo electron double resonance . . . 118
5.8.1 Experimental approach . . . 119
5.8.1.1 Frequency range . . . 119
5.8.2 The EDeELDOR scheme . . . 120
5.8.2.1 Proportion of arsenic excitation . . . 123
5.8.2.2 Identifying overlapping spin-species . . . 127
5.8.3 EDeELDOR measurements . . . 128
5.9 Conclusion . . . 132

6 Radiation induced spin defects in hybrid perovskites 135

6.1 The remarkable rise of organic-inorganic halide perovskites . . . 135
6.2 Magnetic field effects in hybrid perovskites . . . 136
6.3 Degradation of hybrid perovskites thin films . . . 137
6.3.1 UV induced degradation . . . 137
6.3.1.1 UV induced degradation of lead halides . . . 137
6.3.1.2 UV-induced degradation in hybrid perovskites . . . 137
6.4 Defects in hybrid perovskites . . . 138
6.4.1 Previous investigations of hybrid perovskites crystals with ESR . . 139
6.5 Experimentation . . . 140
6.6 EPR-silent irradiated PbI_2 powder . . . 142
6.7 A deceptively similar EPR signal from vacuum grease . . . 143
6.8 EPR of irradiated $MAPbX_3$ crystals . . . 144
6.8.1 Unidentified triplet species . . . 144
6.8.2 Absence of lead, halide or organic spin-active defects . . . 144
6.9 Conclusion . . . 146

7 Conclusion and future work 148

7.1 Rectification . . . 148
7.2 Spin-dependent recombination in arsenic and sulfur doped silicon . . . 149

7.3 Deleterious defects in hybrid perovskites 152
7.4 Closing remarks 154

Bibliography **155**

A Intermodulation products from the microwave amplification **194**

B Perovskite single crystal growth **196**

Abbreviations

B_0	static 'Zeeman' magnetic field.
B_{mod}	field modulation amplitude.
$D-A$	donor-acceptor.
D_0	diffusion coefficient.
E_g	bandgap.
V_{oc}	open circuit voltage.
$\boldsymbol{B_1}$	cavity's magnetic field.
$\boldsymbol{E_1}$	cavity's electric field.
$\boldsymbol{\mu_e}$	electron magnetic dipole moment.
δ	skin depth.
γ	gyromagnetic ratio.
μ	charge carrier mobility.
ω_L	Larmor frequency.
f_c	central frequencies.
$f_{\mu w}$	microwave frequency.
f_{mod}	field modulation frequency.
f_{xBW}	excitation bandwidth in units of Hertz.
lw_{Hz}	linewidth in units of Hertz.
m	modulation depth.
m_S	spin angular momentum quantum number.

AEDMR	Auger electron detected magnetic resonance.
AENDOR	Auger-electron-detected electron nuclear double resonance.
AWG	SpinJet Arbitrary Waveform Generator.
CB	conduction band.
CDMR	capacitance detected magnetic resonance.
CE	conduction electron.
CMOS	complementary metal oxide semiconductor.
cwEDMR	continuous wave EDMR.
cwEPR	continuous wave EPR.
DEER	double electron-electron resonance.
DIBL	drain-induced barrier lowering.
DMM	digital multimeter.
DPPH	2,2-Diphenyl-1-picrylhydrazyl.
EDeELDOR	electrically detected echo electron double resonance.
EDELDOR	Electrically detected electron double resonance.
EDMR	electrically detected magnetic resonance.
EHR	electron-hole recombination.
ELDOR	Electron double resonance.
ENDOR	electron nuclear double resonance.
EPR	electron paramagnetic resonance.
ESR	electron spin resonance.

FWHM	full width half maximum.
HF	hydrofluoric.
HfSiON	hafnium silicon oxynitride.
IPV	impurity photovoltaic.
IR	infrared.
KSM	Kaplan Solomon Mott.
LO	local oscillator.
MFE	Magnetic field effects.
MOSFET	metal oxide semiconductor field effect transistor.
MPE	Multiphonon emission.
MSI	metal-semiconductor interface.
MWA	microwave artefacts.
NDMR	noise detected magnetic resonance.
NMR	nuclear magnetic resonance.
ODMR	optically detected magnetic resonance.
PCB	printed circuit board.
PCE	photovoltaic conversion efficiency.
PDMR	Photovoltaic detected magnetic resonance.
PDMS	poly(dimethylsiloxane).

pEDMR	pulsed EDMR.
pEPR	pulsed electron paramagnetic resonance.
PL	photoluminescence.
PLQE	photo luminescence quantum efficiencies.
QIP	quantum information processing.
SDH	spin-dependent hopping.
SDR	spin-dependent recombination.
SDS	Spin-dependent scattering.
SDT	spin-dependent tunneling.
SIMS	secondary ion mass spectroscopy.
SNR	signal-to-noise ratio.
SOC	spin-orbit coupling.
SOI	silicon on insulator.
SRH	Shockley-Read-Hall.
STE	self-trapped electron.
TDD	thermal double donors.
TOLOP	Towards Low Power.
UV	ultraviolet.
XRD	x-ray diffraction.

1

Introduction

Deliberately engineered defects allow us to change a semiconductor's properties. Charge carrier conductivity, lifetimes, mobility, composition and quantised activation energies are all affected when charge carriers are trapped at defects [1]. The type and concentration of defect can be tailored to transform the electronic properties of a material to match desired behaviour. Unintended defects on the other hand can somethings be destructive by having an undesired effect on these properties that hinders performance.

The effects of defects in state-of-the-art transistors made for the complementary metal oxide semiconductor (CMOS) industry, whether deliberate or unintentional is becoming increasingly significant. With ever shrinking transistor channel lengths that follow Moore's law [2–4], the electrical influence of single defects in a channel only a few atoms wide is more pronounced [5–8]. Whilst providing a fundamental challenge to device performance, it has catalysed research into alternate computational approaches like quantum computing. One of the best methods with which to interrogate defects in a conductive device is through electrically detected magnetic resonance (EDMR) as it relies on the same charge transport function under which the devices operate, and the current is modulated through electron paramagnetic resonance (EPR) of defect centres. The spin-dependent mechanism that modulates the current provides a rich source of information about the nature of the defect [9, 10]. EDMR could detect orders of magnitude fewer defects than traditional EPR [11–13]. In addition to other experiments like

charge pumping that rely on charge transport under microwave excitation, experimental realities like rectification of the microwave fields require ongoing analysis to ensure the robustness and accuracy to such experimental approaches. Recent advances in EPR using superconducting resonators and Josephson parametric microwave amplifiers have extended its sensitivity to the single-shot detection of 200 donor spins [14, 15]. This experimental development propels the usefulness of EPR to nanoscale devices at the quantum limit of electromagnetic field fluctuations and could circumvent the current rectification issues associated with charge transport measurements.

Shallow defects can be effectively modelled by a hydrogen atom, in that they bind a single electron to a positive charge. This makes their behaviour easier to model and creates an isolated quantum system. This unpaired electron causes paramagnetism, where localised electrons are bound at intrinsic or implanted (donor) defects, to create a bi-level 'spin-up' or 'spin-down' system under the influence of a magnetic field [16]. For group V donors like phosphorus or arsenic in silicon, the unpaired electron (and nuclear) spin becomes a potential quantum bit or 'qubit' in a quantum computer. The long coherence times of donor-bound electron and donor nuclear spins in addition to the silicon fabrication expertise from decades of experience in the microprocessor industry makes donor spin qubits viable candidates in the quantum computation field [17]. The demonstration of significant milestones like spin qubit readout and manipulation [13, 18, 19] using EPR and EDMR techniques, qubits with fault-tolerant control fidelity [20], and a two-qubit logic gate [21] solidifies spin qubits in silicon as a front-running candidate in the quantum information processing (QIP) field. It also demonstrates the versatility of spin resonance techniques to various applications in quantum technologies.

Intrinsic defects in silicon have also proved valuable. Interfacial defects like silicon dangling bonds or bulk defects like oxygen vacancy centres in silicon have both been an important tool for electrical spin-dependent readout of donor spin states [22, 23]. These helpful defects however prove to be a hinderance to spin coherence times and charge transport. Despite developments in fabrication of silicon devices, they are difficult to totally exclude from devices.

On the other hand deep, much larger group VI chalcogen dopants like sulfur bring

their own distinct characteristics. Firstly, larger group VI donors greatly distort the silicon crystal lattice, providing greater binding energies, which easily capture free carriers [1]. As their name suggests, they are energetically deep in the bandgap, which gives them unique optical properties that will be important for qubit coupling architectures in the future [24]. Their potential use as an intra-bandgap stepping-stone for electron-hole recombination (EHR) experiments is hoped to extend the functionality of spin-dependent recombination (SDR) experiments and avoid the deleterious effects of interface defects previously used for the spin-state readout of donor spins.

Each impurity type in semiconductors demonstrates remarkably different characteristics that can be manipulated and exploited. The control afforded to trapped charge carriers in defects has been so successful that it is extended to the development of quantum dot systems for QIP [25, 26]. Whilst natural or artificial defects provide a powerful means to manipulate the properties of a semiconductor, their deliberate inclusion is a balancing act. These defects provide unique and varied properties, 'some fatal, some vital' [1].

Photovoltaics is another industry that relies on the remarkable properties of natural or artificial defects in semiconductors. The use of midgap defects like sulfur in silicon facilitate photoexcitation of charge carriers at previously inaccessible infrared (IR) wavelength that can enhance the conversion efficiency of a class of photovoltaic known as 'impurity photovoltaics' [27, 28]. The proposed use of energetically deep-level donors like sulfur in silicon solar cells provides an opportunity to improve their performance. Though their inclusion must balance competing effects: whilst they may improve the optical responsivity of silicon into the IR spectrum, they also facilitate EHR, a pernicious effect to electrical current generation, though advantageous for next generation IR photodiodes [29].

Groundbreaking perovskite photovoltaic absorbers that have transformed the photovoltaic research field have striking defect properties. It is argued that the material's intrinsic defects are critical to the long electron-hole diffusion length in the material [30, 31]. In contrast, UV-radiation induced defects provide unwanted charge traps that will inhibit performance [32]. Some of the best performing perovskite solar cells are com-

posed of mixed halides and triple cations [33]. Their performance limiting defects can be passivated by halide doping [34, 35]. There is still a lot to be learnt from defects in these materials.

Whilst dopants are indispensable defects that have changed semiconductors into malleable electrical materials, uncontrolled defects can have the opposite effect on the same electrical properties. Indeed, defects are at times requisite and at other time ruinous [1]. In this thesis, spin resonance measurements from various novel environments are united into one narrative to emphasise firstly the advantages of EPR as an interrogation technique, and secondly to highlight the importance of understanding defects in all charge-transport semiconductor materials.

In Chapter 2, the theory behind the Kaplan Solomon Mott (KSM) 'spin-pair' model is explained, and the temporal response of a spin ensemble to a microwave pulse is characterised.

One of the primary experimental challenges faced during microwave excitation (like that applied during EDMR of non-linear devices) is rectification of the output current. In Chapter 3, a new approach to modelling rectification in non-linear devices is developed to explain the rectified drain current observed in state-of-the-art Towards Low Power (TOLOP) nanoscale tri-gate transistors [36]. The use of rectified current in these devices as a means to detect foreign paramagnetic species across a broad frequency spectrum is considered. EDMR via donors in nanoscale tri-gate transistors has yet to be demonstrated, though the approach could prove a useful way to interrogate the channel of these devices.

In Chapter 4, continuous wave EDMR (cwEDMR) is used to investigate the SDR signal in a novel doping architecture: silicon co-doped with arsenic and sulfur at a peak concentration 100 nm away from the silicon/silicon-oxide interface. The aim is to demonstrate SDR between arsenic and sulfur spin-pairs. Taking into account the ion-implantation, the thermal treatments used to activate suflur, the background doping concentration of boron to compensate one of the sulfur's two donor electrons, as well as the capture cross section of sulfur, the electrical observation of paramagnetic singly-ionised donors is attempted.

In Chapter 5, pulsed EDMR (pEDMR) is used to further investigate the spin-dependent behaviour that occurs in the samples studied in Chapter 4. The temporal dynamics of the spin system following a saturation microwave pulse are considered to clarify the spin-dependent mechanism that produced the cwEDMR signal in Chapter 4. Coherent spin manipulation is then used to firstly investigate the coherence time of the arsenic donors, whose physical separation from deleterious interface defects was hypothesised to improve their coherence time. Secondly, the electronic transition rates are also investigated by measuring illumination dependent inversion recovery experiments. Thirdly, electrically detected electron double resonance is used to determine the spin-pair partners in the silicon sample under test.

In Chapter 6, the potentially detrimental effects of UV-irradiation on the integrity of lead iodide powder and hybrid perovskite crystals is investigated using EPR. Published literature has shown that UV-irradiation can induce shallow and deep paramagnetic intra-bandgap defects in both materials [37, 38] that would inhibit the photovoltaic performance of perovskite-based solar cells.

Finally in Chapter 7, the conclusions of the thesis are summarised and recommendations for future work are made.

2

The theory of spin-dependent recombination

This chapter first details the theory of EPR necessary to understand the experimental work undertaken and outlined in later chapters. It then details a short history of EDMR, including several models that were derived whilst attempting to explain experimental phenomena. The final model considered (the KSM model) is the most widely accepted and most accurately describes SDR effects. It is used in combination with the variant donor-acceptor ($D-A$) model as a framework to model the behaviour of pEDMR in a weakly-coupled spin-pair system. Its application to EDMR was first derived by Boehme and Lips and their analysis is described in detail in this chapter [39, 40].

2.1 Electron paramagnetic resonance

2.1.1 Spin angular momentum and magnetic moment

EPR[1] is a powerful technique to probe the nature, structure, dynamics and composition of defects [42]. It provides unique insights into free radicals within a sample, and will

[1] Chechik *et al.* note that for a system dominated by spin angular momentum, electron spin resonance (ESR) is typically used to describe induced spin transitions. On the other hand, transitions of a spin system with extra orbital angular momentum that contributes to the total angular momentum is usually described by the term EPR [41].

be shown to be a critical tool with which to interrogate deliberate and unintentional defects in semiconductors. With that in mind, I will consider the theory behind EPR. In developing an understanding of the theory, I begin with an intrinsic property of an electron empirically identified in the Stern-Gerlach experiment: its 'spin', also called its intrinsic angular momentum[2]. Spin is a vector identified as the spin angular momentum ($\boldsymbol{S}$):

$$|\hat{\boldsymbol{S}}| = \sqrt{S(S+1)} \tag{2.1}$$

where S is the electron spin quantum number[3]. For a given value of $\boldsymbol{S}$ there are $2S+1$ projections onto an arbitrary axis with quantised amplitude units of $\hbar = {}^{h}/_{2\pi}$, the reduced Planck constant. The z-direction parallel to static 'Zeeman' magnetic field (B_0) is usually chosen. The $2S+1$ allowed values of $\boldsymbol{S}$ are defined in terms of the spin angular momentum quantum number (m_S) as:

$$m_S = -S, -S+1, ..., S-1, S. \tag{2.2}$$

m_S is the eigenvalue of the operator $\hat{S}$. The spin of an electron creates a magnetic dipole moment. The ratio of the electron magnetic dipole moment ($\boldsymbol{\mu_e}$) to $\boldsymbol{S}$ is given by the gyromagnetic ratio (γ),

$$\boldsymbol{\mu_e} = -\gamma \boldsymbol{S}\hbar = -g_e \frac{e\hbar}{2m_e}\boldsymbol{S} = -g_e \mu_B \boldsymbol{S} \tag{2.3}$$

where $g_e \approx 2.0023$ is the free electron g-value, e is the electron charge, m_e is the mass of an electron, $\mu_B = \frac{e\hbar}{2m_e}$=9.274$\times$ 10^{-24} JT^{-1} is the Bohr magneton. The z-axis projection of μ_e gives $-g_e\mu_B m_S$. Unlike an electron in free space, the g-value of an unpaired electron in a crystal, for example, is affected by crystal fields and spin-orbit interaction [45], which causes its g-value to deviate from g_e. This proves to be quite handy as the variation of the g-value is distinctive of the electron trap and can be used as a fingerprint. The negative sign in equation 2.3 requires that $\boldsymbol{\mu_e}$ is anti-parallel to $\boldsymbol{S}$. The energy of these moments are degenerate until a magnetic field is applied, at which

[2]The theoretical descriptions of spin and EPR in this chapter are derived from refs [41–46].

[3]Operators have a hat: $\hat{S}$.

point the degeneracy is lifted and the energy levels split according to the Zeeman effect. The energy of $\boldsymbol{\mu_e}$ in a magnetic field[4] (B_0) is therefore given by:

$$E = -\mu_e \cdot B_0 \tag{2.4}$$

2.1.2 Single spin Hamiltonian

The spin Hamiltonian operator of an electron in a magnetic field in the z-direction describes the energy levels:

$$\hat{\mathcal{H}}_z = g_e \mu_B \hat{\boldsymbol{S}}_{\boldsymbol{Z}} \cdot \boldsymbol{B_0} \tag{2.5}$$

where $\boldsymbol{B_0} = B_0 \cdot \hat{z}$, $\hat{\boldsymbol{S}}_{\boldsymbol{Z}} = \hat{S}_Z \cdot \hat{z}$. In this instance $\hat{z}$ is not an operator but the z-direction unit vector. EPR is a technique that exploits this interaction of a paramagnetic unpaired electron with a magnetic field. The energy eigenstates of an electron in a magnetic field need to be considered to fully understand EPR. The energy eigenstates of the Hamiltonian operator correspond to the $m_S = \pm{}^1/_2$ eigenstates $|\downarrow\rangle$ ('spin-down') and $|\uparrow\rangle$ ('spin-up') of $\hat{S}$, with the energy difference between the energy eigenvalues:

$$\Delta E = E_\downarrow - E_\uparrow = \frac{1}{2} g_e \mu_B B_0 - (-\frac{1}{2} g_e \mu_B B_0) = g_e \mu_B B_0 = \hbar \omega_L \tag{2.6}$$

where the precession frequency around the B_0 axis is called the Larmor frequency (ω_L). This can be seen in figure 2.1. From equation 2.6, γ can also be derived in terms of ω_L and B_0

$$\frac{\omega_L}{2\pi B_0} = \frac{g_e e}{4\pi m_e} = \frac{\gamma}{2\pi} \approx 28.025 \text{ MHz/mT}. \tag{2.7}$$

Like nuclear magnetic resonance (NMR), EPR studies the interaction of radiation and magnetic moments. Samples are usually placed in a cavity where they can interact with the standing electromagnetic waves. To maximise the strength of the cavity's magnetic field ($\boldsymbol{B_1}$) and $\boldsymbol{\mu_e}$ interaction the sample should be placed at the $\boldsymbol{B_1}$ antinode.

[4]The term magnetic field strength H is proportional to the magnetic flux density B, and they are related by $B = \mu H$. The magnetic permeability μ is equal to the relative permeability of the material μ_r times by the permeability of free space μ_0: $\mu = \mu_r \mu_0$. In silicon, $\mu_r \approx 1$. For this reason, $B = \mu H \approx \mu_0 H$ and B is used instead of H throughout the silicon chapters, as is common in literature regarding magnet effects in silicon. In hybrid perovskites μ_r is less well defined, and has been assumed to be equal to unity [47].

Absorption of a resonant photon with energy $\hbar\omega_{res}$ induces transitions between the two energy levels corresponding to the spin-down and spin-up states. This is shown in figure 2.1, where the energy eigenvalues are proportional to the magnetic field, as per equation 2.4. For this transition to occur, the resonant microwave frequency $\omega_{res} = \omega_L$ [45]. This is the fundamental principle of EPR. The spin selection rules dictate that $\Delta m_S = \pm 1$. Given that the sample is kept at a fixed microwave frequency, B_0 is typically swept until resonant conditions are met. An EPR spectrum like that in figure 2.1 (b) depicts microwave absorption versus the swept B_0 field.

2.1.3 Spin populations

Note from equations 2.7 that $\omega_{res} \propto B_0$. The energy difference between the two spin states in equation 2.6 leads to a population difference. The populations are both determined by the Boltzmann distribution in thermal equilibrium. The population difference, is specified by the spin temperature (T_S) is:

$$\frac{N_\uparrow}{N_\downarrow} = e^{\Delta E/k_B T} = e^{-\hbar\omega_L/k_B T_S} \approx 1 - \frac{\hbar\omega_L}{k_B T_S} \tag{2.8}$$

since $e^{-x} \approx 1-x$ when x is small [44, 45]. Therefore at 5 K, the polarisation corresponds to about 10 % at 10 GHz (an X-band frequency). The polarisation is:

$$P = \frac{N_\uparrow - N_\downarrow}{N_\uparrow + N_\downarrow} = \frac{\hbar\gamma B_0}{2k_B T} \tag{2.9}$$

The net absorption is the difference between the absorption ($\propto N_\downarrow$) and emission ($\propto N_\uparrow$) of microwave quanta and is:

$$N_\downarrow - N_\uparrow = N\frac{\hbar\omega_L}{2k_B T} = N\frac{g_e\mu_B B_0}{2k_B T} \tag{2.10}$$

where N is the number of spins. Absorption of a quantum of energy from a resonance microwave frequency excites some spin transitions, which reduces the population imbalance between the two levels and therefore reduces the spin polarisation of the sample. For the continuous microwave excitation applied in continuous wave EPR (cwEPR), the

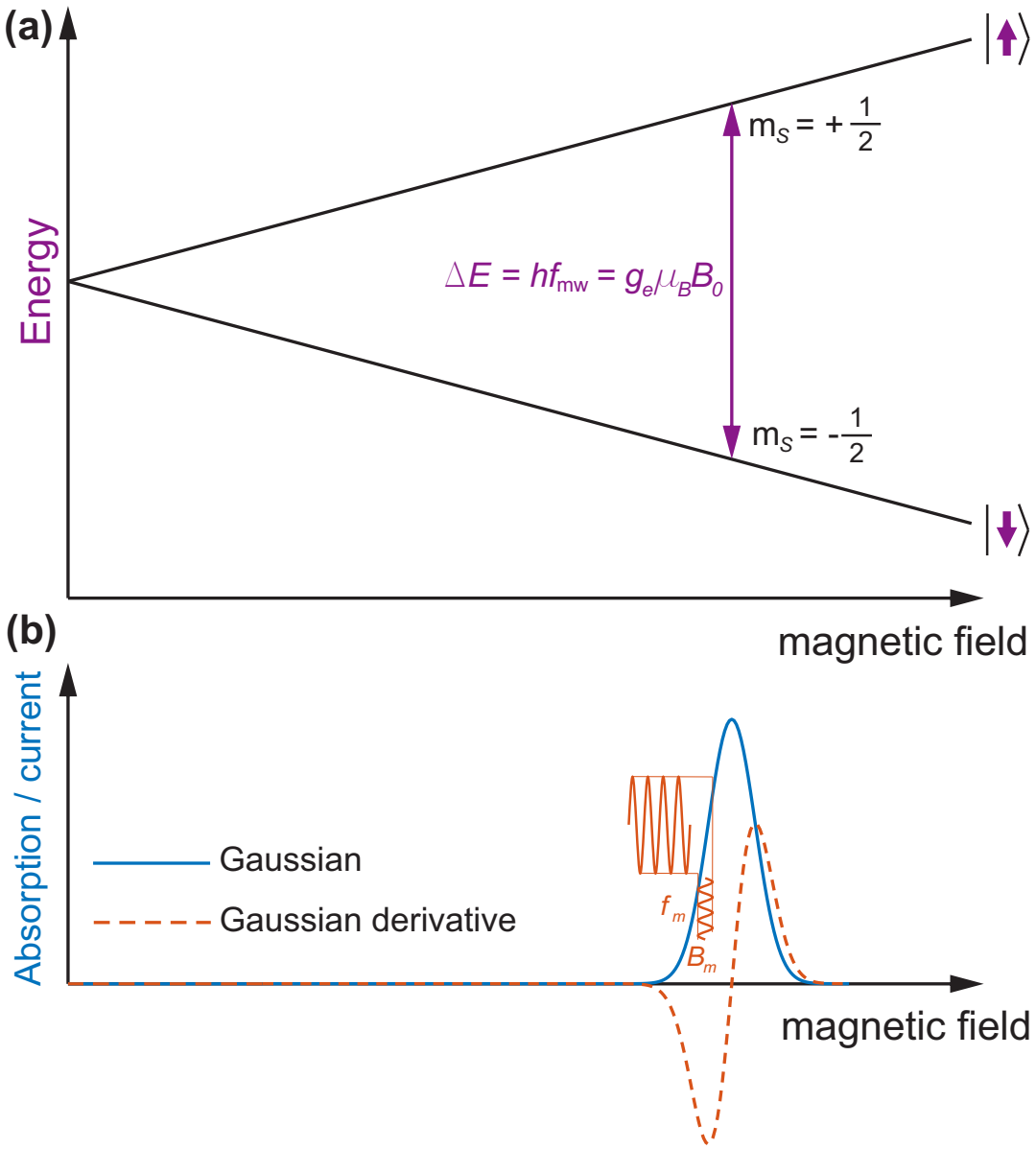


Figure 2.1: Energy levels of a $S = {}^1/_2$ system. (a) The energy of an electron as a function of B_0. As B_0 increases the energy difference known as the Zeeman energy ΔE is governed by the Zeeman effect. The application of resonant photons of energy $\Delta E = \hbar\omega_{res} = g_e\mu_B B_0$ induces a spin 'flip' as the orientation of the magnetic moment switches between spin-up ($|\uparrow\rangle$) and spin-down ($|\downarrow\rangle$). **(b)** On resonance microwave absorption (for EPR) and current change (for EDMR) occurs in a Gaussian lineshape. When the magnetic field is modulated with amplitude B_m and frequency f_m, any non-zero change in microwave absorption/current is modulated at f_m. A lock-in detection technique will result in a derivative of that Gaussian lineshape when plotted as a function of B_0 [41, 42, 48, 49].

spin populations can equilibrate; a state known as *saturation*. At saturation, no further microwave energy is absorbed and the EPR signal disappears [41]. The system returns to thermal equilibrium via energy transfer to the surroundings known as spin-lattice relaxation, which occurs on a time scale identified as the T_1 time. Saturation will be exploited in Chapter 5.

EPR is used in various environments including, but not limited to, defects in solids, biological samples, transition metal ions and organic radicals [41]. In a disordered environment like amorphous silicon, there is a Gaussian distribution of g-values of the same defect due to the their differing orientations within the crystal [41]. The resulting resonant lineshapes of these environments is the superposition of these.

A lot of useful information can be extracted from a resonance excitation. The fingerprint-like g-value has already been discussed. The linewidth is an important tool for understanding the homogeneity of the local environment. The intensity is important for understanding the concentration of the spin, whereas the number of lines and their separation can also be used to identify paramagnetic species based on the strength of several magnetic moments. Finally, anisotropy is an orientational dependence of the B_0 interaction with μ_e, where an electron is localised in a higher orbital that contributes orbital angular momentum to the Hamiltonian. This leads to spin-orbit coupling (SOC), which causes anisotropy [41].

In theory EPR detects microwave absorption, though in practice it is generally not sensitive enough. To overcome this, a technique known as 'lock-in' or 'phase-sensitive' detection is used. To implement this, amplitude or frequency modulation of B_0 or $\boldsymbol{B_1}$ for example, at a chosen frequency (usually between 10-100 kHz) is used. Modulation of B_0 with field modulation frequency (f_{mod}) and field modulation amplitude (B_{mod}) is depicted in figure 2.1 (b). Any resultant changes in the microwave absorption are also modulated at the same frequency. Lock-in detected EPR spectra are recorded as the first derivative of the existing lineshape, where the amplitude of the EPR signal is proportional to the slope of the resonance. The existing lineshape is shown as a solid blue line whereas the derivative is shown as an orange dotted line. When the signal is demodulated, the DC signal is proportional to the amplitude of the EPR signal. By only

being sensitive to a signal at a particular frequency and phase (by using a homodyne detector) signal-to-noise ratio (SNR) can be improved. Improvements to the detection sensitivity of EPR down to the quantum limit have recently been demonstrated [50]. Single electrons spins have been detected optically and electrically [13, 51, 52].

2.2 Recombination

In indirect bandgap materials like silicon, the primary recombination mechanism for electron-hole pairs is non-radiative 'trap-mediated' recombination [53]. Various models have been developed, though this thesis shall focus on two: Lepine's 'spin polarisation' model and Kaplan, Solomon and Mott's 'spin-pair' model [53–56].

The spin-selection rules that are based on the conservation of spin angular momentum dictate that when the spin-orbit interaction is weak, like in silicon, recombination of a free electron-hole will conserve total spin [55]. This means that before the recombination the spin configuration must be $S_i = S_f = 0$, (a singlet) rather than $S_i = 1$ (a triplet).

2.2.1 Lepine's SRH-based spin polarisation model

Seven years after the first optically detected magnetic resonance (ODMR) measurements demonstrated that spin-selection rules could control electronic transitions [57, 58], experiments demonstrated the same effect electrically [59–61]. Following this, Lepine was first to observe and model a change in the photoconductivity in silicon when the magnetisation of a mid-gap centre or conduction electron was reduced [54]. He showed that the recombination described by the Shockley-Read-Hall (SRH) model temporally depended on the relative spin orientation of the free carriers and recombination centres in the bandgap. The model relied on the thermal equilibrium spin polarisation of excess charge carriers according to Boltzmann statistics [53, 62, 63].

Any electron and hole can recombine through the single occupied recombination centre that traps a conduction electron. Importantly anti-parallel singlet conduction electron recombination centre pairs are more tightly bound and result in recombination whereas triplet pairs are trapped though only weakly bound and do not recombine. Spin

resonant conditions equalised the populations of the spin levels, reducing or 'saturating' the centre's polarisation as described in section 2.1.3 and changing the photoconductivity. Lepine's model relied on Pauli spin-blockade, where the inability of two electrons to occupy the same spin state in accordance with Hund's law inhibited the mid-gap mediated recombination with a hole. Lepine's model assumed that recombination could only occur between charge carriers in a singlet configuration. This has been experimentally refuted where slow triplet recombination has been shown to occur [64].

Lepine's model demonstrated a change in the thermal equilibrium spin polarisation p_i ($i = ce$, conduction electrons or rc, recombination centre) affected capture cross section Σ, since $\Sigma \propto (1 - p_{ce}p_{rc})$. This tells us that the *relative* spin orientation is important. This in turn affected excess charge carrier concentration n and thus the conductivity according to equation 2.27. Under saturation $p_i = 0$, room temperature and X-band field strengths (0.3T), the maximum change in conductivity ${}^{\Delta\sigma}/_{\sigma_{ph}}$ achieved is $\approx 10^{-6}$ where on resonance [40, 54],

$$\frac{\Delta\sigma}{\sigma_{ph}} = p_{ce}p_{rc} \approx (\frac{g\mu_B B_0}{kT})^2. \tag{2.11}$$

That is, ${}^{\Delta\sigma}/_{\sigma_{ph}} \propto {}^{B_0^2}/_{T^2}$. A key proof that their observations are modelled by SRH behaviour is the variation of the recombination time with the illumination intensity, which indicates that the change in photoconductivity is a result of a change in carrier concentration rather than mobility [65, 66]. Experimental evidence showed that this polarisation model underestimated the change in the photoconductivity by approximately 2 orders of magnitude. Experimental observations also showed spin-dependent effects could be independent of magnetic field strength and temperature [54, 55, 67, 68]. So although polarisation effects may exist, they are typically overwhelmed by other spin-dependent effects [69].

2.2.2 Kaplan, Solomon and Mott's 'spin-pair' model

This spin-pair model became the archetypal model for SDR transitions in various materials and properly explained the magnitude of the change in conductivity (${}^{\Delta\sigma}/_{\sigma} \approx 10^{-4}$)

that had been experimentally observed [39, 55].

A key deviation from Lepine's model is that before recombination occurs, the charge carriers go through a localised pair state in close proximity before they can recombine [53]. For induced spin resonance to demonstrate an effect, the recombination has to occur on a timescale shorter than the spin relaxation time of either constituent spin element. Such pairs are created randomly and are 'exclusive': from this state they may either dissociate or recombine themselves, but not with other charge carriers [39, 55]. For either charge carrier to recombine with another charge carrier outside the pair, they must first dissociate with the existing partner and form a new pair. This state is called an 'intermediate pair' [39] or 'spin-pair' [42] ('spin-pair' is used hereafter). The pair can be, for example, easily formed by two localised charge carriers trapped at mid-gap energy states like a ^{31}P-P_{b0} spin-pair [10, 22, 70]. This is unlike SRH recombination that firstly, often occurs via only deep defects [11], and secondly, does not seem to require the creation of an 'exclusive' spin-pair. The spin-pair's spatial correlation is sufficiently long-lived that the rate of recombination is higher than the rate of dissociation, leading to an eventual enhancement in the triplet concentration and therefore photocurrent (cf. figure 5.1) [53, 55]. Like SRH recombination however,KSM recombination does not in theory require two localised defects, and can occur with a bound-excitons [39, 71]. This theory is disputed, however [11].

The interaction between the spins in the pair were assumed to be weak, though this is not always the case. Consideration of exchange and dipole interactions show how a change in the four energy eigenstates can change the recombination probabilities [39, 72, 73]. Similarly, triplet rather than singlet recombination is dependent on the host materials spin-orbit interaction, and cannot be assume as insignificant [74].

2.2.2.1 Variations to Lepine's and the KSM model

Adjustments to both the KSM and Lepine's model have continued since their initial publication. In particular, the spin-centres that facilitate EHR vary with material, though with silicon several defect-dependent recombination mechanisms have emerged.

The first is Rong's model [53]. An electron in the conduction band is captured into

the excited state of a deep defect and forms a spin-pair with the defect's ground state electron. Like the KSM model, the electron can dissociate back into the conduction band, or recombine by relaxing into a diamagnetic ground state where it may recombine with a hole. This distinguishing characteristic of this mechanism is that it does not require a nearby defect to facilitate EHR, but instead relies on the excited and ground state of a single defect. This means it can be modelled by modified Shockley-Read statistics.

The second variation to the KSM model is the neutral donor-neutral acceptor pair recombination model (D^0-A^0 pair recombination) [11]. The mechanism is employed in donor-acceptor pair recombination luminescence. The D^0-A^0 recombination adaption of the KSM model has been extensively studied in the past decade [22, 70, 75, 76]. It is graphically depicted in figure 2.2. In this model a spin-dependent transition occurs between two localised paramagnetic intra-gap defects in close proximity. These defect states are provided by a donor-like shallow defect and an acceptor-like deeper defect. Excess free carriers are typically created with above bandgap light. When the Fermi level is below the donor-like level, a free electron is spin-independently captured by an ionised donor. An electron transition to the 'acceptor' energy level is dependent on the spin symmetry. The transition is allowed if the spin-pair has antiparallel configuration; parallel configuration results in Pauli spin blockade. This model has two slightly different interpretations of what constituents the spin-pair. In the first interpretation, the spin-pair is an electron-hole pair, where each are first spin independently captured by the ionised donor and ionised acceptor states respectively [11, 45]. This is followed by recombination. In the second interpretation, the spin-pair is formed by the donor-bound electron and acceptor-bound electron, whose spin symmetry controls the energy level transitions. In this case, the electron and hole recombine *after* the spin dependent transition to the acceptor state [10, 40, 42]. In either case, the KSM modelling focusses on the coupling of charge carriers localised at midgap defect states and the outcomes are the same.

Figure 2.3 is derived from refs. [39, 45, 77] and depicts the changes that happen to the current, recombination rate and spin states for an applied microwave pulse in the KSM picture. The system initially exists at a steady-state where the illumination,

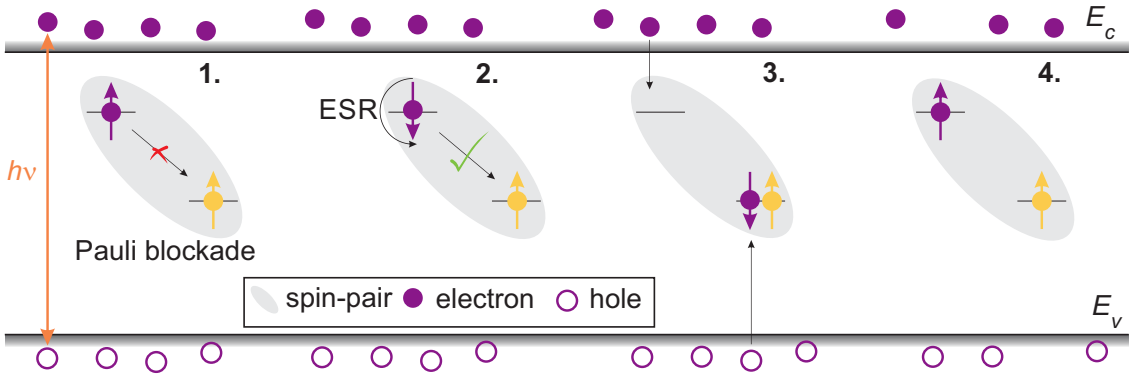


Figure 2.2: Cartoon of the spin-pair recombination model. 1. Above bandgap illumination induces electron-hole pairs in the, silicon semiconductor. Two midgap states form a spin-pair though movement of the bound electrons is inhibited by Pauli-spin blockade. 2. Microwave excitation applied at the higher energy defect 'donor' species changes its spin orientation relative to the lower energy defect 'acceptor' species from a parallel configuration to antiparallel configuration, lifting the Pauli spin bloackade and allowing the electron bound to the donor to relax to the acceptor at rate $^1/_{\tau_{ap}}$. 3. The doubly-occupied acceptor captures a hole to facilitate EHR at the acceptor site. 4. A new spin-pair is spin-independently generated at rate $^1/_{\tau_g}$. Figure derived from ref. [42, 77].

bias voltage and magnetic field are all constant creating a constant photocurrent and recombination rate. Monitoring the photocurrent, rather than the microwave radiation from the procession of a polarised spin ensemble, reveals recombination and therefore parallel and antiparallel densities [39]. A resonant microwave pulse nutates one of the spin-pair at its Rabi frequency as the spin populations deviate from their steady-state populations and tend towards saturation. When the microwave pulse stops, the spins are no longer in energy eigenstates and precess around the applied static field at the Larmor frequency until they dephase. As will be discussed in great detail in section 2.3 and Chapter 5, a flurry of recombination is followed by a quench of the recombination as the antiparallel singlet density is also quenched as the system returns to its steady state. As shown in figure 2.3 (b), spin-pairs can either recombine or dissociate (in addition to the constant spin-pair generation from the constant illumination). Conservation of angular momentum requires that antiparallel spin-pairs are the ones that recombine, though parallel triplet recombination can also occur at a much slower rate (typically three order of magnitudes slower) [78].

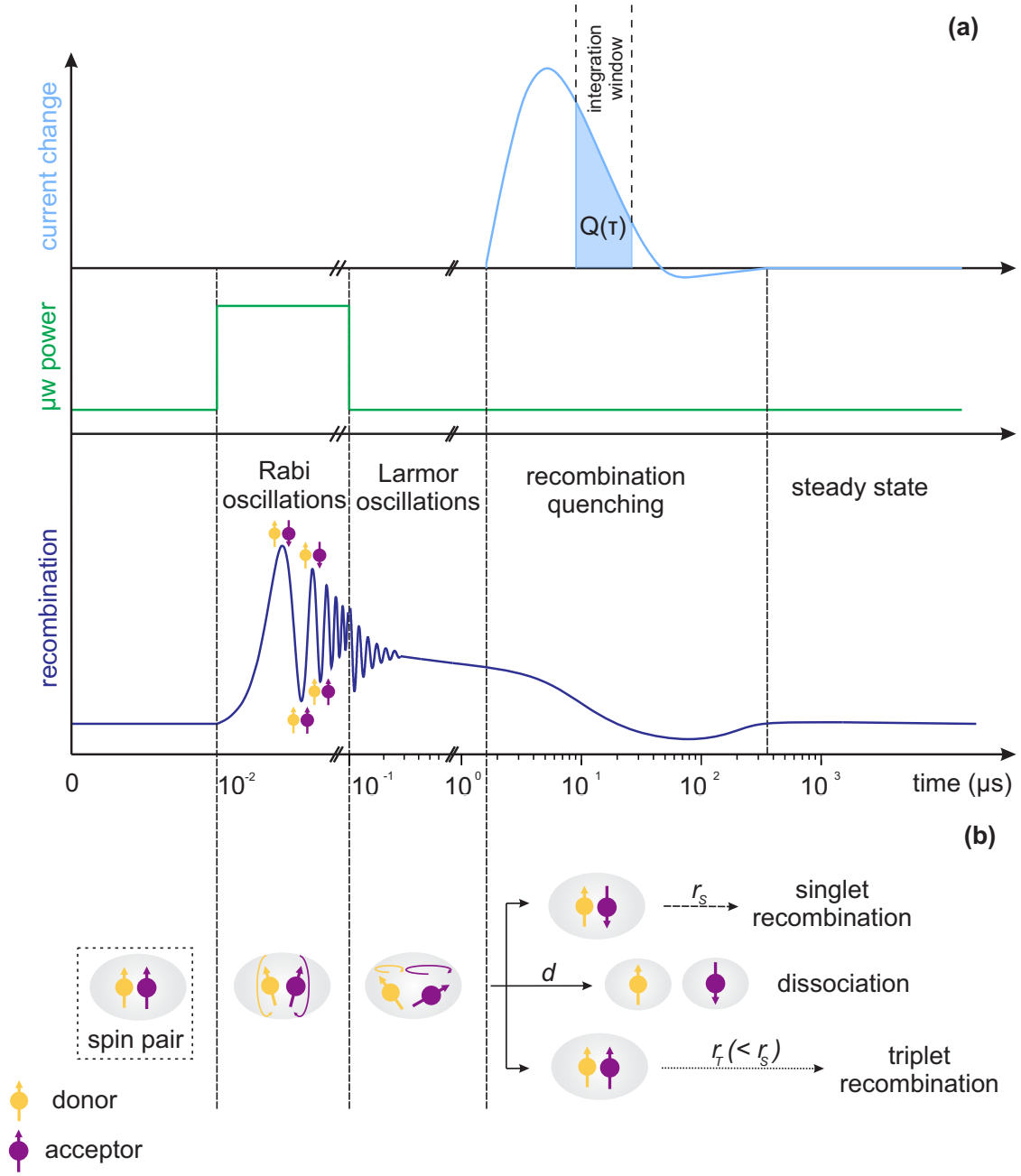


Figure 2.3: Recombination theory. (a) The effects of a microwave pulse (green trace) on the recombination (blue trace) and current change (sky blue trace) **(b)**. The effects of the microwave pulse on the spin-pair leading to either singlet recombination, triplet recombination or dissociation. The 'integration window' labelled in the 'current change' panel is important for spin-echo measurements discussed in Chapter 5. Figure derived from refs. [39, 45, 77].

2.3 Spin-pair Hamiltonian

The Hamiltonian of a spin-pair was first considered in ref. [40]; the following section summarises this seminal work. It contains time-independent and time-dependent components corresponding to the coupling of the spin-pair without, and under the influence of, an external time-varying magnetic field:

$$\hat{\mathcal{H}}(t) = \hat{\mathcal{H}}_0 + \hat{\mathcal{H}}_1(t) \tag{2.12}$$

Let us first consider the time independent component: $\hat{\mathcal{H}}_0$, which consists of a Zeeman term for each electron spin-pair partner (a,b), an exchange coupling term, and and a dipolar interaction term:

$$\begin{aligned} \hat{\mathcal{H}}_0 &= \hat{\mathcal{H}}_{Zee,a} + \hat{\mathcal{H}}_{Zee,b} + \hat{\mathcal{H}}_{\mathcal{J}} + \hat{\mathcal{H}}_{\mathcal{D}} \\ \hat{\mathcal{H}}_0 &= g_a\mu_B \hat{\boldsymbol{S}}_{\boldsymbol{a}} \cdot \boldsymbol{B_0} + g_b\mu_B \hat{\boldsymbol{S}}_{\boldsymbol{b}} \cdot \boldsymbol{B_0} - J\hat{\boldsymbol{S}}_{\boldsymbol{a}} \cdot \hat{\boldsymbol{S}}_{\boldsymbol{b}} - D[3S_{a,Z}S_{b,Z} - \hat{\boldsymbol{S}}_{\boldsymbol{a}} \cdot \hat{\boldsymbol{S}}_{\boldsymbol{b}}] \end{aligned} \tag{2.13}$$

where g_i is the g-value of the i^{th} electron, J is the exchange coupling constant, $S_{i,Z}$ is the spin quantum number of the i^{th} electron in the z-direction and D is the dipolar coupling constant, where in the high field approximation, $|D| \ll |g_i\mu_B B_0|$. This Hamiltonian excludes the hyperfine coupling term as it was considered negligible. Equation 2.18 is non-diagonal in the product base $|\uparrow\uparrow\rangle, |\downarrow\uparrow\rangle, |\uparrow\downarrow\rangle, |\downarrow\downarrow\rangle$ though can be diagonalised by a unitary transformation into the energy eigenstate base $|T_+\rangle, |2\rangle, |3\rangle, |T_-\rangle$:

$$\mathcal{U} = \begin{pmatrix} 1 & 0 & 0 & 0 \\ 0 & cos(\phi) & sin(\phi) & 0 \\ 0 & -sin(\phi) & cos(\phi) & 0 \\ 0 & 0 & 0 & 1 \end{pmatrix} \tag{2.14}$$

with energy eigenvalues of each eigenstate

$$\hat{\mathcal{H}}_0 = \begin{pmatrix} {}^{\hbar\omega_0}/_2 - J + D & 0 & 0 & 0 \\ 0 & -D + \hbar\omega_\Delta & 0 & 0 \\ 0 & 0 & -D - \hbar\omega_\Delta & 0 \\ 0 & 0 & 0 & -{}^{\hbar\omega_0}/_2 - J + D \end{pmatrix} \tag{2.15}$$

where

$$\begin{aligned} \phi &= \frac{1}{2}\arctan\left(\frac{J+D}{\hbar\omega_\Delta}\right) \\ \omega_\Delta &= \sqrt{\frac{(J+D)^2}{\hbar^2} + \Delta\omega^2} \\ \omega_0 &= \omega_a + \omega_b \\ \Delta\omega &= \omega_a - \omega_b \end{aligned} \tag{2.16}$$

For an environment where the spins are weakly-coupled, $J \approx D \approx 0$. The unitary transformation leaves the product states $|\uparrow\uparrow\rangle$ and $|\downarrow\downarrow\rangle$ unaffected as they are independent of J and D. Meanwhile $|2\rangle, |3\rangle$ change from the product states $|\downarrow\uparrow\rangle$ and $|\uparrow\downarrow\rangle$ with mixed symmetry when $\phi = 0$ to the antisymmetric singlet $|S\rangle$ and symmetric triplet $|T_0\rangle$ states when $\phi = {}^{\pi}/_4$ as the exchange coupling increases.

In my case the time-varying magnetic field is the spin excitation microwave field, described in phasor notation as:

$$\boldsymbol{B_1}(t) = \hat{\boldsymbol{x}} B_1 e^{-i\omega_L t} \tag{2.17}$$

where B_1 is the field amplitude. By using the rotating frame approach, $\boldsymbol{B_1}(t)$ becomes time independent, leading to the time-independence of $\hat{\mathcal{H}}_1$ too:

$$\hat{\mathcal{H}}_1 = g_a \mu_B \hat{\boldsymbol{S}}_{\boldsymbol{a}} \cdot \boldsymbol{B_1} + g_b \mu_B \hat{\boldsymbol{S}}_{\boldsymbol{b}} \cdot \boldsymbol{B_1} \tag{2.18}$$

2.3.1 Mathematical description of the current transient resulting from a microwave pulse

The following section summarises the theoretical conclusions made by Boehme and Lips regarding the time domain SDR measurements using pEDMR [40]. Their seminal work laid the foundations for ongoing pEDMR research over the last 15 years and their comprehensive description of the coherent manipulation of the KSM-modelled spin-pair system will also form the foundations of the experimental work detailed in Chapters 4 and 5. Useful insights regarding the model have been made by Behrends in ref. [45] and Hoehne in ref. [79] and are also summarised here when appropriate.

The conductivity of an ideal semiconductor is described by the following equation [80]:

$$\sigma = e[n_e\mu_e + n_h\mu_h] \tag{2.19}$$

where e is the elementary charge, n_e (n_h) is the electron (hole) density and μ_e (μ_n) is the associated mobility. A change in either the charge carrier density or the mobility will result in a change in the conductivity. EDMR measures a spin-dependent change in conductivity when a spin-centre experiences resonant excitation. In this thesis I investigate SDR, where the dynamics of spin-pairs affect the charge carrier density Δn, and therefore the photoconductivity:

$$\Delta\sigma_{ph} = e[\Delta n_e(t)\mu_e + \Delta n_h(t)\mu_h] \tag{2.20}$$

The dependence of SDR on spin dynamics, rather than the result of other transient effects, hinges on the reasonable assumption that the generation, recombination, and dissociation of charge carriers are in equilibrium. When this is true and without any spin manipulation, n and μ, and therefore photoconductivity, are in a steady-state [40].

SDR is based on the spin-pair model. The time evolution of a spin-pair ensemble with recombining spin-pairs can be mathematically described by the Liouville-Von Neumann equation [40, 81]:

$$\frac{d}{dt}\hat{\rho} = \frac{i}{\hbar}[\hat{\rho}, \hat{\mathcal{H}}] + \mathcal{S}[\hat{\rho}] \tag{2.21}$$

where $\hat{\rho} = \hat{\rho}(t)$ is the density operator that describes the state of the two spin-$^1/_2$

system of the spin ensemble, $\hat{\mathcal{H}}$ is the Hamiltonian of an intermediate spin-pair and $\mathcal{S}$ is the operator describing external changes to the system, including spin-pair generation and dissociation, and singlet and triplet recombination in the ensemble. This equation excludes the effects of relaxation (described by the Redfield operator $\mathcal{R}$). $\hat{\rho}$ can also be represented as a 4 $\times$ 4 matrix whose diagonal elements ρ_{ii} are the time evolution of the eigenstate populations; specifically, ρ_{ii} are the probabilities of finding the pair-ensemble in each eigenstates:

$$\frac{d}{dt}\begin{pmatrix}\hat{\rho_{11}}\\ \hat{\rho_{22}}\\ \hat{\rho_{33}}\\ \hat{\rho_{44}}\end{pmatrix} = \begin{pmatrix}-r_T-d & 0 & 0 & 0\\ 0 & -\frac{1}{2}(r_S+r_T)-d & 0 & 0\\ 0 & 0 & -\frac{1}{2}(r_S+r_T)-d & 0\\ 0 & 0 & 0 & -r_T-d\end{pmatrix}\begin{pmatrix}\hat{\rho_{11}}\\ \hat{\rho_{22}}\\ \hat{\rho_{33}}\\ \hat{\rho_{44}}\end{pmatrix}+G\begin{pmatrix}1\\1\\1\\1\end{pmatrix} \tag{2.22}$$

where G is the spin-pair generation rate. The non-diagonal terms reveal the coherent superpositions of the eigenstates. In the incoherent regime after a microwave pulse (see figure 2.3), the timescale of dephasing of the spin-centres is small enough that the coherence averaged across the whole ensemble is zero. The variables r_T and r_S are the recombination probabilities of the pure triplet parallel and pure singlet antiparallel states respectively.

The matrix elements $\hat{\rho_{ii}}$ can be used to determine $\Delta\sigma_{ph}$ resulting from spin-manipulation as they influence the rates of recombination $R(t)$ and dissociation $D(t)$ within the spin ensemble. These equate to:

$$R(t) = \sum_{i=1}^{4} r_i\rho_{ii}(t) \tag{2.23a}$$

$$D(t) = \sum_{i=1}^{4} d\rho_{ii}(t) \tag{2.23b}$$

(2.23c)

where

$$r_i = r_S|\left\langle i|S\right\rangle|^2 + r_T|\left\langle i|T_0\right\rangle|^2 \tag{2.24}$$

Δn_i are proportional to the average charge carrier lifetime τ_L and the change in pair dissociation $\Delta D(t)$ and pair recombination $\Delta R(t)$ [79]:

$$\Delta n_e(t) = \tau_L \Delta[D(t) - G(t)] = \tau_L[D(t) - D^{SS} - (G(t) - G^{SS})] \tag{2.25a}$$

$$\Delta n_h(t) = -\tau_L \Delta R(t) = -\tau_L[R(t) - R^{SS}] \tag{2.25b}$$

where R^{SS} is the stead state rate of recombination. By substituting equations 2.25 into equation 2.20:

$$\Delta\sigma_{ph} = e\tau_L(d+G)\mu_e \sum_{i=1}^{4}[\rho_{ii}(t) - \rho_{ii}^{SS}](1 - \frac{r_i}{d+G}\frac{\mu_h}{\mu_e}) \tag{2.26}$$

An expression for the change in photoconductivity induced by a resonant microwave excitation is obtained by solving the differential equations 2.22 [40, 45, 79]:

$$\begin{aligned}\Delta\sigma_{ph}(t) = e\tau_L\mu_e(d+G)\Bigg[&(\Delta\rho_{11} + \Delta\rho_{44})(1 - \frac{r_T}{d+G}\frac{\mu_h}{\mu_e})e^{-(r_T+G+d)t} \\ &+ (\Delta\rho_{22} + \Delta\rho_{33})(1 - \frac{\frac{1}{2}(r_S+r_T)}{2(d+G)}\frac{\mu_h}{\mu_e})e^{-\frac{1}{2}(r_S+r_T+2G+2d)t}\Bigg]\end{aligned} \tag{2.27}$$

where $\Delta\rho_{ii} = \rho(t_{tr}=0) - \rho_{ii}^{SS}$ is the difference between the the eigenstate density immediately following a microwave excitation(see figure 2.3) and the steady state eigenstate density.

There are several noteworthy insights that can be learnt from equation 2.27. Firstly, $\Delta\sigma_{ph}$ is strongly dependent on the charge carrier probabilities, r_i, d and G. Secondly, after the microwave excitation induces transitions between the pure triplet states $|T_+\rangle$ and $|T_-\rangle$ and the mixed state $|T_0\rangle$, each set of states' transients behave independently, based on their differing recombination rates r_T and $\frac{1}{2}(r_S+r_T)$ and the differing eigenstate populations $(\Delta\rho_{11} + \Delta\rho_{44})$ and $(\Delta\rho_{22} + \Delta\rho_{33})$. Thirdly, the current transient will be a linear combination of two exponentials, with time constants:

$$\tau_q = -^2/_{(r_S+r_T+2G+2d)}, \tau_e = -\frac{1}{r_T+G+d} \tag{2.28}$$

where τ_q is the fast-acting time constant that models the systems return to near thermal

equilibrium as the recombination is 'quenched' and τ_e is the slow-acting time constant that models the system's return to thermal equilibrium after the small current 'enhancement' due to the overshot response following the current quench (cf. figure 5.1). For the weakly coupled spin-pairs in silicon, $\Delta\rho_{11} = -\Delta\rho_{22}$, which means that the two transients will have differing amplitudes too [45].

Spin interactions dictate the photoconductivity because in silicon, spin is conserved as a result of weak spin-orbit coupling. The existence of even weak spin-orbit coupling however, means that parallel recombination must also be considered [39, 82]. The recombination rates of the system can be determined from the sum of the product of the eigenstates populations with their probability of occurring [79].

The SDR mechanism discussed in this thesis reduces the charge carrier concentration, whilst other EDMR mechanisms like spin-dependent scattering, hopping and trapping affect the mobility [45, 83, 84]. This model is for an ideal semiconductor and does not incorporate the complication of non-ideal sample realities like depletion regions and Schottky barriers at the metal-semiconductor interface observed in section 4.4 [45]. Nevertheless, an understanding of the temporal behaviour of the spin-pair system after a microwave pulse is enough information to model the experimental behaviour of the spin systems in novel doping environment in Chapters 4 and 5.

3

Rectification in nanostructures

In this chapter I analyse rectification in tri-gate nanoscale transistors with a mind for future EDMR experiments. Tri-gate transistors were developed as part of the multi-gate suite of devices used to overcome the short channel effect [85–87]. The ability of EDMR to identify paramagnetic defects and their effect on charge transport makes it well suited to interrogating the device channels. The nanoscale channel dimensions make devices susceptible to deleterious effects from charge traps, but also difficult to probe with EDMR. To the best of my knowledge, no EDMR results have been published on nanoscale tri-gate devices, which makes them a novel environment for EDMR experimentation.

Whilst this chapter does not specifically consider spin-dependent effects, it analyses an experimental difficulty that can nullify spin-dependent measurements: rectification. Rectification is an unavoidable consequence of the experimental architecture typically used for measurements that rely on microwave excitation of one form or another. For this reason, it provides a nice introduction to this thesis. The proliferation of nanodevices means that tools like EDMR will continue to be relied on to investigate novel and minute structures.

3.1 Introduction

EDMR experiments are, by their very nature, susceptible to rectification effects. Applications of high-frequency electromagnetic fields to charge sensing and manipulation have become increasingly relevant in mesoscopic devices. Coherent spin manipulation for example has developed into a sophisticated means to interrogate and control spins bound to natural and artificial defects in solid-state nanostructures. Spin-dependent charge transport measurements or radio-frequency reflectometry [88–92] have demonstrated the usefulness of high-frequency excitation for sensitive observations of confined quantum interactions. Numerous experiments have in fact considered EDMR measurements of mesoscopic transistor channels [83, 93–95]. The heightened popularity of donor spins in silicon devices as potential qubit candidates further highlights the applicability of high-frequency fields to nanostructures to coherently manipulate spins centres [10, 13, 18, 19, 22, 96]. Similarly microwave electric fields have been shown to induce mesoscopic currents [97, 98]. High frequency gate voltages can be used to drive transport in electron pumps [99–101] whilst microwave photons can drive tunnelling between GaAs quantum dots [102, 103]. In all of these applications, coupling of the microwave fields to metal components of the device as well as the device leads can lead to spurious currents that veil the coherent effects the high-frequency fields aim to induce.

The manifestation of non-linearities in the output characteristics can be caused by the shrinking of solid state devices to only a few nanometres in length, which brings with it inherent non-linear quantum-confinement effects [87]. These non-linearities will only exacerbate rectification effects that can obscure the observation of important physical effects.

3.1.1 Electric and magnetic field coupling typical in EDMR measurements

Figure 3.1 shows two 2D maps of the current response I_D through a TOLOP transistor with dimensions $h = 11$ nm, $l = 15$ nm and $w = 30$ nm when (a) there is no microwave fields and (b) under 20 mW of microwave irradiation. Irradiation is supplied by a *Bruker*

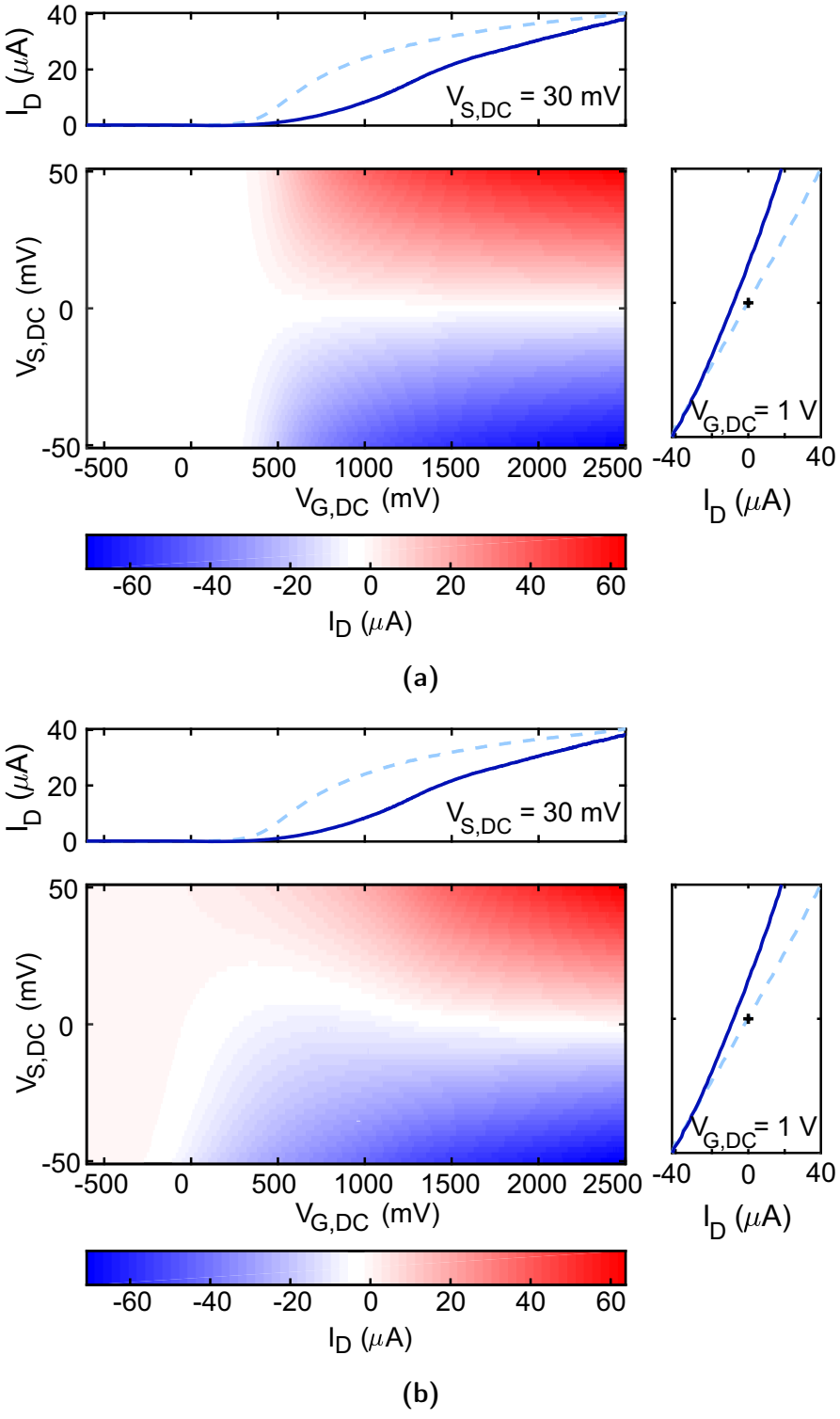


Figure 3.1: I_D response without and with rectification. The 2D maps shows the source voltage $V_{S,DC}$ and gate voltage $V_{G,DC}$ swept without **(a)** and with **(b)** microwave electromagnetic fields coupling to the device circuitry and inducing AC voltages on the device leads. The dashed light blue lines (taken from voltage cuts in the 2D map in **(a)**) are the current response without any microwave fields at $V_{S,DC}$ = 30 mV [top] and $V_{G,DC}$ = 1 V [right], whereas the solid dark blue lines (taken from voltage cuts in the 2D map in **(b)**) include the rectified current response. The device used here has channel dimensions of $h \times l \times w = 11 \times 15 \times 30$ nm.

MD5 TE_{011} cylindrical microwave cavity typically used for EDMR experiments. The plots above and beside the two maps show the variation in the measured current as a result of the coupling of the metal circuitry to the microwave fields. The dashed light blue lines show the current I_D under zero microwave irradiation (P_{mw} = 0 W), whereas the solid dark blue lines are the current responses I_D, which includes coupling to the microwave fields.

The following nomenclature will be used throughout this chapter:

1. The DC gate voltages is represented by $V_{J,DC}$ where $J = S$(source), D(drain), G(gate).

2. AC voltage amplitudes are represented as $\upsilon_j(t)$ where $j = s$(source), d(drain), g(gate). When the AC voltages are superimposed on the applied DC voltages, the total voltage is represented by $V_J(t) = V_{J,DC} + \upsilon_j(t)$; for example, $V_G(t) = V_{G,DC} + \upsilon_g(t)$.

3. $I_{D,DC}$ is the DC drain current, I_{rect} is the rectified current measured at the digital multimeter. Thus, $I_{DMM} = I_{rect} + I_{D,DC}$ is the total (AC+DC) current measured at the digital multimeter.

Coupling of cavity's electric field ($\boldsymbol{E_1}$) and $\boldsymbol{B_1}$ fields to the source and/or drain induces an AC voltages $\upsilon_{s,d}$ superimposed on the existing applied DC voltage $V_{S/D,DC}$ applied to the source or drain. Coupling between the magnetic field in the cavity $\boldsymbol{B_1}$ intended for spin excitation and the 'electronic loop' formed by the device electrical connections leads to Faraday induction [104–106]. In this case, the induced electromotive force is

$$\begin{aligned} emf &= -N\frac{\Delta\Phi}{\Delta t} \\ &= -N\frac{\Delta(\boldsymbol{B_1}\cdot\boldsymbol{A})}{\Delta t} \\ &= -N\frac{\Delta(B_1.Acos\theta)}{\Delta t} \end{aligned} \tag{3.1}$$

where θ is the angle between the normal to the area A of the conductive loop and the cavity's magnetic field $\boldsymbol{B_1}$, whose square is proportional to P_{mw}.

Similarly, coupling of the conductive wires to the $\boldsymbol{E_1}$ field of the cavity can induce

a potential [94]. This is accentuated by distortion of the local field due to the dielectric sample in the cavity [107].

3.1.2 Rectification in a three terminal device

The unwanted coupling between both metallic elements in the cavity and the dielectric sample to the cavity's electromagnetic fields also leads to distortion of the cavity mode's field pattern [107–109]. When there is only coupling to the device bias terminals, the device turn-on voltage remains unchanged, though the magnitude of the current through the device increases since $I_D(t) \propto V_{DS}^2$ as per equation 3.2.

When coupling of $\boldsymbol{E_1}$ and $\boldsymbol{B_1}$ fields to the gate occurs, the induced voltage υ_g has the effect of a virtual reduction of the threshold voltage V_T at a value proportional to the magnitude of the induced gate voltage [104, 110]. Although V_T is a property intrinsic to the device, the net gate voltage is actually $V_G(t) = V_{G,DC} + \upsilon_g$.

Measurement schemes like EDMR are usually performed using a typical EPR setup, where samples are deliberately placed inside a microwave cavity at a $\boldsymbol{B_1}$ field antinode and $\boldsymbol{E_1}$ node. This maximises microwave excitation whilst minimising electric field effects. Conductive circuit elements must traverse the field pattern and therefore unavoidably couple to $\boldsymbol{B_1}$ and $\boldsymbol{E_1}$. Minimising coupling of the cavity's $\boldsymbol{E_1}$ and $\boldsymbol{B_1}$ to these elements, whilst still sufficiently exciting the sample with microwave fields presents an interesting challenge. Several strategies can be employed to minimise the coupling:

1. Minimise the dielectric constant of the sample mount and substrate;

2. Fabricate metallic elements below the skin depth;

3. Apply a capacitive shunt across the active region of a device to protect against transverse $\boldsymbol{E_1}$ field coupling to the sample surface [94];

4. Fabricate long samples so that the wire bonds connecting the sample to its mount are outside the cavity;

5. Deliver microwave excitation via an alternative architecture like a microstrip antenna [13, 111] or a bridged loop gap resonator [112–116] that minimises $\boldsymbol{E_1}$ fields

near the $\boldsymbol{B_1}$ antinode;

6. Minimise the loop height of the bonding wires inside the cavity to reduce Faraday induction; and

7. Change the location of the sample in the microwave cavity or change the cavity type and mode to ensure the sample sits at an $\boldsymbol{E_1}$ node rather just near it.

Bruker EPR Spectrometers regularly rely on dielectric TE_{011} circular mode cavities as they demonstrate high Q-values useful for cwEDMR measurements. $\boldsymbol{E_1}$ fields are a minimum at the cavity's centre though immediately grow radially. As a sample cannot occupy an infinitesimally small space, coupling of the sample to transverse $\boldsymbol{E_1}$ fields parallel to its surface is inevitable. Point 7 listed above considers, for example, placing the sample on the side wall inside a TE_{102} cavity. Here, there still exists a $\boldsymbol{B_1}$ field antinode and $\boldsymbol{E_1}$ node, though the sample's exact location is known as it pressed up again the cavity wall, where the transverse $\boldsymbol{E_1}$ fields are effectively zero and therefore demonstrate minimal coupling to the sample, bond wires and metal tracks. For pre-fabricated start-of-the-art devices that are not purpose built for EDMR like the ones I will discuss in Section 3.2, only recommendations 6-7 and the latter part of 5 can be achieved.

When a generic three terminal device like a metal oxide semiconductor field effect transistor (MOSFET) is operating in the linear regime (when $V_{DS} \leq V_{GS} - V_T$), the drain current $I_D(t)$ Is a function of the drain-source voltage V_{DS} and is described by [80]:

$$I_D(t) = \frac{\mu C_{OX} w}{2l}[2(V_{GS} - V_T)V_{DS} - V_{DS}^2] \tag{3.2}$$

where $k = \frac{\mu C_{OX} w}{2l}$ in the transistor constant, μ is the electron mobility, $C_{OX} = \frac{\epsilon_0 \epsilon_r}{d}$ is the gate capacitance, l is the channel length, w is the channel width, and d is the thickness of the oxide.

Assuming there is no induced voltage on the gate (for now), and using Kirchoff's voltage law in the two separate loops in figure 3.2, I identify that $V_{GS}(t) = V_{G,DC} + \upsilon_s$ and

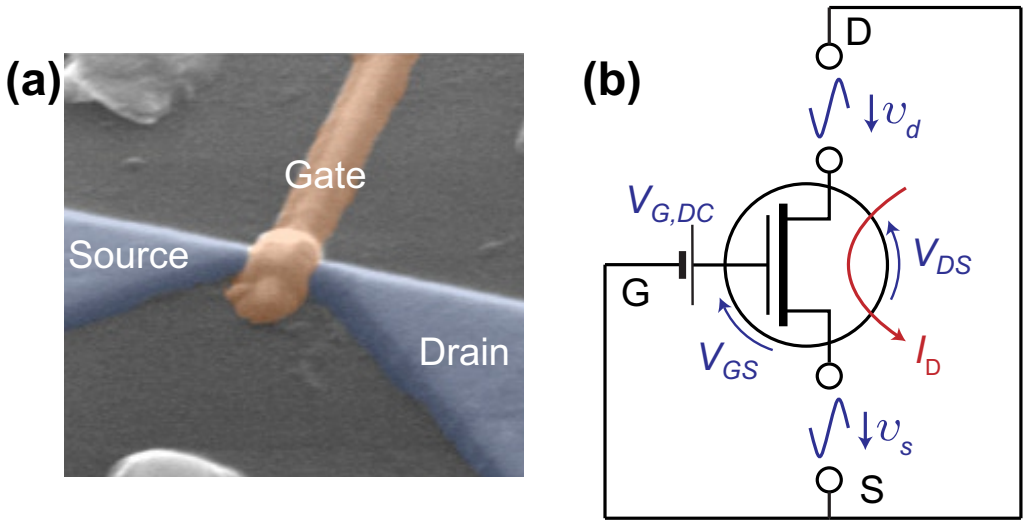


Figure 3.2: The tri-gate transistor. (a) An SEM image of the device. Image taken from [117]. **(b)** A circuit diagram of the tri-gate transistor including the induced AC voltages. Figure (b) created by Dr. Jan Mol, 2016.

$V_{DS}(t) = \upsilon_d + \upsilon_s$ under zero drain/source DC bias voltage ($V_{DS,DC} = 0$). Substituting these into equation 3.2, I get

$$I_D(t) = k[2(V_{G,DC} + V_T)(\upsilon_d + \upsilon_s) - (\upsilon_d^2 - \upsilon_s^2)] \tag{3.3}$$

When the device is operated around a quiescent point so that it operates in the linear regime for the whole period of the oscillating voltages, that is $\upsilon_d, \upsilon_s < (V_G - V_T) > 0$, equation 3.3 remains true for the whole period too. The subsequent average rectification current (ignoring the existing current from normal transistor operation using DC biases) is given by:

$$\overline{I_D(t)} = k[(\overline{\upsilon_d} + \overline{\upsilon_s}) - (\overline{\upsilon_d^2} - \overline{\upsilon_s^2})] \approx -k(\overline{\upsilon_d^2} - \overline{\upsilon_s^2}) = \gamma P_{mw} \tag{3.4}$$

Ferrari *et al.* note that γ is dependent on the area of the electronic loop coupled to $\boldsymbol{B_1}$ where they only consider magnetic induction as a cause of the oscillating voltages [104]. Equation 3.4 importantly highlights that the average stationary current depends on the induced voltage mismatch between the source and drain [104]. If the induced voltages υ_d and υ_s are equal and in-phase, the rectification effect would be symmetric and therefore the net rectification current would be zero.

The biasing voltages ($V_{G,DC}, V_{S,DC}$) also play a critical role in the rectifying behaviour of AC voltages. For ohmic behaviour where the output current is linearly proportional to applied DC voltage $I_D \propto aV_I$, $I = \{G, S, D\}$ and $a \in \mathbb{R}$, the induced AC voltages are cancelled out during the rectification process by the time-averaged integration resulting from measurements $\int_0^T (\cos(\omega t + \varphi)dt = 0$. This can occur when υ_i is small enough for the current response to appear ohmic, when the device is operating in the linear regime ($V_S(t) < V_G(t) - V_T$) or when there is linear $V_G(t)$ to $I_D(t)$ transfer for $V_T < V_G(t) < V_{SAT}$, where V_{SAT} is the voltage at which the channel is completely opened. Any non-linear voltage-to-current conversions on the gate or source-drain terminals however, rectify the induced voltage. MOSFETs, particularly at the nanoscale, are characteristically non-linear [87], and rectification effects in such instances are more dramatic. A non-ohmic metal-semiconductor interface (MSI) is another culprit that rectifies induced voltages [94, 104]. For this non-linear behaviour, in time-averaged observations the rectified voltage results in net DC offsets where $\int_0^T I_D(V_S(t) + V_G(t))dt \neq 0$ [94].

3.1.3 Rectification in EDMR measurements of non-linear devices

EDMR is an important tool for spin manipulation and readout. Rectification in EDMR measurements of novel, non-linear gated nanodevices is therefore an important consideration [94]. Given the lock-in scheme used in cwEDMR measurements is a time-averaged process, the induced antisymmetric current in the rectification process will offset the bias voltage induced current [104].

The effects of microwave absorption by anything other than the device-under-test in a cavity will induce noise in EDMR measurements. Unwanted microwave absorption from conductive elements or spin-active foreign species in the cavity (to be discussed further in sections 3.4.1-3.4.2) alters the local microwave environment of a MOSFET, increasing $\boldsymbol{E_1}$- and $\boldsymbol{B_1}$-field induction and varying the spin behaviour expected in the channel. Microwave absorption of any sort within the cavity modifies the field experienced by the device [107, 108]. Typical EDMR signals are of the order of $\Delta I/I \sim 10^{-5}$, providing little leeway for noisy and unintended current fluctuations. Coupling between leads of

a MOSFET device and microwave fields induces AC voltages on the device terminals which are rectified and provide unintended bias conditions. Absorption at the device leads, which have a microstrip-like structure can cause broadening due to enhancement of $\boldsymbol{B_1}$ at the device [118]. Similar absorption can occur in a chip of devices like in our measurements, which includes approximately 150 devices and a $\sim$1 mm thick substrate. Absorption of microwave energy by the device 2DEG is necessary for EDMR measurements of the channel donors [93, 119, 120], though absorption by the substrate does not facilitate channel measurements [105]. Vibrations of the experimental setup result in fluctuations in the bias voltages. υ_G variation opens and closes the channel at the microwave frequency ($f_{\mu w}$) but also varies the potential at channel charge traps causing (de)trapping related charge fluctuations [121]. In MOSFETs induced voltages also vary the carrier density at the terminals affecting the channel resistance [104]. In state-of-the-art devices this is particularly relevant for two reason: first, the wrap-around gate of modern multi-gate devices gives greater electrostatic control of the channel but also makes the device performance more susceptible to voltage noise on the gate. Second, charge build-up in a channel of nanometre dimensions makes the device more susceptible to drain-induced barrier lowering (DIBL) [87]. This is manifested as variations of the current through the device and therefore noise in the EDMR signal [94].

3.2 TOLOP tri-gate transistors

TOLOP devices were used for my rectification measurements with the aim to ultimately measure EDMR in the device channel. The device fabrication and make-up is in ref. [89]. The devices were fabricated at the Atomic Energy Commission (CEA) in Grenoble, France. CMOS technology is used to develop a triple- or 'tri-gate' transistors, where the gate maintains electrostatic control of the channel on its top and two sides [87]. Quantum transport through their nanoscale channels has been investigated in numerous publications [88–92, 122]. The channel is a nanowire etched from a 300 nm silicon on insulator (SOI) film. The gate stack consists of a insulating SiO_2 layer of a few angstrom underneath a hafnium silicon oxynitride (HfSiON) layer. This is followed by a titanium

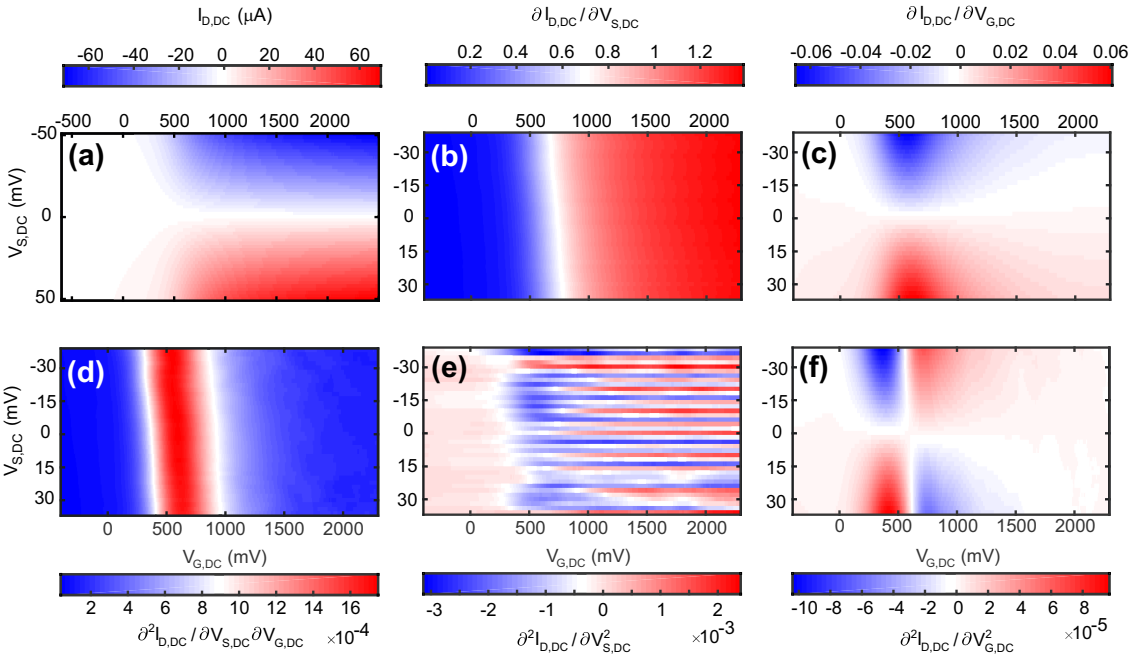


Figure 3.3: Voltage dependent current and conductance. (a) $I_{D,DC}$, (b) ${}^{\partial I_{D,DC}}/_{\partial V_S}$, (c) ${}^{\partial I_{D,DC}}/_{\partial V_G}$, (d) ${}^{\partial^2 I_{D,DC}}/_{\partial V_G V_S}$, (e) ${}^{\partial^2 I_{D,DC}}/_{\partial V_S^2}$, (f) ${}^{\partial^2 I_{D,DC}}/_{\partial V_G^2}$.

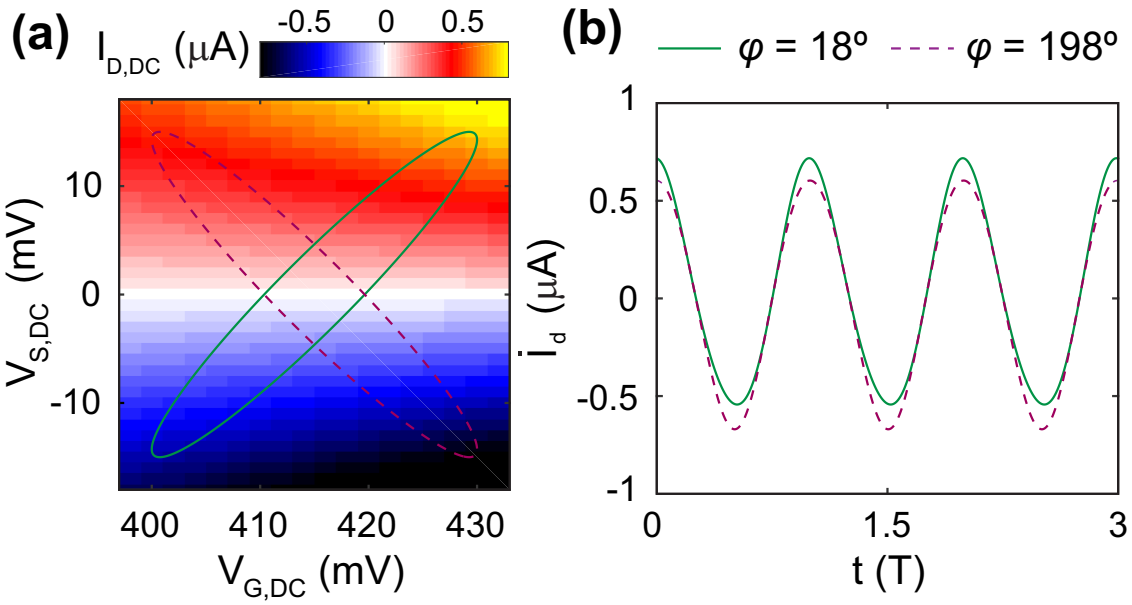


Figure 3.4: The effect of a change in phase φ. **(a)** A trajectory of the current for two arbitrarily chosen φ values. **(b)** Unrectified AC current i_d for two arbitrarily chosen phases 180° apart; in this case φ=18° and 198°. When rectified, the measured DC currents I_{DMM} for each phase differ in magnitude. Figure created by Dr. Jan Mol, 2016.

nitride and polycrystalline silicon conducting layer. The device is in figure 3.5.

It is worth noting that a typical antenna element is a quarter wavelength, $\lambda/4$. The devices I used had dimensions $l \times w \times h$. For the microwaves used for spin excitation, $\frac{\lambda_{mw}/4}{l,w,h} \approx 10^6$ and as such, the coupling of the microwaves to the conducting channel region is not the cause of the rectifications effects. The chip that has dimensions of an order of magnitude smaller than the wavelength, and the longer wirebonds and printed circuit board metal tracks are more likely to couple to fields and distort the field patterns.

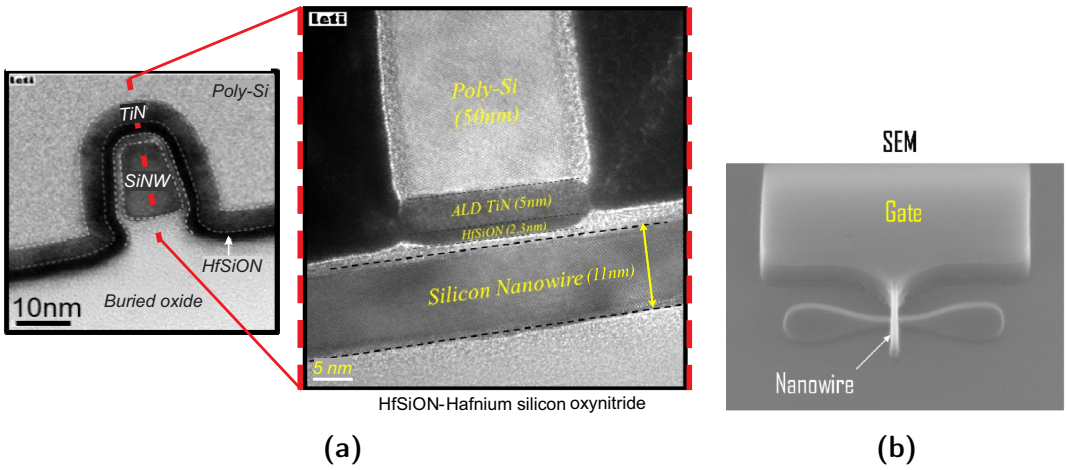


Figure 3.5: TOLOP tri-gate transistor. A typical TOLOP transistor. **(a)** Cross-sectional views of the [Left] silicon nanowire that acts as the channel. The red dotted line shows the cross-sectional cut along the source/drain axis depicted in [right] figure. **(b)** SEM image of a TOLOP device showing the wrap-around gate over a silicon nanowire. Images taken from ref. [89].

3.3 Rectification model

Quantifying the rectification contribution is essential when analysing experimental results because it may obscure the phenomenon under investigation [94, 123]. However this requires detailed knowledge of the device under test. Theories and work-arounds have been developed for specific environments and experiments such as MOSFETs and quantum dots [94, 98, 101, 104, 110]. Here, I present an approach for evaluating the rectification current in non-linear three-terminal devices. My method is not limited by the types of devices and is valid as long as the frequency of the microwave radiation is in the regime where the parasitic capacitances between source/gate-drain are negligi-

ble. In the presence of microwave radiation, the drain current measured at the digital multimeter (DMM), $I_{DMM}(V_S, V_G)$ (sometimes called the 'stationary current' [104] or 'time-averaged current' [94]) for a given set of applied DC source-drain (V_S) and gate-source (V_G) voltages can written as

$$I_{DMM}(V_{S,DC}, V_{G,DC}) = \frac{Q(t)}{T} = \frac{1}{T}\int_0^T I_{D,DC}(V_S(t), V_G(t))dt \tag{3.5}$$

where $I_D = I_{D,DC} + i_d$ and $I_{D,DC}$ is the DC current in the absence of microwave radiation and i_d is the microwave induced current. $T = 1/f_{mw}$ is the periodicity of the microwaves and $V_S(t)$ and $V_G(t)$ are the sum of the applied DC and microwave-induced AC voltages on the source and gate respectively. These equal

$$\begin{aligned} V_S(t) &= V_{S,DC} + \upsilon_s \cos(\omega t), \text{ and} \\ V_G(t) &= V_{G,DC} + \upsilon_g \cos(\omega t + \varphi) \end{aligned} \tag{3.6}$$

where $\omega = 2\pi f_{mw}$ and υ_s and υ_g denote the amplitudes for the microwave-induced oscillating source-drain and gate-source voltages, respectively and φ is the phase difference between these oscillating voltages is φ. The measured current I_{DMM} can always be evaluated numerically by equation 3.5 if the normal source/gate voltage dependence of the device has been characterised without microwave radiation. Alternatively, I can express the instantaneous device current $I_{D,DC}(V_S(t), V_G(t))$ by a Taylor series and calculate the I_{DMM} by considering the leading non-zero terms. For a generic Taylor series described by

$$\begin{aligned} f(x,y) = {} & f(x_0,y_0) \\ & + (x+x_0)\frac{\partial f(x_0,y_0)}{\partial x} + (y+y_0)\frac{\partial f(x_0,y_0)}{\partial y} \\ & + \frac{1}{2!}[(x+x_0)^2\frac{\partial^2 f(x_0,y_0)}{\partial x^2} + 2(x+x_0)(y+y_0)\frac{\partial^2 f(x_0,y_0)}{\partial x \partial y} \\ & + (y+y_0)^2\frac{\partial^2 f(x_0,y_0)}{\partial y^2}] + ... \end{aligned} \tag{3.7}$$

the two-dimensional Taylor series to the second order for $I_D(V_S(t), V_G(t))$ can be written as

$$\begin{aligned} I_D(V_S(t), V_G(t)) = I_{D,DC}(V_{S,DC}, V_{G,DC}) \\ + \upsilon_s \cos(\omega t)\frac{\partial I_{D,DC}}{\partial V_{S,DC}} + \upsilon_g \cos(\omega t + \varphi)\frac{\partial I_{D,DC}}{\partial V_{G,DC}} \\ + \frac{1}{2}[\upsilon_s^2 \cos^2(\omega t)\frac{\partial^2 I_{D,DC}}{\partial V_{S,DC}^2} + \upsilon_g^2 \cos^2(\omega t + \varphi)\frac{\partial^2 I_{D,DC}}{\partial V_{G,DC}^2} \\ + 2\upsilon_s\upsilon_g \cos(\omega t)\cos(\omega t + \varphi)\frac{\partial^2 I_{D,DC}}{\partial V_{S,DC}\partial V_{G,DC}}] + O(3), \end{aligned} \tag{3.8}$$

where all derivative terms are evaluated at $V_S(t) = V_{S,DC}$ and $V_G(t) = V_{G,DC}$. The first term is the time-independent current, unperturbed by the oscillating voltages υ_i, where $i : \{s, g\}$. The second and third terms represent the ohmic response of the device, which cancel out in time-averaged measurements. The remaining fourth, fifth and sixth terms describe the non-linear response of the device, which are important for the outcome of rectification effects. To determine the measured current under rectification I_{DMM}, I consider the time-averaged current by substituting in the Taylor series expression in equation 3.8 into equation 3.5. The ohmic terms disappear as I know that $\int_0^T \cos\omega t dt = 0$, and the measured current is therefore

$$\begin{aligned} I_{DMM}(V_{S,DC}, V_{G,DC}) &= I_{D,DC}(V_S, V_{G,DC}) + \frac{1}{4}[\upsilon_s^2\frac{\partial^2 I_{D,DC}}{\partial V_{S,DC}^2} + \upsilon_g^2\frac{\partial^2 I_{D,DC}}{\partial V_{G,DC}^2} \\ &+ \ 2\upsilon_s\upsilon_g \cos\varphi\frac{\partial^2 I_{D,DC}}{\partial V_{S,DC}\partial V_{G,DC}}] \\ &= I_{D,DC} + i_{rect} \end{aligned} \tag{3.9}$$

where $i_{rect} = I_{DMM} - I_{D,DC}$ is the measured rectification current. Equation 3.9 presents a straightforward way with which to simulate the rectification current. The fit of a rectified current-voltage sweep is in figure 3.6. As expected, the rectification is dominated by non-linear terms. The partial derivative terms can be derived directly from the 2D map of the voltage dependent current response as seen in figure 3.1, whilst the coefficients and therefore i_d are purely determined by the magnitude and phase of the field induced AC voltages on the device terminals. i_d is also linearly dependent on the microwave power P_{mw} since the square of each voltage term is proportional to the microwave

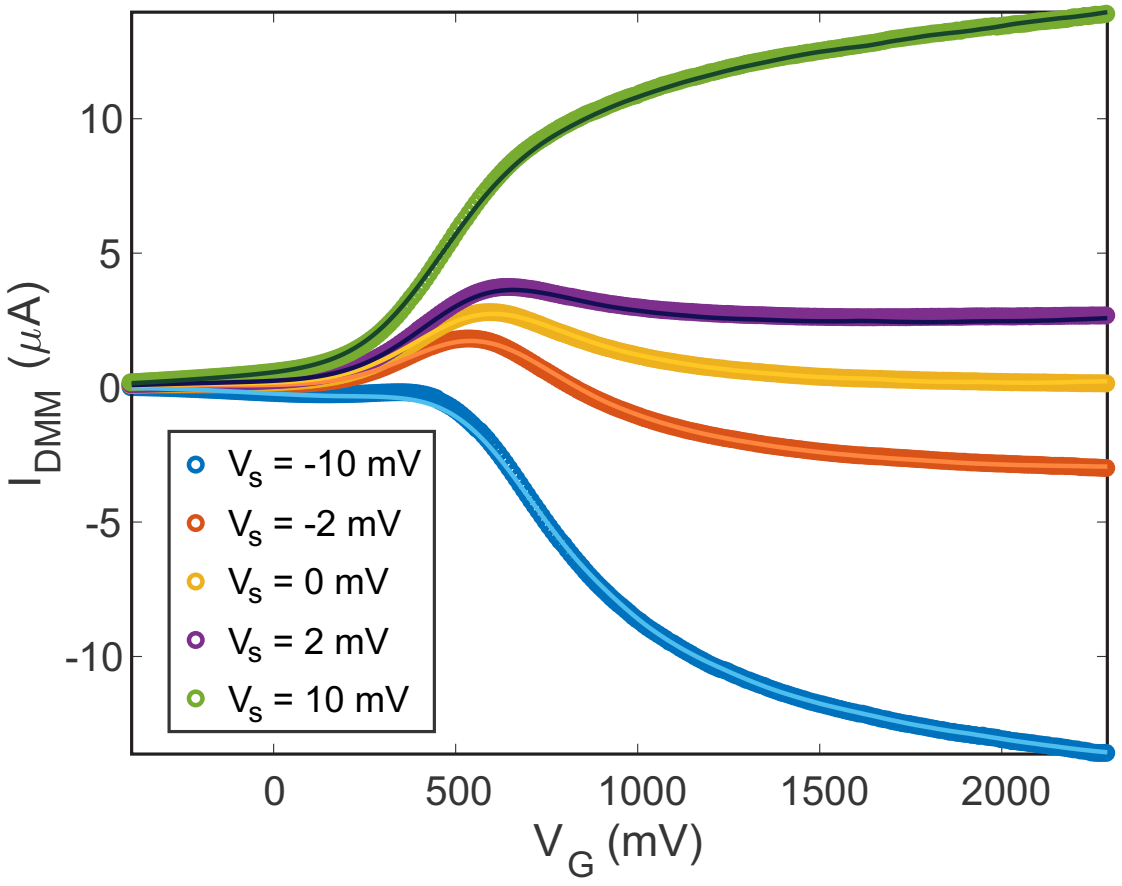


Figure 3.6: Fitted rectified current response. Measured current I_{DMM} for a swept V_G for V_B = 0,±2, ±10 mV. The overlapping circles that appear to be a thick line is the data, the thin line is the fit. The fitted parameters are υ_g = 174.2 mV, υ_s = 21.1 mV and φ=0°.

power; that is, $P_{mw} \propto |\upsilon_i|^2$ [104]. As previously specified, υ_s denotes the AC voltage difference between the source and drain terminals. In practice an oscillating voltage is induced on both the source and drain electrical leads, though it is their difference that is relevant to the current flow in the device. Because of this, I expect $\upsilon_s < \upsilon_g$. Previous studies have focused on the varying conductance terms, where either the partial derivative of the conductance ${}^{\partial^2 I_{D,DC}}/_{\partial V_{S,DC}^2}$ or the partial derivative of the transconductance ${}^{\partial^2 I_{D,DC}}/_{\partial V_{G,DC}^2}$ does not equal zero [98, 104, 110]. In equation 3.9 I see that the rectification current is proportional to the cross term of the conductance times the transconductance. In my investigation I find this term to be particularly dominant to the rectification behaviour relative to the quiescent-point output. By swapping the source and drain terminals (that is, $\Delta\varphi = 180°$) I am able to observe the significance of φ relative to the other non-linear terms in equation 3.9 and also to i_d. The experimental results are in figure 3.7.

I simulate i_d for two arbitrary phases 180° apart (the equivalent of swapping the leads) to observe the induced current oscillations of i_d. The phase change shifts the net offset of i_d in the positive or negative direction for 0$\leq \varphi <$180° and 180° $\leq \varphi < 0$ respectively. Importantly this translates to a change in the polarity of the time-averaged signal of the rectification current $i_{rect} = \frac{1}{T}\int_0^T i_d dt$ and therefore the total time-averaged current I_{DMM}. Figure 3.7 shows the relative change in $I_{DMM}(V_{S,DC} = 0) = i_{rect}$'s polarity when the leads are swapped and highlights the dominance of the last of the non-linear terms in equation 3.9 (specifically the phase φ) in determining the magnitude and polarity of the measured rectification current. Figure 3.4 on the other hand shows a simulation of the unrectified AC current i_d for the $\Delta\varphi$=180°. Of the non-linear terms in equation 3.9,

$$|2\upsilon_s\upsilon_g \cos\varphi \frac{\partial^2 I_{D,DC}}{\partial V_{S,DC}\partial V_{G,DC}}| \gg |\upsilon_s^2 \frac{\partial^2 I_{D,DC}}{\partial V_{S,DC}^2} + \upsilon_g^2 \frac{\partial^2 I_{D,DC}}{\partial V_{G,DC}^2}|. \tag{3.10}$$

The dominance of this term is most obvious in the zero-bias ($V_{S,DC}$ = 0) case, where

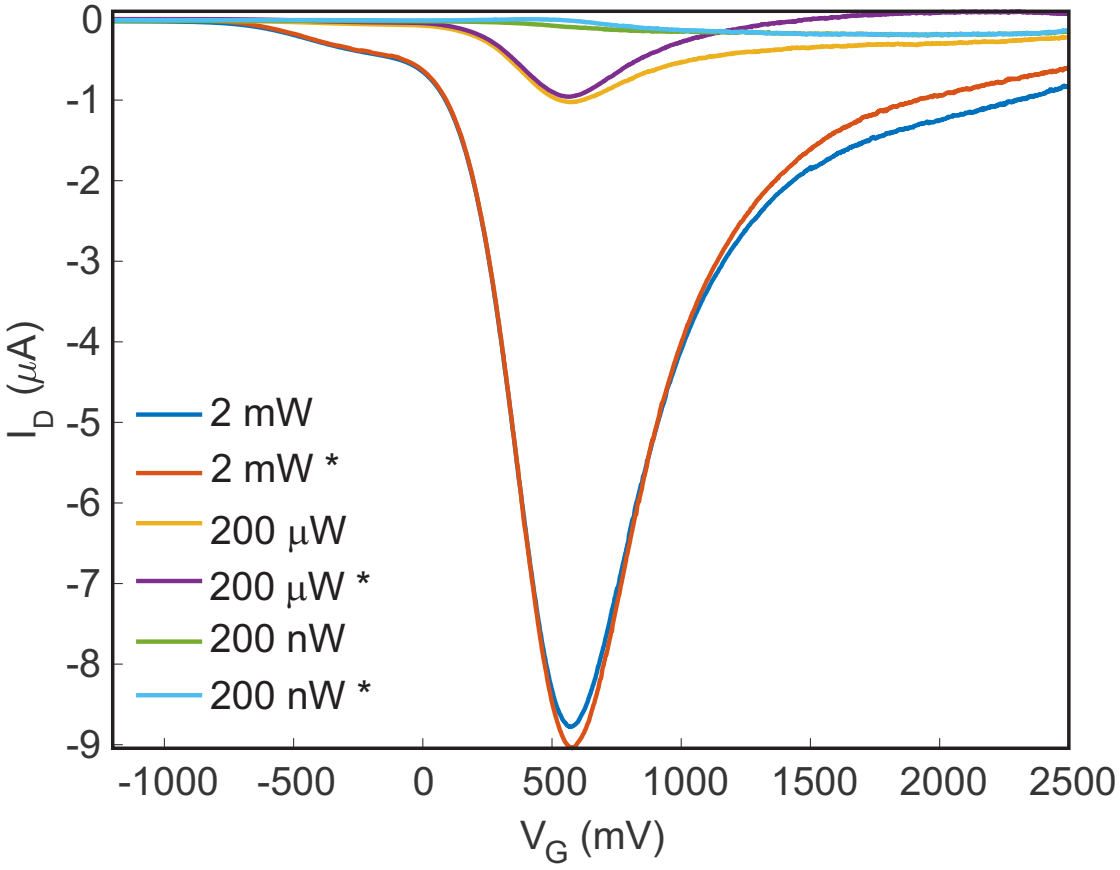


Figure 3.7: Zero-bias current response for various microwave powers. The total drain current I_D as a function of the DC gate voltage $V_{G,DC}$ with $V_{S,DC}$ = 0 mV for increasing microwave power: P_{mw} = 200 nW, 200 μW, 2 mW. Of the six measurements, the leads on the source and drain are swapped in three of them to enact a 180° phase change. The three legend entries labelled with a * have had their source and drain leads swapped and the signal I_D inverted ($\times$-1) in the plot. This is so they can be compared to the induced drain current without swapped leads. The fact that equivalent $I_D(V_{G,DC})$ sweeps mostly overlap demonstrates the dominance of the non-linear phase dependent term in the rectification current in equation 3.3.

I_{DMM} is almost equal to this last term since $I_{D,DC}(V_{S,DC} = 0, V_{G,DC}) = 0$:

$$I_{DMM}(V_{S,DC} = 0, V_{G,DC}) \approx \frac{1}{2} v_s v_g \cos\varphi \frac{\partial^2 I_{D,DC}}{\partial V_{S,DC} \partial V_{G,DC}} \tag{3.11}$$

This is plotted in figure 3.8:

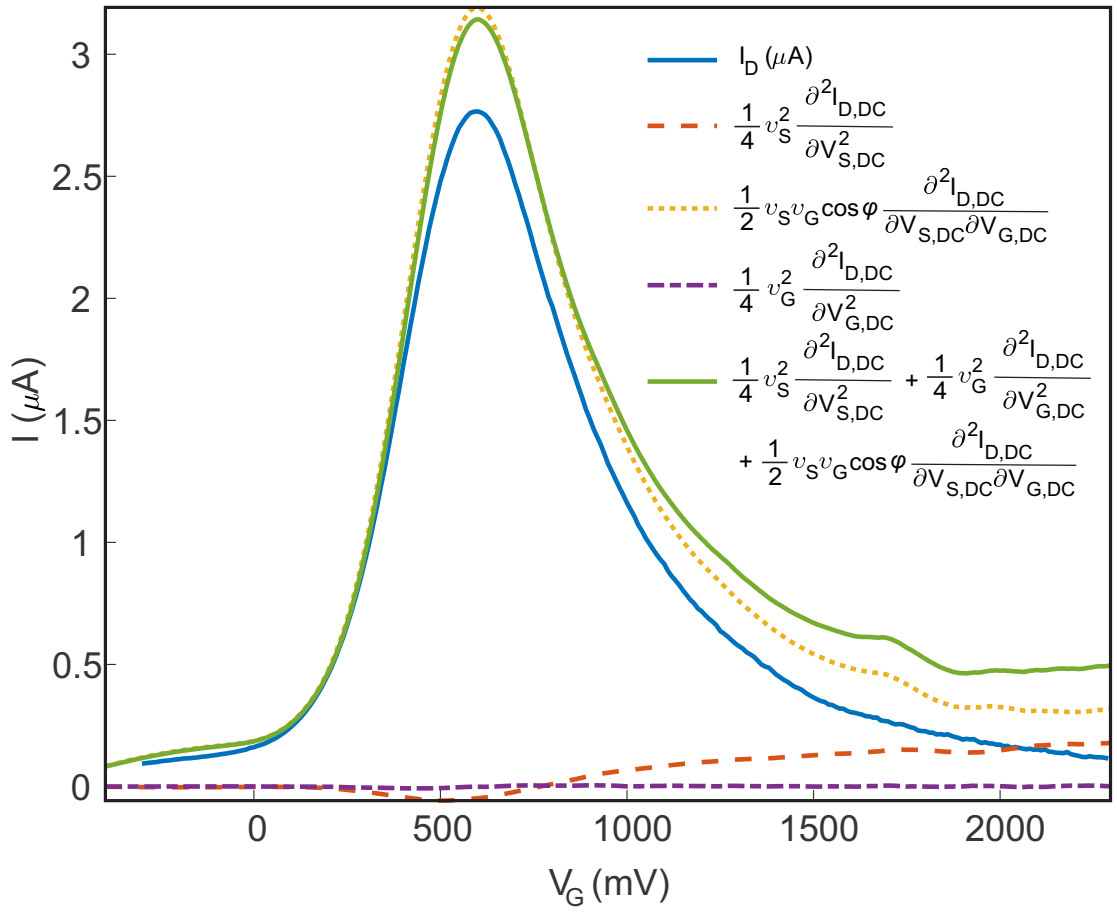


Figure 3.8: Comparison of second order partial derivative terms from equation 3.8. The cross partial derivative term $\frac{\partial^2 I_{D,DC}}{\partial V_{S,DC} \partial V_{G,DC}}$ dominates. $I_D < \frac{\partial^2 I_{D,DC}}{\partial V_{S,DC} \partial V_{G,DC}}$ because not all terms are plotted here. Inclusion of the higher order terms allow the Taylor series to tend towards $I_D(t)$.

Figure 3.3 shows that of the second order terms there is most variation in the cross derivative term ${}^{\partial^2 I_{D,DC}}/_{\partial V_{S,DC} \partial V_{G,DC}}$, which is a coefficient of the phase term $\cos\varphi$. Around the threshold voltage is where I_D variation as a function of $V_{G,DC}$ is the most non-linear and where the rectification current i_d is largest. As $V_{S,DC}$ is swept, the cross derivative term maximum value remains constant across $\Delta v_G \approx 100$ mV, which is approximately equal to $V_S (= V_{S,DC} + v_s)$. This is attributed to DIBL, which moves the gate dependent current response into the non-linear regime.

3.4 Multi-frequency EPR detected by rectification effects

Rectification introduces unwanted noise particularly in time-averaged measurements like EDMR and so it is common practice to suppress it [94]. However, when a device is operated in a non-linear regime where rectification effects are greatest, the induced voltages are also sensitive to the microwave power. The resonance of foreign spin-active species in the cavity can be detected via the change in device current I_{DMM}. Although this is an electrical detection of spin resonance, it is not EDMR in the traditional sense.

To demonstrate this, I performed experiments at both X-band (10.64 GHz) and D-band (130.5 GHz) frequencies where both the TOLOP device and a foreign spin species were exposed to microwave radiation. At constant device bias conditions, the device drain current was monitored as the B_0 was swept. Upon resonance conditions of the foreign spin-species in the cavity, microwave absorption occurred. The resultant change in the cavity's microwave standing wave power could be detected by a change in the rectification current since the AC current $i_d \propto P_{mw}$, as per equation 3.4 [104]. The experiment is very similar to a typical cwEDMR experiment where the spin-resonance of spin-species in the device channel also modulate its throughput current. Because of the potential of a device EDMR signal from the spin-interactions in the channel of the device, the output current must be corrected for any channel effects or operated in a mode where no EDMR detection occurs. Spin-dependent scattering (SDS) for example can be minimised by limiting the channel length so that the conduction electrons do not have the opportunity to polarise [93]. Alternatively a drawback of using this method with D-band experiments is that the it opens the possibility of spin-dependent tunneling (SDT).

3.4.1 Detection of DPPH in the rectification current at X-band microwave excitation

X-band measurements were performed in a home-made rectangular TE_{102} cavity of dimensions 40 × 20 × 15 mm. A TOLOP device mounted on a PCB was inserted through

a 1 × 15 mm hole cut into the side-wall of the cavity, The hole also provided access to the device for the electronic circuitry. The hole was cut in a direction parallel to the direction of the cavity's wall current density so as to cause minimal disruption to the cavity's field patterns and Q-value. The sample mounted in half of the cavity is in figure 3.9a. Several design choices were made in this setup so that rectification was not minimised:

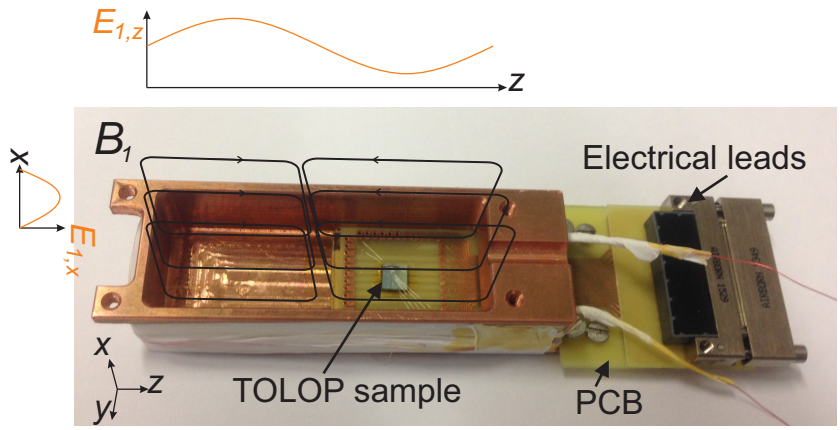
1. Some bondwires were not only perpendicular to the $\boldsymbol{E_1}$ field lines, which minimises coupling, but were also parallel, which maximises $\boldsymbol{E_1}$ coupling.

2. The bondwire loops extended several millimetres above the sample and there was also a height difference between the sample and the PCB. This mismatch increased the magnitude of the area $|A|$ for Faraday induction as per equation 3.1.

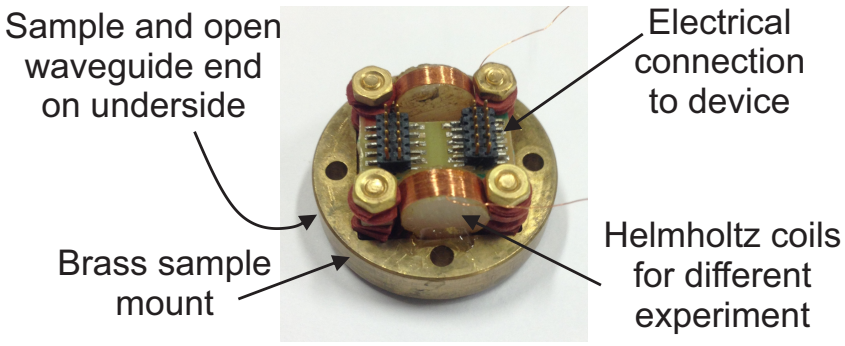
3. The sample was mounted facing the centre of the cavity. Although an $\boldsymbol{E_1}$ node exists on the walls surface, $\boldsymbol{E_1}$ increases to an anti-node midway between the walls. The sample, the metal components of the chip and the bond wires were all in non-zero $\boldsymbol{E_1}$ fields. This increased $\boldsymbol{E_1}$-coupling and mode distortion [108].

For the X-band measurement, an EPR standard substance known as 2,2-Diphenyl-1-picrylhydrazyl (DPPH) in powder form mixed with vacuum grease and the TOLOP device were mounted at the $\boldsymbol{B_1}$ field node (as depicted in figure 3.9a). This device had channel dimensions of $h \times l \times w$ = 11 × 100 × 30 nm and was biased at V_G = 600 mV and V_S = 30 mV. The microwave source was set to the frequency absorption maxima of the cavity's TE_{102} mode at f_{mw} = 10.64 GHz and was amplitude modulated at 1 kHz for lock-in detection. A superconducting magnet was used to apply the B_0 and the experiment was performed at 2.3 K. The field was swept through the range 220-420 mT.

Throughout the B_0 sweep range, a single resonance was observed at 381 mT (g=1.996) with a FWHM of 1.6 mT. This is the resonance depicted in figure 3.10 (a) and resembles DPPH with an anticipated resonance at g = 2.0023 for a low temperature measurement [124]. The difference in g-value is attributed to the remnant fields in the superconducting magnet of the spectrometer.



(a)



(b)

Figure 3.9: TOLOP device mounted for detection of resonance of foreign spin-species at X-band and D-band. **(a)** The bottom half of the TE_{102} cavity used to detect DPPH EPR. The PCB mounted sample is inserted in a gap in the cavity in the right side of the photo. The sample is at the B_1 antinode. **(b)** The brass sample mount for the D-band measurement. The sample is mounted on the underside of the 'H' shaped PCB visible on the top of the brass mount. Black multi-pin connectors facilitate the electrical connection. The wire loops were used as Helmholtz coils for field modulation in a separate measurement. The opening of a waveguide faces the underside of this mount to deliver microwaves.

It was mentioned above that these spin-detection experiments must take into account unwanted cwEDMR signals. From the reciprocal perspective, the absorption of microwave power from other spin species in the microwave cavity can prove detrimental to cwEDMR measurements, even if rectification is effectively avoided. Heavily doped sample substrates for examples, could provide phantom signals that are not the result of typical SDR, SDS or SDT signals in a device channel. As with these measurements, EDMR measurements need to consider artificial signals and isolate them where appropriate.

3.4.2 Detection of O_2 molecules in the rectification current at D-band microwave excitation

Having successfully identified the X-band resonant signal of DPPH in the measured rectification current of a tri-gate nanostructure, I examine the possibility of observing the same effect with solid O_2 molecules at D-band frequencies. Solid O_2 molecules were created at the microwave excitation space by cooling the sample without evacuating air from the sample space, which is normally in vacuum. Using this approach, the signal of $N_{2(s)}$ should also be observable. Microwaves were delivered to the sample via a waveguide to the exposed sample on the underside of the mount shown in figure 3.9b. This device was mounted on a PCB connected to an oxygen-free brass platform approximately 1 cm from the open end of the waveguide. Frequency modulation of 5 MHz at 10 kHz was enacted for lock-in detection. As with the X-band measurements, the field is swept (this time over the range 0-3 T) and I_{DMM} is monitored. The output is in figure 3.10(b). The experimental signal (black) is at the top of the figure whereas the theoretical simulation (red) is at the bottom. The simulation of $O_{2(s)}$ molecules is enacted using the following Hamiltonian:

$$\hat{\mathcal{H}} = D\hat{S}_z^2 + \mu_B g\mathbf{B}\cdot\hat{\mathbf{S}} \tag{3.12}$$

with $S = 1$, the zero field splitting parameter $D = 3.572\,\mathrm{cm}^{-1}$ with axial anisotropy and isotropic $g = 1.996$ [126, 127]. The simulation of the spectra was performed in *EasySpin* [125]. The frozen oxygen molecules behave like a powder sample, where the alignment of the molecular axis and B_0 is randomly distributed. A signal arises

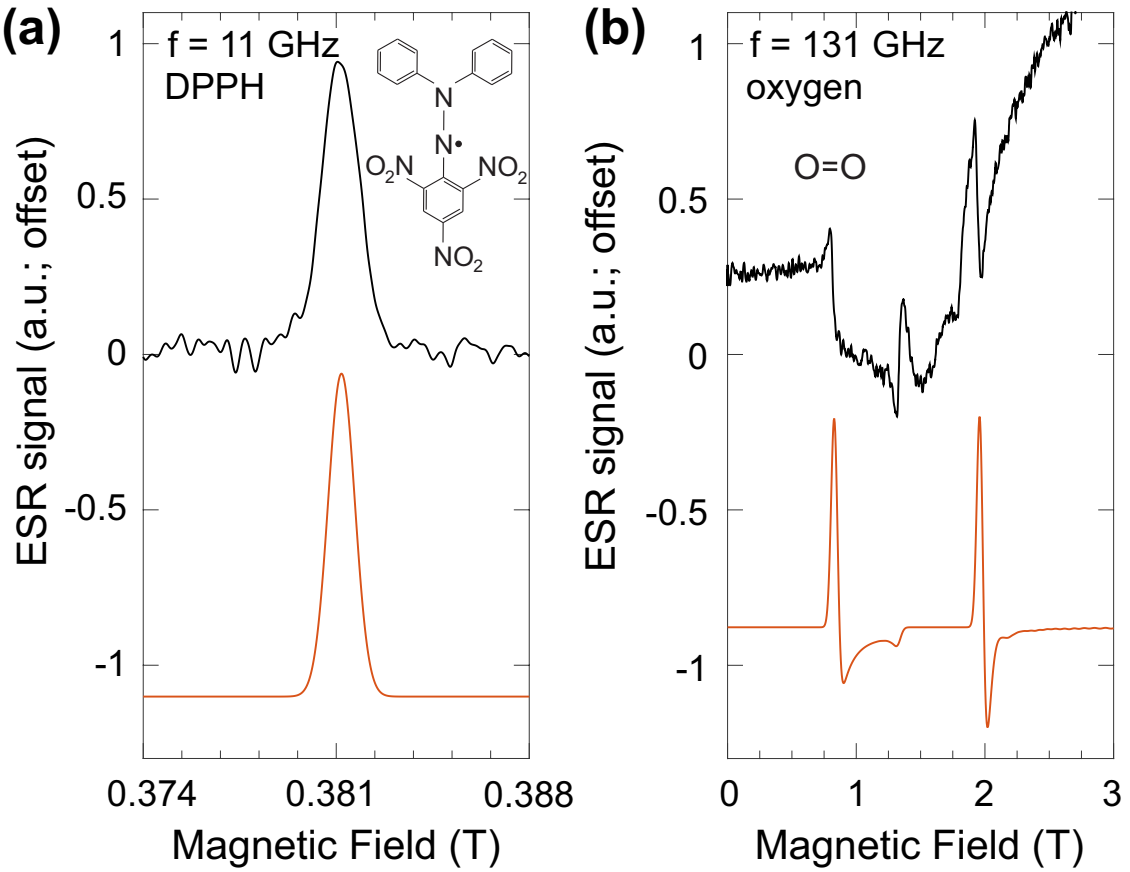


Figure 3.10: EPR detection through changes in the rectification current of a TOLOP tri-gate transistor. Experimental data (black) and theoretical simulation (red) of the EPR signals. **(a)** Current as a function of the Zeeman field averaged five times at f_{mw} = 10.64 GHz, amplitude modulated at 1 kHz for lock-in detection of DPPH. The simulation uses $S = {}^1/_2$ and $g = 1.996$. Amplitude modulation induces Gaussian absorption spectra lineshapes rather than the Gaussian derivative lineshapes usually seen in lock-in detection. **(b)** Current as a function of the Zeeman field for a single sweep at f_{mw} = 130.5 GHz, frequency modulated at 10 kHz with 5 MHz modulation depth for lock-in detection of $O_{2(s)}$ molecules. The simulation is the result of the Hamiltonian in equation 3.12, with $S = 1$, $D = 3.572$ cm^{-1} and $g = 2$. The distortion of the anticipated Gaussian derivative lineshape is likely due to a combination of over modulation and the nonlinearity of the detector device. The ordinate axis is labelled EPR as the output is a reflection of the foreign species spin resonance. A label of i_{DMM} is equally valid as it is a measurement of the current through the device. The measurement is not EDMR in the traditional sense. Simulations were performed in *EasySpin* by Dr. Junjie Liu, 2016 [125].

at the two turning points corresponding to molecular axis parallel and perpendicular to B_0. These transitions are identified in figure 3.11. The bump at ~ 1.3 T in the simulation is the result of the superposition of all the angle dependent resonances that contribute to the powder spectrum. Whilst the experimental lineshape at ~ 1.3 T differ somewhat from the simulation, this can be attributed to distortion of superposition of angle dependent resonances caused by the signal background and potential power saturation of the transitions. There is no other obvious transition in figure 3.11 that could explain the spectrum at ~ 1.3 T, particularly since it is not the correct B_0 for a half-field transition ($\Delta m_S = 2$).

A broad background exist in the D-band measurement, possibly as a result of the frequency modulation scheme used or mechanical vibrations in the setup. Regardless, the sharp oxygen signals are distinguishable and superimposed on this. This signal is a demonstration of the EPR of $O_{2(s)}$ being observed through the change in the rectification current I_{DMM} as a function of B_0 at $f_{mw} > 130$ GHz. Our measurement scheme

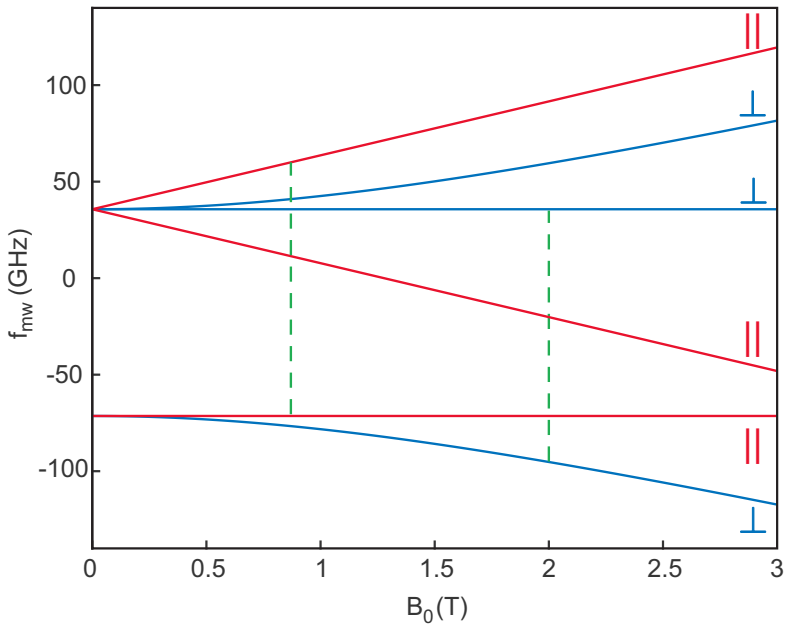


Figure 3.11: Energy level diagram of $O_{2(s)}$. The energy level diagram for the molecular axes parallel (red) and perpendicular (blue) to B_0. The two green dashed lines at approximately 0.87 and 2 T show the two spin transition seen in figure 3.10 at $f_{mw} = 130.5$ GHz for $\Delta m_S = 1$.

provides several unique advantages of typical EPR measurements schemes at D-band frequencies. Firstly, this setup reduces the size of the detection apparatus and the typical

signal attenuation that is unavoidable at D-band frequencies. The chip used in these measurements contains approximately 150 devices. By dicing the chip into individual samples my detection apparatus could occupy an even smaller area in the experimental setup.

Secondly, for protection from the large static field needed for EPR at D-band frequencies, the detection apparatus' ferromagnetic components are often spatially isolated from the magnet. Particularly at D-band frequencies, this long transmission distance can lead to attenuation of the microwaves (if free space transmissions are not available). My setup also avoids the need for the long waveguides used to return the reflected radiation signal back to the detection setup.

Thirdly, some part of the D-band microwave frequency to DC conversion occurs at cryogenic temperatures when the induced AC voltages are non-linearly transferred to a drain current. The transistor has a gain, which means it also acts like a cryogenic amplifier. Johnson-Nyquist or 'thermal noise' is proportional to $\sqrt{T}$, which means this conversion makes use of the 10 times lower thermal noise at 2.3 K. Although the digital multimeter has room temperature thermal noise, the signal is converted to DC and amplified whilst the thermal noise floor is low, thus improving the SNR. The SNR ratio however, is still affected by other factors like the sample concentration and field inhomogeneity due to the position of the $O_2(s)$.

3.5 Conclusion

I have analysed the rectification current induced by microwave radiation in tri-gate transistor nanostructures. The term $2\upsilon_s\upsilon_g \cos\varphi \frac{\partial^2 I_{D,DC}}{\partial V_{S,DC}\partial V_{G,DC}}$ from the 2D second order Taylor expansion was found to be dominant in determining the nature of the rectification current. The phase difference φ between the induced AC voltage on the gate and the source/drain dictates the polarity of the rectification current, whilst the partial derivative term $\frac{\partial^2 I_{D,DC}}{\partial V_{S,DC}\partial V_{G,DC}}$ was shown to dictate the magnitude of the rectification current.

Whilst detrimental to time-averaged measurements like cwEDMR, the change in the rectification current was shown to be a sensitive microwave detector by measuring the

EPR signal of foreign spin-species in the sample space across a broad range of frequencies ($\sim$10-130 GHz). This scheme relies on typical EDMR apparatus, though it uses the sensitivity of non-linear nanoscale tri-gate TOLOP transistors to observe changes in the microwave power induced by EPR transitions. When free space transmissions are not possible, this could be particularly advantageous for high-frequency measurements susceptible to attenuation of the reflected microwave signal due to the spatial separation of the experimental apparatus. It also completes the microwave-DC frequency transition at cryogenic temperatures where the Johnson-Nyquist noise is an order of magnitude smaller.

Noting the significant influence the phase difference term ($\cos\varphi$) has on the magnitude of the rectification current, manipulation of the phase value could suppress a large part of the rectification. To manipulate the field-coupling elements so that $\varphi \rightarrow 90^{\circ}$, the coupling between the gate and the bias terminals would have to remain small or be nonexistent.

4

Identification of electrically active spin species in arsenic and sulfur doped silicon

In this chapter I investigate SDR using cwEDMR in crystalline silicon ion-implanted with ^{75}As and ^{33}S. The aim of this investigation is to observe spin-active isolated $^{33}S^{+}$ ions through their resonant quartet caused by the hyperfine coupling with ^{33}S's $I = {}^{3}/_{2}$ nuclear spin. Based on results previously published, that will only be possible if sulfur ions were to form spin-pairs with a shallow defect (like arsenic) to allow D^0-A^0 recombination, as discussed in section 2.2.2.1 [11].

The chapter begins with an introduction to the topic: this includes a description of the scientific interest in sulfur-doped silicon in terms of practical applications, and then a description of the properties of sulfur in silicon. In preparation for the description of experimental results, the experimental setup of my experiment and the device design and fabrication is detailed. Finally, the experimental results are described, which includes the current voltage response and the cwEDMR spectra.

4.1 Introduction

Chalcogen-doped silicon became a topic of scientific interest about 40 years ago due to the double-donor nature of chalcogens in silicon and the various intragap deep energetic defects they produced [128, 129]. In the last 10 years, a renaissance of chalcogens in silicon has occurred predominantly thanks to their unique optical properties. Sulfur atoms in silicon for example, preferentially occupy substitutional sites resulting in occupied states deep into the bandgap [130]. As a deep donor, sulfur provides an otherwise inaccessible sub-bandgap energy level in silicon to absorb a range of IR wavelengths. This has recently been exploited in silicon 'hyperdoped' or 'supersaturated' with sulfur ($\sim 10^{20}$ cm^{-3}) [28, 130–133]. The utility of existing expertise in silicon combined with access to IR frequency excitation levels has paved the way for novel photoelectric applications like photodetectors. These optical properties can be extended to applications in silicon-based donor spin qubit readout or coupling mechanisms in silicon for QIP.

My investigation will focus on the electrical detection of sulfur. For electrical detection using SDR, sulfur needs to be able to capture a hole so that it can be in the singly ionised paramagnetic state S^+. Selenium and tellurium are two other commonly studied group VI deep double donors that also have interesting optical properties that will be discussed further in section 4.1.4. Sulfur has a larger cross-section for hole capture compared to selenium and tellurium and an isotope with nuclear spin $I = {}^3/_2$, which allows the quadrupolar effect to be exploited.

This chapter will first consider recent literature regarding sulfur doped silicon and potential applications that exploit its optical properties. It will then outline important properties of chalcogens (specifically sulfur) in silicon, after which the proposed electrical readout mechanism will be outlined. The design of an experiment to test the mechanism will be detailed followed by the experimental results and recommendations for future work.

4.1.1 Sulfur doping in photodetectors

Supersaturated sulfur in silicon has become a promising material for optoelectronic applications because of its IR absorption potential due to deep defect sulfur states within the energy bandgap. Supersaturation is achieved by ion implantation and pulsed-laser-melting-induced rapid solidification [134, 135]. In addition to repairing ion-implantation damage and activating implanted ions, the unique advantages of laser annealing is that it enables dopant concentrations beyond the standard uniform solubility limit and can lead to an abrupt step in the concentration profile at the laser penetration depth [136, 137]. The supersaturation concentration of sulfur in silicon typically reaches $\sim 10^{20}$ cm^{-3}. A silicon sample supersaturated with sulfur to 0.6 at. % has been reported to have an optical absorption coefficient of 2.5×10^4 cm^{-1} over the optical range 1200-2500 nm [134]. This absorbance is at least an order of magnitude higher than that attributed to free carriers. The authors attribute the high absorptivity to a broad distribution of band-like sulfur states in the bandgap that result from the high sulfur concentration.

Implantation by diffusion combined with pulse femtosecond laser irradiation of silicon was also shown to be an effective way to supersaturate a sample [132].

4.1.2 Sulfur doping in photodiodes

The laser pulse doping approach described in section 4.1.1 was similarly applied to the development of a photodiode. The responsivity of 100 A/W observed at 1064 nm (near the bandgap) was two orders of magnitude greater than that of silicon photodiodes. Below the bandgap, responsivities up to 50 A/W at 1330 nm and 35 A/W at 1550 nm were observed [29]. The impurity concentration and annealing temperature are particularly important to the responsivity of these reported results. The increasing influence of sulfur dopants with increasing anneal temperature was observed through rectification of the device current due to the free carrier concentration mismatch between the laser affected surface layer and the rest of the sample. The rectification effects were maximised after a 30 minute anneal at 1075 K compared to lower temperatures. The rectification also probably removed free carrier-trapping defects and precipitated sulfur donors to the

surface with longer anneal times [138].

The experiments in ref. [29] demonstrated visible and near-IR doped-silicon based photodiodes with high-responsivity. They described the laser fluence, doping and annealing conditions with which to optimise performance.

4.1.3 Sulfur doping in photovoltaics

The absorption of IR frequencies has application in photovoltaics too. Known as the multilevel impurity photovoltaic (IPV) effect, sub-bandgap absorption by intra-gap defects is used to facilitate a broader excitation spectrum into the IR range and improve photovoltaic conversion efficiency (PCE) in silicon solar cells [139]. Modelling of the type and quantity of sulfur induced defects in silicon demonstrated an enhanced IR response, as well as a 2 % improvement in the PCE [28, 139, 140]. A modified SRH model that incorporated the IPV effect has been used to model the PCE. It showed that a further increase in the number of sulfur related defects that were modelled reduced the improvement in the PCE, most likely due to an increase in the EHR [28]. This last point is particularly interesting to my experimental proposal as I investigate SDR through sulfur defects in silicon. So while IPV effects might prove beneficial, the dopant concentration must be balanced against SRH EHR to maximise improvements to PCE.

4.1.4 Chalcogen doping for quantum information

4.1.4.1 Chalcogens as donor spin qubits

A quantum computer based on chalcogen nuclear spin qubits in silicon was proposed in 2001 [141, 142]. Using a deep donor in silicon and magnetic resonance force microscopy, the system relies on the large hyperfine interaction to implement a CONTROL-NOT gate [142]. The application of the strong hyperfine interaction of donor impurities in silicon makes them handy for quantum readout. Group VI chalcogens' already large hyperfine interactions can be accentuated in silicon nanowires due to quantum confinement [143]. When singly ionised chalcogens are isoelectronic with group V donors and therefore possess the same property considered advantageous for qubits: $S = {}^{1}/_{2}$, though with a much larger thermal ionisation energy (see figure 4.1). This allows an outer electrons to

remain bound at room temperature and the two electron singlet ground state to remain tightly bound compared to shallow donors [144]. The energetic difference between the ground state and first excited state $E_{1s(A_1)} - E_{1s(T_2)}$ is suspected to result in larger relaxation times.

4.1.4.2 Chalcogens for qubit coupling

With silicon based spin qubits established as a competitive platform for QIP, researchers grapple with how to couple qubits for multi-qubit gate operations. Coherent coupling of the quantum states of a cavity and two level systems like an electron spin through cavity quantum electrodynamics has garnered attention [145]. The strong coupling regime in cavity quantum electrodynamics can enable the long-range qubit interactions needed for scaled up quantum computation [146, 147].

Likewise, the optical properties of deep-level group VI double donors like sulfur, selenium and tellurium make them useful for QIP applications too. Recent work has demonstrated coupling between chalcogen deep donors and an optical cavity in the strong coupling regime [24]. The authors report their photonic platform demonstrates the viability of spin-to-photon conversion and qubit coupling, among other applications. The advantages they identify with their proposed architecture are specified below. The strong coupling between a single electron in a double quantum dot and a microwave cavity [145] is a competing qubit coupling strategy. I shall consider the application of chalcogen donors because it overlaps with my proposed readout system.

As previously mentioned, chalcogens have helium like electron structure in their neutral ground state, binding two electrons, whereas they exhibit hydrogen-like structure when singly ionised. Much like ESR and EDMR linewidths, the optical absorption linewidths of shallow impurities was shown to be limited by inhomogeneous broadening in ^{nat}Si due to ^{29}Si's nuclear spin [148, 149]. By using isotopically enriched silicon, not only can decoherence effects be removed [20, 150], but the homogeneous linewidths of S^+ and $^{77}Se^+$ $1s(T_2)\Gamma_7$ absorption transition from the ground to excited states can also be observed [149, 151].

Even at zero magnetic field, $^{77}Se^+$ (7.60% naturally abundant) in isotopically purified

^{28}Si has a photoluminescence (PL) linewidth narrow enough to observe hyperfine coupling with its $I = {}^1/_2$ nuclear spin between the ground state $1s(A_1)$ and first excited state $1s(T_2)\Gamma_7$ [152]. The large hyperfine interaction in the $1s(A_1)$ manifold is the result of its s-like character [24]. This provides a means with which to optically determine electron and nuclear spin states in these chalcogen double donors. Whilst the optical transitions resulting from ^{28}Si:^{33}S$^+$'s electron and nuclear spin states are yet to be resolved, I am not aware of any previous failed attempts. There are three reasons why Si:^{77}Se$^+$ has been preferred over Si:^{33}S$^+$: first, the ^{77}Se$^+$ excitation spectrum could be observed in ^{28}Si:^{nat}Se and fabricating ^{28}Si:^{77}Se was a logical scientific progression for the research group responsible for these results [152]. Secondly, ^{77}Se$^+$ hyperfine coupling is notably larger than that of ^{33}S$^+$, which makes spectroscopy easier. Thirdly, isotopically purified selenium is cheaper to fabricate than purified sulfur [153]. This financial overhead of isotopically purified ^{33}S is a one hurdle that detracts from its ubiquity in silicon-based experiments.

Compared to shallow donors, selenium and sulfur's large energetic difference between their ground and first excited state makes them relatively impervious to effects like electrical field and uniaxial strain [24]. This allows long coherence times [144]. If on the other hand electric fields and strain perturbations are required for specific qubit addressability, manipulation of the quadrupolar effect of ^{33}S, that is unavailable with selenium, will prove advantageous [24, 96]. The linewidths of S$^+$ and ^{77}Se$^+$ are 1.5 times narrower than the homogeneous linewidths of shallow impurities [152]. Similarly, shallow donors commonly used for qubits have small binding energies. Their excited state have lifetimes limited by phonon-assisted relaxation [154] and optical transitions are in the terahertz range, which are experimentally difficult to access [24].

These advantages over shallow donors and make experimental investigations of chalcogen-doped silicon a worthwhile pursuit [144]. Although past studies have focussed on more easily accessible selenium, the similarities in electron structure, narrow linewidths and binding energy make sulfur a worthy replacement.

4.1.5 Sulfur doping for quantum readout of donor spin qubits using spin-dependent recombination

EDMR provides a unique tool to interrogate spin-dependent conductivity as well as the type and concentration of paramagnetic species within a semiconductor (including defects [155–157]) beyond the limit of normal EPR sensitivity. The technique, used extensively under titles like 'spin-dependent photoconductivity' [68, 158] and 'spin-dependent recombination' [54, 67], has been important to understanding spin interactions and charge transport within silicon. Within charge transport devices like diodes [68] and photovoltaic cells [45, 159–161], it provides a means to identify performance limiting defects [67]. More recently the method has extended to more advanced spin interactions [22, 96, 162]. Additional measurement approaches of spin-dependent mechanisms like capacitance detected magnetic resonance (CDMR) and noise detected magnetic resonance (NDMR) have been developed for detection of defect states at a higher sensitivity than EPR though have not replaced EDMR [163]. A type of ODMR known as Auger electron detected magnetic resonance (AEDMR) has gained more traction in recent years because of the improved distinguishability of different resonances in purified silicon. It will be discussed further in Chapter 5. Photovoltaic detected magnetic resonance (PDMR), which also compliments ODMR, measured SDR through a change in open circuit voltage (V_{oc}) on resonance [164].

The development of pEDMR [40] led to its extensive use over the last 15 years for the investigation of spin defects in silicon [13, 18, 19, 22, 45, 70, 165, 166]. The device architecture and EDMR measurement techniques used for the electrical detection of a single donor electron [13] and nucleus [18] became the state-of-the-art for silicon based donor spin qubits [20, 21]. SDR effects observed with pEDMR however has proved continually useful for understanding spin-interactions in silicon [76, 78, 96, 167, 168] and organic semiconductors [61, 84, 162].

A major shortcoming of EDMR in silicon is that SDR with spin-pairs predominantly relies on deleterious interface defects to provide energetically deep traps. This further restricts donors to the interface for donor-interface defect spin-pair recombination. To

circumvent this, donors can be intentionally located away from the interface to avoid the deleterious effects of interface defects on coherence times of donors [70, 169–172]. Although recent work suggests that isolated silicon dangling bonds at the interface can be engineered to control their electronic properties [173], moving one component of a spin-pair away from the interface is equally viable. My proposed solution is the use of an energetically deep-level donor in the bandgap to facilitate EHR of spin-pairs via SDR. Specifically, sulfur is a deep level double donor, whose S^+ paramagnetic state is 614 meV below the conduction band (CB). By accurately and strategically implanting both arsenic and sulfur donors in close proximity away from the interface they may form a spin-pair and provide an alternative mechanism to readout the spin state of the donor or donor electron. Not only does a deep level donor like sulfur provide a more controlled means with which to facilitate SDR through a two-levelled system and readout the spin-state of a shallow donor like arsenic, EDMR can be used to electrically measure the spin states of activated sulfur in silicon too. This is something that is yet to be experimentally demonstrated though will be important to understanding the behaviour of Si:S with the increased interest in chalcogens' optical properties in silicon.

The aim of this work is to facilitate SDR between 'shallow' arsenic donors and 'deep' sulfur donors through the formation of a As-S spin-pair.

4.1.6 Properties of sulfur in silicon

Sulfur is a group VI chalcogen with four stable isotopes: ^{32}S,^{33}S, ^{34}S and ^{36}S. Sulfur has one non-zero nuclear spin isotope, ^{33}S, with a nuclear spin of $I = {}^3/_2$ sulfur with a natural abundance of 0.76%.

The electronic structure of the neutral charge state S^0 is considered 'helium-like' in that it behaves like a double donor with two bound electrons in a small 'electron cloud' and with large hyperfine interactions [143]. Sulfur has an electron configuration of [Ne]$3s^2 3p^4$, making it diamagnetic.

Sulfur dopants that have experienced an activation anneal regularly occur at substitutional tetrahedral sites in a silicon host lattice [152]. Two sulfur-related sub-bandgap centres in silicon were initially identified at 0.18 and ∼0.38 eV, known as 'sulfur I', and

at 0.32 and 0.53 eV, know as 'sulfur II' [174]. Their capture cross sections varied with temperature. These energy values roughly compare to what is now know to be the charge states of S_2 and sulfur respectively [175]. The binding energy of S^0 is 318 meV (cf. selenium: 308 meV and tellurium: 140 meV). When singly ionised however, S^+ closely resembles the hydrogenic state (like the commonly used qubit species ^{31}P) with a binding energy of 614 meV (cf. selenium: 593 meV and tellurium: 340 meV) [129, 175]. Impurity energy levels of chalcogen compounds compared to other commonly used shallow donors in silicon at room temperature can be seen in figure 4.1. ^{31}P, ^{75}As, ^{33}S and ^{nat}B are all dopants used in these experiments whereas ^{nat}Cr is included because of its involvement the in $D-A$ recombination mechanism discussed in section 4.1.7 [11].

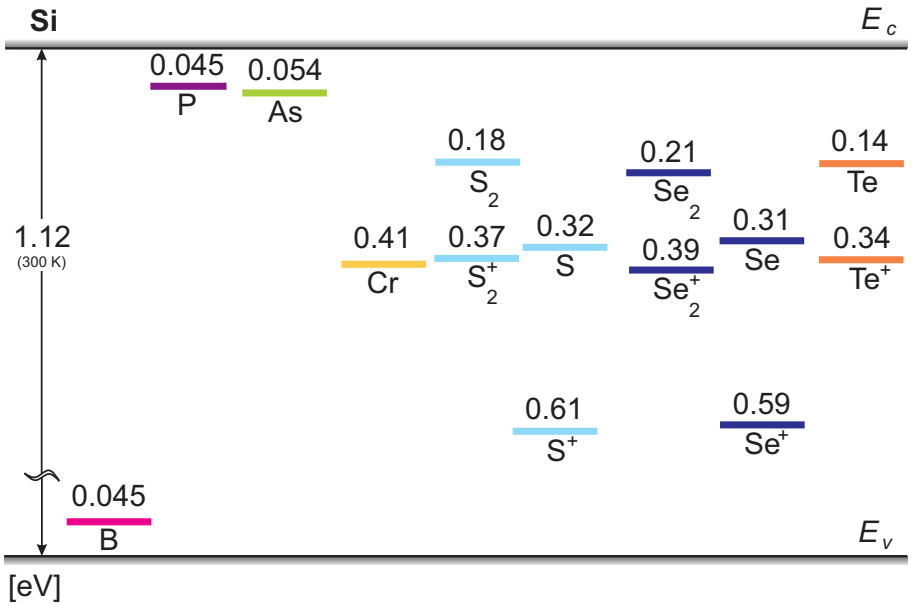


Figure 4.1: Impurity energy levels in the silicon bandgap. The silicon bandgap at room temperature including relevant dopant impurity energy levels discussed in this work. B is 45 meV above the valence band whereas all other dopants specified energy value is from the bottom of the conduction band. Energy levels taken from [175–177].

4.1.6.1 Hole capture

The hole capture process of deep donors is particularly important to the readout proposal laid out in section 4.1.5 [178]. For sulfur to be spin-active, it must be in the S^+ charge state, which requires the neutral state to capture a hole. Consider the hole capture process for deep donors.

A group VI double donor can exist in three charge states: neutral D^0, in an ionised state D^+, or a doubly ionised state D^{2+}. A double donor is ionised by the release of an electron to the conduction band [179]:

$$D^0 \rightarrow D^+ + e^- \tag{4.1}$$

an energy absorptive process, or the capture of a hole from the valence band

$$D^0 + h^+ \rightarrow D^+ \tag{4.2}$$

an energy emissive process. For capture to occur, the hole must be in the vicinity of the defect. Whether the emitted energy is reused determines the final charge state of the defects involved. Based on the dissipation mechanism, there are four processes by which a carrier can be captured in a deep level trap state [180]:

1. **Radiative capture process.** A photon is emitted by the captured carrier. Typical capture cross sections are often $<10^{-19}$ cm^2.

2. **Multiphonon emission (MPE) process.** A defect vibrates sufficiently for the electronic level to enter the conduction band and capture an electron. The lattice subsequently relaxes by releasing many phonons so that the energy level can move to its steady state position within the bandgap. The repulsive Coulombic force experienced by h^+ at deep D^+ centres suggests that an ionised donor like S^+ is believed to capture a hole through either this MPE process (which shows a growth of the capture cross-section with temperature, $\sigma \propto T$) or a combination of the MPE and radiative capture process

   $$D^+ + h^+ \rightarrow D^{2+} \tag{4.3}$$

   Typical MPE capture cross-sections are 10^{-21}-10^{-15} cm^2, but reduce to 10^{-24}-10^{-22} cm^2 below approximately 100 K [179].

3. **Auger process.** The capture and relaxation of a first carrier emits energy that is

recaptured to induce excitation of a second carrier [181]. The Auger process is not radiative and the donor can in fact become double ionised for a He-like centre. The Auger process is the hole capture process for isolated neutral chalcogen double-donors (including S) in silicon [179]:

$$D^0 + h^+ \rightarrow D^{2+} + e^- \tag{4.4}$$

The cross-section is almost temperature insensitive and is of the order 10^{-20}-10^{-14} cm^2.

4. **Cascade capture process.** An electron is captured in an excited state and transitions down 'laddered' energy levels in an impurity, releasing a phonon each time. This process explains much larger capture cross-sections of 10^{-14}-10^{-12} cm^2 [180].

Of the three chalcogens sulfur, selenium and tellurium, S^0/S^+ have the largest cross-sections for holes, where the D^0 cross-section increases with binding energy [179].

4.1.6.2 Spin characteristics of sulfur donors

Spin characteristics of sulfur donors in silicon have previously been investigated in ref. [182]. There, background boron doping partially compensated sulfur's two surplus electrons to make sulfur a singly occupied paramagnetic state by forming S^+. The spectrum attributed to S^+ was isotropic and included a central resonance due to $^{32}S^+$ and a hyperfine quartet due to $^{33}S^+$ (since number of resonance lines $= 2I + 1 = 4$). The signal was enhanced by tungsten lamp illumination through the capture of photoelectrons to form paramagnetic S^+, which reduced the number of S^{2+} which were overcompensated by high boron concentrations.

Further ESR studies of ^{33}S donors in silicon have been reported several times. These are listed in table 4.1.

Donor	g-value	|A| (MHz)	A (G)	*I*	Ref.
Si:^{33}S	2.0054 ± 0.0002	312.4 ± 0.6 MHz	114	$^{3}/_{2}$	[182]
Si:^{33}S-^{32}S	2.0008 ± 0.0001	115.1 MHz	41		
Si:^{33}SH – two defects	$g_{\parallel}$ = 1.99886	$A_{\parallel}$ = 143.1	51.1	$^{3}/_{2}$	[183]
	$g_{\perp}$ = 2.00126	$A_{\perp}$ = 126.8	45.3		
	$g_{\parallel}$ = 1.99823	$A_{\parallel}$ = 124	44		
	$g_{\perp}$ = 1.99974	$A_{\perp}$ = 117.9	42		
Si:^{33}S	$g_{\parallel}$ = 1.9985± 3× 10^{-4}	$A_{\parallel}$ = 133.55 ± 9.55	51	$^{3}/_{2}$	[183]
	$g_{\perp}$ = 2.00050 ± 7.6 × 10^{-4}	$A_{\perp}$ = 126.8 ± 9.9	49		
Si:S_2^+;(^{33}S-S)$^+$;$^{33}S_2^+$	$g_{\parallel}$ = 1.99992	$A_{\parallel}$ = 114.956	41	0;$^{3}/_{2}$;0,1,2,3	[184]
	$g_{\perp}$ = 2.00115	$A_{\perp}$ = 112.323	40		

Table 4.1: EPR parameters of sulfur in silicon. EPR parameters of sulfur in silicon previously observed. In the table the chemical symbol for sulfur 'S' without a specified mass number is one of the even zero nuclear spin isotopes.

4.1.7 Electrical observation of deep donor state

Spin-dependent electron transfer from a shallow to deep level defect was proposed in ref. [11]. There they demonstrated SDR in silicon co-doped with a shallow donor (^{31}P, $I = {}^{1}/_{2}$) and deep double donor ($^{53}Cr^{+}$, $I = {}^{3}/_{2}$). A series of experiments were performed to demonstrate how various donors interacted with free charge carriers in SDR experiments. When only doped with ^{31}P, the typical ^{31}P hyperfine doublet was measured with EPR, though no electrically detected signal was observed. The authors attribute this to the lack of a deeper defect to facilitate the two level spin-dependent transition needed for 'donor-acceptor' D^0-A^0 recombination; so named because both midgap state captures an electron and a hole respectively. Perhaps due to its shallow defect level, ^{31}P was not able to facilitate SRH recombination either. When illuminated with above bandgap light and co-doped with chromium however, both dopants (chromium in interstitial lattice positions) were detected electrically. The ionised donor $^{31}P^{+}$ captured a conduction electron to form the neutral charge state $^{31}P^{0}$ and the neutral interstitial acceptor Cr^{0}_{int} ([Ar]3d^{5}4s^1) captured a hole, to create the paramagnetic 'neutral acceptor' (A^0) charge state Cr^{+}_{int}. Concentrations of neither dopant were specified though they are assumed to be comparable to maximise the formation of P-Cr pairs. Without illumination, the Fermi level exists between the $^{31}P^{0/+}$ and Cr^0 states, yielding spin-silent $^{31}P^{+}$ and Cr^0 but with illumination EPR/EDMR active $^{31}P^{+}+e^{-} \rightarrow {}^{31}P^{0}$ and $Cr^{0}+h^{+} \rightarrow Cr^{+}$ could be observed. Although no measurements were performed to coherently control the spin-species and verify their relative dependence, the existence a spin signal for both species suggests

D^0-A^0 recombination occurred, as described by the authors.

Whilst chromium has proved useful for the spin state readout of a shallow donor commonly used as a qubit, ^{31}P, it does not demonstrate the remarkable optical properties of the deep level chalcogens discussed in section 4.1.4.2.

In amorphised silicon, sulfur exists at interstitial sites nearby existing defects, or substitutional sites replacing the defects. In this material, annealing can lead to energetically favourable sulfur-pairs, which do not offer a intra-bandgap energy defect state [130]. Thermal quenching should help avoid the pairing of sulfur atoms. This will be an important consideration in Section 4.5, where I experiment on amorphous crystalline samples and aim to dope with isolated interstitial sulfur donors.

Previous SDR measurements have relied on the formation of a spin-pair between ^{31}P and P_{b0} interface defects and ^{75}As and SL1 oxygen vacancy defects [10, 22, 23, 76]. The crystal defects have provided the deep level defects, whose charge state has not required careful attention. For more controlled measurements, the dependence on defects is unsustainable.

4.1.7.1 Compensation of double donor's D^0 state with background acceptor doping

Ref. [11] also describes successful attempts to perform EDMR with ^{31}P and a double donor species: the thermal double donors (TDD) NL8 defect, induced by annealing silicon containing oxygen. This species is in a paramagnetic charge state 'TDD^+' when the sample is co-doped with boron to compensate for one of TDD^0's free electrons. Interestingly, the concentration of boron was greater than the sum of TDD^0 and TDD^+ states, which you would expect to doubly ionise TDD [11]. In a similar experiment in the same paper, the use of a lower concentration of boron compared to the sum of co-doped sulfur and selenium in silicon yielded EPR signals from the paramagnetic double donors, though no EDMR signal. This is attributed to too few boron acceptors, to reduce the Fermi level below the $S^{+/++}$/$Se^{+/++}$ energy levels though this conclusion does not equate with the existence of an EPR signal. The chalcogen doped samples did not contain a shallow donor state. No SRH or Rong-style recombination, where a

charge carrier is captured into the excited state of an energetically deep, single level recombination site has been observed using chalcogens in silicon [53].

In ref. [182], the relative concentration of the acceptor (boron) to the double donor (sulfur) is not specified, though the authors note that too many acceptors (one assumes orders of magnitude more than donors) reduced the EPR signal intensity by compensating the second of sulfur's electron to form EPR silent S^{2+}. This can be overcome with optical illumination to create photoexcited free carriers that can be captured by S^{2+}. Alternatively, when selenium's optical transitions were recently characterised, comparable ^{nat}B ($\sim 5 \times 10^{13}$ cm^{-3}) and $^{77}Se^{+}$ ($\sim 2 \times 10^{13}$ cm^{-3}) concentrations were used, which led to the concentration of $^{77}Se^{+}$ being an order of magnitude more than $^{77}Se^{0}$ [24]. An increased ^{nat}B concentration of 1×10^{15} cm^{-3} gave stronger yet broader $^{77}Se^{+}$ absorption lines. This suggests not all boron atoms compensate the double donors, probably because of their proximity. Whilst other measurements with EPR active group VI double donors had a ^{nat}B concentration ($\sim 5 \times 10^{13}$ cm^{-3}) two orders of magnitude less than the Se^{+} concentration ($\sim 5 \times 10^{15}$ cm^{-3}) [144, 152].

In short, the concentration of boron dictates the proportion of double donors singly ionised [185]. Although SDR experiments are well suited to observing the spin interactions between a shallow and deep donor and the advantages of sulfur have been outlined in section 4.1.5, the need to generate a photocurrent can be inherently detrimental or productive to the experiment. At 5 K, above bandgap light allows an ionised shallow donor to capture an electron ($e^{-} + {}^{75}As^{+} \rightarrow D^{0}$) and become paramagnetic. For some species illumination also potentially allows charge capture at a double-donor ($Cr^{0} + h^{+} \rightarrow Cr^{+}$, $TDD^{++} + e^{-} \rightarrow TDD^{+}$) to generate the neutral 'acceptor' A^{0} state and thus both become paramagnetic. However, illumination can also photoneutralise ionised double donors and acceptors depending on their initial charge state determined by the Fermi level [144]. Whilst my proposed spin-dependent readout mechanism relies on the formation of an As-S spin-pair, considerations of the potential $D - A$ recombination resulting from S-B pairs must also be taken into account [186, 187]. Recent results show that when illuminated with above bandgap light, optically excited free carriers can be captured ($Se^{+} + e^{-}$ and $B^{-} + h^{+}$) to form (ESR silent) non-equilibrium Se^{0} and

B^0 respectively, which don't return to their thermal equilibrium state (Se^+ and B^-) via $D-A$ recombination until after minutes or hours at liquid helium temperatures [144]. Ionisation of the now ESR-silent Se^0 donors can be expedited by IR illumination ($\sim$ 4 μm).$D-A$ recombination has been observed between TDD-B pairs and P-Cr. In both cases the deeper state (B^0 and Cr^0) could capture a hole. This could explain why electrical measurements on group VI donors has proved elusive: photoexcited free electrons are captured by double donors making them ESR silent. Illumination is an inherent part of the SDR mechanism though may photoneutralise the double donors. With all of this in mind, a carefully formulated balance between relative impurity concentrations, photoionisation, and temperature must be created to ensure the right charge state of the intended spin-pair constituent elements.

4.2 Experimental setup

The experimental setup used for both cwEDMR and pEDMR measurements is in figure 4.3. A *Stahl* BS series multichannel precision voltage source biases the samples. The sample is mounted on a custom made PCB made of low-dielectric kapton tape with patterned copper track to complete the electrical circuit. The PCB is soldered to a CMR-direct 4-way female cryogenic connector (product code: 02-31-034) [188]. The male connector (product code: 02-31-038) is fixed to the EPR insertion rod hole that is intended for EPR quartz tubes. Copper wires run from the male connector to BNC connectors mounted at the top of the insertion rod. A diagram of the mounted sample is in figure 4.2. The sample current is amplified by a *Femto* DLPCA-200 variable gain low noise current preamplifier as in figure 4.3 before being connected to one of three points depending on the measurement. For a direct current response, the current is acquired by a *Keithley* 2100 Multimeter. When a direct current measurements is not being undertaken, the *Keithley* is disconnected from the circuit due to the noise it contributes [189]. For cwEDMR measurements, the output of the current amplifier is fed to the internal lock-in amplifier of the *Bruker* spectrometer. For pEDMR measurements, the output of the current amplifier is fed to a *Stanford Research Systems* SR560 low-noise

voltage preamplifier. There it is bandpass filtered, with 6 dB/octave dropoff at 1 kHz to remove DC and mains power noise, and at 100 kHz to remove a noise signal of unknown origin between 100-300 kHz.[1]

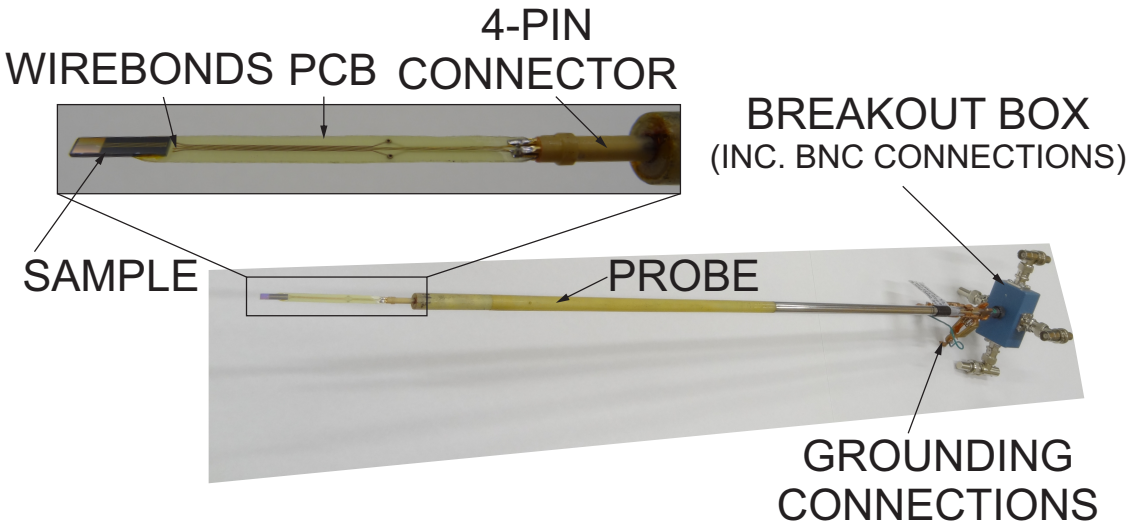


Figure 4.2: Probe photo. The EPR probe used to insert the sample into the *Bruker* E580/E680 cavity.

The EPR apparatus included both *Bruker* BioSpin EleXSys I E680 and EleXSys II E580 spectrometers. Microwaves were applied in a *Bruker* Biospin ER 4118X-MD5W1 X-band sapphire dielectric cavity operating in the TE_{011} mode. An *Oxford Instruments* CF935 continuous flow cryostat was used, and the temperature was maintained by either an *Oxford Instruments* ITC503S or MercuryiTC temperature controller.

4.2.1 Thermal treatment experimental setup

Following ion-implantation with the energies and doses in table 4.2, donor activation was conducted. Donor activation within the silicon samples was performed in a *Carbolite STF single zone tube* furnace. The samples were quenched in H_2O (DI) as previously reported [184, 190, 191]. The experimental setup is in figure 4.4. The thermal treatment process was as follows:

1. The furnace was preheated to 1200° C. A quartz tube was inserted into the furnace to enclose the sample space, minimise contamination from the furnace and provide

[1]For transient measurements no low-pass filter was applied as it changed the time constants of the transient behaviour discussed in Section 5.3. For echo readout measurements used in chapter 5, the application of a low-pass filter made no noteworthy difference to the echo response.

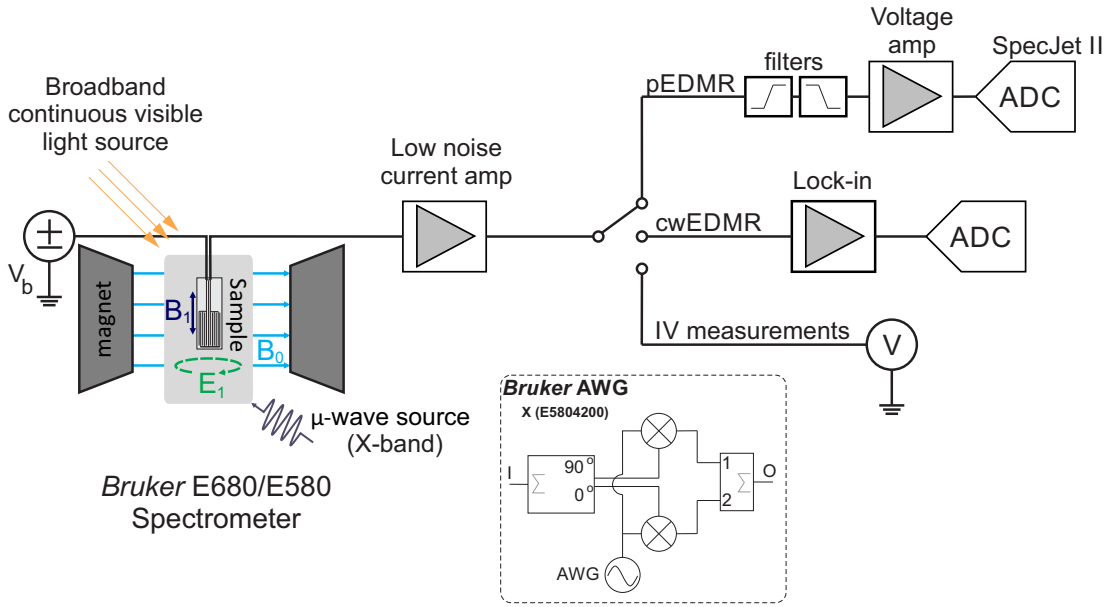


Figure 4.3: Experimental setup diagram. Experimental setup diagram for cwEDMR and pEDMR measurements used through this thesis. Both *Bruker* E580 and 680 spectrometers were used.

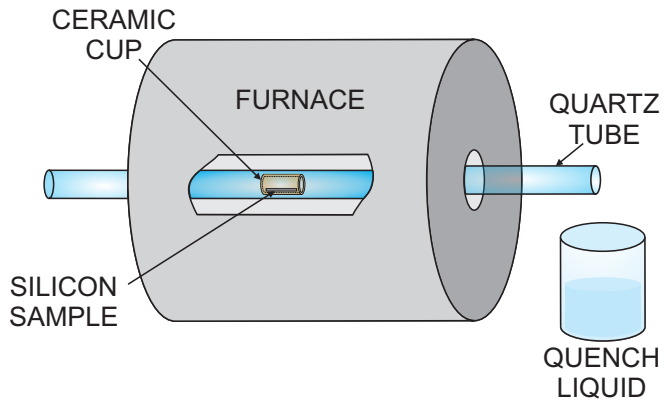


Figure 4.4: Thermal anneal and quench setup diagram. The cylindrical furnace heats the sample to 1200° C. The quartz annealing tube sits within the furnace to guard against impurities in the furnace core. A ceramic cup holds the sample and protects it from damage as the cup moves in and out of the quartz tub. A beaker of H_2O awaits the ceramic cup containing the silicon sample to thermally quench it.

a surface upon which a *Almath* alumina crucible (detailed in the next step) could smoothly and rapidly slide into the furnace [192].

2. Samples were placed in a CC12 - Alumina cylindrical crucible for the thermal treatment. Whilst being suitably thermally conductive to allow the samples to heat to the furnace temperature, the crucible encapsulated the sample to protect it from damage to its surface.

3. The crucible containing the sample was inserted into the centre of the furnace inside the quartz tube with a long quartz rod where the temperature was uniform and preset. The duration at this central position is in table 4.3.

4. The quartz rod was used to push the crucible (including the sample) completely through the quartz tube into a bath of liquid H_2O (DI) to thermally quench the sample. To minimise the formation of a silicon oxide during the thermal treatment, the atmosphere inside the quartz tube would ideally be filled with N_2 gas. However, the need to rapidly extract the sample meant that connecting the gas apparatus and purging the environment of air was not feasible. The oxide could later be removed by hydrofluoric (HF) acid so an atmosphere of air during the thermal treatment was inconsequential.

4.2.2 Light source

Halogen or xenon light sources with a broad emission band in the visible spectrum are most commonly used in silicon-based SDR experiments [159, 165, 171]. Although the wavelength needed to photoexcite free carriers for silicon's $\sim$1.1 eV bandgap is $\sim$1.1 μm, its absorption depth at this wavelength is approximately 1 mm. Higher energy photons in the visible spectrum are typically used for their shallower absorption depth. IR is excluded from the illumination spectrum to avoid heating of the sample, whilst ultraviolet (UV) is not needed. Recently published results suggest that the wavelength and therefore penetration depth of the photoexcitation light source can favour donor-defect or defect-defect pair recombination [82]. I chose to use a broadband excitation to observe all possible recombination paths. Data presented here was measured using

a *Oriel* Xe arc lamp filter with a 435 nm long pass filter and a water filter to remove IR components. For the illumination dependent measurements in section 5.6, a *Schott* KL 2500 LED lamp with their halogen filter (to remove high energy blue wavelengths around 400 nm) was also used.

4.3 Device design

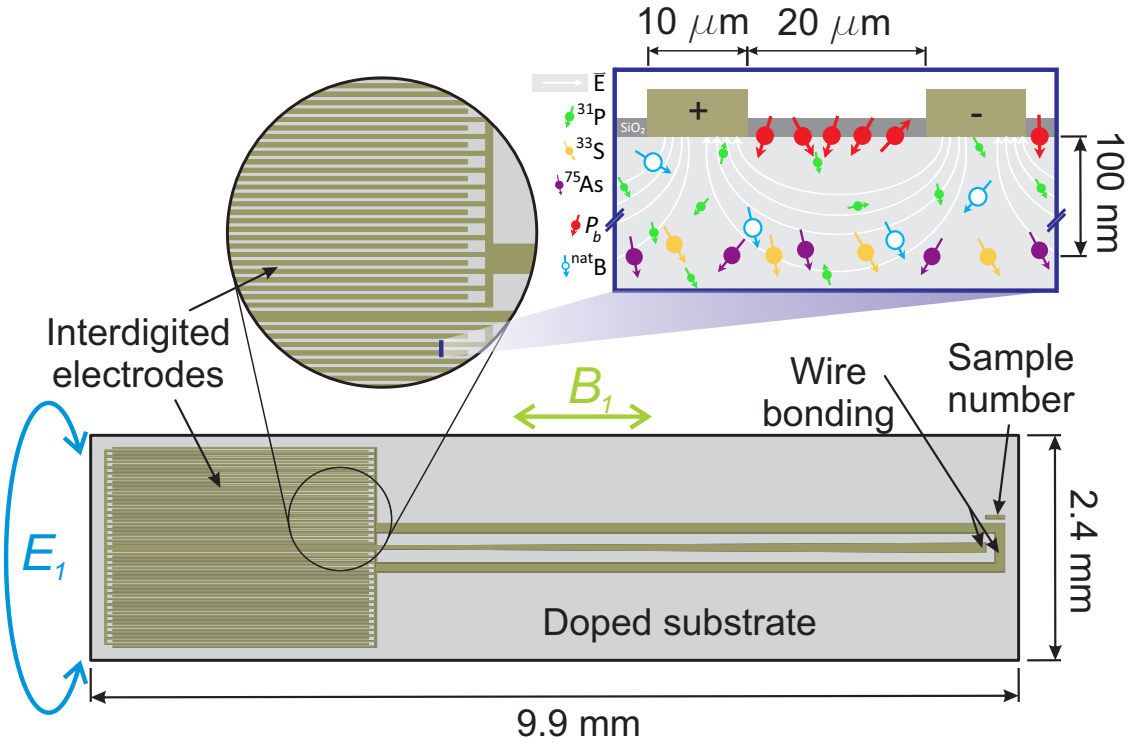


Figure 4.5: Sample design used for EDMR experiments. [top] Cartoon of intended doping profile with arsenic and sulfur 100 nm below the surface. The dopants exist throughout the whole sample. [bottom] Electrode design of the sample with interdigited electrodes. The directions of $\boldsymbol{E}_1$ and $\boldsymbol{B}_1$ when the sample is in the cavity are shown for visual context.

The sample design is in figure 4.5. With approximate dimensions of 2.4 × 9.9 mm, the sample is small enough to be fit inside a typical *Bruker* Biospin ER 4118X-MD5W1 cavity whilst still maximising the substrate surface area illuminated through the resonator's optical window. In the past, samples designed for EDMR experiments in the standard *Bruker* spectrometer resonator were typically about 25 mm long so that the wire bonds and sample bonding pads were outside the resonator [45, 48, 159]. This minimised the amount of metal in the resonator, which would couple to $\boldsymbol{E}_1$ and $\boldsymbol{B}_1$ and distorts

the field patterns felt by the sample (cf. chapter 3). For cwEDMR measurements lock-in detection helps avoid the deleterious effects of microwave artefacts (MWA)-induced currents, since the output of the lock-in amplifier considers the change in current $^{\Delta I}/_{I}$ at a modulation frequency $f_{mod} \sim 10kHz \ll f_{mw}$. For pEDMR measurements various techniques have been developed to remove MWA-induced currents in the time dependent signals that will be discussed in Section 5.4. The result is effectively a totally resonant signal. The fact that MWA signals can be effectively removed means that samples can be made smaller, even if it results in the bonding wires residing inside the cavity. The effect on the results is insignificant.

Smaller doped volumes are also commonly used to reduce signal broadening. If the active spin-centres are spread throughout a larger region of the sample and therefore the cavity, they experience the distributed field strength of the resonant mode; in the case of the MD5 resonator this is the circular TE_{011} mode. When this occurs, the sample extends beyond the relative B_1 field uniformity at the cavity's centre intended for microwave excitation. As I was concerned about signal strength from my sample, the entire substrate was doped with all three donors (^{75}As, ^{33}S, ^{31}P) to increase the number of spins in the cavity.

4.3.1 Donor concentration profile

Donor	Implantation dose (cm^{-2})/energy (keV)	Sample	Anneal duration (s)	[donor] at Si/SiO_2 interface (cm^{-3})
^{75}As	6×10^{11} / 140	A,B,C	0	7.3×10^{14}
		A	10 ± 8	1.3×10^{15}
		B	60 ± 7	1.6×10^{16}
		C	180 ± 5	1.8×10^{16}
^{33}S	1×10^{13} / 70	A,B,C	0	4.8×10^{16}

Table 4.2: Simulated donor impurity implantation and anneal parameters. The ^{31}P, ^{75}As, ^{33}S impurity's implantation dose and energy. After a 1200° C anneal for the durations specified, the resulting simulated interface donor concentrations caused by donor diffusion are listed. The diffusion of ^{33}S could not be simulated so the simulated interface concentrations are therefore not listed. Simulated donor impurity concentrations are in figure 4.6.

The samples were implanted with sulfur and arsenic donors via ion implantation according to the parameters in table 4.2. A cartoon of the doping profile is also in figure

4.5. Each donor is implanted with an unavoidable depth straggle that is not depicted. In my samples residual background ^{31}P donors existed in the substrate epilayers like in the samples used in ref. [169]. After an anneal, the donors diffuse away from the Si/SiO_2 interface, which makes the resistivity change from the metal electrodes to the silicon substrate quite gradual. The energetically shallow donor, ^{75}As, intended for SDR was ion implanted with an energy of 140 keV and dose 6×10^{11} cm^{-2} whereas the deep donor ^{33}S was implanted with an energy of 70 keV, and dose 1×10^{13} cm^{-2}. Both the arsenic and sulfur implants have peak concentration $\sim$100 nm below the surface after implantation. The impurities were implanted into a p-type (boron doped) float zone silicon [100] crystalline substrate with resistivity $\rho > 10\ \Omega.m$. This resistivity is the result of background uniform boron doping with [B]<10^{12} cm^{-3} and residual phosphorus.

Metal	Work function (ϕ_m)
Al	4.25
Au	4.8
Cr	4.5

Table 4.3: Metal work functions for electrodes. The work function of commonly used metals deposited as electrodes on silicon wafers for EDMR measurements. Values taken from refs. [176, 193, 194].

4.3.1.1 Annealing

It is common to perform an 'activation anneal' on ion-implanted donors in silicon as a means to electrically activate them. Electrically active donors can be substitutional or interstitial.

An important step for this electrical activation of isolated sulfur in silicon is the thermal quenching of the sample immediately after the activation anneal [182, 183]. The quench immobilises donors and allows them to remain isolated rather than encouraging the formation of S-S pairs. Pairs form if the sample was gradually cooled to room temperature [184]. Dissociation of spin-active S-S pairs to form isolated S^+ is possible if a sample is reheated to above 800° C, and then rapidly thermally quenched. An anneal below 800° C would result in the formation of EPR silent higher-order complexes [184]. The EPR signal intensity of isolated sulfur complexes has been shown to decrease with

increasing cooling times following an anneal [182, 183]. A increase in the thermal quench duration from three seconds to 20 seconds decreased the EPR signal intensity by five.

Longer thermal treatments of silicon samples supersaturated with energetically shallow dopants tends to cause electrical deactivation and the formation of inactive precipitates (boron) or clusters (arsenic and phosphorus) [136]. This reduces conductivity. Diffusion through a sample of energetically deep dopants like sulfur would be expected for dilute sulfur concentrations [176, 182]. For higher concentrations diffusion is limited by clustering [134] or precipitation to grain boundaries [132, 138]. This cumulative behaviour has dictated the anneal conditions used in my samples, which are in table 4.3.

The simulated donor densities after implantation and annealing are in figure 4.6. The simulated concentrations of ^{75}As and ^{33}S at the Si/SiO_2 interface are in table 4.2. It is important to note that whilst the concentration is highest $\sim$100 nm below the surface, the concentrations at the interface are still large enough for EDMR signals to be observed via SDR between donors and interface defects. It is anticipated that both shallow donor-defect spin-pairs and deep donor-shallow donor spin pairs will form. The diffused interface concentrations in table 4.2 are calculated using ref [195]. The concentration of ^{33}S after implantation is calculated using ref. [196]. An easy calculation for ^{33}S's doping profile after thermal treatment was not readily available though a fairly accurate picture can be painted from its relative diffusion coefficient and solubility in silicon, as well as previous investigations on the effect of heat treatment on ^{33}S's mobility and tendencies.

In silicon, sulfur has a diffusion coefficient of $\sim 10^{-8}$ cm^2/s [176] and a predicted solubility of $\sim 10^{16}$ atoms cm^{-3} at 1200° C [176, 197]. From this I can hypothesise a much faster diffusion of sulfur away from its peak concentration at a depth of 100 nm below the interface.

The mobility of dopants is of interest for us for several reasons:

1. I specifically wish to observe electrically active isolated $^{33}S^+$ ions, which, to the best of my knowledge, have never been observed with EDMR. I therefore want to avoid clustering. This is why I thermally quench the sample.

2. ^{75}As and ^{33}S donors were deliberately implanted with a peak density at approximately 100 nm below the sample surface to try to isolate them from unwanted spin-pair partners and deleterious interface defects. Diffusion of large densities of donors in proximity to the surface improves the likelihood of donor-interface defect spin-pairs signals dominating the EDMR spectra. Although the donor densities at the surface are above the minimum concentration required to observe EDMR, I wish to also encourage the formation of As-S spin-pairs. This can be done at a depth of 100 nm, beyond the overlap distance of donor-bound electron wavefunctions with the wavefunctions of defects.

3. Diffusion of atoms could reduce the peak concentrations of arsenic or sulfur donors below the sensitivity limit of my detection setup. Alternatively diffusion would reduce the likelihood of As-S donor existing in close enough proximity to form spin-pairs. Either would inhibit my ability to observe As-S spin pairs via EDMR. This is why I focus on short anneal times so that donors may be electrically activated though only diffuse a minimal distance.

4. If I understand the location of sulfur within the sample, it could help to identify the nature of any sulfur signals observed. Sulfur precipitation, for example, could lead to the formation of sulfur/impurity complexes on the sample surface.

The diffusion coefficient (D_0) is dependent on temperature and impurity concentration. For impurity concentrations less than the intrinsic carrier concentration n_i, the diffusion coefficient becomes independent of concentration. At 1200° C, $n_i \approx 10^{19}$ cm^{-3} and $n_i \gg$ [As],[S], which means the diffusion coefficient can be modelled by the equation

$$D(T) = D_0 e^{-\Delta E/kT} \tag{4.5}$$

where ΔE is the activation energy of diffusion. These values have been determined experimentally at my annealing temperature of 1200° C for boron and arsenic as $D_{0,B} =$ ($D_{0,P} =$) 6×10^{-12} cm^2/s, $\Delta E_B =$ 3.4 eV, $D_{0,As} \approx$ 2.45×10^{-13} cm^2/s, $\Delta E_{As} =$ 3.3 eV [198–200]. As can be seen in figure 4.6, a 10 second anneal has minimal effect on

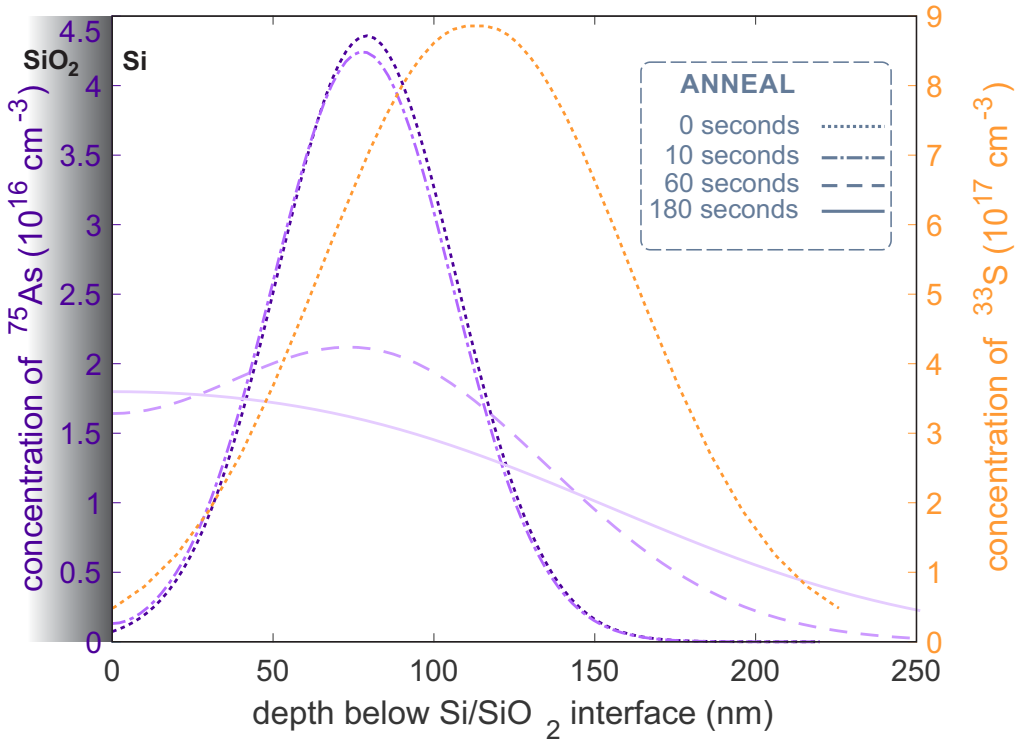


Figure 4.6: Simulated donor concentration profiles. The orange dotted ($\cdots$) line represents the donor concentration profiles of ^{33}S after ion-implantation. The purple dotted ($\cdots$) line represents the donor concentration profile for ^{75}As after ion-implantation, and then after three different anneal durations. Annealing causes donors to diffuse within the sample, which changes their concentration profile. For ^{75}As, the dash-dot ($-\cdot-$) line represents the donor concentrations after a 10 second anneal, the dashed ($-$ –) line the concentrations after a 60 second anneal, and the solid (—) line the concentrations after a 3 minute anneal. The concentrations of ^{75}As are on the lefthand y-axis, whereas the concentrations of ^{33}S are on the righthand y-axis.

^{75}As's doping profile. For increasing anneal durations, the diffusion of donors through the sample is much more dramatic. The energetically shallow donor ^{75}As precipitates to the surface and then diffuses to reduce the localised concentration. With a higher diffusion constant, sulfur is expected to diffuse more rapidly than arsenic, though preferentially to a grain boundaries [138].

The ^{33}S concentration depicted in figure 4.6 is in the same order of magnitude as typically seen in EDMR experiments, though at the higher end of what is considered acceptable [12, 22, 171, 201]. The concentration limit of $\sim 10^{17}$ cm^{-3} is usually to maximise the signal intensity yet avoid the Mott transition concentration. Hyperfine lines and signal intensities have been shown to fade away above concentrations of 10^{18} cm^{-3} too [12, 202]. The ^{33}S concentration used does however surpasses the predicted solubility of ^{33}S, even at the anneal temperature of 1200° C [176, 197]. Whilst a higher anneal temperature (or alternate anneal mechanisms [134]) may have resulted in a higher interstitial ^{33}S concentration, the ^{nat}B concentration of 10^{12} cm^{-3} is only able to electrically compensate a comparable quantity of ^{33}S double donors to form the $^{33}S^{+}$ paramagnetic state. Without a clear explanation from the device designers as to why this concentration was used, I surmise that it was to maximise the interstitial ^{33}S concentration after annealing and potentially therefore the EDMR signal without surpassing the conventional concentration limits.

During the preparation of these sample, several fabrication attempts led to poor electrical contact at the MSI. It was caused by remnant SiO_2 on the silicon surface. In one instance a contact anneal was attempted to improve the metal-semiconductor contact. During this, sample B was exposed to 475° C for approximately 10 minutes in a 95 % N_2/5 % H_2 (20:1) forming gas. This treatment is not reflected in figure 4.6. This temperature is below the eutectic temperature of the Si/Al eutectic composition, which is the lowest possible melting temperature of the any composition of Si/Al [203, 204]. By annealing in a forming gas, the Al can react with the SiO_2 to form Al_2O_3. Although this is detrimental to the contact between the sample and wirebond, I believed the bonding strength could break through the resultant Al_2O_3, whilst benefiting from a clean MSI.

The temperature was also kept much lower than the activation anneal to reduce the mobility of the donors. Based on the known diffusion constants at higher temperatures I can predict them at 475° C by assuming the same exponential relationship. There was expected to be minimal diffusion of all donors at this temperature. Unfortunately however the second anneal had no positive affect on the contact and in fact reduced the current for a given voltage at room and cryogenic temperatures. The effect of this contact anneal becomes evident in the cwEDMR spectra in figure 4.9.

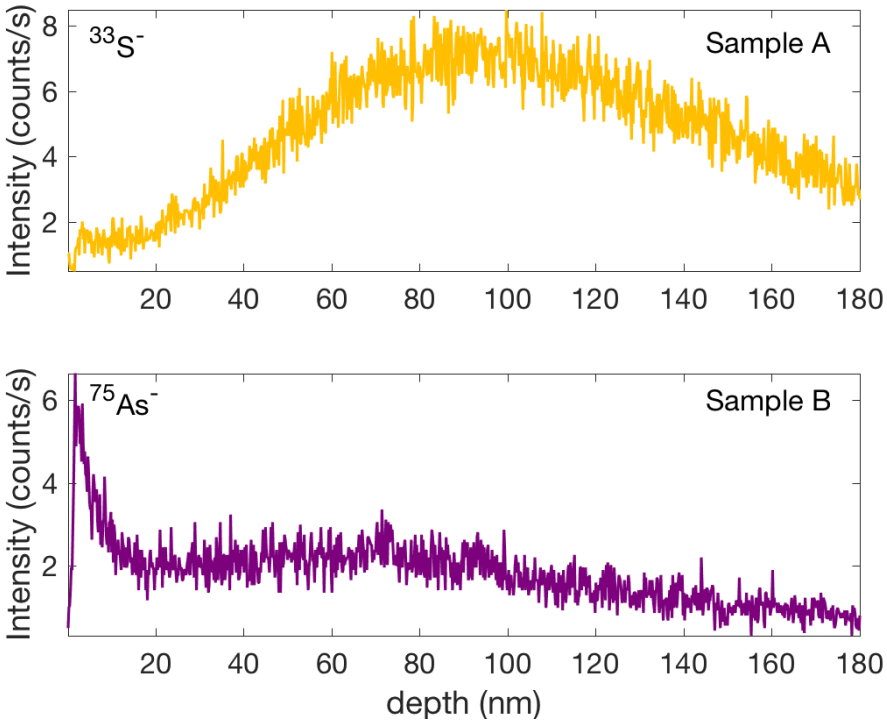


Figure 4.7: NanoSIMS donor concentration measurements. [top] The dopant profile of ^{33}S in sample A, and [bottom] the dopant profile of ^{75}As in sample B. Only negative charged secondary ions could be detected ($^{75}As^-$ and $^{33}S^-$) because of the use of a positively charged caesium (Cs^+) reactive primary ion beam. Measurements performed by Dr. Kexue Li, 2017.

A *CAMECA NanoSIMS 50* was used to depth profile the dopants using secondary ion mass spectroscopy (SIMS) techniques and a caesium (Cs^+) reactive primary ion beam [205]. A raster area of 100×100 μm was used. Without a calibration sample we are unable to translate the SIMS concentration measurements into standard units of cm^{-3}, however the dopant depth profile is still obtained and is useful. The donor concentrations were generally below the nanoSIMS sensitivity limit and so only the ^{33}S concentration in sample A, and the ^{75}As concentrations in sample B could be detected. As expected,

the ^{33}S barely diffused after the 10 second anneal time of sample A. The ^{75}As in sample B however, has diffused towards the interface.

From the profiles in figures 4.6 and 4.7 I can predict potential spin-pair formation. The doping concentrations of both arsenic and sulfur are well above the sensitivity limit for EDMR detection both at and away from the interface in all samples [11]. It is therefore likely that numerous spin-pairs will be seen in the samples.

4.3.2 Electrode design and the metal semiconductor contact

Both aluminium [45, 84, 206] and chromium/gold [10, 64, 207] contacts have been shown as effective current electrodes on silicon surfaces. A low work function is important for forming Ohmic contacts at the MSI. N-type doping of the semiconductor raises the Fermi level of the sample and helps to reduce the Schottky barrier at the MSI. A focussed contact doping, where $n+$ doping region are created below the electrodes at the MSI can further reduce the Schottky barrier.

Whilst aluminium has a lower work function (4.25 eV) than chromium and gold (4.5 and 5.0 eV) [176, 208] and has the added benefit of being superconductive at cryogenic temperatures, the electrode metal is not critical to an EDMR measurements success; either aluminium or bilayer chromium and gold are suitable. Chromium provides the added benefit of a lower work function than gold and as an adhesive between the gold and silicon. Importantly, the choice of chromium and gold electrodes with a hydrogenated silicon surface may also partially hydrogenate the chromium at the interface through diffusion, thereby increase the Fermi level and reduce the work function of chromium. This would reduced Schottky barrier at the MSI and explain both Ohmic and Schottky contacts observed at room and cryogenic temperatures in figure 4.8 [209].

Native oxides (1-2 nm) are littered with paramagnetic charge traps. By first dipping samples in HF acid, the SiO_2 is etched away. A subsequent and immediate submersion in H_20 performed the dual function of neutralising any remaining HF and passivating the silicon dangling bonds with H. This hydrogenated surface takes hours at room temperature to be replaced by a new native SiO_2 [210–212].

The electrode design is in figure 4.5. It is based on a typical photodetector, where a balance must be struck between electrode surface area (for maximum current detection) and exposed semiconductor (for maximum charged generation through illumination). The electrodes are made in an interdigited fashion, whereby the fingers of opposing electrodes fit between each other. In my design, the thick electrode 'bus' tracks run down the centre of the sample away from the edges to supply an opposing voltage to half the interdigited fingers. The bus electrode runs to the sample's base (the left side in figure 4.5) where it then reaches across the width of the sample (the top and bottom in the figure). From there the electrode fingers extend back toward the top of the sample (right side in the figure). The other electrode has two arms that run down the middle of the sample from which extend its fingers. By applying a bias voltage to one side of these electrodes I generate a current from the charge carriers under the electrode fingers.

A primary design consideration is to minimise the electromagnetic coupling to metal in the cavity. Coupling not only induces non-resonant currents in the electronic detection circuitry, but also distorts the electromagnetic field pattern in the cavity. Minimum electromagnetic coupling is achieved by

1. orientating the metal electrodes perpendicular to $\boldsymbol{E_1}$,
2. minimising the amount of metal in the cavity that will distort the field but if necessary fabricating electrodes below the skin depth (δ) of the metal.

For my samples, the detrimental effects of coupling between the sample's metal components and the electromagnetic standing waves in the cavity are negated in three ways:

1. In cwEDMR measurements, the lock-in detection method circumvents some of the noise by modulating the signal at a frequency ($\sim$10 kHz) different to the microwave frequency ($\sim$10 GHz).
2. In pEDMR measurements, phase cycling methods will be used to remove the non-resonant microwave background. These will be discussed in section 5.4.1.
3. The relative linearity of the current response around the operating bias voltage means the induced AC current at frequency f_{mw} is not heavily rectified by the

measurement equipment, nor is there a gate terminal that can also couple to the cavity's fields and affect the current channel [94].

Lengths of electrodes parallel to $\boldsymbol{E_1}$ (along the short width of the sample surface) were minimised to avoid electromagnetic coupling. The electrodes were an order of magnitude shorter than the typical antenna length of $\lambda/4$, which means the coupling should be minimal anyway [48, 213].

Wire bonding between the sample and the printed circuit board (PCB) occurs at the top of the sample at the end closest to the exit of the cavity. The δ is calculated using the following equation:

$$\delta = \sqrt{\frac{2\rho}{\omega\mu}} \tag{4.6}$$

where $\omega = 2\pi f_{mw}$ is the angular frequency, ρ is the resistivity and $\mu = \mu_0\mu_r$ is the permeability of the metal. Although the wirebonds are 0.01"= 25 μm $> \delta_{Au} \approx 750$ nm, the increase in signal strength from inserting the whole sample into the cavity outweighs the distortion the wirebonds cause to the cavity mode's field-pattern.

Whilst maximum current is detected at the site of the interdigited electrodes, the sample was inserted so that it is centred on the centre of the cavity in the insertion direction. Since the whole sample is doped, this increases the number of impurities that experience $\boldsymbol{B_1}$. The illumination is therefore also focussed over the centre of the sample. This setup maximises the SNR. The electrodes were separated from the sample edge by approximately 100 μm so that firstly, any misalignment between the e-beam and the sample during electrode patterning does not extend the electrode pattern over the edge of the sample and secondly, to avoid the deposit of electrodes on the unevenly spun 'heaped' resist at the sample's edges. Variations in the thickness of the resist can result in incomplete etching and poor electrode fabrication. That the samples are pre-cut to only 2.4 mm wide means any resist heaping can affect a large proportion of the sample. Given the importance of the bus electrodes to supplying the bias voltage to the rest of the sample, they are also run along centre of the samples for the same reasons.

4.3.2.1 Patterning of electrodes

Conductive metal electrodes were evaporated onto the sample to measure the sample current. During the deposition of metal contacts I am primarily concerned with ensuring the MSI is as clean as possible. Grit or SiO_2, which is an insulator and occurs at the sample surface, increases the contact resistance and increase noise in sensitive current measurements like EDMR. The following procedure was used to deposit the electrodes:

1. **Sample cleaning.** The samples were cleaned of organic matter with piranha (3:1 H_2S0_4 (98%):H_2O_2 (31%)), then RCA1 (5:1:1 vol, DI H_2O:NH_4OH:H_2O_2 at 70○ C) followed by RCA2 (6:1:1 vol, DI H_2O:HCl:H_2O_2 at 70○ C) and then washed of with H_2O (DI). This removed organic remnants and semiconductor and metallic impurities respectively. Each sample was viewed under an *Olympus* dark field microscope to ascertain its cleanliness. The samples were also cleaned with acetone and isopropanol to remove any dirt that may have stuck to the sample surface in the period between the piranha dip and resist deposit.

2. **Resist deposit**. Two types of resist were deposited on to the cleaned samples: 6 % poly(methyl methacrylate) (PMMA) of chain length 4.95×10^5 in an anisole solvent and then 3 % PMMA of chain length 9.5×10^5 in an anisole solvent. The resists were spun onto the samples so that the resist thickness was consistent. The samples were warmed to 180° C for three minutes after each deposit to solidify the resists.

3. **Lithography**. A *JEOL 5500FS e-beam lithographer* was used to expose the resist for the electrode pattern. The exposed resist was then developed in MIBK:IPA = 1:3 for 45 seconds before being washed with isopropanol.

4. **Removal of native SiO_2**. Each sample was dipped in HF acid for at least one minute or until the sample became hydrophobic when it was subsequently dipped in H_2O (DI). As a rule of thumb, hydrophobic samples are a good indication that the surface is predominantly passivated with H from the H_2O.

5. **Metal electrode deposit**. Following the HF acid dip, the samples were immediately attached to the evaporation disk in the evaporation chamber. The chamber was evacuated to vacuum conditions as quickly as possible (within 10 minutes of the HF acid dip) to reduce the chance of SiO_2 formation from atmospheric oxygen content. Approximately 10 nm of Cr and 100 nm of Au were deposited on the samples. Importantly, these thicknesses are well below the skin depth of Cr ($\sim$1.8 μm) and Au ($\sim$753 nm) at the cavity's operating frequency of approximately 10 GHz. As discussed above, this minimises the distortion of the electromagnetic standing wave within the cavity from coupling of the field to the metal electrodes. These electrode thicknesses are also experimental standards in published EDMR experiments [10, 64, 207].

4.3.2.2 H-passivation and oxide reduction

Limiting the ability of the sample to form a native oxide proved fundamentally important for clean EDMR measurements. Both the H-passivation of the surface after the removal of the native SiO_2 and the rapid deposit of metal electrodes resulted in a dramatic reduction in the resistivity of the MSI and associated Schottky barrier ($\sim$6 V). The EDMR signal rose above the noise floor, most likely because of the drastic reduction in charge traps that littered the Si/SiO_2 interface. H-passivation of the interface has been shown to increase spin coherence times [169], which will be considered in section 5.5.2.

4.4 Current-voltage response

The current-voltage response at room temperature and 5 K for the devices is in figure 4.8. Different behaviour between RT and 5 K temperatures is the result of a change in the charge carrier mobility (μ) as free carriers freeze at cryogenic temperatures [8, 214]. The best demonstration of a clean electrical contact between the electrodes and silicon with minimal Schottky barrier is a low resistant Ohmic (linear) relationship between the applied voltage and output current. A poorly fabricated MSI interface not only results in noisey current-voltage characteristics but also a noisey EDMR signal. A native oxide beneath the metal contact, though probably only 1-2 nm thick, is rich in charge

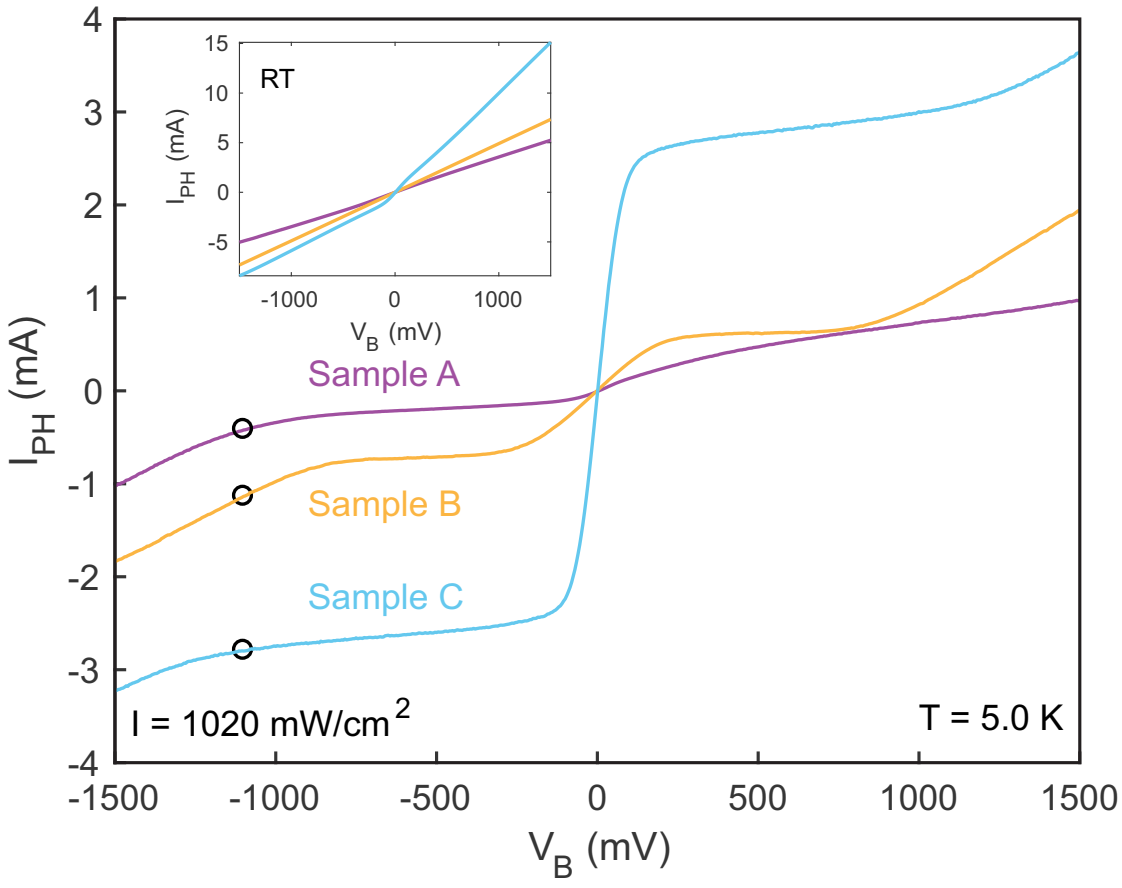


Figure 4.8: Current-voltage response of silicon samples. The current response under illumination with the Xenon arc lamp at 1020 mWcm^{-2} at a temperature of 5 K. [inset] The same samples current response at room temperature. The black circles demonstrate the operating point at $V_b = -1100$ mV.

traps and results in Fermi level pinning and therefore a Schottky barrier to overcome in order to achieve unencumbered and sensitive current flow. However, ohmic contacts are not necessary for clean EDMR signals and Schottky barriers from devices without contact dopants are commonly used [42, 45]. A Schottky barrier can in fact be useful for tunnelling from the metal to shallow defects in the semiconductor at higher ($\sim$3 V) bias voltages [23].

Despite each device being prepared in the same way, the IV curves are markedly different. Whilst each sample was dipped in hydrofluoric acid to remove the SiO_2 until the sample became hydrophobic, a dirty contact surface (as might be the case with sample B) or the inadvertent incomplete removal of the SiO_2 insulator is still probable. Although the etch rate of silicon in hydrofluoric acid is extremely low relative to SiO_2, the dip duration was minimised to ensure maximum separation between the silicon surface and the peak doping concentration at 100 nm depth.

The shoulder in the current response of devices B and C measured at 5 K at around $\pm$150 mV demonstrates low resistance at smaller V_b and higher resistance at high V_b. This suggests a low contact resistance and a higher bulk resistance, which is approximately consistent across all three devices.

The most probable cause of the variation in the IV characteristics between the three devices is the unresolved amorphisation from ion-implantation. Amorphous silicon also demonstrates reduced optical absorption compared to crystalline and microcrystalline silicon [215]. In my sample, there is a drop in resistivity at low bias voltages as the anneal duration increases. Increased amorphisation leads to a larger bandgap [216] and therefore a reduction in the optical bandwidth available for photoexcitation. Both the reduced absorption and increased bandgap would result in a lower photocurrent and support the hypothesis that the three devices demonstrate improved anneal-induced crystallisation and that sample A in particular is still heavily amorphised in the active region of the device. This will be discussed further in section 4.5.1.

4.5 Spin-dependent recombination in arsenic and sulfur doped crystalline silicon

As previously stated, my aim is to observe the formation of As-S spin-pairs in silicon. The first step to achieving this was to fabricate silicon samples suitable for EDMR measurements. Spin-pairs are most easily observed through the electrical detection of SDR, as it has been shown that spin-pairs consisting of an energetically 'shallow donor' and deep 'acceptor' (in this case a deep double-donor) facilitate the SDR of electron-hole pairs when Pauli blockade is lifted.

Following the fabrication of crystalline silicon samples co-doped with ^{75}As and ^{33}S (and containing residual ^{31}P and ^{nat}B) outlined in section 4.3, cwEDMR measurements could be performed. The experimental setup is described in section 4.2 and depicted in figure 4.3.

4.5.1 Ion implantation damage

The damaging effects of ion implantation must also be taken into account when considering the spectra in figure 4.9. The deceleration of ions with kinetic energies of the order of keV causes damage to the crystal lattice through energy transfer processes to the semiconductor known as 'electron and nuclear stopping' [217]. The resulting amorphisation is often investigated using EPR techniques to quantify the density of spin-active defects in the crystal. EPR investigations have shown that amorphisation is considered to be the result of overlapping implantation pathways or 'damage clusters' [218, 219]. The sameness of properties of ion-implantation induced charge traps and charge traps in amorphous silicon led to the realisation of the amorphisation process from ion-implantation. The resonance that established this connection had a g-value of 2.0059 and linewidth of about 5 G for phosphorus and arsenic implanted silicon [219, 220]. It does not seem that this particular resonance is observed in my spectra. These amorphous silicon defects are in fact the same as interfacial defects in crystalline silicon [221]. Additionally dopant implantation in SiO_2 has been shown to cause E' centres, when the bond structure of SiO_2 (≡Si-O-Si≡) is broken [222]. This is also a typical interfacial defect.

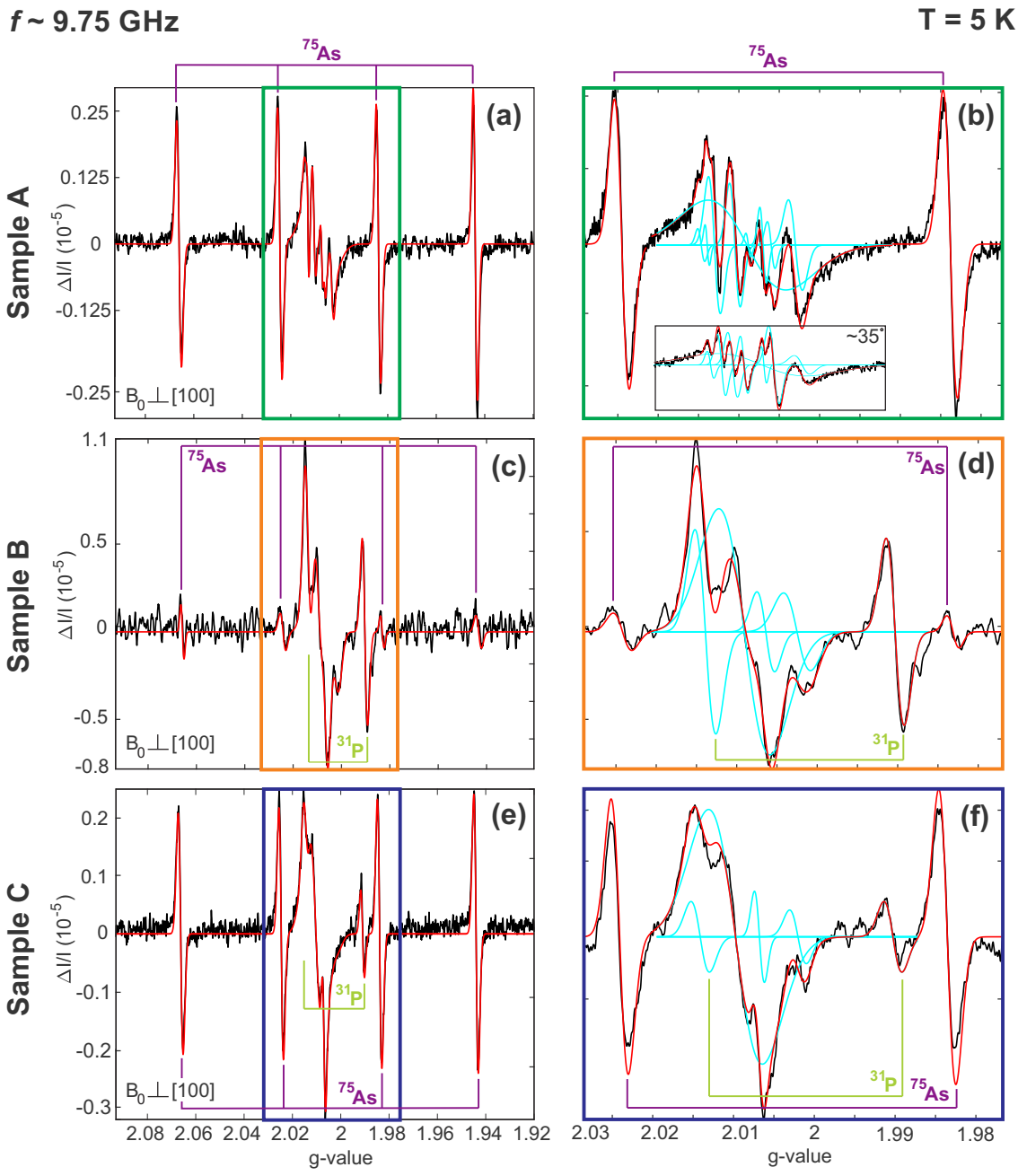


Figure 4.9: Fitted cwEDMR spectra. cwEDMR spectra of **(a)** sample A, **(c)** sample B and **(e)** sample C measured at 5 K. **(b)**,**(d)** and **(f)** are the magnified fitted spectra of **(a)**,**(c)** and **(e)** respectively. f_{mod} = 9.02 kHz and V_B = -1.1 V.

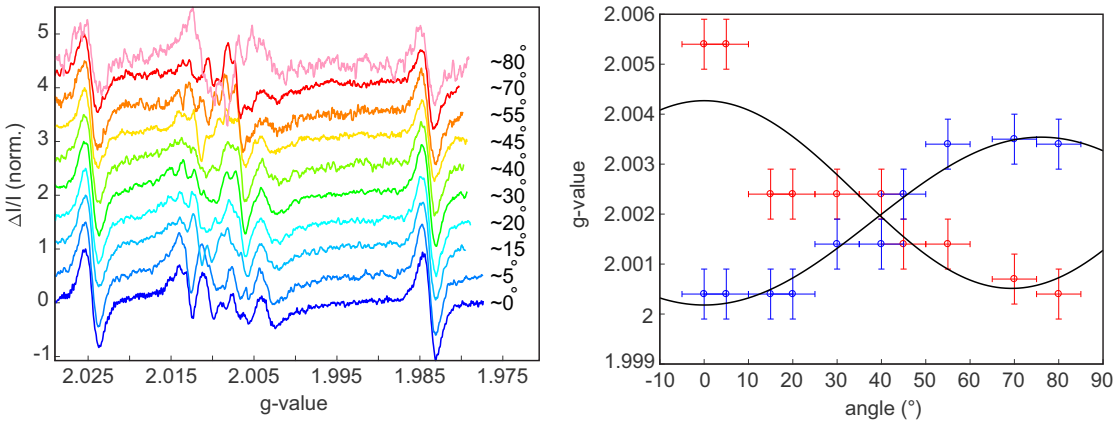


Figure 4.10: Anisotropy in sample A. (a) cwEDMR signal of the sample rotated with respect to B_0. Each EDMR field sweep is offset for visual clarity. The approximate angle of rotation is to the right of each sweep. (b) Angularly dependence of P_{b0} and E' defects.

Because of the causal relationship between ion-implantation and amorphous silicon-like defects, the spin density of the defects from ion-implantation should match the dopant concentration profile.

For low energy density implantation, the damage created is the same as that created by electron or neutron-irradiation. For high energy density implantation the overlap of lattice damage occurs, at which point the trapped charges are delocalised over a complex of defects in high concentration [223]. High atomic mass atoms like bismuth cause more implantation damage than lower ones like phosphorus, arsenic and sulfur. At high implantation doses ($\geq 10^{14}$ cm^{-2}) and implant concentration ($\sim 10^{19}$ cm^{-3}), Bi^+ can amorphise a crystal lattice [218, 223, 224]. So too can lower atomic mass P^+ given a critical energy density (implantation does/unit volume) [219]. Generically, this was identified as $\sim 10^{21}$ keV/cm^3 for any impurity in silicon [223]. As will be shown in the following section, my dosage exceeds that.

Amorphous silicon lacks the long-range order typically associated with crystalline silicon. It is further characterised by a lack of structure and periodicity within the crystal, which causes dangling bonds amongst the silicon atoms. These act as electron traps, much like dangling bonds at a silicon surface and create large densities of permissible states within the bandgap [216]. An atmosphere of a hydrogen-containing compound like silane SiH_4 can be used to create a amorphous silicon-hydrogen alloys (a-Si:H),

where the hydrogen atoms passivate the dangling bonds in the crystal. This reduces the density of midgap states. Whilst my H_2O dip following the SiO_2 HF acid dip temporarily passivated silicon dangling bonds at the surface, H^+-ion would not have reached the bulk crystal dangling bonds to saturate them.

By applying an annealing thermal treatment, the density of ion-implantation induced defects can be removed (at increasing efficiencies for increasing temperatures). The amorphous layer will re-crystallise epitaxially when treated to an anneal above 550° C [218, 225]. For deliberate doping profiles, this requires balancing minimal ion diffusion with the longer anneal durations needed to repair the lattice after implantation damage to thereby achieve a higher activation yield of the dopants [224]. The dopants within a recrystalised region are electrically activated and charge-uncompensated. Crystals with implantation doses below the amorphisation threshold level [218, 226] can be re-crystalised at lower anneals (250-500° C) though they still form defects from compensating point defects. These defects can then be removed with another anneal at 800-1000° C [218].

With the ion-implantation induced interfacial defect-like charge traps in mind, I can now consider my samples. Whilst most amorphisation research has focussed on shallow impurities commonly used in silicon like boron, phosphorus and arsenic, the comparable atomic mass of sulfur makes similar effects probable.

Sample A in particular (figure 4.9 (a) and (b)) was only annealed for 10 ± 8 seconds at 1200° C. Although the sample was annealed above the threshold temperature needed to re-crystallise the ion-implantation induced amorphous silicon, it was not annealed for long enough. This explains the high density of resonances around g$\sim$2 in sample A compared to samples B and C.

4.5.2 Spin species identities

The cwEDMR spectra for samples A, B and C are in figure 4.9. The figure show the spectra as a function of g-values across a range of 300 mT (figures (a), (b) and (c)) and approximately 100 mT (figures (b), (d) and (f)). The cwEDMR signal intensities are of the same approximate size making comparison between the spectra of the three samples

$g_\perp$	lw_{pp} (G)	Identity	In sample B and C?	Reference
2.0091	1.5	??	✗	
2.0083	0.9	??	✗	
2.0074	2.5	Light induced 'excitonic state'	✗	[158]
2.0049 ($g_\parallel$=2.0014)	2.3	P_{b0}	✗	[227, 228]
2.0032	1.0	P_{b1}		[229]
2.0014	1.4	P_{b0}	✓	[227, 228]
2.0004 ($g_\parallel$=2.0054)	1.6	E' centre	✓	[230]
1.9974	3.0	CE	✓	[45]

Table 4.4: Resonances observed in sample A. The g-values and identity of the resonances fitted in the cwEDMR spectra of sample A. The resonances in samples B and C are in table 4.5.

simpler. Each sample shows the typical quartet of ^{75}As hyperfine resonances associated with its nuclear spin $I = {}^3/_2$, split by approximately 7.1 mT. The spectrum of sample A is very busy around g∼2 with nine resonances (in addition to the arsenic lines), though contains no obvious ^{31}P lines. Samples B and C show a strong resemblance to each other. They have the same resonances around g∼2 as outlined in table 4.5 though in sample B the ^{31}P hyperfine doublet, split by approximately 4.1 mT is more dominant than in samples C, whereas sample C shows a stronger ^{75}As hyperfine quartet. The only difference between the two samples during the preparations was the heat treatment they experienced. Whilst sample C was annealed at 1200° C for three times sample B's 60 seconds, sample B was treated to an additional contact anneal at 475° C. Published results show the formation of inactive clusters of (seven) arsenic donors around a single vacancy for anneal temperatures less 750° C [231]. This clustering as a result of the contact anneal seems to explains why sample B has a lower signal intensity for the arsenic donors.

To confirm the identity of these spin species, their angular dependent g-values were measured by rotating the crystallographic axis of the sample relative to B_0. Complicated by the overlapping resonance spectra, the approximate results are presented in figure 4.10 and again in table 4.4 and 4.5.

Three resonances are observed above g =2.007 in sample A. To the best of my

$g_{\perp,B}$	$lw_{pp,B}$ (G)	$g_{\perp,C}$	$lw_{pp,C}$ (G)	Identity	In sample A?	Ref.
2.0086	4.2	2.0092	3.9	^{31}P	✗	[232]
2.0036	12.0	2.0045	11.5	P_{b0}	✗	[158, 233]
		$g_{\parallel} = 2.0054$				
2.0014	2.3	2.0015	2.1	P_{b0}	✓	[227, 228]
		$g_{\parallel} = 2.0027$				
1.9973	4.3	1.9968	3.6	CE	✓	[45]
1.9851	4.0	1.9853	3.9	^{31}P	✗	[232]

Table 4.5: Resonances in sample B and C. The g-values and their identities are tabulated. Only two resonances match those found in sample A: P_{b0} interface defect and the conduction electron (CE) signal.

knowledge, no g-values like this have been reported in crystalline or amorphous silicon except the isotropic g-value I observe at $g = 2.0074$ matches light induced excitonic states observed in amorphous silicon. This state is a exciton bound to a shallow conduction band tail state [158].

There are various interface defects too. The P_b centre is an interface dangling bond whereby a silicon has unsaturated bonds; it is only bonded to three other silicon atoms in the crystal lattice ($\cdot$Si$\equiv$Si$_3$) [234]. These occur at the Si/SiO$_2$ interface has been associated with [111] and [100] crystal orientations [235]. The trapped electrons are highly localised and strongly anisotropic with predominantly orbital p-content perpendicular to the [111] crystal orientation [230]. These defects are a common electronic trap in the energetic range 0.15-0.95 eV below the conduction band when unpassivated by H [236].

E' is a dangling bond of a silicon atom bonded to three oxygen atoms also typically seen at the Si/SiO$_2$ interface and acts as an electron trap. There are several variations of this that involve other oxygen and hydrogen atoms, and also a *E'* centre coupled to a diamagnetic silicon-bound hole at an oxygen vacancy [230, 237]. The *E'* centre demonstrates weak axial anisotropy.

The broad resonance at approximately g=1.9975 is commonly known as a 'conduction electron (CE)' state, and is a shallow electron trap energetically close to the conduction band in microcrystalline silicon [45]. The g-value and small amount of anisotropy matches that of the 'NL54' defect observed in ref. [183], which is a sulfur-complex in silicon passivated by hydrogen. The only way that would be possible in my samples would be if sulfur diffused to the sample surface and was then passivated by the hydrogen

from the H_2O dip that followed the HF acid dip, or from the H_2O quench that followed the anneal. Alternatively, although diffusion of hydrogen into silicon can occur when a silicon sample is annealed at 1250° C in H_2O, my samples' temperature immediately dropped at a rate of 2000 K/s when quenched (rather than the 30 minutes needed to diffuse hydrogen into the sample) and so is improbable [238]. Indeed, quenching of the sample in H_2O was used in ref. [184], where they did not observe any H-passivated sulfur related complexes in silicon.

Given that the sulfur content was isotopically purified with ^{33}S, isolated ^{33}S would be expected to contain the hyperfine quartet symbolic of its $I = {}^3/_2$ nuclear spin. The boron acceptors are not expected to be EPR visible as the silicon is not under uniaxial stress [11, 239].

4.5.3 Thermal treatment effects on activation

As identified in section 4.5.1, the short anneal duration of sample A resulted in minimal re-crystalisation of the amorphised silicon from ion-implantation. This explains the rich resonance spectra around $g \sim 2$ in sample A. Sample A does also however, demonstrate strong ^{75}As resonances though no activated ^{31}P signal.

The absence of a ^{31}P signal from sample A could be the result of two things: either ^{31}P was not electrically activated in the anneal, or a critical concentration of ^{31}P donors did not coexist in proximity to a suitable spin-pair partner. Possible spin-pair defects could be dispersed throughout the amorphised implantation depth or at the interface where the ^{31}P can precipitate to. It is unlikely that any deactivation would have occurred in only a 10 second anneal. And whilst phosphorus has a larger activation energy (4.1 eV) than arsenic (3.6 eV), 10 seconds of *effective* anneal time at 1200° C should be enough to activate at least 50 % of the donors [240].

It is probably that the samples was not actually raised to the anneal temperature for long enough to engage enough ^{31}P donors to demonstrate an EDMR signal above the noise floor. In sample A, arsenic is quite dramatic and phosphorus is not obvious. The lower activation energy of arsenic meant that it was activated before phosphorus and at this time scale, that difference is significant enough to demonstrate differences in the

EDMR spectrum.

It is important to note that the absence of donor spin signatures from the cwEDMR spectra in figure 4.9 (a) and (b) dose not correlate with electrical deactivation through precipitation, clustering or interstitial positioning [136]. This is a symptom of my measurement scheme. To verify deactivated dopants, EPR, optical absorption, x-ray diffraction (XRD), Hall conductivity measurements and cross-section electron microscopy to observed the distribution of dopants in a control samples would be needed. My measurements show that a critical concentration of ^{31}P is not involved in SDR. ^{31}P on its own does not make an effective SRH recombination centre [11] and its independent cwEDMR signal has not been observed in SDR experiments. An insufficient density of interface defects exist in sample A for ^{31}P-P_{b0} spin-pairs to form [22]. The relatively larger signal intensity of ^{31}P in sample B compared to sample C could be due to the larger P_{b0} signal at $g \approx 2.004$ also forming spin-pairs with ^{31}P.

Samples B and C show approximately the same resonant identities with differing intensities. This suggests that the anneal of more than 10 seconds re-crystalised the samples. After a minute anneal (sample B), the cwEDMR spectra has simplified to what appears to be only active donors and interface defects that cannot be passivated by an anneal as outlined in table 4.5. Following the thermal activation anneals, additional thermal treatments can cause deactivation of donors. For supersaturated samples, 475° C can cause deactivation of shallow donors through clustering [136]. This concentration dependent deactivation mechanism, which incorporates diffusion effects too, explains why the contact anneal had minimal effect on the activated ^{31}P concentration in sample B (figure 4.9 (c) and (d)). In fact, the activation and contact anneal seemed to have a positive effect on the ^{31}P signal intensity, which was not present in sample A. This is most probably due to the diffusion and precipitation of the ^{31}P to the sample surface.

The spectra of sample C in figure 4.9 (e) and (f) demonstrate a small ^{31}P resonance intensity relative to the other resonances in the sample. What is most probable is that the contact anneal applied to sample B increased the proportion of ^{31}P donors forming spin-pairs. Sample C meanwhile, demonstrates a small ^{31}P signal intensity (similar to sample A) because the residual ^{31}P in the sample was poorly diffused to areas of the

sample with viable spin-pair partners.

The ^{75}As signal intensity was high for sample A, low for sample B and high again for sample C. Unlike ^{31}P, it seems the contact anneal at 475° C applied to sample B reduced the proportion of electrically active, EDMR-visible ^{75}As donors. This is most probably due to clustering of ^{75}As in sample B [136, 231]. As can be seen in figure 4.7, there is an ^{75}As concentration at the interface.

When determining the effects of the activation and contact anneals on the samples, it is important to compare the activation energy for the rate of activation ($E_{a,P} = 4.1$ eV and $E_{a,As} = 3.6$ eV), to the thermal activation energy of diffusion ($E_{d,P} = 3.3$ eV and $E_{d,As} = 3.4$ eV) previously specified in section 4.3.1.1 [198, 199, 240]. This similarity suggests that the process of activation and diffusion are the same [240] and whilst there is a small difference in the activation energies for the rate of activation, their activation and diffusion behaviour should remain markedly the same for a given heat treatment.

SIMS measurements were attempted on these samples though the concentrations of ^{75}As, ^{31}P and ^{33}S were unfortunately too small to measure a dopant profile, except for the ^{33}S concentration in sample A and the ^{75}As concentration in sample B, as depicted in figure 4.7.

4.5.4 Absence of As-S spin-pairs

Despite the prevalence of arsenic in all three samples, no sample shows any sulfur-related spin centre signature. Published sulfur g-value data is in table 4.1. Indeed, the likely formation of higher-order EPR-silent sulfur complexes after the contact anneal at 475° C rules out a ^{33}S hyperfine quartet is sample B. Given that isotopically purified ^{33}S was used, the characteristic quartet hyperfine signature of isolated ^{33}S is expected. As detailed in table 4.1 and ref. [182], the typical quartet is split by approximately 114 G apart and centred on 2.0054 (or 41 G apart centred on 2.0008 for the ^{33}S-S pair).

There are several likely explanations for the absence of ^{33}S signals in the EDMR spectra. First, my concentration of boron is several orders of magnitude below that of sulfur. The concentration of boron determines the concentration of charge compensated sulfur that will form paramagnetic S^+ ions. The concentration of spin-active sulfur due to

boron charge compensation was therefore, at most, approximately 10^{12} cm^{-3}. Based on the SNR of ^{75}As ($\approx$ 12) in figure 4.9 (a), the sensitivity limit of my EDMR measurements is $\sim 10^{-15}$ cm^{-3} ($\approx 10^{9}$ ^{75}As atoms), which is therefore about three orders of magnitude above the maximum concentrations of ^{33}S. Measurement sensitivities for SDR as low as 10^{7} atoms in a bulk sample [11] and 100 atoms for a nanostructure consisting of a gap between high-dose metallic leads [12] have been demonstrated, which suggests that improvements to the measurement sensitivity are possible. Improved sensitivity would allow for the low dopant implant concentrations suited to maximum dopant activation.

Second, as outlined in section 4.1.7.1, recently published results has demonstrated photoneutralisation of spin-active double donors and acceptors [144]. Whilst a photocurrent allows an ionised shallow donor at 5 K and a neutral deep defect in a A^{-} state to capture an electron and hole respectively, photoexcited free carriers are captured by ionised chalcogen double-donors to become EPR-silent and charge neutral (A^{-}). From an EDMR perspective, it inhibits the cascade of an captured electron at the shallow arsenic donor to recombine with a hole via the deep donor. Ionisation of ESR-silent double-donors can be expedited by selective IR illumination ($\lambda \sim 4$ μm) though at cryogenic temperatures ionisation still takes seconds to minutes, when not illuminated. There is potential that the observation of chalcogen double-donors via SDR is an inherently flawed measurement technique as it resets the double-donor charge state.

Third, critical to the SDR process is hole capture by the deep level defect. As was outlined in section 4.1.6.1, sulfur has a larger hole capture cross section than either selenium or tellurium. For sulfur ions that has recently captured an ^{75}As donor's ionised electron ($e^{-} + S^{+} \rightarrow S^{0}$ (A^{-})), the most likely hole capture mechanism is the Auger process, which can also result in sulfur becoming doubly ionised [179]. Between Auger double hole capture and photoneutralisation, sulfur is rarely in a singly ionised form, which makes it unresponsive to EPR experimentation. With such large binding energies the ground state wave function is very compact, which makes inter-state transitions like EHR improbable or slow at low temperatures [144, 153]. This explains the Auger capture cross section being as small as 10^{-20} cm^{2} [179].

Finally, the current level in the IV curves in figure 4.8 seemed to saturate when the

resistivity of the sample changed at approximately 100 mV. This is most probably the change between the surface and bulk resistance. Measuring the change in the electrical current caused by EHR requires the electric fields of the applied bias voltage to penetrate to the level of the donors 100 nm below the surface, though no calculations have been performed of whether this is occurring.

4.6 Conclusions

Three samples with the same ion-implantation profiles of ^{33}S and ^{75}As were annealed for differing durations (sample A: 10 seconds; sample B: 60 seconds; sample C: 180 seconds) at 1200° C and thermally quenched in H_2O (DI). By varying the anneal time I intended to observe differing levels of electrical activation of sulfur as the anneal should move sulfur ions into interstitial crystal lattice and the thermal quench should inhibit diffusion.

cwEDMR experiments were performed on the samples. In all three samples, ^{75}As's hyperfine quartet were observed with varying intensities, whilst residual ^{31}P hyperfine doublets were only observed in samples B and C. The cwEDMR signature of ^{33}S was not observed in any of the samples. Sample A demonstrated SDR between ^{75}As and various interface defects and amorphous silicon charge traps of the same nature. Sample B demonstrated a reduction in the density of defects as the sample was re-crystalised by the thermal anneal. The cwEDMR signature of ^{31}P was also observed in this sample, a remnant of the substrate doping. Sample C revealed a similar cwEDMR spectra to sample B, with identical resonance identities of different intensities. The comparable activation energies and activation energies of diffusion of arsenic and phosphorus meant they behaved very similarly for the thermal treatment the samples received. The differences in their respective cwEDMR resonance intensities is attributed to their ability to form spin-pairs in the samples, most probably with interface defects. The nature of the spin-pairs shall be further investigated in the following chapter.

Unlike ref. [182] where ^{33}S donors were diffused by annealing in a sulfur atmosphere, my ion-implantation to a peak depth is more likely to result in dopant diffusion, with

dopants concentrated in a Gaussian distribution centred at 100 nm below the sample surface. The several minutes annealing was short enough to avoid clustering, whilst still being acceptable for my intended doping profile.

The absence of any ^{33}S signal in the cwEDMR measurements was most probably due to difficulties in obtaining measurable quantities of the paramagnetic S^+ state. Both an insufficient boron concentration and photoneutralisation contributed to limiting the S^+ state concentration. Boron's concentration of $\sim 10^{12}$ cm^{-3} was three orders of magnitude below the sensitivity limit ($\sim 10^{15}$ cm^{-3}) of my measurement setup. Illumination could be used to regulate an imbalance in the relative concentrations of B:S [11]. In my case, where $[S] \gg [B]$ a weaker light intensity may be one way to encourage boron donors to soak up as many sulfur electrons as there are boron atoms, and therefore increase the proportion of singly occupied sulfur. The reduced density of free carriers should encourage the background acceptor doping to provide effective charge compensation.

5

Characterisation of spin-dependent processes in arsenic and sulfur doped silicon

In this chapter I characterise the spin-dependent interactions that result in the cwEDMR spectra in Chapter 4. I describe how pEDMR has two key advantages over cwEDMR. Firstly, with megahertz sampling I can observe the current transient resonance to a microwave pulse, and secondly, I can coherently manipulate spin-centres to control spin-dependent interactions. I utilise both of these advantages to experimentally interrogate my novel EDMR device doping architecture involving shallow and deep donors in silicon. I therefore initially analyse the current transient response to a microwave pulse. This is followed by a description of the spin-to-charge conversion process that maximises the SNR in pEDMR measurements. I then use coherent manipulation to determine coherence, charge generation and spin-pair electronic transition times. The final pEDMR analysis relies on electrically detected echo electron double resonance (EDeELDOR) to identify spin-pair partners in my sample. Conclusions from the experiment are made at the end of the chapter.

5.1 Introduction

In Chapter 4 naturally occurring silicon samples co-doped with ^{75}As and ^{33}Swere investigated by cwEDMR. This technique is useful for spin-active defect-state identification. When faced with the difficult task of discriminating between overlapping resonance spectra, in the absence of a high field/ high frequency excitation (ca. 240 GHz, 8.6 T) [171, 241], cwEDMR is a more effective than pEDMR. This is due to the more distinctive anti-symmetric nature of the Gaussian derivative line shape produced by the cwEDMR lock-in measurement technique compared to the Gaussian line shape observed in pEDMR.

However, cwEDMR provides a limited ability to investigating spin interactions and pEDMR is needed for charge transport and recombination analysis [155, 242]. pEDMR can be used to coherently manipulate spins as described in Chapter 2 and therefore probe their relative interactions. Short intense microwave pulses applied to a spin species and subsequent readout on a nanosecond timescale greatly expands the usefulness and the functionality of EDMR measurements. From the perspective of SDR experiments, coherent manipulation of spin-species allows us to interrogate the dissociation and recombination probabilities of spin-pairs [243]. This is achieved through deliberate and controlled disturbance of the steady state KSM modelled spin-pairs described in Chapter 2. Pulse lengths are tailored to the application; for temporal analysis of current transients I use longer ($\tau_{sat} \sim$ 500 ns) pulses to resonantly saturate the spin-states whereas for coherent spin manipulation that allows a spin-pair to transition from a singlet to triplet spin state, I use shorter pulses equivalent to half a rotation period (a 'π' pulse) at a species' Larmor frequency for $\sim$1 kW microwave pulses ($\tau_{\pi} \sim$ 80 ns).

In this chapter, I aim to characterise the interactions of the spin-species observed in Chapter 4. To start with I consider electrical measurements of coherently manipulated spin-species. I first consider the temporal behaviour of resonant pulsed microwave excitation, before I consider the spin to charge conversion process and the use of Hahn echo detection. I then investigate coherent manipulation of donor species and complete a decoherence measurement of the arsenic donors. An inversion recovery measurement is used to determine the generation rate of new electron-hole pairs and the recombination

rate of antiparallel pairs. Electron double resonance (ELDOR) measurements are then outlined, which identify the spin-species that form a spin-pair with arsenic donors.

5.1.1 Alternative spin-state readout techniques

Besides EDMR, there are several other indirect readout techniques for investigating spin interactions. One such technique is ODMR, which utilises 'photon flux' instead of photocurrent to observe spin-dependent transitions. This can prove useful for PL and radiative EHR investigations. ODMR was in fact the first to demonstrate that spin-selection rules could influence solid state electronic transitions [57, 58, 61, 171, 244].

As previously mentioned, SDR between a shallow (e.g. arsenic) and deep (e.g. sulfur) donor provides a viable means to avoid coupling to a interface defect as a means to readout a donor's spin state. Interface defects in close proximity to a donor limit coherence times [172]. This can be overcome with AEDMR via neutral shallow donor-bound exciton states (D^0X), which also provide a means to avoid coupling to corrupt interface defects to implement a spin-to-charge conversion [167, 245, 246]. In AEDMR, optical excitation just below silicon's indirect bandgap excites a valence band electron to the donor resulting in the localisation of two indistinguishable electrons and one hole in the D^0X state. Auger recombination results in EHR and the excitation of the excess electron to the conduction band

$$D^0 + \nu \rightarrow D^0X \rightarrow D^+ + e^- \tag{5.1}$$

where D is a donor, ν is a below bandgap optical excitation frequency (E_ν ~1.15 eV [246]) for silicon, X is an exciton and e^- is an ionised free electron. The excess electrons can be measured as a photocurrent, potentially allowing for electrical detection for the electron [247] and nuclear spin state in isotopically purified ^{28}Si [245]. The electrical measurement of the donor bound electron spin state (though not the nuclear spin state due to excitation broadening induced by strain from the electrical contact) was realised recently [246]. Auger-electron-detected electron nuclear double resonance (AENDOR)

could be used to measure the nuclear spin state overcoming the concerns of strain and temperature [167]. The authors also demonstrated the feasibility of AEDMR electron spin state readout and electron nuclear double resonance (ENDOR) control of ^{31}P in ^{nat}Si.

The spin-state of a single ^{31}P donor-bound electron and donor nuclear spin has been demonstrated by coupling the donor to a single electron transistor [13, 18, 19]. These achievements demonstrate the forefront of donor spin qubit measurement techniques and propelled donor spin qubits forward as a leading qubit architecture candidate. This measurement approach surpasses SDR as a qubit readout technique in sensitivity and sophistication, though EDMR still provides unique advantages for charge transport measurements.

Whilst these other readout mechanism can provide useful insights, I am interested in spin-pair interactions in silicon that are most effectively read out electrically. I will therefore focus on investigations of pEDMR.

This chapter aims to exploit the functionality of pEDMR to probe and characterise the spin interactions within ^{75}As, ^{33}S and ^{31}P doped silicon. It will first consider the temporal response of the electric current to resonant microwave pulses. This will elucidate the spin-dependent mechanism occurring in the samples and their timescales. To further investigate the spin-interactions, coherent spin manipulation experiments will then be described. Through a process known as ELDOR, the mutual coupling of the spin-active defects outlined in Chapter 4 can be interrogated to identify SDR spin-pairs. Since I am primarily interested in the donor-bound electron spin states, I will focus my investigation on a donor signal clearly visible in figure 4.9: ^{75}As.

5.2 Experimental setup

The experimental setup is outlined in section 4.2. For pulse microwave experiments, the *Bruker* EleXSys I 680 or EleXSys II 580 pulsed spectrometers are used. A SRS560 Low-Noise Voltage Preamplifier amplifies the pEDMR signal before it is fed to the *Bruker* Spec Jet II. For the ELDOR experiments described later, a *Bruker* Spin Jet Arbitrary

Waveform Generator is used. An additional light source is also used for the inversion recovery experiments; a *Schott* KL 2500 LED light source.

5.3 Current transient analysis

To begin the investigation of the temporal response of my spin system I consider the effects of a resonant microwave pulse on the photoconductivity. The pulse induces coherent spin rotations in the resonant species, which disturbs the equilibrium populations of the singlet and triplet spin-states established amongst the spin-pairs. The unsettled spin-pair populations cause a change in the rate of recombination and therefore a change in the photoconductivity after a microwave pulse [10, 40]. The resulting current transient provides an insight into the resulting spin-state populations as they return to equilibrium.

A more detailed current transient following a 480 ns EPR microwave pulse is in figure 5.1. The change in current is plotted against time. Before the microwave pulse, the antiparallel and parallel populations are considered equal since the spin-pairs are assumed to be weakly coupled [78]. For a microwave pulse typically of the order of 100 ns, the current reduction happens within $\sim$ 100 μs and returns to its steady state on a millisecond time scale, as seen in figure 5.4. The resonant microwave pulse at $t = 0$ excites one of the spins in the spin-pair to dramatically increase the antiparallel population. This results in an increase of electron-hole recombination and a reduction of the current signal. For a positive bias voltage, this is manifested as a decrease in ΔI and vice-versa for a negative bias voltage. The rate of antiparallel recombination is much faster than either parallel recombination or longitudinal relaxation $\tau_{ap} \ll \tau_p, T_1$, which will be discussed further in Section 5.6. This results in a return of the antiparallel population to its steady-state population much faster than the parallel population. The drop in the singlet population resulting from recombination as well as the slow return to the triplet steady-state population leads to a current *enhancement* at time $t = t_e \sim$ 100 μs, manifested as an increase in the ΔI for positive voltage and vice-versa for a negative bias voltage. The increased parallel population enhances the current beyond its steady state level as the Pauli-spin blockade limits recombination events. The current

then settles to its steady state of $\Delta I = 0$ at $t = t_{ss}$ [77].

The transient can be fit with three mono-exponentials with time constants $\tau_{LPF} \approx 0.3\ \mu$s, $\tau_q \approx 12\ \mu$s and $\tau_e = 233\ \mu$s showing the competing transient dynamics in the current response following a microwave pulse excitation. These values are comparable to those published in different doping strategies [42, 45]. τ_{LPF} reflect the low pass filtering of the transient current due to bandwidth limitations in the Femto current amplifier in the detection circuit (cf. figure 5.2), whereas τ_q and τ_e are representative of the spin dynamics in the system and show the reduction in the rate of reduction and enhancement of the photocurrent respectively [45, 243, 248]. Rate equation analysis has shown that variation of the parallel and antiparallel content of the system at the end of the microwave pulse is proportional to the amplitude of current transient modelled by a multi-exponential fit. The increased rate of EHR evident in the transient current can be explained by the rate of dissociation and generation of spin-pairs as well as the rate of antiparallel and parallel recombination [40, 45, 79]. The two characteristic time constants τ_q and τ_e can be used to determine rates of recombination, generation and dissociation. As demonstrated in Chapter 2,

$$\begin{aligned} \frac{1}{\tau_q} &= \frac{1}{2}(R_s + R_t) + G + d \\ \frac{1}{\tau_e} &= R_t + G + d \end{aligned} \tag{5.2}$$

where τ_q is a fast process and τ_e is a slow process. This leads to [79]:

$$R_s = R_t + 2(\frac{1}{\tau_q} - \frac{1}{\tau_e}) \tag{5.3}$$

where

$$\begin{aligned} {}^{2}/_{\tau_q} \leq \quad R_s \leq \quad & \frac{1}{\tau_q} - \frac{1}{\tau_e} \\ 0.3\,\mu s \leq \quad \frac{1}{R_s} \leq \quad & 13.3\,\mu s \end{aligned} \tag{5.4}$$

Similarly,

$$233\,\mu s = \tau_e \leq \frac{1}{R_t}, \frac{1}{d}, \frac{1}{G} \tag{5.5}$$

where $R_s > R_t$ because triplet recombination is forbidden, and for the system to return

to its steady state after a resonant microwave pulse $^1/_d$ and $^1/_G$ must be more than the slow time constant τ_e.

By applying a pulse of sufficient duration, the spin populations approach saturation as described in Chapter 2. At saturation the spin-up and spin-down populations equalise [44] as demonstrated diagrammatically in figure 5.1. This increases the likelihood of SDR as the spin system returns to its steady state. The change in current ΔI in sample A for a typical pEDMR field sweep measurement following a 480 ns low power (7.9 W at -21 dB) microwave pulse is in figure 5.2(b). Low power is chosen to reduces broadening. The microwave $\boldsymbol{E_1}$ and $\boldsymbol{B_1}$ fields couple to the metal components of the sample generating MWA or a 'non-resonant microwave background' current that dominates the current response. These are the same artefacts that induce the rectification currents discussed in Chapter 3, though in this case the microwave power is about six orders of magnitude larger. Through a combination of the device design, where there is less conductive material in the cavity, and the use of a two terminal device, the markedly detrimental effects on electron transport seen in nano-devices are not troublesome here. The MWA will be discussed further in Section 5.4.1 and has been subtracted from the current response in figure 5.2 to leave the spin-dependent resonant current change only. From the time cut at t =6.6 μs in figure 5.2(c) the resonance spectrum of the sample contains the same resonant features as in figure 4.9. Figure 5.2(a) shows the temporal current response up to 90 μs for $B_0 = 336.2$ mT at the $m_i = {}^3/_2$ ^{75}As resonance line and shows the reduction, and part of the enhancement, of the current. Because the bias voltage of -1.1 V resulting in a current of $\sim$400 μA is negative, a reduction in the photoconductivity corresponds to a positive $DeltaI$ response.

The four isolated resonances 7.1 mT apart at 336.1 343.2, 350.3 and 357.4 mT correspond to an electron bound to an ^{75}As donor, which has nuclear spin $I = {}^3/_2$. These are centred on a g-value of 1.99837 [249]. There appears to only be four distinct resonances in close proximity to $g \approx 2$ at 345.3, 346.1 and 346.7 mT; these are actually nine overlapping resonances, as was seen in figure 4.9. Despite using a low power to reduce broadening, the time cut lacks the fidelity of echo field sweep measurements discussed in section 5.4.1. The Gaussian resonance line shapes that occur in pEDMR

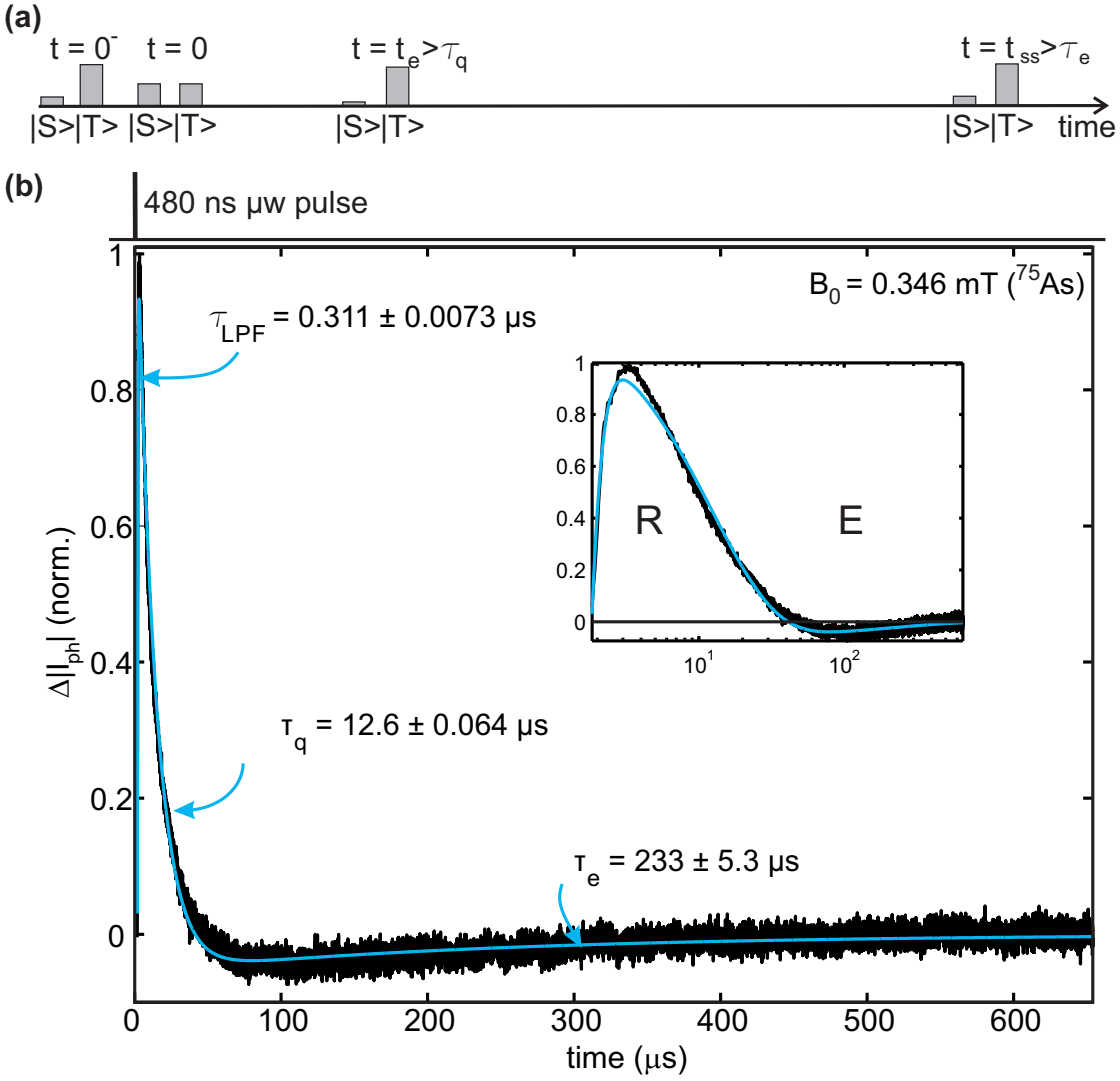


Figure 5.1: Current transient following a microwave pulse. (a) Histogram of singlet $|S\rangle$ and triplet $|T\rangle$ populations as a function of time. **(b) [top]** The microwave pulse that unsettles the triplet:singlet population equilibrium to change the rate of EHR and therefore the photocurrent. **[bottom]** A typical current transient following a microwave pulse that disturbs the steady state spin populations. In this case, B_0 is set on resonance with electrons bound to ^{75}As in sample B biased at -1.1 V at a temperature of 5 K. The transient data (black line) is fit (blue line) by three exponentials with time constants: τ_{LPF}, τ_q and τ_e. ΔI is *reduced (R)* when recombination reduces the singlet $|S\rangle$ population and then *enhanced (E)* as the triplet $|T\rangle$ population dominates as per the population histograms in (a). A response of $\Delta I < 0$ for a current reduction would occur for a positive bias voltage.

spectra are also more difficult to differentiate than the Gaussian derivative line shapes seen in cwEDMR spectra, though differentiating both can be achieved numerically.

There appears to be no obvious sign of ^{33}S's spectrum, which also displays a resonant quartet due to the $I = {}^{3}/_{2}$ nuclear spin. As seen in table 4.1, the hyperfine lines can be separated by 11.4 mT and centred on a g-value of 2.0054 [182]. In my spectrum in figure 5.2(c) there are two broad, very weak resonance at 340.9 and 352.1 mT. They are approximately 0.8 mT on the low field side of where ^{33}S should exist and the high field resonance does not appear as intense as the low field one, though this could be because it overlaps with arsenic's tail. Whilst it might appear that ^{33}S has been observed electrically, I was unable to perform pEDMR spectroscopy on the resonances. Whilst the current transients at 340.9 and 352.1 mT appear to match the other resonances shown in figure 5.4, the transient could be that of the arsenic resonances. Due to the weakness of the signals, they have been difficult to reproduce, including in my cwEDMR spectra in figure 4.9(a) and in a broad B_0 sweep that encompasses the full B_0 range of ^{33}S's four resonances in figure 5.3.

Figure 5.4 (b) demonstrates the resonance current transients for the different field position specified by the purple and yellow arrows in the fields sweep of figure 5.4 (a). Excluding the MWA between 1-2 μs, the current transients demonstrate the same form suggesting they follow the same recombination process. The reduction then enhancement behaviour of the current transients suggest they are also reflective of SDR occurring within the sample.

5.4 Spin-to-charge conversion

The spin-to-charge conversion process relies on Pauli-blockade controlled changes in current. By observing the relative changes in the photocurrent I can learn about the proportion of spin-pairs in parallel configuration, which experience Pauli-blockade, and the proportion of spin-pairs in antiparallel configuration, which are free to facilitate EHR.

A primitive and early adopted technique for spin-to-charge conversion for pEDMR relied on direct detection of the raw current following a microwave pulse [40]. This

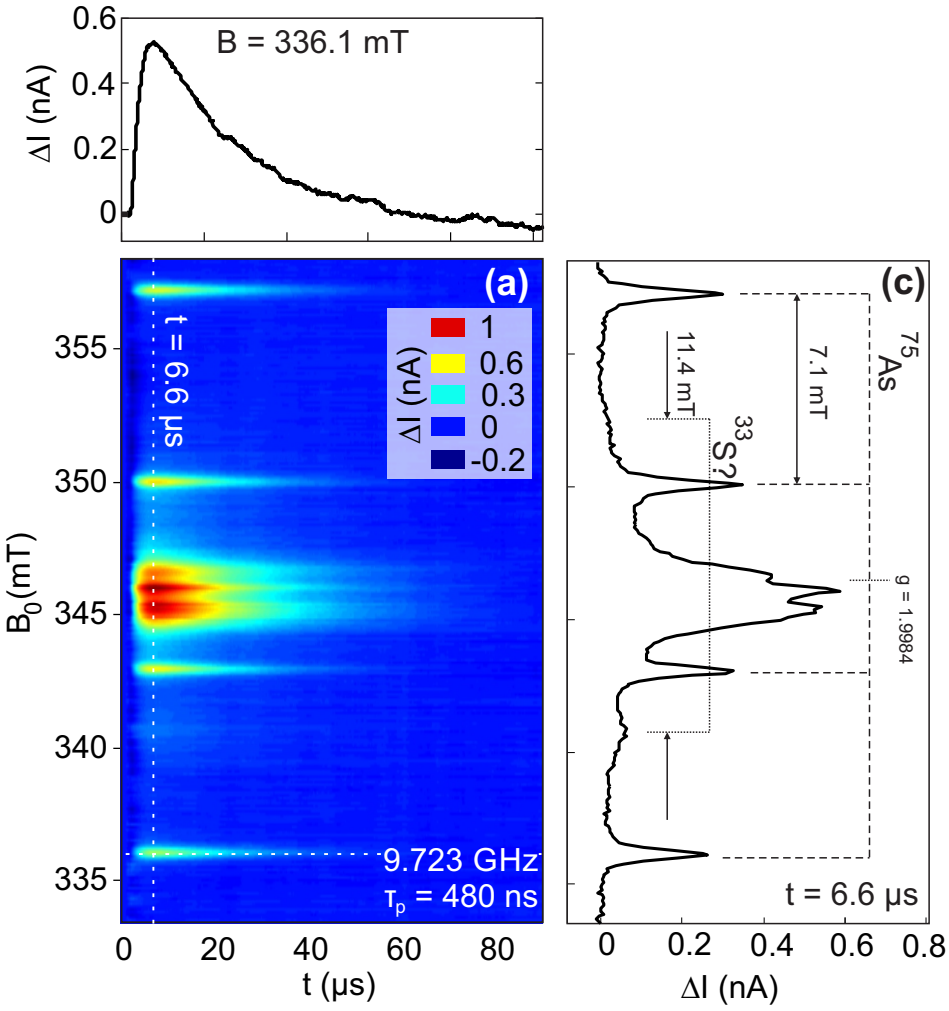


Figure 5.2: Current temporal response to a 480 ns microwave saturation pulse. (a) Contour plot of ΔI up to 90 μs after a 8 W microwave pulse 480 ns long on sample A. The device is biased with -1.1 V. The microwave artefacts have been subtracted. **(b)** A Zeeman field B_0 cut at the lowest ^{75}As hyperfine line at 336.1 mT. The temporal dynamics of this transient are described in figure 5.1. **(c)** A time cut at 6.6 μs.

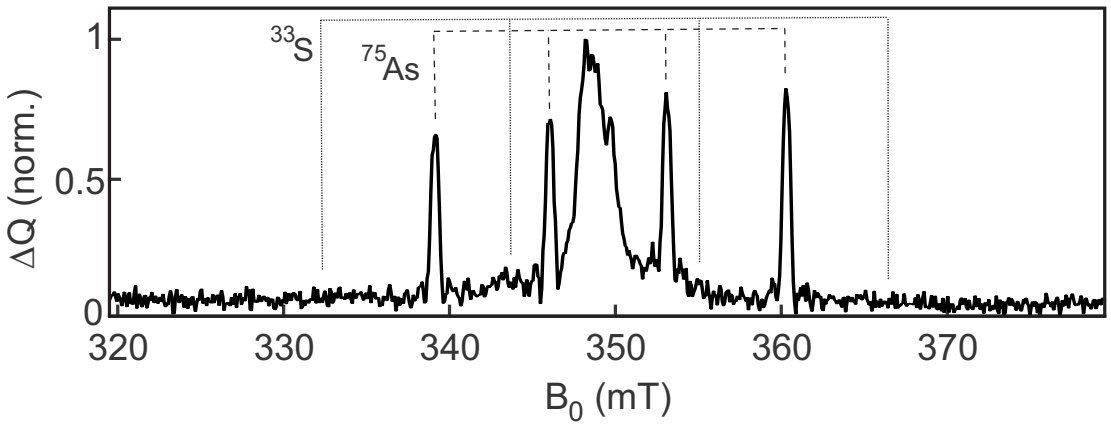


Figure 5.3: Absence of ^{33}S resonances. This broad B_0 sweep encompasses the full range of ^{33}S's four resonances (11.4 mT apart) though they are not visible above the noise floor. Their expected positions are labelled. The small rise at $\sim 343mT$ is also seen in figure 5.2(c), though it seems to be caused by something other than ^{33}S given that there is not a full resonance quartet at the expected B_0 values. This is an electrical spin echo measurement, which is described in Section 5.4.1. Variation in the interface defect line shape when compared to figure 5.2 (c) is the result of signal anisotropy.

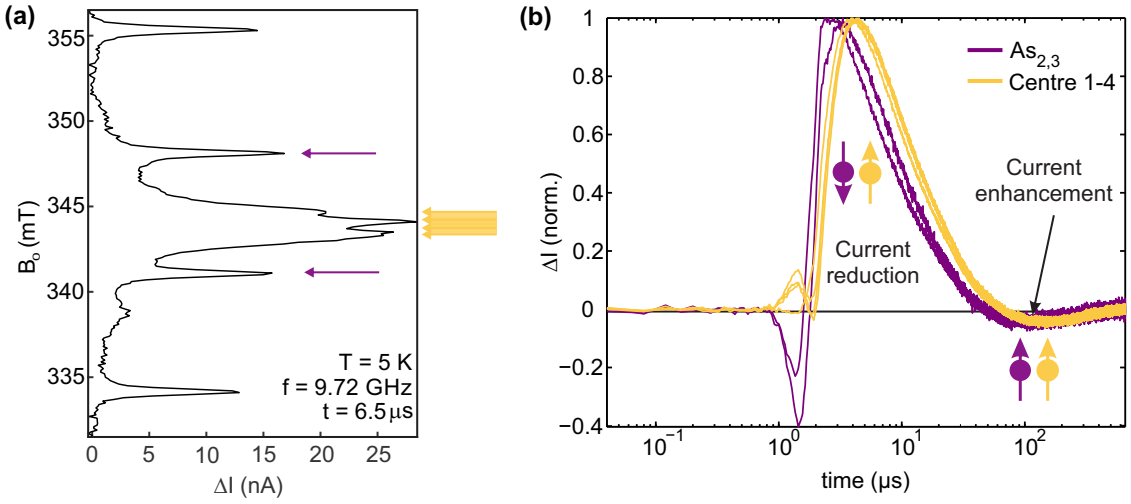


Figure 5.4: Resonant current transient comparison. (a) A time cut of the current transient in figure 5.2 at 6.6 μs. **(b)** B_0 cuts at the values marked by the arrows in (a). The transients demonstrate the same current reduction/enhancement behaviour at the same time constants suggesting the recombination process is consistent across all resonances tested.

measured current following a microwave pulse is a superposition of the resonant current and the MWA that results from coupling between the cavity's $\boldsymbol{B_1}$ and $\boldsymbol{E_1}$ fields to the metal components of the current detection setup in the cavity (wirebonds, metal electrodes etc). The resonant current results from a short microwave pulse that unsettles the equilibrium of parallel and anti-parallel spin-pairs within the sample and causes a rapid current reduction from EHR. This resonant current manifests itself as a current transient. To extract the resonant current change, the current transient across three B_0 points is needed. The high and low field value measurements are off-resonance whilst the centre field value is on-resonance. By performing linear interpolation across the three field points, the MWA current component can be subtracted from the raw current measurement.

5.4.1 Spin echo electrical detection

A more sophisticated spin-to-charge conversion relies on the spin echo technique and on phase-cycling used in ESR [250]. Firstly, let's consider spin echoes.

The pulse sequence used for spin echo detection is in figure 5.5. The Hahn echo pulse sequence has previously been used in silicon-based solid state ESR systems to measure decoherence (T_2) of donor electron spins [24, 150, 251]. These decoherence measurements will be discussed in more detail in section 5.5.2. The first pulse in the echo is a $^{\pi}/_{2}$ pulse that rotates the net spin magnetisation from the z-axis (B_0 direction) into the x-y plane. The second pulse is an inversion π-pulse applied after a delay of τ_1. It reverses the fan-out of the magnetisation caused by the static distribution of precession frequencies present in the local environment of the spin of interest. The fan-out occurs in the x-y plane, perpendicular to B_0. The refocusing of the precessing spin-packets causes an echo at delay time $\tau_2 = \tau_1$. Unlike a typical ESR sequence measured by an emitted radiation 'echo' signal, in electrical measurements that observe SDR the sequence is followed by a $^{\pi}/_{2}$ projection pulse at the time of the echo to reorientate the spin magnetisation from the x-y plane to the eigenstate parallel to the z-axis [61, 70, 171, 252]. The Hahn echo will form the basis to undertake coherent manipulation measurements. The spin echo sequence produces a current transient. By completing a

boxcar integration of the area under the transient I obtain a charge Q that is proportional to the relative spin-pair populations before the readout pulse sequence [78]. For pEDMR, the echo allows us to phase cycle, which I will now discuss.

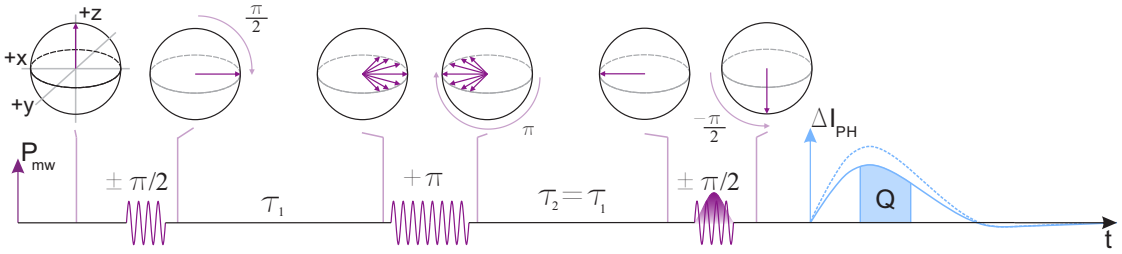


Figure 5.5: Spin echo pulse sequence for electrical detection. In addition to the normal Hahn echo pulse sequence, a third pulse ($\pm^{\pi}/_{2}$) reorientates the spins to the eigenstate parallel to the z-axis. A boxcar integration of the current transient quantifies the pre-pulse spin-pair anti-parallel populations. The spin-dependent resonant echo is a positive or negative change in current superimposed on the much larger non-resonant MWA.

Phase cycling is a common ESR technique used to differentiate between different types of coherences induced by excitation pulses [46]. It can be used to suppress imperfect quadrature detection artefacts or other unwanted excitations [253]. The technique can be applied to EDMR and is termed 'lock-in detection' because the pEDMR signal is modulated by cycling the phase of the microwave projection pulse on a periodic timescale of the shot repetition time τ_{srt} [64]. It is advantageous for pEDMR measurements because it removes the MWA, which is independent of the microwave pulse phase, and reduces low-frequency noise by an order of magnitude [64]. Unlike post-acquisition linear interpolation and subtraction of the MWA, phase cycling on a *Bruker* spectrometer updates the data output as it is being acquired.

Phase cycling the first or last $^{\pi}/_{2}$ pulse of the electrical detection echo sequence in figure 5.5 through the application of x-axis pulses π radians out of phase (from the $\pm x$-axis in the cavity) produces resonant spin-dependent current responses that differ. A cumulative pulse duration of 0 or 2π ($=\pm^{\pi}/_{2}+\pi+\pm^{\pi}/_{2}$) produces a spin-dependent echo proportional to the number of spin-pairs in antiparallel configuration before the pulse sequence [40]. Alternatively a cumulative pulse duration of π ($=\pm^{\pi}/_{2}+\pi+\mp^{\pi}/_{2}$) inverts the resonant spins causing a current reduction proportional to number of parallel spin-pairs. If I subtract one integrated current transient from the other I achieve a

quantity ΔQ that is proportional to the difference between the number of parallel and antiparallel spins before the readout pulse sequence [78]. A four-step phase cycle is in figure 5.6. The second $^{\pi}/_{2}$ pulse is phase cycled for each phase of the first $^{\pi}/_{2}$ pulse. Each step of the phase cycle is multipled by $-/+/+/-$ respectively to produce a positive outcome for the negative bias voltage used for all of my pEDMR measurements. $\Delta Q_{2-1} = Q_2 - Q_1 = \int \Delta I_1 dt - \int \Delta I_2 dt$ and $\Delta Q_{3-4} = Q_3 - Q_4$ (each two step phase cycles) are both proportional to the pre-pulse spin populations. By then adding them $(\Delta Q_{2-1} + \Delta Q_{3-4})$ I implement a four step phase cycle that more effectively removes MWAs so as to observe the spin signal.

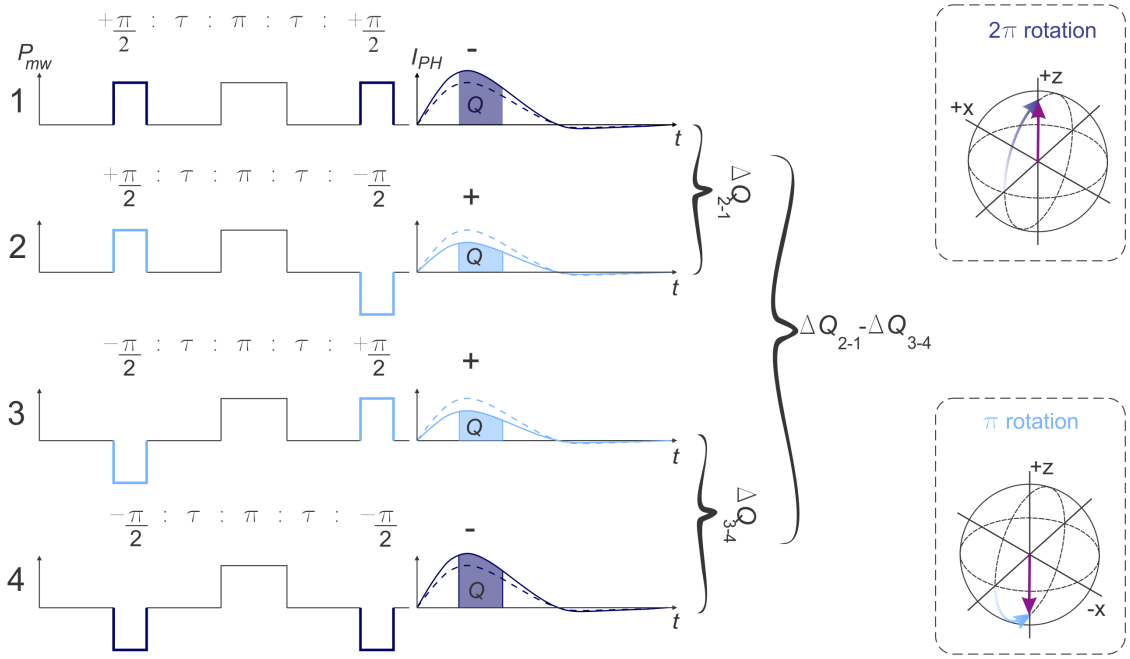


Figure 5.6: Four-step phase cycle. The pulse sequence of a four step phase cycle as used in ref [42]. Both the first and last $^{\pi}/_{2}$ pulses are phase cycled to produce an effective π or 2π pulse. By subtracting one integrated current transient from its out of phase equivalent, the MWA (dashed line) in I_{PH} is removed and the spin-dependent charge difference ΔQ is obtained. ΔQ that is proportional to the difference in population between the spin-pairs in parallel and anti-parallel configuration. A two-step phase cycle only cycles the phase of one of the $^{\pi}/_{2}$ pulses.

5.5 Coherent spin manipulation

5.5.1 Coherent spin oscillations

There are two approaches used here to measure nutations with an echo sequence: a three pulse sequence or a four pulse sequence. The four pulse sequence is a nutation pulse followed by a full Hahn echo sequence. Importantly a delay of $5 \times T_2$ is included after the nutation pulse to avoid coherence effects. The duration $\tau = 5 \times T_2$ ensures that roughly 98 % decoherence occurs. The three pulse sequence in figure 5.7a on the other hand, creates an echo though does not avoid T_2 effects. In my experience it produced cleaner nutations, most likely because there is less opportunity for the spins to relax.

The linear fit in figure 5.7 (b) identifies the oscillations as Rabi nutations. The fit is modelled by:

$$\omega_{Rabi} = \gamma B_1 \tag{5.6}$$

where the gyromagnetic ratio $\gamma = {}^{g\mu_B}/_{\hbar} \approx 178\ rad.s^{-1}.T^{-1}$. From figure 5.7b, I extract an experimental value of $\gamma_{exp} \approx 138\ rad.s^{-1}.T^{-1}$. Therefore, $\gamma_{exp} \approx 1.29\ \gamma$. Since ${}^{\gamma_{exp}}/_{\gamma} \approx 1$ for weakly coupled spin-pairs, and 2 for strongly coupled spin-pairs I can say the system is approximately weakly coupled [10, 254].

5.5.2 Spin coherence measurements

Classical spin states can use the binary 'spin-up' or 'spin-down' orientation relative to the magnetic field for information processing. The deterioration of this spin orientation is characterised by the 'spin-relaxation time' T_1. Donor-bound qubits have demonstrated remarkably long T_1 times of hours demonstrating the viability of electron spins for spintronics [150, 166, 232].

Quantum information storage and processing however, requires the superposition of the two basis states ($|\uparrow\rangle$ and $|\downarrow\rangle$), which makes their relative phase important. The deterioration of this phase information is characterised by the spin-spin relaxation time or 'coherence lifetime' T_2. T_2 is a fundamental property of qubits, as it is the timescale on which they lose their superposition and become classical bits. It is a key metric with which to judge the suitability of a quantum system for quantum computation. T_2 is limited by the T_1 time at higher temperatures though is regularly much shorter as a result

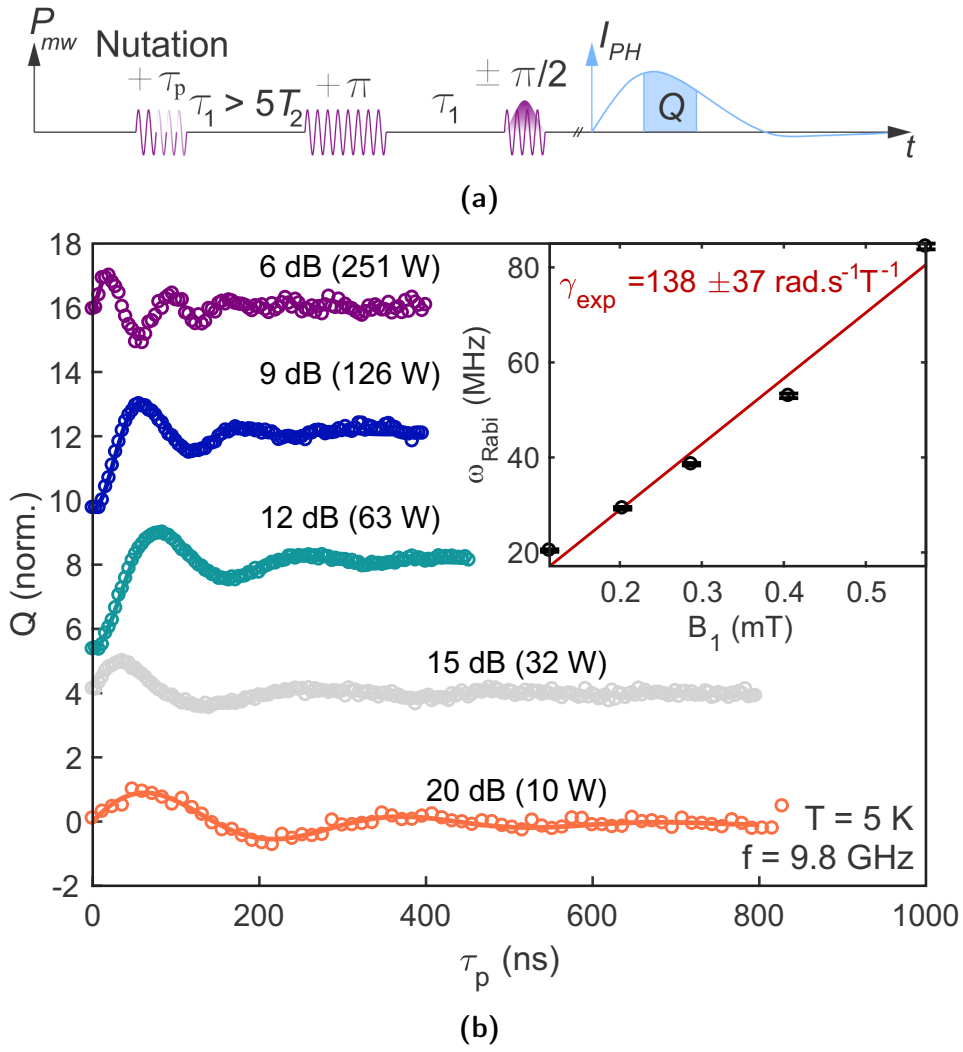


Figure 5.7: ^{75}As Rabi nutations. (a) The pulse sequence used to measure the Rabi nutations of **(b)**. The latter two pulses in the sequence are 64 and 32 ns respectively. The blue (9 dB) and green (12 dB) nutations involved no echo sequence and were the result of integrating a transient response to a single microwave pulse of increasing duration. **(b)** Rabi nutations for different $\boldsymbol{B_1}$ powers. [inset] Rabi nutation frequency versus B_1. The fit (dark red line) is linear with gradient $\gamma = {}^{g\mu_B}/_{\hbar}$. The B_1 values are derived using the relationship $B_1 = \kappa.10^{-\boldsymbol{P_{att'n}}/20}$, where $\boldsymbol{P_{att'n}} = [20, 15, 12, 9, 6]$ dB and $\kappa = 1.144$ is taken from ref. [77].

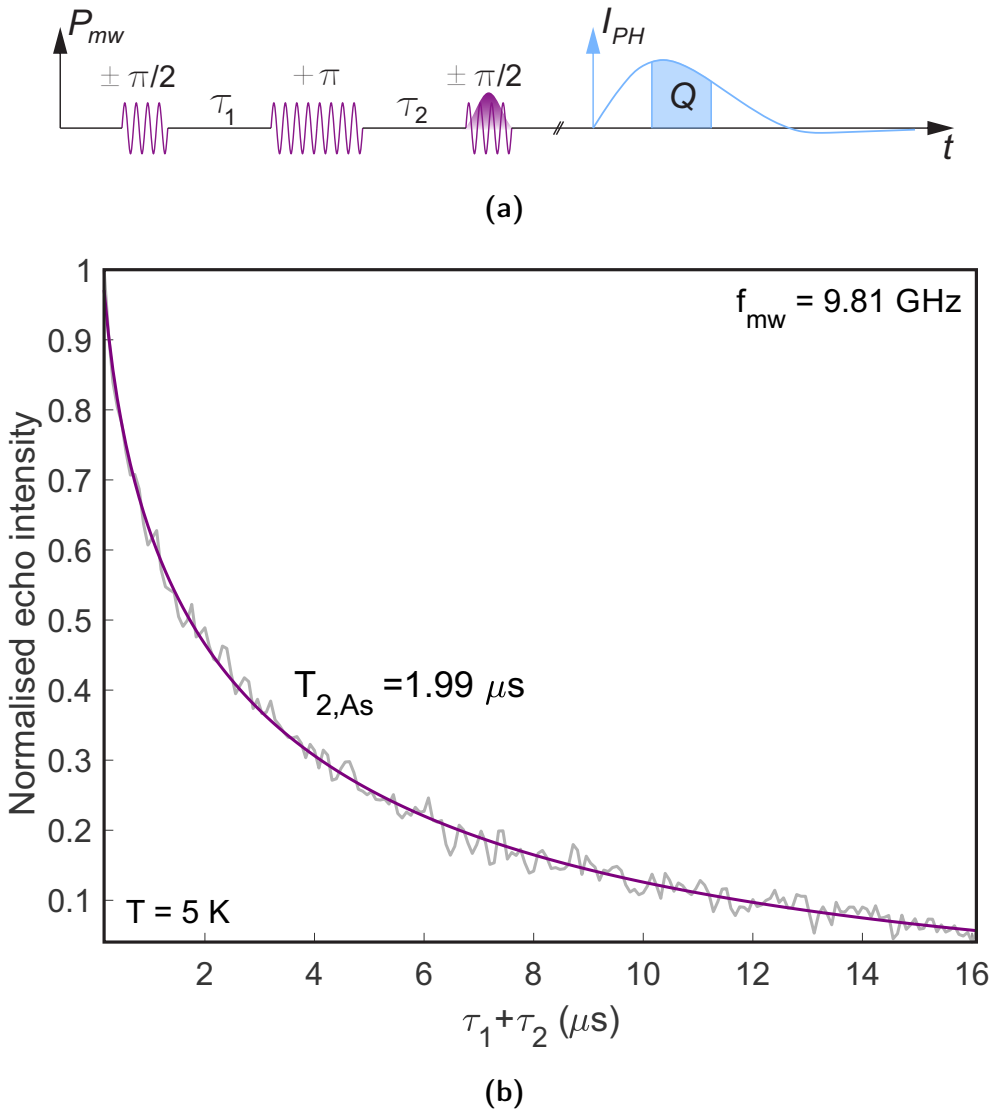


Figure 5.8: ^{75}As-bound electron coherence measurements. [top] Pulse sequence used to electrically measure the coherence time. [bottom] Coherence measurement of ^{75}As-bound electrons.

of additional decoherence mechanisms. Several established techniques have been used to reduce the degradation of a quantum state through a donor spin's interactions with the quantum environment and thereby dramatically increase coherence times. Random field fluctuations caused by spin flip-flops of non-zero ^{29}Si nuclear spins are sensed by the donor-bound electron and result in what is termed 'spectral diffusion' [255]. This induces decoherence in the electron spin [256–259]. My samples are made of naturally occurring silicon with 4.7 % naturally abundant ^{29}Si and thus experience nuclear spin diffusion. Isotopic purification of silicon enriched with ^{28}Si is uninhibited by the nonzero nuclear magnetic moment of naturally occurring ^{29}Si [150, 259, 260].

Alternatively, dynamic decoupling refocuses the effects of unwanted environment spin interactions on a timescale faster than a Hahn echo sequence though comparable to the system's memory time. Radio frequency pulses periodically reverse the effects of decoherence [261–263]. At low temperatures, T_2 times do have to saturate at a level inversely proportional to donor concentration [260]. A decoherence mechanism results from donor concentrations known as 'instantaneous diffusion'. Instantaneous diffusion is dependent on microwave pulse rotation angles. A long microwave pulse like the second π-pulse in an echo measurement for example (see figure 5.5) causes flips of neighbouring donor electron spins from the electron bath that are dipole-coupled as far as 200 nm away. Instantaneous diffusion can be suppressed by using shorter pulse rotation angles though this must be balanced against diminishing spin-echo amplitudes for shorter pulse lengths [150, 264]. Suppression of these dipolar interactions lifts the limit on longer T_2 times at low temperatures [150]. Neither nuclear spin diffusion nor instantaneous diffusion were suppressed in my measurements. My measurements are however, performed in the same way as ref. [172] so should give us a comparable measure of interface decoherence effects. Decoherence measurements build on the Hahn sequence in figure 5.5. The spacing between pulses τ_1 and τ_2 are iteratively and equally increased, to determine the effects of decoherence in the x-y plane on the spin echo detected value, ΔQ [70]. Figure 5.8 shows the pulse sequence used to electrically measure the coherence time as well as a coherence measurement on the $As_{m_I=1/2}$. The data is fit with a stretched exponential

of the form:

$$\Delta Q = Ae^{-t^n/T_2} + B \tag{5.7}$$

where $A, B, n \in \mathbb{R}$ and $n \approx 0.5$. A coherence time of approximately 2 μs is observed. As previously discussed, one of the main advantages of attempting SDR with donors away from the interface was to avoid the deleterious decoherence effects of magnetic noise from charge traps at the interface [70, 169, 172]. Coherence times of donors spatially isolated from the interface have previously been measured [169, 171], though in their case isotopically purified silicon was used. With donor doping concentration peaking at 50 nm below a hydrogen passivated Si/SiO_2 surface, they achieve T_2= 0.75 ms at 5.2 K. This result is two orders of magnitude longer than what I observe. In a focussed investigation of the effects of the Si/SiO_2 on coherence times, coherence times of $\sim$1 μs, comparable to mine, were observed for ^{31}P-bound electrons [70, 172]. They attribute these values to being limited by interface-defect induced field noise [170]. I attribute my low coherence times to an unpassivated Si/SiO_2 interface and amorphised bulk, rich in defects that induced field noise [172], and the diffusion of a large number of arsenic dopants to the interface where the donor-bound electron wavefunction can overlap with that of interface defects [169]. My devices have comparably 'low' dopant dosage. To avoid donor diffusion to the interface I should first, anneal for shorter durations and second, consider implantation to a greater depth. The shorter anneal duration ensures atoms do not have the opportunity to diffuse as far whereas the deeper implantation requires a longer diffusion to reach the surface. The ability to probe donors at a greater depth with the interdigited electrodes needs to be considered however. Even at my intended donor depth of 100 nm, there is no evidence that I am in fact probing the donor-bound electrons sufficiently separated from the deleterious interface defects. If my coherence measurements are dominated by donors at the interface, which is probable based on the coherence time of $\sim$2 μs, my aim to measure coherence times away from the interface is void.

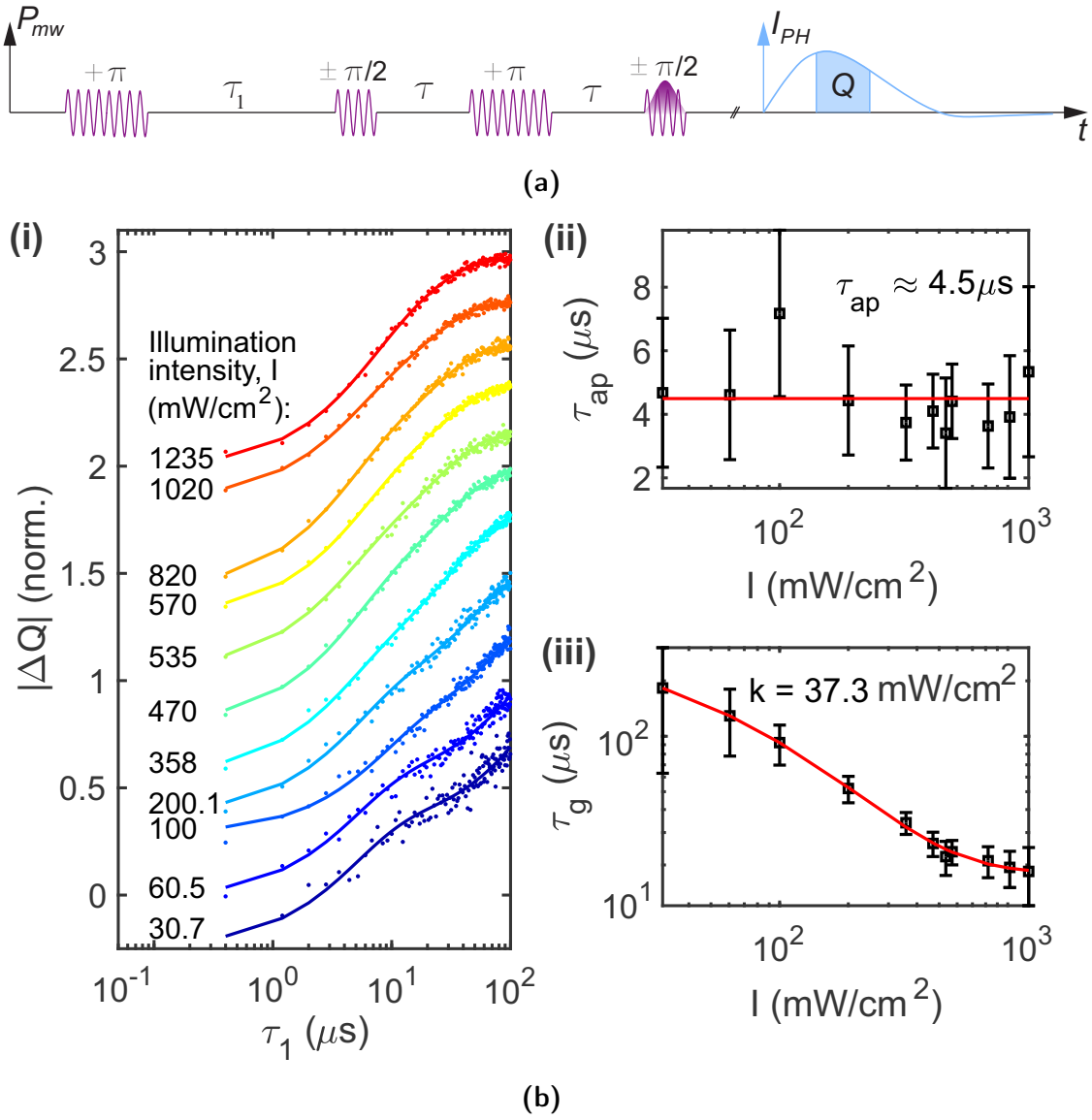


Figure 5.9: Illumination dependent ^{75}As inversion recovery measurements. **(a)** Inversion recovery pulse sequence. **b(i)** Normalised echo intensity of As ($m_I = {}^1/_2$) as a function of normalised echo intensity. The data (dots) are offset for clarity and the lines are bi-exponential fits. Each data set and fit has been offset for visual clarity. **(ii)** Antiparallel spin recombination time constant as a function of illumination intensity. **(iii)**Charge carrier generation time constant as a function of illumination intensity. The solid lines are fits, black dots are echo detection data, and open squares are the two time constants extracted from the fits in (i). Figure derived from similar experiments of different defects in ref. [78, 172].

5.6 Recombination and generation rates

A typical inversion-recovery pulse sequence used in pulsed electron paramagnetic resonance (pEPR), followed by a $^{\pi}/_{2}$ electrical detection pulse, is in figure 5.9. It is an inversion (π) pulse followed by a electrical detection Hahn echo sequence.

For my EDMR measurement scheme, the experiment provides information about the spin-pair generation and antiparallel recombination rates. The sample is under continuous illumination throughout the pulse sequence, which means the spin-centres begin in a state steady of occupancy. Following the inversion π-pulse applied to ^{75}As, the population of antiparallel spin-pairs dramatically increases and upsets the steady state. EHR of the inverted donor-bound electrons ensues and results in a reduction of the current as the singlet-triplet populations begin to stablise. The newly ionised ^{75}As donors can now be reoccupied by the illumination-induced free carriers. The density of free carriers scales with the illumination intensity and therefore the rate of reoccupation. As described in section 5.4.1, the donor-bound electron population is most effectively measured electrically by a phase-cycled spin echo on the donor-bound electron. By phase-cycling I subtract the charge Q determined by the boxcar integration of the current transient with time for a net π-pulse from the boxcar integration of the current transient for a net 2π-pulse to produce a value ΔQ. This value is proportional to the difference between the quantity of antiparallel and parallel spins when the echo sequence commences [78]. It also quantifies the donor-bound electron occupation. My inversion recovery measurement was performed for varying illumination intensities (30.7-1235 mW·cm^{-2}). Figure 5.9b (i) demonstrates the variation of ΔQ from the inversion recover echo detection measurement detailed in figure 5.9a as a function of τ_1, the delay between the inversion pulse and Hahn echo. The greatest ΔQ occurs for small τ_1. The box-car integration of the echo current transient, which produces Q, is also a minimum then. As τ_1 increases, the magnitude of the echo decreases due to both the recovery of the inversion due to relaxation and the reduction in donor-bound electron population due to EHR. In figure 5.9b(i) the illumination intensity I for each plot is specified to its left, and each plot has

been offset for visual clarity. For each illumination intensity, the data is fit with

$$\Delta Q = -A \cdot e^{-\tau_1/\tau_{ap}} - B \cdot e^{-\tau_1/\tau_g} + C \tag{5.8}$$

where $A, B, C, \tau_{ap}, \tau_g \in \mathbb{R}$ and τ_1, the independent variable, is shown in figure 5.9.

This experiment was first performed and reported in ref. [78]. As in similar experiments completed between ^{31}P and P_{b0} centres, the lowest I trace of ΔQ on the log x-axis scale includes a bump, indicating the existence of two exponential processes occurring throughout the measurement. The highest illumination measurements are either dominated by a single exponent process or the fit tends towards a bi-exponential fit with comparable time constants [42]. The fast time constant of the bi-exponential process is allocated to the recombination of antiparallel pairs τ_{ap}, and the slow time constant to the generation of new pairs τ_g from the continuous illumination of above bandgap light [78].

The inversion pulse flips the steady-state spin population, which relaxes back to its steady-state over a spin-lattice ('longitudinal') relaxation time T_1. It is important at this point to distinguish between the T_1 time and the 'electronic transition' time T_{IR} (where $'I.R.'$ stands for inversion recovery), which is dominated by the fast recombination time of antiparallel spin-pairs τ_{ap} rather than that of parallel spin-pairs τ_p [172]. Figure 5.9b(ii) plots τ_{ap} as a function of I. It is independent of I as expected. The free charge carrier density does not influence the rate of recombination. In figure 5.9b (iii) on the other hand, τ_g is plotted as a function of I, the longer of the two time constants from figure 5.9b(i). The data points are fitted with a stretched exponential [78]

$$\tau_g = Ae^{-kI^n+B} \tag{5.9}$$

where $A, B, k, n \in \mathbb{R}$, $k = 37.3$ cm^2/mW is the rate τ_g changes with I, $A = 405.7$ μs, $B = 18.1$ and $n \approx 0.54$ is the stretching exponent. Naturally the rate of generation increases with increased I.

In the pulse sequence in figure 5.9a, the steady state Pauli-blockade that exists prior to the inversion pulse is lifted, resulting in an increase in the rate of recombination due

to antiparallel spin-pairs, and therefore a current transient. Whilst spin-lattice relaxation occurs during τ_1, the echo amplitudes ΔQ in figure 5.9b are not just due to T_1. Another T_1 approach previously used in the literature relies on a simple $\pi - \tau - \pi$ pulse sequence, though it still measures T_{IR} [252]. The measured time constants should be comparable for the manipulation of either partner of a spin-pairs since the measurement scheme considers the relative spin-orientation of the pairs rather than absolute spin-orientations [172]. If $T_1 < \tau_{ap}$ for the spin being manipulated I would be able to ascertain the T_1 time of that spin-species with this measurement scheme. T_1 times could be verified by pEPR measurements and compared to my measurements, as done in ref. [171]. Equal T_1 and T_2 times would be a key indication that the observed time constant is the result of τ_{ap} but, as in ref. [172], $T_{I.R.} \approx 2T_2$. Ref. [23, 76, 78] have made the rational assumption that $\tau_{ap} \ll T_{1,i}$ where i is either spin partner. Based on their identification of parallel spin-pair recombination on a time scale of $\tau_p \sim 1$ ms $\gg T_{I.R.}$ [78] and measured T_1 times of constituent partners of the spin-pair [259] this is a rational and worthy assumption. Thus in my sample the measured time constant is a reflection of the antiparallel spin-pair pair recombination time; that is, $\tau_{I.R.} = \tau_{ap}$.

If the sample was not illuminated during the pulse sequence no new spin-pairs would form. In this case, ΔQ would reflect only τ_{ap}. The recombination of parallel spin-pairs occurs on a much greater time constant ($\sim$1 ms) and can therefore be discounted in these measurements [78].

5.7 Identification of spin-dependent recombination mechanism

Spin-dependent charge transitions in semiconductors are commonly facilitated by midgap states. The Pauli exclusion principle is the fundamental rule governing these transitions, where it states that no two fermions can exist in the same quantum state at once. cwEDMR measurements like those detailed in Chapter 4 are limited in their ability to distinguish between various recombination mechanisms. Continuous and mono-frequency microwave excitations delivered during these measurements only highlight a resonant

change in current. Whilst the (phase-corrected) sign of the current change can point to SDR for a resonant decrease in current, and spin-dependent hopping for a resonant increase in current [45], little insight can be gained whilst using cwEDMR. I could gain further information about a system using two frequencies or two magnetic field values in cwEDMR whilst still applying unsophisticated and blunt continuous microwave excitation [46, 265]. However, coherent spin rotations for deliberate angles across resonance conditions is even more sophisticated [266].

We have already demonstrated some of the benefits of pulsed microwave excitation. Saturation nanosecond microwave pulses produced insightful microsecond current transients that demonstrate the time scales of EHR in arsenic and sulfur doped samples. Similarly, coherently controlling spin states has facilitated echo measurements and Rabi nutations of arsenic donor-bound electrons.

The functionality of pEDMR can be extended by increasing the effective excitation bandwidth [46]. This would allow for the manipulation of various spin species that are often separated by a excitation frequency greater than the excitation bandwidth of mono-frequency microwave pulses. Application of these pulses within the relaxation times of the targeted spin species allows us to interrogate their spin-dependent interactions. By first knowing the relative spin-states before excitations, I can probe mechanisms like SDR, where the relative, rather than absolute spin states of potential spin-pair partners are adjusted [55].

ELDOR is a multifrequency spin manipulation technique in which spin centres with different excitation frequencies can be manipulated concurrently to observe the relative effects of the spin-spin interactions. Whilst the experiment can theoretically be performed using different B_0 values, it is experimentally impractically to change B_0 on the microsecond timescale I require. The application of two (or more) microwave frequencies is more practical. This can be achieved with either multiple microwave sources or a single microwave source modulated by several local oscillator (LO) frequencies.

5.8 Electrically detected echo electron double resonance

Electrically detected electron double resonance (EDELDOR) has previously been used to investigate the interaction between lattice defects and either ^{31}P or ^{75}As donors in crystalline silicon [22, 75]. Based on the double electron-electron resonance (DEER) technique commonly used to measure separation dependent dipolar coupling between two electron spins [46], EDELDOR identifies KSM modelled spin-pairs and their primary EHR pathway.

EDELDOR is a pEDMR multifrequency 'pump-probe' scheme. Spin species are individually addressed by applying coherent microwave pulses at their resonance frequency. By changing the relative spin orientation of one species (the 'pumped' spin) and observing the effects on the current at the frequency of its proposed spin-pair partner as it is coherently manipulated (the 'probed' spin) one can determine how the spin species facilitate EHR.

If the two spin species form a spin-pair, pumping on one should change the output current observed at the probe frequency. If the species are independent and generate EDMR signals via SRH recombination for example, the pump should have no effect on output current as the probe species is coherently manipulated.

We have incorporated the lock-in detection echo sequence [64] previously described in Section 5.4.1 in EDELDOR measurements to capitalise on its improvement to the SNR. For this I therefore use EDeELDOR to differentiate from the EDELDOR sequence used in ref. [22].

For multifrequency measurements, driving the amplification of the SpinJet Arbitrary Waveform Generator (AWG) and TWT too hard can lead to non-linear amplification and intermodulation products in the transmitted microwave frequency. This, together with how I negated the effects, is described in Appendix A.

5.8.1 Experimental approach

We are not only concerned with identifying the existence of spin-pairs within my sample, but also identifying which spin-pairs have formed. As such, EDeELDOR measurements were attempted between arsenic and a range of resonant locations across the overlapping central resonances around g∼2. These are identified in figure 5.10. The probe frequencies shall be labelled as f_α.

In my EDeELDOR experiments B_0 is kept constant as the *Bruker E580* cannot change the field fast enough for different spin species to be addressed before one relaxes (T_1 ∼5 μs). The *Bruker* AWG provides four channels with which to modulate a carrier frequency and supply four frequencies to the cavity. I use a single microwave source (the *Bruker* AWG) centred on the probe resonances, which includes two LOs to up-shift and down-shift to the pump frequencies of the inner two ^{75}As hyperfine lines. This technique can be seen in the experimental setup diagram in figure 4.3. Various frequency settings are tabulated in table 5.1. As ELDOR measurements are conducted across the frequency range in figure 5.10, the central frequencies (f_c) of the cavity are moved to each probe frequency and the LO frequencies are adjusted to ensure the pump continues to match the donor electron frequencies.

Resonance	f (GHz)	g-value	Δf_{As2} (MHz)	Δf_{As3} (MHz)
1	9.8283	2.00917	53	-145.4
2	9.8189	2.00724	62.4	-136
3	9.8096	2.00534	71.7	-126.7
4	9.8021	2.00381	79.2	-119.2
5	9.7909	2.00151	90.4	-108
6	9.7816	1.99962	99.7	-98.7
7	9.7751	1.99828	106.2	-92.2

Table 5.1: Pump f_{As} and probe f_α frequencies. Calculations of the LO frequencies $\Delta f_{As,i}$ where $i = 2, 3$ (hyperfine lines two and three) for seven f_c corresponding to seven peaks around g∼2 field sweep.

5.8.1.1 Frequency range

The obvious limitation of ELDOR measurements is the bandwidth of the cavity. By over-coupling the cavity as is necessary for pEPR microwave excitation, I extend its bandwidth by reducing the Q: $\Delta f = {}^{f}/_{Q} = {}^{9.8GHz}/_{126} \approx$ 80 MHz. At X-band frequencies a rule of

thumb for ELDOR measurements is not to extend the excitation pulses beyond 100 MHz apart for a single mode cavity [46]. This limits my measurements somewhat though I exceed the rule to excite $^{2}/_{4}$ ^{75}As hyperfine lines simultaneously, which are still ∼71 G ≈ 200 MHz apart [249] (cf. [23, 42, 76]). This approximately matches the bandwidth of my MD5 cavity, who's Q-value diminishes to ∼126 when maximally over-coupled (cf. figure 5.10).

We choose to 'pump' on only the inner two ^{75}As hyperfine lines, in close proximity to the 'probe' resonances in the EDMR spectrum. This also ensured the pump frequencies were not only addressable but also gave more flexibility over the microwave power received at the extremities of the cavity's response. The spacing of the resonance lines as a function of frequency are represented graphically in figure 5.10. It is also common to set the probe frequency to the cavity's centre frequency to maximise sensitivity.

The non-linear response of the cavity was also considered. I found that pump pulses beyond 40 % of the AWG's maximum power generated excessive noise in the cavity from long-lived intermodulation products. This noise suppressed the EDeELDOR signal below the noise floor.

If the two species do constitute the partners of a spin-pair, the experiment should demonstrate symmetric coupling when performed in reverse too; that is, when I pump on the resonance g∼2 and probe the ^{75}As donors.

5.8.2 The EDeELDOR scheme

My EDeELDOR scheme makes use of an echo spin readout pulse sequence in Section 5.4.1. I apply a nutation pump pulse at frequencies f_{As2} and f_{As3} (the inner arsenic lines that are closest to the cavity's central frequency and within its bandwidth) and then use the echo spin readout at f_{α} to observe any change in the echo magnitude as ($^{2}/_{4}$ of the) arsenic donor(s) are nutated. By phase cycling the spin echo readout sequence, the total spin rotation angle at the observation frequency switches between 2π (when the phase cycled pulse is $^{+\pi}/_{2}$) and π (when the phase cycled pulse is $^{-\pi}/_{2}$). The difference between the integrated transients gives a value ΔQ proportional to $n_p - n_{ap}$, the difference in the pre-observation populations of parallel and antiparallel spin-pairs [23, 42].

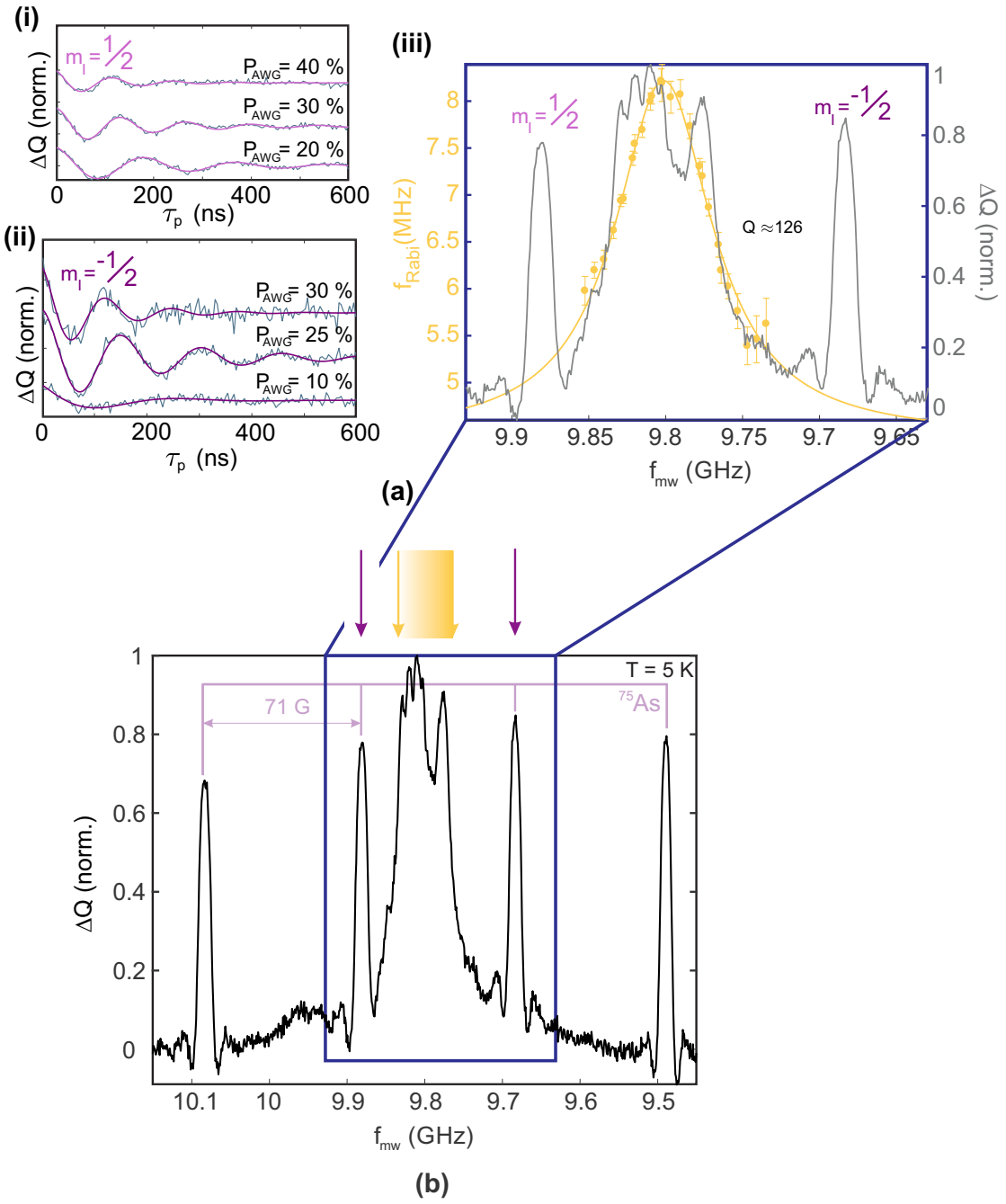


Figure 5.10: Multifrequency measurements with a non-linear cavity response. **(b)** Echo field sweep of the sample with purple and orange lines showing the different species to interrogate in EDeELDOR experiments. **(a)** Multifrequency measurements are limited by the bandwidth of the over-coupled microwave cavity. The hyperfine spacing of the ^{75}As lines is ∼71 G. Whilst the frequency locations of the inner ^{75}As hyperfine lines are on the fringes of the cavity's bandwidth, Rabi nutations could still be performed on them in **(i,ii)**. **(iii)** Rabi nutation on the central resonances with a fixed field and varying microwave frequency (orange full circles). The nutation frequency, which is proportional to microwave power, reflects the cavity frequency response. The points have been fit with a Lorentzian line shape, from which I can extract a cavity Q-factor of $Q \approx 126$. In the background is a grey echo field sweep. The echo in the nutation measurements was measured using a 40-80-40 ns pulse sequence.

The use of echo detection in combination with phase cycling also makes the EDeELDOR measurement scheme robust against variation in the quantum spin number S of the α species that I probe. This measurement technique was first used in ref. [42], when probing the coupling between a ^{31}P-bound electron with $S = {}^{1}/_{2}$ and the SL1 defect in silicon with $S = 1$. The experiment is also run in reverse with the pump and probe frequencies (species) swapped. This aims to demonstrate the reciprocity of the measurement; if a spin-pair exists, in ideal experimental conditions the outcome should be independent of which species of the pair is pumped and which is probed. This will be discussed further in Section 5.8.3.

The pulse sequence and the progression of the spin orientations of the species involved are depicted pictorially in figure 5.11. The top of the figure demonstrates the pulse sequence. As shown in the left-most energy diagram, the potential spin-pair exists in a predominantly parallel configuration and therefore Pauli-spin blockade inhibits EHR. The ^{75}As-bound electrons are nutated by increasing amounts with the pump pulse of duration τ_p. The proportion of anti-parallel spin-pairs is modulated by the relative spin orientation of ^{75}As and the α species. This results in an oscillating and decaying EDeELDOR output ΔQ as shown in figure 5.11 (c). As previously outlined, the echo measurement relies on the difference in the integrated current transient Q for each phase cycle. The topmost energy diagram in figure 5.11b, 'A: 2π echo', depicts the case where the observation pulse is an effective 2π pulse when the cumulative spin echo readout sequence is ${}^{\pi}/_{2} + \pi + {}^{\pi}/_{2}$. The bottommost energy diagram, 'B: π echo', depicts the case where the observation pulse is an effective π pulse when ${}^{\pi}/_{2} + \pi + {}^{-\pi}/_{2}$. The resulting resonant current transients I_{PH} are shown, with the MWAs excluded. These MWAs cancel out in the phase cycling so excluding them in the diagram for explanatory purposes is inconsequential.

When a $\tau_p = n\pi$ pump pulse is applied to the ^{75}As-bound electron, where $n = 0, 2, 4, ...$, $\Delta Q = Q_A - Q_B$, from the integrated A transient Q_A [top current transient] minus the integrated B transient Q_B [bottom current transient], is a maximum. When a $\tau_p = m\pi$ pump pulse is applied to the ^{75}As-bound electrons, where $m = 1, 3, ...$ [middle current transient], the integrated current transient Q_A minus Q_B, is a minimum. The decaying signal is the result of a decreasing excitation bandwidth of ^{75}As-bound electrons

as the pulse duration increases; that is, $f_{x,BW} \propto {}^{1}/_{\tau_p}$. This is described further in Section 5.8.2.1. As can be seen, ΔQ is not completely gone. This is because only half of the ^{75}As electron spins are pumped, half of the ^{75}As-bound electrons may still recombine through the α species in case 'A', the 2π echo. If all four ^{75}As hyperfine lines could be pumped at once, a π pump pulse would lead to a complete reduction of ΔQ [23, 42, 76]. That is, $\Delta Q = 0$. Alternatively, all ^{75}As-bound electrons can recombine in 'B', the π echo, leading to $\Delta Q > 0$.

For a $S = 1$ system where I am only pumping on ${}^{2}/_{4}$ ^{75}As-bound electrons, an effective π pulse always leads to recombination of all ^{75}As-bound electrons. If the two species (^{75}As and α) at the pump and probe frequencies do not form a spin-pair, nutating ^{75}As-bound electrons should have no effect on ΔQ.

For a $S = {}^{1}/_{2}$ α species, the spin state progression of the prospective spin-pair is depicted in the energy diagrams in figure 5.11(b). The change in S makes the understanding of the spin progression simpler. As per the $S = 1$ case, in the steady state Pauli blockade dominates due to the prevalence of parallel spin-states between the potential spin-pair. The $S = {}^{1}/_{2}$ α spin-state means that only pumping on ${}^{2}/_{4}$ ^{75}As donors results in $\Delta Q = 0$ for a π-pump pulse (if there was no signal decay).

To summarise and compare, the theoretical EDeELDOR signals for $S = 1, {}^{1}/_{2}$ are plotted in figure 5.12 with no decay (dashed lines). Also depicted are the experiment equivalents, where the signal decays (solid lines). The signal for $S = {}^{1}/_{2}$ α species is the same as pumping on ${}^{4}/_{4}$ ^{75}As hyperfine lines with an $S = 1$ signal.

5.8.2.1 Proportion of arsenic excitation

It is not possible to identify the spin quantum number S based solely on my EDeELDOR measurement for two reasons. Firstly, the difference between EDeELDOR signals for differing S is only the modulation depth of the EDeELDOR oscillation. The modulation depth is a function of the proportion of ^{75}As-bound electrons excited during the measurement. In addition to the number of hyperfine lines addressed, the bandwidth of excitation of each pulse must be taken into account. For that reason, quantifying the proportion of ^{75}As-bound electrons excited is not simply a matter of considering how

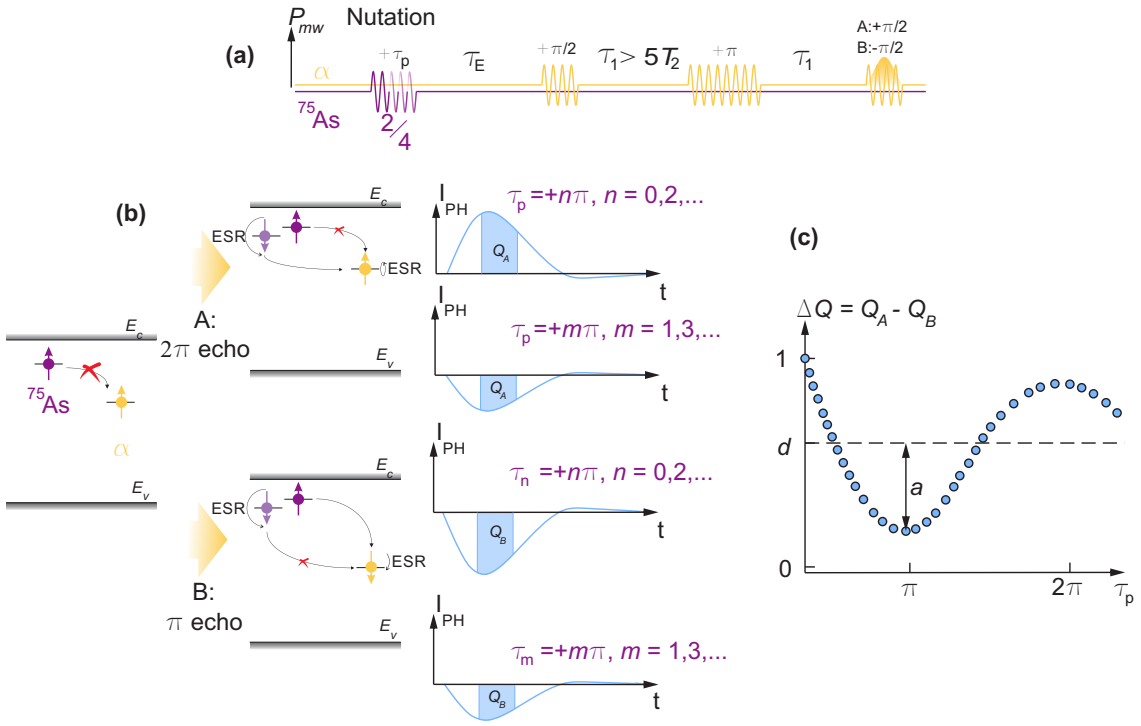


Figure 5.11: EDeELDOR spin manipulation mechanism. (a) The pulse sequence used for EDeELDOR on $^2/_4$ of the ^{75}As donors. **(b)** The spin state progression for EDeELDOR on an α species with $S = {}^1/_2$. [top] Case A is for when the total spin rotation of the echo is 2π ($^{\pi}/_2 + \pi + {}^{\pi}/_2$), whereas [bottom] case B is for when the total spin rotation of the echo is π ($^{-\pi}/_2 + \pi - {}^{\pi}/_2$). This figure only demonstrates two-step phase cycling, which was repeated for an inverted first pulse to do four-step phase cycling. **(c)** The resulting EDeELDOR signal ($\Delta Q = Q_A - Q_B$). The offset of ΔQ, d, and the decayed oscillation amplitude, a, are used to determine the modulation depth m in equation 5.13. Figure derived from ref. [42].

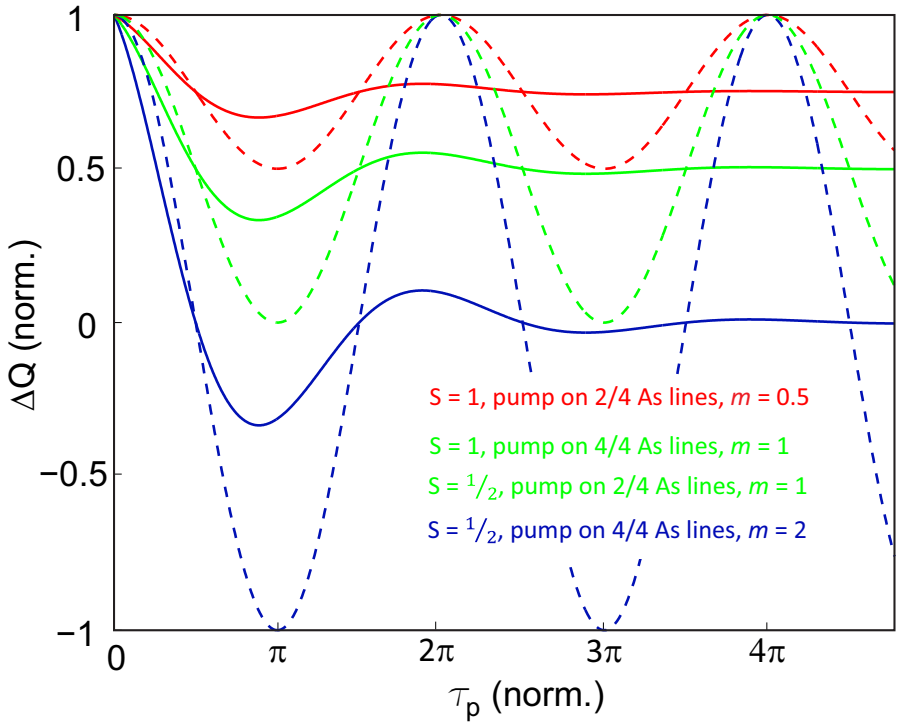


Figure 5.12: Simulation of EDeELDOR as a function of the pump pulse length τ_p. The expected EDeELDOR response for different spins $S = i, i : [1/2, 1]$ and different excitation proportions of the total ^{75}As population (modulation depth m) $m : [0, 2]$ [23]. The oscillations of ΔQ with varying τ_p on the ^{75}As lines demonstrates the α species echo amplitude shown in figure 5.11. Dashed lines demonstrate the undamped oscillations, solid lines demonstrate damped oscillations due to a decreasing pump excitation bandwidth.

many hyperfine lines are addressed. Secondly, in my case there is significant overlap between a range of resonance making it difficult to single out a less-likely $S = 1$ spin-pair partner in the midst of several potential $S = {}^1/_2$ partners. Results from the EDELDOR pulse sequence [22], which is different to the EDeELDOR pulse sequence and is sensitive to the spin quantum number, were inconclusive.

Besides the fractional excitation of ^{75}As hyperfine lines, the observation echo pulses used in the EDeELDOR measurement sequence causes the opposite problem of insufficient bandwidth excitation: they excite multiple overlapping spin species. My inability to probe a specific species limits my sensitivity. This can be seen in figure 5.13, where the excitation bandwidth is overlayed on the pEDMR spectrum. The figure shows three pulses of differing durations and the corresponding excitation in the frequency domain. As the pulse duration narrows, the excitation bandwidth increases. The Fourier transform of a square pulse is

$$\mathcal{F}\{g(t)\} = F(f) = \frac{sin(\pi f)}{\pi f} = sinc(f) \tag{5.10}$$

where f is frequency, $F(f)$ is a time pulse in the frequency domain and

$$g(t) = \begin{cases} 1, & \text{if } {}^{-\tau_p}/_2 \leq t \leq {}^{\tau_p}/_2 \\ 0, & \text{otherwise} \end{cases}$$

where τ_p is the pulse length. As a rule of thumb, I know that for $g = 2$, $\frac{f[MHz]}{B[mT]} \approx 28.025$ MHz/mT. So for a typical 80 ns pulse, the excitation bandwidth is 12.5 MHz $\approx$ 4.5 G. The actual excitation bandwidth is more complicated than this. A description of the calculations can be found in ref. [46]. The full width half maximum (FWHM) of the absolute value of the power spectrum of the pulse is

$$\begin{aligned} FWHM = & \quad \frac{1.207}{\tau_p} \\ \approx & \quad 15 \text{ MHz} \end{aligned} \tag{5.11}$$

5.8.2.2 Identifying overlapping spin-species

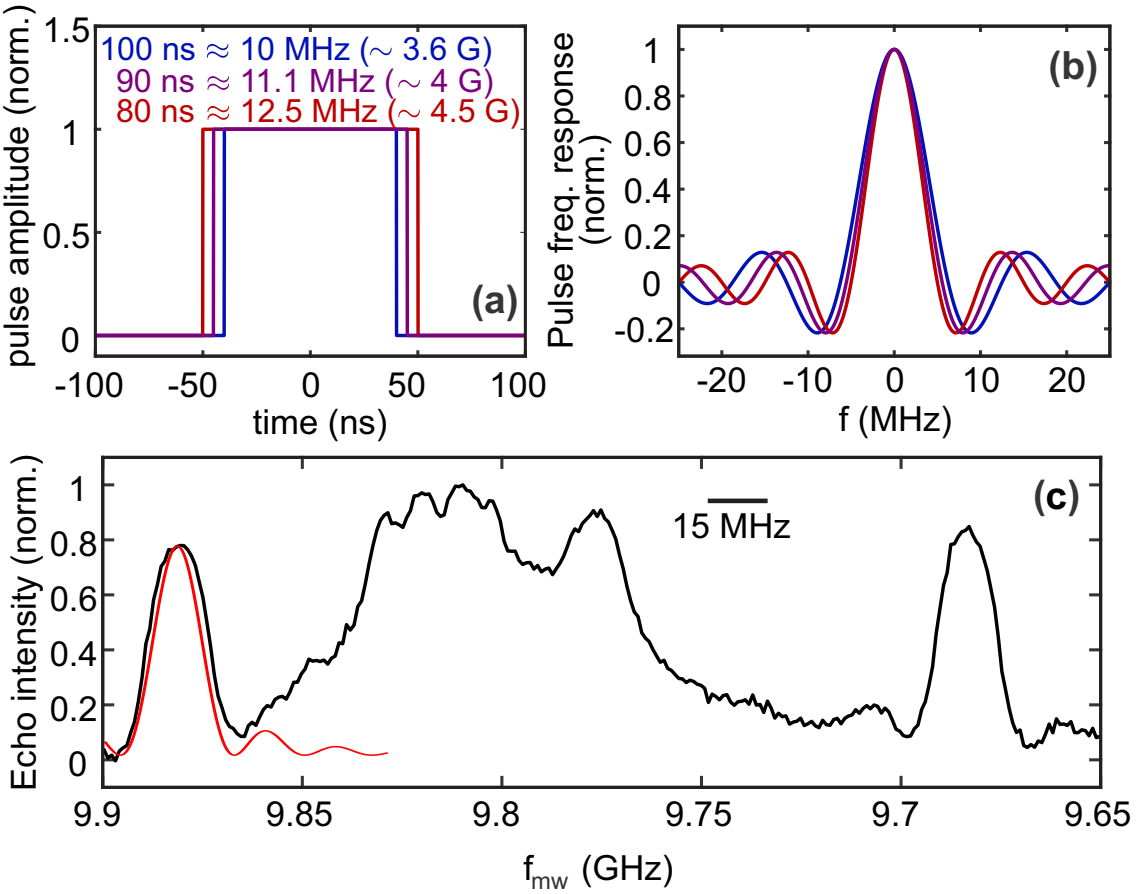


Figure 5.13: Excitation bandwidth of microwave pulses. **(a)** Differing pulse length correspond to differing excitation bandwidths. **(b)** The Fourier transform of the square pulses in (a) correspond to sinc functions in the frequency domain. **(c)** The frequency domain sinc pulse shape (red) from a 80 ns pulse overlapping with the EDMR spectrum. As can be seen, not all of the arsenic-bound electrons for $m_I = {}^1/_2$ are excited. According to equation 5.11, $FWHM \approx 15$ MHz.

Various approaches have been used to differentiate between differing spin-species with overlapping spectra. The Fourier transform of coherent Rabi nutations at a targeted frequency can prove an insightful way with which to differentiate between species with overlapping resonances at X-band. The differing species will nutate at different frequencies and therefore be distinguishable in the Fourier transform, even if indistinguishable in the time domain [69]. The Fourier transform of either Rabi nutations or ELDOR oscillations could be used as part of this deconvolution process. Unfortunately in my measurements, the signal decay is too rapid for enough nutations to be observed to perform a high fidelity Fourier transform.

Alternatively a higher excitation frequency (like Q-band) and therefore higher B_0 could be used. This would spread the overlapping resonances to allow them to be individually addressed. Such experiments present experimental challenges as they require the sample to be trimmed to fit in a much smaller (x3) microwave cavity. The cutting of the sample and repatterning of the metal interdigited electrodes were considered impractical.

For fewer overlapping spectra the resonant transient behaviour can also be used to differentiate different species. This becomes particularly easy when the resonant behaviour subtracts (SDR) or contributes (spin-dependent hopping (SDH)) from the steady state current [45, 159]. Though even when the different resonances have the same effect on the current transient, differences in the time constants of the spin-dependent behaviour is also a useful way to differentiate between them.

The modulation depth m can also be a useful tool for differentiating between species with overlapping spectra as some of them form a spin-pair with arsenic and some do not. Those that do will demonstrate modulation depth (m) proportional to the EHR, whilst those that do not form a spin-pair will demonstrate no EDeELDOR oscillations and therefore have $m = 0$.

By considering the variation in m as a function of the EDeELDOR observation frequency, I can highlight the spin-pair partners as the modulation depth should follow the resonance (Lorentzian or Gaussian) lineshape of the partner I sweep B_0 across. In this instance, the fidelity of this approach increases with decreasing excitation bandwidth and therefore increasing pulse duration due to the overlapping resonances. For a give pulse length (in this case, a $\pi/2$ pulse), a longer pulse duration corresponds to a weaker power and therefore a weaker signal. Thus, a longer pulse must be balanced against its effect of a lower SNR.

5.8.3 EDeELDOR measurements

Three EDeELDOR nutations at different probe frequencies are in figure 5.14. The three plots correspond to three different cavity f_c, which are annotated in each plot. The upper blue traces represent EDeELDOR oscillations when $2/4$ arsenic lines are excited

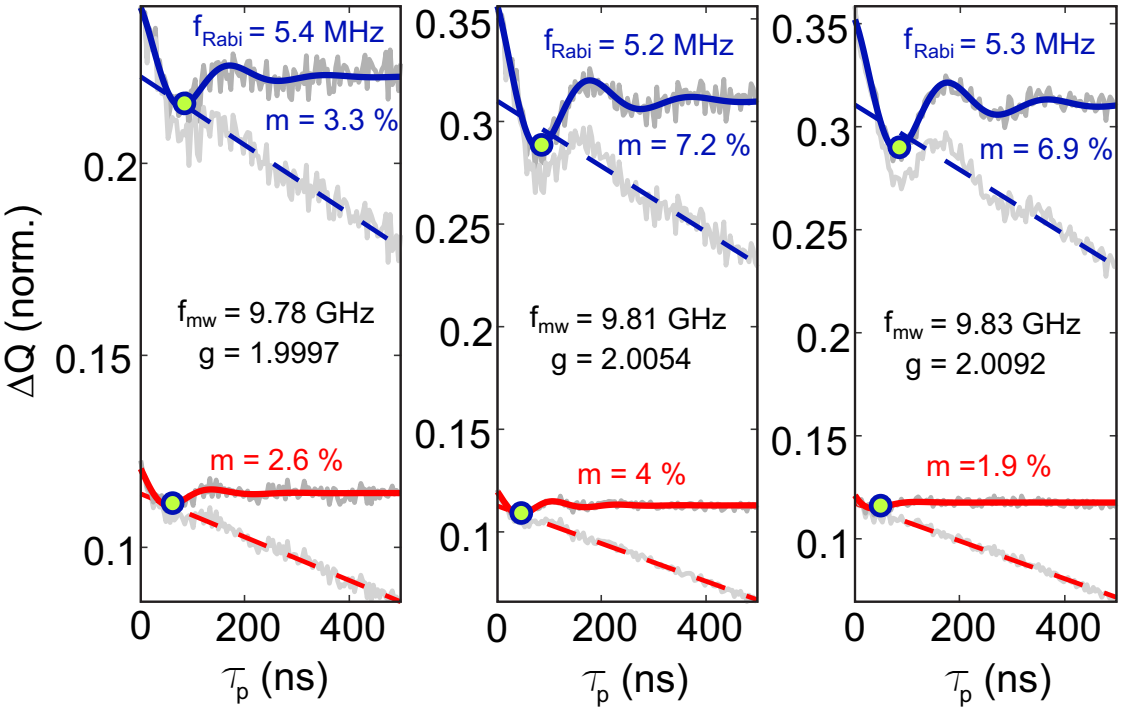


Figure 5.14: EDeELDOR oscillations and modulation depths at three observation frequencies when pumping on the ^{75}As-bound electrons [upper] and vice-versa [lower]. The three plots correspond to three different cavity central frequencies for EDeELDOR measurements. The upper blue fits represent EDeELDOR oscillations when addressing $^{2}/_{4}$ ^{75}As lines with the pump frequency, and the observation frequency is the cavity central frequency. The lower red fits represent EDeELDOR oscillations for the reverse. $B_0 = 0.3495$ mT. The green-filled blue circle demonstrates the τ_p where m was calculated. The echo in the EDeELDOR measurements was measured using a 40-80-40 ns pulse sequence.

with a pump pulse, and the observation frequency is f_c. The dotted line above the grey noisey oscillation with a linear background can be fit with the equation

$$\Delta Q(\tau_p) = a\cos(\omega\tau_p + b)e^{-c\tau_p} + d - h\tau_p \tag{5.12}$$

where $a, b, c, d, h \in \mathbb{R}$ and τ_p is the prepartion 'pump' pulse duration in nanoseconds. The linear background $h\tau_p$, which is probably due to heating can be subtracted to give the grey noisy oscillation with a constant offset. This oscillation is fit with equation 5.12 without the $h\tau_p$ term. The red lines represent the same EDeELDOR oscillations though for the reciprocal pulse sequence: pumping at f_c and observing the echo at $^1/_4$ arsenic lines. What is most obvious is the difference in m. This exists for several reasons:

1. Performing an echo on only $^1/_4$ of the arsenic lines is half the proportion of arsenic spins manipulated for the forward direction (dark blue lines), which reduces m by $^1/_2$.

2. The offset d is inversely proportional to m. There is likely to be some error in d due to the phase cycling not completely removing the MWA background. This could increase or decrease m.

3. The α species pumped in the reciprocal EDeELDOR measurements have various linewidths. This means that for a given pulse length, the proportion of the α species excited by the pump pulse is likely to be different to the proportion of arsenic excited, whose linewidth is also different. The α species linewidth relative to the arsenic linewidth will determine whether linewidth variability increases or decreases m.

4. The α species overlap. For two (or more) overlapping species that form spin-pairs with arsenic, a pump pulse targeting at a particularly species most likely excites several spin-pair partners, which should increase m.

The m of these EDeELDOR nutations with the linear background subtracted (though not the offset) is defined in the typical way

$$m = \frac{a}{d} \tag{5.13}$$

where a and d are defined in equation 5.12 and labelled in figure 5.11 (c). In my measurements, B_0 was kept constant at 0.3495 mT and f_c was swept over the range of interest. The values of m are plotted in figure 5.15 on top of the echo field sweep to compare to the resonance locations. The colours represent the same measurements they did in figure 5.14; blue square represent EDeELDOR measurements where the arsenic is pumped, whereas red triangles represent reciprocal measurements where the α species is pumped. As outlined in Section 5.8.2.2, by measuring m across a range, I can observe the relative variation in m at different microwave frequencies to help determine arsenic spin-pair partners. I can see that for values of about $g >$2, there is a increase in m, which is maintained until $g \approx$ 2.013. For $g <$2, where the CE resonance dominates, m remains relatively low. This suggests that CEs do not form a spin-pair partner with arsenic, as would be expected. There is neither the accuracy nor fidelity of m (2$<$ g $<$2.013) to single out, which of the overlapping resonances are spin-pairs and which are not. Though given that that region is dominated by the interface defect resonances, which I know form spin-pairs with arsenic donors, I can postulate that they are most likely to be spin-pair partners.

EDeELDOR experiments have previously been undertaken with arsenic [23]. In that case, the authors pumped on only one of four arsenic hyperfine lines, the consequence of which is a reduction in the proportion of excitation and therefore in the modulation depth of the EDeELDOR nutations. The theoretical modulation depth can be found from the proportion of spins excited by the pump pulse. For my measurements the arsenic linewidth in units of Hertz (lw_{Hz}) is 32 MHz, which is wider than the excitation bandwidth in units of Hertz (f_{xBW}). A 2π-pulse of $\tau_{2\pi}$ $\sim$180 ns ($= {}^{1}/_{5.6\times10^{6}}$) corresponds to an excitation bandwidth of 5.6 MHz. In our experiments I pump on ${}^{2}/_{4}$ ^{75}As hyperfine lines. Therefore the theoretical proportion of ^{75}As donors excited by the pump

pulse is:

$$\frac{f_{xBW}}{lw_{Hz}} \times \frac{2}{4} \approx 8.75\% \tag{5.14}$$

This value is plotted in figure 5.15 (orange dashed line) and is comparable to the experimental values of m when $2 \leq g \leq 2.013$. This supports the conclusions that these values of g correspond to the formation of spin-pairs between an interface defect and ^{75}As that facilitate SDR.

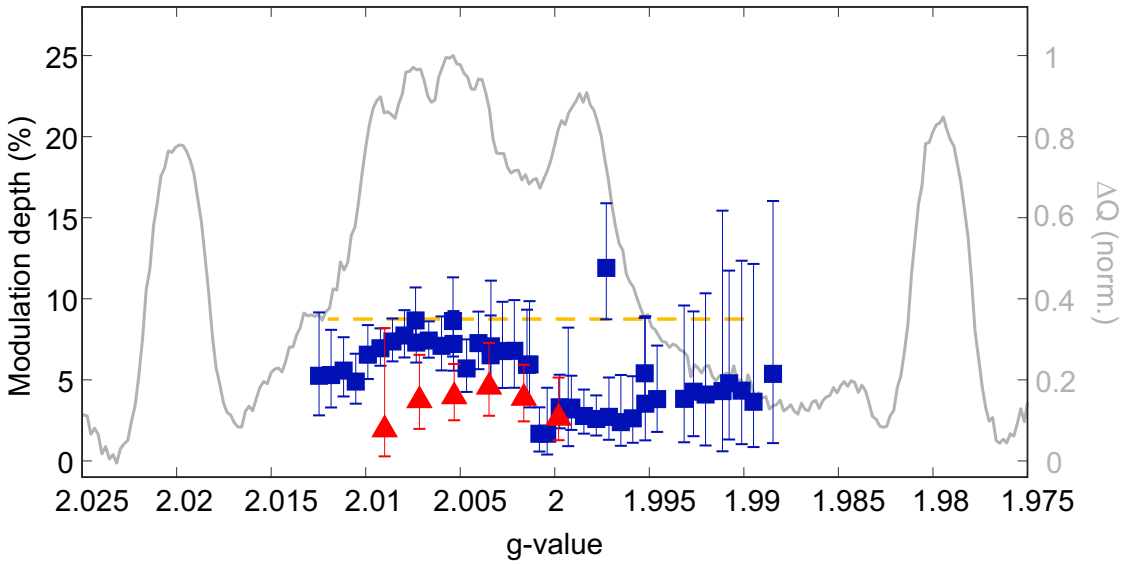


Figure 5.15: Microwave frequency dependent modulation depth. The modulation depth of EDeELDOR nutations superimposed over the pEDMR spectra. The blue squares correspond to EDeELDOR measurements where the ^{75}As was pumped, whereas the red triangles correspond to pumping on the spin centre around g$\sim$ 2 and observing on the ^{75}As ($m_I = {}^1/_2$) donor. The dashed orange line is the theoretical m calculated in equation 5.14. The echo in the EDeELDOR measurements was measured using a 40-80-40 ns pulse sequence.

5.9 Conclusion

Pulsed microwave excitation was used to interrogate spin-dependent interactions within a [100] crystalline naturally occurring silicon sample doped at a depth of 100 nm with ^{75}As and ^{33}Sand containing background ^{nat}B and residual ^{31}P. Through pEDMR measurements, transient SDR behaviour was observed. For a 480 ns pulse, antiparallel spin-pair partners facilitated EHR on a microsecond timescale. It took the spin system $\sim$1 ms to return to equilibrium. What was also obvious from the temporal analysis

was the common transient behaviour across numerous resonances. The decrease in the current on resonance suggested all spin centres in the sample contributed to SDR of electron-hole pairs. The transients also demonstrated matching time constants across the full cwEDMR spectra.

Coherent spin manipulation was then used to probe spin dynamics of the system. A phase cycled echo approach improved the SNR and helped removed the MWA from the signal. It was intended that donors isolated from deleterious interface defects would exhibit longer coherence times. In our sample, the combination of amorphised defect-rich silicon from ion-implantation damage and diffused donors at the interface resulted in silicon dangling bonds in close proximity to donors. An ^{75}As-bound electron spin coherence time of $\sim$2 μs was measured, which was unremarkable compared to the longest measurements reported, like an EDMR measured $T_2 = 100$ μs [171, 255, 259, 267, 268].

The electronic transition times were investigated using an electrical inversion recovery measurement. The antiparallel spin recombination time was shown to be 4.5 μs, whereas the electron-hole generation rate was shown to be exponentially dependent on the illumination intensity as expected.

By varying the relative spin orientation of potential spin-pair partners, I could analyse their spin interactions. Using an approach known as EDeELDOR, I measured variation in the echo amplitude of various resonances whilst incrementally increasing the duration of a preparation pump pulse on the arsenic bound electrons. I then performed the reciprocal measurement where the echo on the arsenic bound electron was measured. The results suggested the formation of spin-pairs between arsenic and interface defects of the type P_{b0},P_{b1},E'. These exist at the interface but also through the amorphised crystal resulting from ion-implantation damage.

Amorphisation effects of implantation can be reversed through annealing though annealing also facilitates dopant diffusion. Alternate implantation mechanisms should be used for sensitive QIP experiments. Ion-implantation damage can also be bad for donor-bound electron coherence [172], and provides mid-gap defects through which a donor may ionise leading to EHR. Whilst diffusion might be suitable for bulk donor

samples, precise donor placement requires a recently developed technique that relies on scanning tunnelling microscopy and hydrogen-resist lithography [269, 270].

This chapter showed the power of pEDMR in elucidating spin interactions, though clearly verifiable and reproducible evidence of paramagnetic sulfur-bound electron signatures was not obtained. Recommendations to improve the likelihood of electrically detecting paramagnetic sulfur ions were made in the previous chapter.

6

Radiation induced spin defects in hybrid perovskites

In this chapter I describe EPR experiments performed on irradiated lead iodide powder and irradiated methylammonium lead iodide/bromide single crystal. The chapter first outlines some of the theory and published literature regarding magnetic fields effects, degradation of hybrid perovskites, EPR in lead halides and hybrid perovskites as well as the intrinsic defect theory that underpins the material's remarkable optoelectronic properties. It then outlines the experimental conditions used to conduct my own investigation of EPR measurements. The results of these measurements are presented whilst also considering a deceptive EPR signal intrinsic to my experimental setup that closely matches what one would expect for the irradiated hybrid perovskites. I then discuss my results and draw conclusions.

6.1 The remarkable rise of organic-inorganic halide perovskites

Organic-inorganic halide perovskites have quickly emerged as a leading photovoltaic absorber material contender [271]. Of the methylammonium lead halides compounds,

the nascent archetypal methylammonium lead triiodide $CH_3NH_3PbI_3$ initially showed the most promise [272], though the use of mixed-cation and mixed-halide variants quickly outperformed their predecessors [30, 33, 35, 271, 273]. Their remarkable optoelectronic performance includes the unprecedented rapid rise in their power conversion efficiency (now up to a verified efficiency of 22.1 % in just five years), which has triggered somewhat of a gold-rush in the materials and renewable energy communities [274–276]. Their varied fabrication schemes and device architectures suggest they are still yet to be optimised [277]. The potential applications of this exciting class of materials extends beyond photovoltaics, to light emitting diodes and light-emitting field effect transistors [278, 279]. Their stability, which can be affected by moistures and UV light amongst other things, is an unresolved issue [280].

Stranks describe how a semiconductor's suitability to act as a solar cell predominantly relies on firstly, its capacity to generate free carriers, secondly, maintenance of a high density of charge carriers under continuous illumination and thirdly, having low electronic disorder. Maintenance of the second criterion is dependent on the electron lifetime and therefore the electron-hole recombination pathways available to them [31].

Deep states within the bandgap known as 'intra-gap trap states' facilitate SRH non-radiative recombination of electrons and holes, which contributes to shorter carrier lifetimes and lower photo luminescence quantum efficiencies (PLQE). A better understanding and control of intra-gap trap states will facilitate improvements in PLQE [281–283] as well as solar cell efficiencies closer to the Shockley-Queisser limit [277, 284].

6.2 Magnetic field effects in hybrid perovskites

The role of the spin degree of freedom in the interaction of charge carriers cannot be discounted. Recently, spin was shown to play an important part in the recombination of triplet excitons in other organic semiconductors [285].

The long lifetime of electron-hole pairs in hybrid perovskites, each with an intrinsic spin [30], make interactions predisposed to the effects of magnetic fields. Magnetic field effects (MFE) are useful phenomena to investigate spin-dependent effects

[286, 287]. Despite a large spin-orbit coupling resulting from the heavy lead and iodine atoms that would typically limit MFE and potentially reduce spin-lattice relaxation times, magneto-absorption, magneto-photocurrent, magneto-luminescence and magneto-photoluminescence have still to be observed in methylammonium lead halide materials. Here B_0 can modulate the singlet and triplet populations, which affects their dissociation and recombination rate. The MFEs are explained by the B_0-mixing of the spin-sublevels of photoinduced electron-hole spin-pairs, who have different precession frequencies and therefore g-values (the 'Δg model') [288].

6.3 Degradation of hybrid perovskites thin films

6.3.1 UV induced degradation

6.3.1.1 UV induced degradation of lead halides

Past studies of UV, γ- and X-ray irradiated lead halides used EPR to identify spin active defects and have been succinctly summarised [289]. These forms of radiation have been showed to degrade the lead halide crystal chemical makeup, largely resulting in EPR-active defect species. UV-irradiated $PbBr_2$, PbI_2 and $PbCl_2$ formed clusters of two or three Pb^{2+} ion with bound electrons forming paramagnetic Pb^{+}, or Pb^{2+} with a bound hole forming paramagnetic Pb^{3+}. These were the first paramagnetic species to be experimentally observed in irradiated lead halides [37, 290]. Similarly, a lead-related resonance at g $\approx$ 2 was assigned to colloidal lead particles [37, 291]. An unpaired $2p$ electron bound to a O^{-} impurity ion in $PbCl_2$ that interacted with two neighbouring $Pb^{+}+$ ions was later observed [292, 293]. A self-trapped electron (STE) was observed at a pair of nearest-neighbour substitutional Pb_2^{+} formed Pb_2^{3+} lead dimers in a NaCl:$PbCl_2$ and $PbCl_2$ crystal [294, 295]. More recently, isolated Pb^{3+} has been observed in lead halides [32].

6.3.1.2 UV-induced degradation in hybrid perovskites

Along with moisture [275, 277, 296, 297], heat [298], trapped charge [299] and electric fields [283, 300, 301], the detrimental effects of UV radiation on the stability of perovskite

solar cells has been identified [297, 302, 303]. UV-induced desorption of surface-absorbed oxygen results in deep surface electron trap sites in mesoporous TiO_2-sensitised solar cells [304] close to the perovskite/TiO_2 interface, for example. Alternatively, an electron deficiency following UV-irradiation results in trapped holes that remove an electron from the crystal's iodine anion and facilitate the formation of PbI_2 [302]. Interestingly this perovskite degradation byproduct, PbI_2, has been shown to reduce electron-hole recombination as a blocking layer between the TiO_2 and perovskite [305] or by passivating trap states [302].

6.4 Defects in hybrid perovskites

In thin film hybrid perovskites, the nature of defect trapping states and the dominant charge carrier type is dependent on the fabrication technique and conditions [306, 307]. The unusual properties of hybrid perovskites' intrinsic defects partially explains their remarkable optoelectronic properties. The low rate of nonradiative SRH recombination associated with shallow defects and fewer deep defects accounts for firstly, long electron-hole diffusion lengths greater than the film thickness necessary for complete light absorption [30, 308, 309] and secondly, high V_{oc} to bandgap (E_g) energy ratio V_{oc}/qE_g [310]. Although a better understanding of the defects is still needed.

Although the defects within inorganic perovskite like $BaTiO_3$ are known to include electronic disorder, ionic disorder, dislocations and grain boundaries, much less is known about hybrid perovskites [311]. Intrinsic defects, though prolific in hybrid perovskites, show extended state characteristics whereby charge carriers are delocalised and do not form intra-gap trap states that would otherwise encourage carrier lifetime-limiting SRH recombination and the associated low V_{oc} [306, 312].

Schottky disorder is predominant in inorganic and hybrid perovskites [311]. This is characterised by Schottky defect pairs, involving a stoichiometric ratio of anion and cation vacancies in a lattice. The ionic rather than electronic disorder within the organic-inorganic hybrid perovskite $MAPbI_3$ limits point defect formation through minimisation of free energy in the crystal and through the creation of charge-compensative lattice

vacancies to regulate the carrier concentrations. Both Schottky disorder and low charge carrier concentration provide conditions conducive to long charge carrier diffusion lengths [311]. It has also been shown that a small contribution of chlorine (both substitutional and interstitial) to $MAPbI_3$ improves the electron-hole diffusion length by passivating deep traps and inhibiting nonradiative SRH recombination [30, 34].

In $MAPbI_3$ thin films, the dominant p(n)-type defects are V_{Pb} and MA_{Pb} (MA_i and V_I) and they have low formation energy [306, 311–314]. Defects with low formation energies only create shallow defects. For the dominant donors this is due to the high ionicity of the MA and lead ions, whereas for the dominant acceptors the shallowness results from an antibonding state at the valence band maximum caused by coupling between lead lone-pair s and iodine p orbital.

Shallow defects can act as unintentional dopants of the perovskite [312]. These defects facilitate good n- and p-type conductivity as well as radiative recombination processes necessary for optoelectronic applications [34]. Deep level intra-gap defect states on the other hand have high formation energies and facilitate defect mediated nonradiative SRH recombination contributing to short electron-hole diffusion lengths and low V_{OC}. The occupation of these deep intragap trap states has important implications for EHR. At low illumination fluence, the filling of intra-gap traps is not saturated and SRH nonradiative recombination dominates [31, 307].

6.4.1 Previous investigations of hybrid perovskites crystals with ESR

The use of EPR techniques, in particular, EDMR to investigate solar cell material is not new, though has primarily focused on established materials like silicon [45, 159, 315] or organic photovoltaic materials [161, 316, 317]. cwEDMR has been used to identify defects whereas pEDMR has been advantageous for probing charge transport mechanisms in solar cells [45, 161]. Despite the dramatic improvements in perovskite power conversion efficiencies, the insight provided by EPR has not been fully capitalised on. I am aware of two investigations of hybrid perovskite solar cell materials, where the authors have observed spin resonance effects, the first through manganese doping [318]. Ref.

[319] identifies a single resonance in pristine (though what appears like polycrystalline) $MAPbI_3$ at $g = 2.0048$ measured at room temperature. The single resonance is most likely due to a paramagnetic state of lead (either Pb^{3+} or Pb^{+}), potentially induced by displacement of the lead from its lattice position. The second EPR investigation of hybrid perovskites that I am aware of is through UV and 3 MeV electron irradiation-induced defects [32]. The irradiation induced radical cation $CH_2NH_3^+$, and Pb^+ clusters that can form spin-active permutations. One possible explanation for the formation of the paramagnetic molecule $CH_2NH_3^+$ under UV irradiation notes that a trapped charge on the methylammonium cation $CH_3NH_3^+$ decomposes the material when in a hydrated environment [299]. The local electric field of the trapped charge triggers deprotonation of the organic cation to yield unstable methylamine, CH_3NH_2. This decomposition can be irreversible if the methylamine evaporates, though is potentially reversible if the resultant components remain in the local environment. Oxidation of the methylamine molecule produces $CH_2NH_3^+$ [297], which is paramagnetic and has been observed in $MAPbBr_3$ [32].

Three properties that are commonly measured to characterise defects are PL, conductivity and EPR. PL measurements have been previously used to investigate charge carrier dynamics within hybrid perovskites [31, 307, 320]. Whilst this can be useful for approximating defect density, is it most directly useful for quantifying direct radiative EHR. Conductivity measurements on the other hand consider the movement of free carriers, whilst EPR is best suited to observing paramagnetic defect states.

6.5 Experimentation

Here, I conduct EPR measurements of irradiated PbI_2 powder and hybrid perovskite single crystals. EPR measurements were conducted at cryogenic temperatures between 30-107 K. The samples were cooled below their normal operating temperatures to overcome thermal noise. Three different spectrometers were used for the measurements presented here:

1. An X-band Bruker EMX Micro spectrometer, ESR-900 cryostat and SHQE-W

cylindrical TE_{011} cavity (9.4 GHz) operated with microwave power 2 mW;

2. An X-band *Bruker* ElexSys I E680 ESR spectrometer with an *Oxford instruments* CF935O continuous flow cryostat and *Bruker* Biospin ER 4118X-MD5W1 cylindrical TE_{011} sapphire dielectric cavity (9.7 GHz) operated with microwave power 626 μW.

3. A Q-band Elexsys II E580 spectrometer with the same cryostat and a *Bruker* Biospin ER5107D2 cylindrical TE_{011} sapphire dielectric cavity (34 GHz) operated with microwave power 3.2 mW.

The microwave field strength was modulated for lock-in detection by 2 G at 100 kHz for X-band and 50 kHz for Q-band. The samples were irradiated with a broadband (300 - 1100 nm) Oriel xenon arc lamp for varying durations at 1000 W (76.4 Wcm^{-2}) to photoinduce ESR-visible spin defects. The light was filtered with a water filter (to suppress infrared [321]) and a UV 200 - 400 nm (3.1 - 6.2 eV) optical filter.

$$\begin{gathered} I = \frac{E/\tau}{A} \approx 80 \text{ mW/cm}^2 \\ \therefore E \approx 7 - 29 \text{ J} \end{gathered} \tag{6.1}$$

for τ is 3-12 minute irradiation duration, where I is intensity, E is energy and A is area of irradiation.

In a separate experiment, samples were also irradiated with a *Continuum Surelite Series* 355 nm laser. Initially, the samples were exposed to 10 mJ ($E = P_{Peak} \times \tau_{pulse} = P_{mean}/k_{repetition}$) of light for 10 seconds at a pulse rate of 10 Hz ($\sim$100 pulses) with a beamwidth of approximately 5.5 mm. This is the same as the irradiation method used in ref. [32]. Our samples were then exposed to two addition irradiation periods of 20 seconds each (totally 50 seconds of exposure).

The hybrid perovskite crystals were held in a *Qsil* fused quartz EPR tube [322] with vacuum grease. Lead iodide powder was also contained in a *Qsil* EPR tube. Samples were cooled to the required temperature before being irradiated with UV light for 12 minutes (unless otherwise specified). There was no EPR signal before illumination. The EPR cavity was tuned and the power level adjusted to maximise the signal and

minimise power distortion. The EPR spectrum was averaged over 10 scans to improve the SNR, and then measured again. This was repeated over a period of hours to observe the temporal behaviour of the defects. Each set of 10 scans took approximately 710 seconds.

To verify that none of the EPR signal resulted from defects like silica dangling bonds E'_γ in the quartz sample holder [32], an empty quartz tube was mounted in the EPR cavity, irradiated with the same UV light for 12 minutes and its spectrum measured. No EPR signal was observed.

6.6 EPR-silent irradiated PbI_2 powder

EPR measurements on the PbI_2 powder were conducted. PbI_2 is a fabrication precursor in the popular $MAPbX_3$ thin films used for experiments in current literature. The powder used was bought from *TCI Chemicals*, and is their lead (II) Iodide (99.99 %, trace metal basis). The use of highly purified dehydrated PbI_2 is necessary to form reproducible and highly efficient (PCE>10 %) perovskite solar-cells [323, 324]. Before this purity level the water content of the PbI_2 precursor inhibited PbI_2 dissolving in dimethylformamide $(CH_3)_2NCH$ (another precursor), which was necessary for solution processed thin-film devices.

As previously discussed, various experiments on PbI_2 crystals have been completed in the past [37, 325] as well as other lead halides now used as fabrication precursors in perovskite solar cells [38, 289, 291, 293, 326–328]. The powder was irradiated with 122 Wcm^{-2} for a period of 12 minutes (corresponding to an irradiation energy of 7 - 29 J, as described in equation 6.1). EPR measurements were performed at room temperature and also cryogenic temperatures (95 K) before and after irradiation in the X-band setup described in section 6.5. In all cases, no EPR signal was observed above the cavity background noise floor.

6.7 A deceptively similar EPR signal from vacuum grease

In my experiment hybrid perovskite samples were mounted on the inner wall of an EPR quartz tube using vacuum grease. Subsequent radiation produced the EPR signal in figure 6.1, which is deceptively similar to what one would expect from a degraded $CH_3NH_3PbX_3$ compound. The signal *appears* to be divided into two components: a signal resulting from a methyl radical $CH_3^\bullet$ and a signal from the hyperfine interaction with the nuclear spin of ^{207}Pb at three consistent distances from a spin-active defect. Methyl is indeed a constituent compound of $MAPbX_3$ and has been theoretically demonstrated as a product of UV radiation induced degradation [34], whilst the relative peak heights of the other resonance closely match the 0.14:1:0.14 intensity ratio of naturally occurring lead, which contains 22.6 % $I = {}^1/_2$ ^{207}Pb.

However, whilst both of these signals appear to be due to paramagnetic elements of $MAPbX_3$, the spectrum is in fact the result of the irradiated silicone poly(dimethylsiloxane) (PDMS), a polymer in the *Dow Corning* vacuum grease used. This has been verified by control experiments. Unirradiated vacuum grease is EPR-silent at room and cryogenic temperature, though ionising radiation at cryogenic temperatures induces unstable free radicals when the PDMS polymer chains crosslink [329]. The spectrum is rationalised to be the superposition of three spectra resulting from methyl, vinyl and siloxane (O-Si-O) radicals. A methyl radical resonance quartet, which is also a byproduct of methylammonium degradation [34]. A resonant triplet from a vinyl radical group and a resonant singlet due to a silicon radical in a siloxane group bound to a methyl compound together closely resemble and their specturm are justifiable as charge carriers interacting with $^{207}Pb^{2+}$ nuclei [289, 330]. The PDMS-derived molecules are in figure 6.1. I observed bi-exponential temperature-dependent temporal decay of $CH_3^\cdot$ radicals and bi-exponential temperature-dependent temporal growth of the remaining EPR signals. Self-rejuvenation has been reported in hybrid perovskites [331] and could incorrectly be considered a possible explanation for the temporal behaviour of the EPR-active defects.

One EPR signal that is not explained by PDMS or the quartz tube is the pink triplet

in figure 6.1. It was observed in $MAPbI_3$ crystals irradiated below 95 K. The likely cause is unknown though I tentatively assign it to degraded $MAPbI_3$.

6.8 EPR of irradiated $MAPbX_3$ crystals

6.8.1 Unidentified triplet species

EPR experiments of $MAPbI_3$ samples revealed a triplet at ∼340 mT (g∼1.9725) at temperatures below 95 K. This triplet has peak-peak spacing of 1.7 G and is in the inset pink circle in the lower right corner of figure 6.1. It is observable immediately after irradiation though grows to its full intensity within 20 minutes and maintains this intensity. No triplet signal like this has previously been observed in lead halides and its source is unknown. It proved difficult to reproduce.

6.8.2 Absence of lead, halide or organic spin-active defects

EPR measurements were also conducted on $MAPbI_3$ and $MAPbBr_3$ single crystals. Besides the triplet tentatively assigned to $MAPbI_3$ no EPR signal was observed above the cavity background noise and vacuum grease signal. This result, in combination with the EPR-silent PbI_2 discussed in section 6.6, is in contrast to previously published results for both measurements [32, 37, 290]. The conflicting results raise the question of what differs in the experiments. The irradiation intensities are stronger than those previously used [326] and optical bleaching has been demonstrated [144, 290, 295, 332, 333]. Optical bleaching is a mechanism whereby midgap charge traps are passivated by photoexcited free carriers. The light's energy is usually below the bandgap though equal to or larger than the defect's energy. As my radiation was filtered to UV frequencies, optical bleaching seems unlikely as the $NH_2CH_3^+$ defect at the very least is a deep defect [32, 34]. Thermal bleaching via a similar mechanism can be ruled out as the temperature was kept constant. It is hypothesised that the lack of spin-active defects is due to the quality of the crystal [323, 324].

Interestingly although no EPR signal could be observed in pure single crystal, EPR

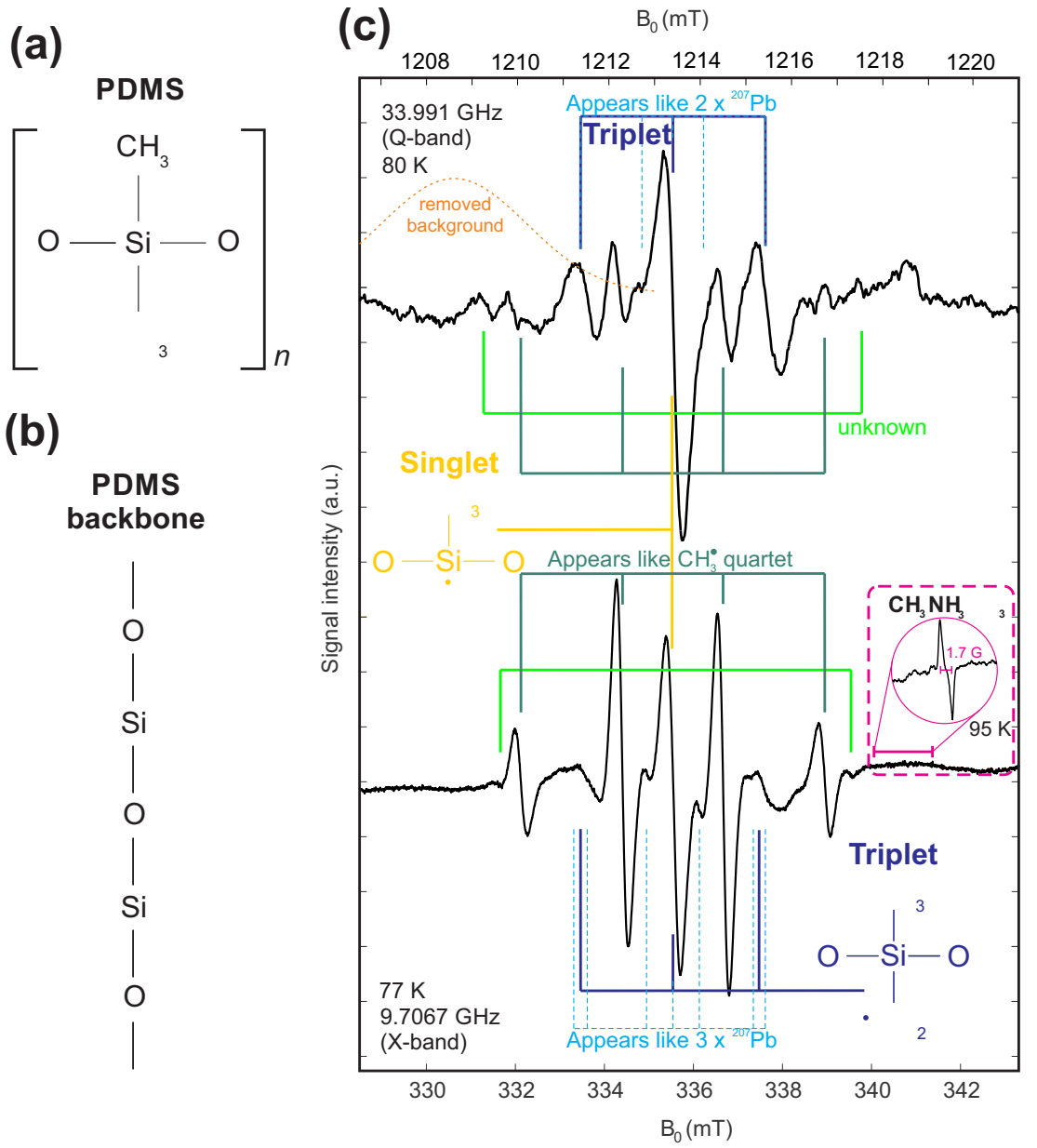


Figure 6.1: Molecular structure and EPR spectra of PDMS and radiation induced radical species. **(a)** Molecular structure PDMS and **(b)** its silicone backbone. **(c)** The Q-band [upper] and X-band [lower] spectra of the radiation induced radical species inducing a quartet, triplet and singlet of resonance lines. The PDMS radicals and their role as the source of the EPR spectra are determined in ref. [329]. A spin triplet was identified in the spectra when both PDMS and $MAPbI_3$ were irradiated. This spin triplet is tentatively assigned to irradiated $MAPbI_3$.

signals have been observed in crystals fabricated using the same methods but with added impurities like cobalt, whose EPR signature is due to it existing in substitutional lead lattice locations [334, 335].

Alternatively bismuth impurities should in theory substitute lead ($[Xe]4f^{1}45d^{1}06s^{2}6p^{2}$) ions in the sample lattice too, which has one less electron than bismuth. In its stable state, divalent lead contributes two electrons and occurs ionically in $MAPbX_3$ as Pb^{2+}. EPR experiments demonstrate no bismuth EPR signal, which suggests bismuth exists as diamagnetic EPR-silent Bi^{3+} in the crystal. Unlike cobalt dopants, XRD on bismuth doped $MAPbX_3$ materials demonstrated no bismuth in crystal lattice positions [334, 336]. Based on the EPR signal g-value, the bismuth appears to have induced lead defects in the perovskite to form Pb^{+} or be involved in further ionisation of lead to form the self-trapping hole centre of Pb^{3+} [326]. A lead ion is only paramagnetic when it either gains or loses an electron to form Pb^{+} and Pb^{3+}, which have electron configuration $[Xe]4f^{14}5d^{10}6s^{2}6p^{1}$ and $[Xe]4f^{14}5d^{10}6s^{1}$ respectively. The inclusion of bismuth in $MAPbBr_3$ also induces a colour change in the crystal from orange to dark brown, indicating the introduction of ESR-silent colour centre defect, even if they were not paramagnetic.

6.9 Conclusion

The absence of any definitive EPR signal in the highly purified lead iodide precursor predicted the quality of hybrid perovskite crystals used in subsequent measurements. The crystal quality was subsequently demonstrated when no EPR signal was observed in single crystals of $MAPbBr_3$ and $MAPbI_3$. UV-irradiation also has no observable effect on the crystal's paramagnetic defect concentration. Despite numerous reports of the degrading effects of high energy irradiation on hybrid perovskites, and past observations of UV-irradiation induced spin-active defects, the high quality crystals used in these experiments remained stable and appeared unaffected. The deprotonation process described in ref. [32] was triggered by the trapping of a hole at the organic cation $NH_3CH_3^{+}$. For a pure crystal the Coulombic force provides a deterrent to hole trapping, which may therefore

inhibit the deprotonation process.

7

Conclusion and future work

Defects, whether deliberately or unintended, change the properties and function of semiconductors. Characteristic bandgaps of various semiconductors act as templates, from which to develop more sophisticated environments for charge transport or interaction. Materials with established fabrication practices like silicon rely on calculated impurity doping strategies to implement exacting control over these material properties. This includes control over optical absorption and luminescence spectrum, charge carrier mobility and concentration and electron-hole lifetime to name a few. In contrast to deliberately doping, intimate contact with other materials, isotopes and unintended defects like impurities in semiconductors also change their electrical properties.

7.1 Rectification

In Chapter 3, I considered the rectification of induced currents in non-linear devices.

Using a two-dimensional Taylor series approximation, I modelled the rectification current in terms of the gate and bias voltage inputs. I demonstrated the dominance of a second order term that included the phase difference between the AC voltages on the gate and bias leads. In my TOLOP devices, this phase difference determined the phase and magnitude of the resulting rectification current.

The difficulty with developing a universal theory for rectification effects is that devices and their operating conditions differ. For example, the voltage coupling between leads due to stray impedances was found to be insignificant in my devices though were critical in refs [98, 110]. My method for analysing the rectification current however, is novel and should prove useful for future rectification dependent measurements.

I also demonstrated broadband EPR detection of foreign paramagnetic species could be achieved by measuring the variation of the rectification current on resonance. This was achieved for DPPH at X-band and oxygen molecule at D-band frequencies and presents a new way to detect microwave absorption, without the need to isolate the detection circuitry from the large static magnetic field.

7.2 Spin-dependent recombination in arsenic and sulfur doped silicon

In Chapters 4 and 5, I investigated SDR in ^{75}As and ^{33}S doped silicon using EDMR. Whilst the inclusion of sulfur in an EDMR experiment is novel, the properties I have relied on are relatively common to the chalcogens sulfur, selenium and tellurium. I investigated sulfur in silicon with three potential applications in mind.

First, SDR measurements have previously been mediated by energetically shallow phosphorus and energetically deeper interface defects in QIP measurements. This has several disadvantages including an inability to control the lattice position of interface defects and the defect's deleterious effects on the donor coherence times. An energetically deep donor like sulfur provides a viable alternative, whose doping profile and concentration can be better controlled. Despite the state-of-the-art single electron/single donor spin measurements that have been demonstrated for QIP [13, 18], SDR ensemble experiments are still a useful testbed for developing spin-state measurement, interaction and control techniques [96, 167, 168]. Better control of these experiments with deliberate charge traps is a worthwhile pursuit. Second, the access to IR wavelengths of chalcogens in silicon makes them useful for optoelectronic devices like IR detectors and photodiodes. Third, chalcogens in silicon have been proposed as qubits [141, 142]. Their large bind-

ing energies, paramagnetic singly ionised state, long relaxation and coherence times, and their potential to be coupled to optical cavities for long-range qubit interactions are all favourable properties [144].

Specific samples were developed for these experiments. In the samples, background boron doping was used to compensate one of sulfur's two donor electrons to make the chalcogen singly ionised and paramagnetic. The population of singly ionised chalcogens was determined by the boron concentration. In order to electrically activate the sulfur donors, a thermal heat/quench treatment was applied. Three samples were annealed at 1200°C for 10 seconds, one minute and three minutes respectively and then thermally quenched in room temperature water. The sample that was annealed for 10 seconds showed cwEDMR spectra rich in interface defects as well as ^{75}As's resonant quartet, whilst the samples annealed for one and three minutes had much simpler spectra with fewer dangling bond defects and ^{75}As's resonant quartet. Literature has shown that ion-implantation can cause amorphisation of a crystal, which results in the same dangling bond defects observed at the interface. I observed recrystalisation of the two samples that had been annealed for longer. The resonant quartet of ^{33}S was not definitively identified in any of the samples despite SIMS measurements suggesting sulfur in proximity to arsenic throughout the sample annealed for 10 seconds.

As was demonstrated in Chapter 4, thermal treatment for donors isolated from the interface is a balance between activation, recrystalisation, and precipitation. A sample must be annealed for long enough to recrystalise the amorphised crystal and activate donors whilst also avoiding their precipitation to the sample's surface. The best way to overcome this is by reducing the donor concentration to minimised diffusion, which will allow for longer or hotter anneals.

A boron concentration of only $\sim 10^{12}$ cm^{-3} would result in, at most, a comparable number of charge compensated sulfur ions. This was below the measured EDMR sensitivity limit of $\sim 10^{15}$ cm^{-3} for the sample size and number of spectrum averages taken. Nevertheless, the heat treatment method has been shown to spin-activate chalcogens in EPR measurements. Lower doping concentrations improve the proportion of electrically activate donors and reduces donor diffusion. With this in mind, an improved measure-

ment sensitivity would allow for a maximised activation through low concentration, whilst a comparable concentrations of boron and sulfur of the order of 10^{12} cm^{-3} would allow for suitable charge compensation of one of sulfur's electron by boron.

Assuming a measurable concentration of ^{33}S, the detrimental effects of photoneutralisation of S^+ and B^- states can not be underestimated. Whilst sulfur has been shown to capture both electrons and holes in its S^+ state [179] a penchant for photoexcited electron capture is what leads to photoneutralisation [144]. More attention is needed to balance the photoexcitation necessary for SDR and shallow donor electron capture against the charge neutralisation of double-donors and acceptors. A much higher boron concentration that sufficiently lowers the Fermi level to create S^{++} state could negate the photoneutralisation effect as electron capture will lead to the S^+ charge state [11]. Alternatively, a decreased light intensity may avoid photoneutralisation of thermal equilibrium states and therefore increase the proportion of singly occupied sulfur necessary for EDMR [144]. The reduced density of free carriers should encourage the background boron acceptor doping to be the primary cause of charge redistribution. Illumination should be used as a tool to regulate an imbalance in the relative concentrations of B^-:S^+ [11].

My samples were prefabricated at the specified dopant concentrations, inhibiting my ability to experiment with various illumination intensities for a range of sample concentrations. A range of samples with differing concentrations would allow a systematic EPR study of the effects of competing sulfur/boron concentrations, which, to the best of my knowledge, has not previous been undertaken. Based on previous experiments, the most interesting concentration range is [S]>[B] to $^{[B]}/_{[S]} \sim 10^8$ [24, 144, 152]. This study would build on previous studies that describe the deep-donor hole capture process. A complimentary EDMR study like that conducted in ref. [11] would verify whether EHR occurs via these states, not just the states' existence.

To improve my ability to differentiate overlapping signals in the samples, a high B_0 would be useful. Reduced signal linewidths would also help. This could be achieve by first, the use of isotopically purified ^{28}Si and second, creating a smaller doped region, which would experience a more uniform $\boldsymbol{B_1}$. High B_0 and low temperatures would also

steer the system into the spin-dependent trapping regime. This would negate the need for spin-pairs and also generate a larger EDMR signal.

My results highlighted the fine balance required for EPR and EDMR measurements of double-donors. A deliberate balance between impurity concentrations, photoionisation, temperature and dopant distribution needs to be careful formulated for future measurements.

Spatially isolating the donors from the interface was expected to increase the coherence time by reducing coherence limiting spin flips in paramagnetic charge traps at the interface [169, 259]. I observed a coherence time of 2 μs for ^{75}As, which is unremarkable in naturally occurring silicon. I attributed this to measurable arsenic concentrations at the interface.

I used an electrical inversion recovery pulse sequence to measure the electronic transition times. By inverting a constituent component of a spin-pair, I measured the antiparallel spin recombination time as 4.5 μs. As expected, the electron-hole pair generation rate was shown to be exponentially dependent on the illumination intensity.

Finally, EDELDOR measurements were performed across a field range corresponding to the rich cwEDMR spectrum around g$\sim$2. By measuring the change in state of one potential spin-pair after manipulating the other, I could identify which spin-centres formed a spin-pair with arsenic and which did not. My results revealed the formation of spin-pairs between arsenic and interface defects that resulted from the ion-implantation amorphisation.

7.3 Deleterious defects in hybrid perovskites

I performed EPR measurements on UV-irradiated PbI_2 powder and $MAPbI_3$/$MAPbBr_3$ single crystals. Despite a history of publications on the EPR-active defects in UV-irradiated powder [37, 295, 326], and two previous reports of EPR-active defects in hybrid perovskite crystals [32, 318] I observed no EPR signal in either measurement. The perovskite experiments, whilst benign, raised several research questions important to understanding charge carrier dynamics in the material. There is intense scientific and

commercial interest in these materials and charge carrier dynamics is an ongoing area of research necessary for the practical implementation of perovskite solar cells [30, 31, 277, 320]. The localisations of trapped charge carriers is a primary hinderance to charge transport and therefore the PCE. EPR based measurement schemes are ideally suited to identifying radical species. I propose two further areas of research that follow the results presented in this thesis.

Firstly, it has been highlighted that the purity of the lead (II) iodide precursor is critical in determining the PCE of solution-processible devices [323]. I concluded from my measurements that the same precursor was a potential cause of the defects resulting from the irradiated material observed in ref. [32]. In their measurements irradiated lead (II) iodide precursor revealed the EPR signature of the hole trapped at a lead cation, Pb^{3+}. They observed the same EPR signal in their hybrid perovskite, $CH_3NH_3PbBr_3$. In comparison, in my measurements no EPR signals were observed in either precursor powder or perovskite crystal. A systematic approach should be undertaken to investigate the effect of the precursor on the creation of localised charge traps in both the precursor lead (II) iodide and hybrid perovskite materials, $CH_3NH_3PbX_3$.

Secondly, whilst EDMR relies on EPR to induce an effect, its output is the influence of charge carrier interactions on charge transport. Since charge transport occurs in photovoltaic materials, the same charge carrier interactions controlled in EDMR can modulate photovoltaic material transport behaviour. For photovoltaics, EDMR measurements will compliment EPR measurements of spin active defects to determine how shallow and deep defects influence device performance. This thesis has demonstrated the power of pEDMR to investigate performance limiting processes like EHR. SDR experiments can identify not only defects and mechanisms that facilitate EHR but also where in the materials these defect reside, as has been exemplarily demonstrated in silicon solar cells [45, 159–161]. SDR can be extended to control charge carrier interactions in perovskites too. Photoluminescence measurements are currently used to investigate SRH, free electron-hole and Auger recombination in perovskite materials [31, 307, 320]. EDMR can also compliment these experiments.

7.4 Closing remarks

In conclusion, I have investigated defects in novel environments using spin resonance techniques. Although EPR is a common method for the manipulation and measurement of radical species, my work extended to EDMR, which utilises charge transport to observe resonant effects.

The deliberate use of defects like dopant impurities provide unique material properties that have been exploited by the semiconductor industry for decades. Dopants in silicon are utilised for QIP experiments too. In another prominent example of productive defects, the long electron-hole diffusion length of the remarkable hybrid perovskite photovoltaic absorbers has been attributed to intrinsic defects. However, unintended defects can prove debilitating to experiments and semiconductor devices too. For example, charge trapping defects in photovoltaic materials can inhibit their PCE. As Queisser and Haller so earnestly recognised, when it comes to defects in semiconductors, some are 'fatal', some are 'vital' [1]. Nevertheless, whilst Moore's law draws to a close, practical applications of new semiconductors and new defect states continue to be discovered, and new techniques like precise donor placement [270] expands the opportunities for experimental exploitation of these defects.

Bibliography

[1] H. J. Queisser. "Defects in Semiconductors: Some Fatal, Some Vital". In: *Science* 281.5379 (1998), pp. 945–950.

[2] Gordon E Moore. "Cramming more components onto integrated circuits". In: *Electronics* 38.8 (1975).

[3] Robert H Dennard, Fritz H Gaensslen, Hwa-Nien Yu, V Leo Rideout, Ernest Bassous, and Andre R LeBlanc. "Design of Ion-Implanted Small MOSFET's Dimensions with Very Small Physical Dimensions". In: *IEEE Journal of Solid-state Circuits* 9.5 (1974), pp. 256–268.

[4] M. Lundstrom. "Device physics at the scaling limit: what matters? [MOSFETs]". In: *IEEE International Electron Devices Meeting 2003* (2003), pp. 789–792.

[5] Igor L. Markov. "Limits on fundamental limits to computation". In: *Nature* 512.7513 (Aug. 2014), pp. 147–154.

[6] Linda Geppert. "The amazing vanishing transistor act". In: *IEEE Spectrum* 39.10 (2002), pp. 28–33.

[7] Robert Service. "Is silicon's reign nearing its end". In: *Science* 323.February (2009), pp. 1000–1002.

[8] C. C. Lo and John J L Morton. "Silicon's Second Act". In: *IEEE Spectrum* 51.8 (2014), pp. 37–43.

[9] F. C. Rong, G. J. Gerardi, W. R. Buchwald, E. H. Poindexter, M. T. Umlor, D. J. Keeble, and W. L. Warren. "Electrically detected magnetic resonance of a transition metal related recombination center in Si p-n diodes". In: *Applied Physics Letters* 60.5 (1992), pp. 610–612.

[10] Andre R. Stegner, Christoph Boehme, Hans Huebl, Martin Stutzmann, Klaus Lips, and Martin S. Brandt. "Electrical detection of coherent 31P spin quantum states". In: *Nature Physics* 2.12 (Nov. 2006), pp. 835–838.

[11] B. Stich, S. Greulich-Weber, and J.-M. Spaeth. "Electrical detection of electron paramagnetic resonance: New possibilities for the study of point defects". In: *Journal of Applied Physics* 77.1995 (1995), p. 1546.

[12] D R McCamey, H Huebl, M S Brandt, W D Hutchison, J C McCallum, R G Clark, and A R Hamilton. "Electrically detected magnetic resonance in ion-implanted Si:P nanostructures". In: *Applied Physics Letters* 89.18 (2006), p. 182115.

[13] Andrea Morello, Jarryd J Pla, Floris A Zwanenburg, Kok W Chan, Kuan Y Tan, Hans Huebl, Mikko Möttönen, Christopher D Nugroho, Changyi Yang, Jessica a van Donkelaar, Andrew D C Alves, David N Jamieson, Christopher C Escott, Lloyd C L Hollenberg, Robert G Clark, and Andrew S Dzurak. "Single-shot read-out of an electron spin in silicon." In: *Nature* 467.7316 (Oct. 2010), pp. 687–91.

[14] A. Bienfait, J. J. Pla, Y. Kubo, M. Stern, X. Zhou, C. C. Lo, C. D. Weis, T. Schenkel, M. L.W. Thewalt, D. Vion, D. Esteve, B. Julsgaard, K. Mølmer, J. J.L. Morton, and P. Bertet. "Reaching the quantum limit of sensitivity in electron spin resonance". In: *Nature Nanotechnology* 11.3 (2016), pp. 253–257.

[15] S Probst, A Bienfait, P. Campagne-Ibarcq, J J Pla, B Albanese, J. F. Da Silva Barbosa, T. Schenkel, D. Vion, D Esteve, K Mølmer, J. J.L. Morton, R Heeres, and P Bertet. "Inductive-detection electron-spin resonance spectroscopy with 65 spins/sqrt Hz sensitivity". In: *Applied Physics Letters* 111.20 (2017).

[16] B E Kane. "A silicon-based nuclear spin quantum computer". In: *Nature* 393.6681 (1998), pp. 133–137.

[17] John J L Morton and Brendon W Lovett. "Hybrid Solid-State Qubits: The Powerful Role of Electron Spins". In: *Annual Review of Condensed Matter Physics* 2.1 (Mar. 2011), pp. 189–212.

[18] Jarryd J Pla, Kuan Y Tan, Juan P Dehollain, Wee H Lim, John J L Morton, David N Jamieson, Andrew S Dzurak, and Andrea Morello. "A single-atom electron spin qubit in silicon". In: *Nature* 489.7417 (Sept. 2012), pp. 541–5.

[19] Jarryd J Pla, Kuan Y Tan, Juan P Dehollain, Wee H Lim, John J. L. Morton, Floris A. Zwanenburg, David N Jamieson, Andrew S. Dzurak, and Andrea Morello. "High-fidelity readout and control of a nuclear spin qubit in silicon". In: *Nature* 496.7445 (Apr. 2013), pp. 334–8.

[20] M Veldhorst, J C C Hwang, C H Yang, A W Leenstra, B de Ronde, J P Dehollain, J T Muhonen, F E Hudson, K M Itoh, A Morello, and A S Dzurak. "An addressable quantum dot qubit with fault-tolerant control fidelity". In: *Nature nanotechnology* 9.12 (2014), pp. 981–985.

[21] M. Veldhorst, C. H. Yang, J. C. C. Hwang, W. Huang, J. P. Dehollain, J. T. Muhonen, S. Simmons, a. Laucht, F. E. Hudson, K. M. Itoh, a. Morello, and a. S. Dzurak. "A two-qubit logic gate in silicon". In: *Nature* (2015), pp. 1–5.

[22] Felix Hoehne, Hans Huebl, Bastian Galler, Martin Stutzmann, and Martin S. Brandt. "Spin-Dependent Recombination between Phosphorus Donors in Silicon and Si/SiO2 Interface States Investigated with Pulsed Electrically Detected Electron Double Resonance". In: *Physical Review Letters* 104.4 (Jan. 2010), p. 046402.

[23] David P. Franke, Felix Hoehne, Leonid S. Vlasenko, Kohei M. Itoh, and Martin S. Brandt. "Spin-dependent recombination involving oxygen-vacancy complexes in silicon". In: *Physical Review B* 89.19 (May 2014), p. 195207.

[24] Kevin J. Morse, Rohan J. S. Abraham, Helge Riemann, Nikolai V. Abrosimov, Peter Becker, Hans-Joachim Pohl, Michael L. W. Thewalt, and Stephanie Simmons. "A photonic platform for donor spin qubits in silicon". In: *Science Advances* e.July (2017), pp. 1–10.

[25] Daniel Loss and David P. DiVincenzo. "Quantum computation with quantum dots". In: *Physical Review A* 57.1 (Jan. 1998), pp. 120–126.

[26] T. F. Watson, S. G. J. Philips, E. Kawakami, D. R. Ward, P. Scarlino, M. Veldhorst, D. E. Savage, M. G. Lagally, Mark Friesen, S. N. Coppersmith, M. A. Eriksson, and L. M. K. Vandersypen. "A programmable two-qubit quantum processor in silicon". In: *ArXiv* 2 (2017).

[27] Andrew S. Brown and Martin A. Green. "Impurity photovoltaic effect: Fundamental energy conversion efficiency limits". In: *Journal of Applied Physics* 92.3 (2002), pp. 1329–1336.

[28] E.T. Hu, G.Q. Yue, R.J. Zhang, Y.X. Zheng, L.Y. Chen, and S.Y. Wang. "Numerical simulations of multilevel impurity photovoltaic effect in the sulfur doped crystalline silicon". In: *Renewable Energy* 77 (2015), pp. 442–446.

[29] James E Carey, Catherine H Crouch, Mengyan Shen, and Eric Mazur. "Visible and near-infrared responsivity of femtosecond-laser microstructured silicon photodiodes". In: *Optics Letters* 30.14 (2005), p. 1773.

[30] Samuel D Stranks, Giles E Eperon, Giulia Grancini, Christopher Menelaou, Marcelo J P Alcocer, Tomas Leijtens, Laura M Herz, Annamaria Petrozza, and Henry J Snaith. "Electron-hole diffusion lengths exceeding 1 micrometer in an organometal trihalide perovskite absorber." In: *Science (New York, N.Y.)* 342.6156 (2013), pp. 341–344.

[31] Samuel D. Stranks, Victor M. Burlakov, Tomas Leijtens, James M. Ball, Alain Goriely, and Henry J. Snaith. "Recombination Kinetics in Organic-Inorganic Perovskites: Excitons, Free Charge, and Subgap States". In: *Physical Review Applied* 2.3 (2014), p. 034007.

[32] Ilya A. Shkrob and Timothy W. Marin. "Charge trapping in photovoltaically active perovskites and related halogenoplumbate compounds". In: *Journal of Physical Chemistry Letters* 5.7 (2014), pp. 1066–1071.

[33] Michael Saliba, Taisuke Matsui, Ji-Youn Seo, Konrad Domanski, Juan-Pablo Correa-Baena, Mohammad Khaja Nazeeruddin, Shaik M. Zakeeruddin, Wolfgang Tress, Antonio Abate, Anders Hagfeldt, and Michael Grätzel. "Cesium-containing

triple cation perovskite solar cells: improved stability, reproducibility and high efficiency". In: *Energy Environ. Sci.* 9.6 (2016), pp. 1989–1997.

[34] Pietro Delugas, Alessio Filippetti, and Alessandro Mattoni. "Methylammonium fragmentation in amines as source of localized trap levels and the healing role of Cl in hybrid lead-iodide perovskites". In: *Physical Review B - Condensed Matter and Materials Physics* 92.4 (2015), pp. 1–11.

[35] Woon Seok Yang, Byung Wook Park, Eui Hyuk Jung, Nam Joong Jeon, Young Chan Kim, Dong Uk Lee, Seong Sik Shin, Jangwon Seo, Eun Kyu Kim, Jun Hong Noh, and Sang Il Seok. "Iodide management in formamidinium-lead-halide-based perovskite layers for efficient solar cells". In: *Science* 356.6345 (2017), pp. 1376–1379.

[36] CORDIS. *Towards Low Power ICT*. 2017.

[37] J. Arends and J. F. Verwey. "ESR on UV Irradiated Lead Halides at 80 K". In: *Physica Status Solidi (B)* 23.1 (1967), pp. 137–145.

[38] Masanobu Iwanaga. "Charge separation of excitons and the radiative recombination process in PbBr2 crystals". In: *Physical Review B* 62.16 (2000), pp. 766–773.

[39] Christoph Boehme. "Dynamics of spin–dependent charge carrier recombination". PhD thesis. University of Marburg, 2002, pp. 1–146.

[40] Christoph Boehme and Klaus Lips. "Theory of time-domain measurement of spin-dependent recombination with pulsed electrically detected magnetic resonance". In: *Physical Review B* 68.24 (Dec. 2003), p. 245105.

[41] Victor Chechik, Emma Carter, and Damien Murphy. *Electron paramagnetic resonance*. 1st ed. Glasgow, UK: Oxford University Press, 2016.

[42] Felix Hoehne. "Electrical detection of hyperfine interactions in silicon". PhD thesis. Technische Universität München, 2012, p. 181.

[43] Stephen Blundell. *Magnetism in Condensed Matter*. New York, 2001.

[44] Phil Rieger. "Electron Spin Resonance". In: (2007).

[45] Jan Behrends. "Spin-dependent Transport and Recombination in Solar Cells studied by Pulsed Electrically Detected Magnetic Resonance". PhD thesis. Freien Universität Berlin, 2009.

[46] Arthur Schweiger and Gunnar Jeschke. *Principles of Pulsed Electron Paramagnetic Resonance*. 1st. New York, 2001.

[47] Krystyna Kolwas and Anastasiya Derkachova. "Modification of Solar Energy Harvesting in Photovoltaic Materials by Plasmonic Nanospheres: New Absorption Bands in Perovskite Composite Film". In: *Journal of Physical Chemistry C* 121.8 (2017), pp. 4524–4539.

[48] Hans Huebl. "Coherent manipulation and electrical detection of phosphorus donor spins in silicon". PhD thesis. Technische Universität München, 2007.

[49] Stephen Blundell. *Magnetism in Condensed Matter*. 15th ed. New York: Oxford University Press, 2014.

[50] A. Bienfait, J. J. Pla, Y. Kubo, M. Stern, X. Zhou, C. C. Lo, C. D. Weis, T. Schenkel, M. L. W. Thewalt, D. Vion, D. Esteve, B. Julsgaard, K. Moelmer, J. J. L. Morton, and P. Bertet. "Reaching the quantum limit of sensitivity in electron spin resonance". In: (2015).

[51] M Xiao, I Martin, E Yablonovitch, and HW Jiang. "Electrical detection of the spin resonance of a single electron in a silicon field-effect transistor". In: *Nature* 430.July (2004), pp. 435–439.

[52] J M Elzerman, R Hanson, L H Willems van Beveren, B Witkamp, L M K Vandersypen, and L P Kouwenhoven. "Single-shot read-out of an individual electron spin in a quantum dot". In: *Nature* 430.July (2004), pp. 431–435.

[53] F. C. Rong, W. R. Buchwald, E. H. Poindexter, W. L. Warren, and D. J. Keeble. "Spin-dependent Schokley-Read recombination of electrons and holes in indirect band-gap semiconductor p-n junction diodes". In: *Solid-State Electronics* 34.8 (1991), p. 835.

[54] D J Lepine. "Spin-dependent transport on silicon surface". In: *Physical Review B* 6.2 (1972), pp. 436–441.

[55] D Kaplan, I Solomon, and NF Mott. "Explanation of the large spin-dependent recombination effect in semiconductors". In: *Journal de Physique Lettres* 39.4 (1978), pp. 51–54.

[56] Z. Xiong and D. J. Miller. "General expression for the electrically detected magnetic resonance signal from semiconductors". In: *Applied Physics Letters* 63.3 (1993), pp. 352–354.

[57] S. Geschwind, R. J. Collins, and A. L. Schawlow. "Optical Detection of Paramagnetic Resonance in an Excited State of Cr 3 + in Al 2 O 3". In: *Physical Review Letters* 3.12 (1959), pp. 545–548.

[58] J. Brossel, S. Geschwind, and A. L. Schawlow. "Optical Detection of Paramagnetic Resonance in Crystals At Low Temperatures J." In: *Physical Review Letters* 3.12 (1959), pp. 1958–1959.

[59] Toshikazu Hirose, Hide Yoshioka, and Kazumi Horai. "Conductivity Increase of Reduced Rutile with the Saturation of Electron Spin Resonance". In: *Journal of the Physical Society of Japan* 21.3 (1966), pp. 559–559.

[60] R Maxwell and A Honig. "Neutral-impurity scattering experiments in silicon with highly spin-polarized electrons". In: *Physical Review Letters* 17.4 (1966), pp. 3–5.

[61] Christoph Boehme and Hans Malissa. "Electrically detected magnetic resonance spectroscopy". In: *eMagRes* 6.1 (2017), pp. 83–100.

[62] W. Shockley and W. T. Read. "Statistics of the Recombination of Holes and Electrons". In: *Physical Review* 87.46 (1952), pp. 835–842.

[63] R. N. Hall. "Electron-Hole Recombination in Germanium". In: *Phys. Rev.* 87 (2 July 1952), pp. 387–387.

[64] Felix Hoehne, Lukas Dreher, Jan Behrends, Matthias Fehr, Hans Huebl, Klaus Lips, Alexander Schnegg, Max Suckert, Martin Stutzmann, and Martin S. Brandt. "Lock-in detection for pulsed electrically detected magnetic resonance". In: *Review of Scientific Instruments* 83 (2012).

[65] W. Zimmerman. "Experimental verification of the Shockley-Read-Hall Recombination theory in silicon". In: *Electronics Letters* 9.16 (1973), pp. 378–379.

[66] Thierry Goudon, Vera Miljanovic, and Christian Schmeiser. "On the shockley–Read–Hall model: generation-recombination in semiconductors". In: *Journal of Applied Mathematics* 67.4 (2007), pp. 1183–1201.

[67] I. Solomon. "Spin-dependent recombination in a silicon p-n junction". In: *Solid State Communications* 20.3 (1976), pp. 215–217.

[68] I. Solomon, D. Biegelsen, and J. C. Knights. "Spin-dependent photoconductivity in n-type and p-type amorphous silicon". In: *Solid State Communications* 22.8 (1977), pp. 505–508.

[69] Christoph Boehme, Peter Kanschat, and Klaus Lips. "Time domain measurement of spin-dependent recombination - A novel defect spectroscopy method". In: *Nuclear Instruments and Methods in Physics Research, Section B: Beam Interactions with Materials and Atoms* 186.1-4 (2002), pp. 30–35.

[70] Hans Huebl, Felix Hoehne, Benno Grolik, Andre R. Stegner, Martin Stutzmann, and Martin S. Brandt. "Spin echoes in the charge transport through phosphorus donors in silicon". In: *Physical Review Letters* 100.17 (2008), p. 177602.

[71] M Lannoo, D Stievenard, D Deresmes, and D Vuillaume. *ICDS-17: Proceedings of the 17th International Conference on Defects in Semiconductors*. Gmunden, Austria: Trans Tech Publications, 1993.

[72] Kôichi Fukui, Toshiyuki Sato, Hidekatsu Yokoyama, Hiroaki Ohya, and Hitoshi Kamada. "Resonance-field dependence in electrically detected magnetic resonance: Effects of exchange interaction". In: *Journal of Magnetic Resonance* 149.1 (2001), pp. 13–21.

[73] T. Eickelkamp, S. Roth, and M. Mehring. "Electrically detected magnetic resonance in photoexcited fullerenes". In: *Molecular Physics* 95.5 (1998), pp. 967–972.

[74] L. S. Vlasenko, Yu. V. Martynov, T. Gregorkiewicz, and C.A.J. Ammerlaan. "Electron paramagnetic resonance versus spin-dependent recombination- Excited triplet states of structural defects in irradiated silicon". In: *Physical Review B* 52.2 (1995), pp. 1144–1151.

[75] David P. Franke. "Electrically detected magnetic resonance on γ -irradiated , phosphorus-doped silicon". PhD thesis. Technische Universität München, 2013.

[76] David P Franke, Manabu Otsuka, Takashi Matsuoka, Leonid S Vlasenko, Marina P Vlasenko, S Martin, Kohei M Itoh, and Am Coulombwall. "Spin-dependent recombination at arsenic donors in ion-implanted silicon". In: *Applied Physics Letters* 112111 (2014), pp. 3–6.

[77] Andre R Stegner. "Spin Properties of phosphorus donors in silicon epilayers". PhD thesis. Technische Universität München, 2005.

[78] Felix Hoehne, Lukas Dreher, Max Suckert, David P. Franke, Martin Stutzmann, and Martin S. Brandt. "Time constants of spin-dependent recombination processes". In: *Physical Review B - Condensed Matter and Materials Physics* 88 (2013), pp. 1–15.

[79] Felix Hoehne. "Multi-Frequency Spectroscopy of Phosphorus Donors at the Si/SiO2 - Interface". PhD thesis. Technische Universität München, 2007.

[80] S.G. Burns and P.R. Bond. *Principles of Electronic Circuits*. Second. West Engineering Series. PWS Publishing Company, 1997.

[81] R. Haberkorn and W. Dietz. "Theory of Spin-Dependent Recombination in Semiconductors." In: *Solid State Communications* 35.6 (1980), pp. 505–508.

[82] Lihuang Zhu, Kipp J. Van Schooten, Mallory L. Guy, and Chandrasekhar Ramanathan. "Optical Dependence of Electrically Detected Magnetic Resonance in Lightly Doped Si:P Devices". In: *Physical Review Applied* 7.6 (2017), pp. 1–12.

[83] C C Lo, J Bokor, T Schenkel, A M Tyryshkin, and S A Lyon. "Spin-dependent scattering off neutral antimony donors in 28Si field-effect transistors". In: *Applied Physics Letters* 91.24 (2007), p. 242106.

[84] D. McCamey, G. Morley, H. Seipel, L. Brunel, J. van Tol, and C. Boehme. "Spin-dependent processes at the crystalline Si-SiO2 interface at high magnetic fields". In: *Physical Review B* 78.4 (July 2008), p. 045303.

[85] X Baie, J P Colinge, V Bayot, and E Grivei. "Quantum-wire effects in thin and narrow SOI MOSFETs". In: *IEEE International SOI Conference* 1993 (1995), pp. 66–67.

[86] B. S. Doyle, S. Datta, M. Doczy, S. Hareland, B. Jin, J. Kavalieros, T. Linton, A. Murthy, R. Rios, and R. Chau. "High performance fully-depleted tri-gate CMOS transistors". In: *IEEE Electron Device Letters* 24.4 (2003), pp. 263–265.

[87] Isabelle Ferain, Cynthia A Colinge, and Jean-Pierre Colinge. "Multigate transistors as the future of classical metal-oxide-semiconductor field-effect transistors." In: *Nature* 479.7373 (Nov. 2011), pp. 310–6.

[88] J. Verduijn, M. Vinet, and S. Rogge. "Radio-frequency dispersive detection of donor atoms in a field-effect transistor". In: *Applied Physics Letters* 104.10 (Mar. 2014), p. 102107.

[89] Alexei O Orlov, Patrick Fay, Gregory L Snider, Xavier Jehl, Sylvain Barraud, and Marc Sanquer. "Dual-Port Reflectometry Technique". In: *IEEE Nanotechnology Magzine* 9.2 (2015), pp. 24–32.

[90] A. C. Betz, R. Wacquez, M. Vinet, X. Jehl, a. L. Saraiva, M. Sanquer, a. J. Ferguson, and M. F. Gonzalez-Zalba. "Dispersively Detected Pauli Spin-Blockade in a Silicon Nanowire Field-Effect Transistor". In: *Nano Letters* (2015), p. 150615160818000.

[91] M F Gonzalez-Zalba, S Barraud, a J Ferguson, and a C Betz. "Probing the limits of gate-based charge sensing". In: *Nature communications* 6 (2015), p. 6084.

[92] M. Fernando Gonzalez-Zalba, Sergey N. Shevchenko, Sylvain Barraud, J. Robert Johansson, Andrew J. Ferguson, Franco Nori, and Andreas C. Betz. "Gate-Sensing Coherent Charge Oscillations in a Silicon Field-Effect Transistor". In: *Nano Letters* 16.3 (2016), pp. 1614–1619.

[93] C. C Lo, V Lang, R E George, J J L Morton, A M Tyryshkin, S A Lyon, J Bokor, and T Schenkel. "Electrically Detected Magnetic Resonance of Neutral Donors Interacting with a Two-Dimensional Electron Gas". In: *Physical Review Letters* 106.20 (May 2011), p. 207601.

[94] C C Lo, F R Bradbury, A M Tyryshkin, C D Weis, J Bokor, T Schenkel, and S A Lyon. "Suppression of microwave rectification effects in electrically detected magnetic resonance measurements". In: *Applied Physics Letters* 100.6 (2012), p. 063510.

[95] Alexander R Barbaro. "Literature review on: Quantum readout of spin resonance in a silicon transistor". In: *Materials Science and Technology* 32.8 (2016), pp. 823–845.

[96] David P. Franke, Florian M. Hrubesch, Markus Künzl, Hans Werner Becker, Kohei M. Itoh, Martin Stutzmann, Felix Hoehne, Lukas Dreher, and Martin S. Brandt. "Interaction of Strain and Nuclear Spins in Silicon: Quadrupolar Effects on Ionized Donors". In: *Physical Review Letters* 115.5 (2015), pp. 1–5.

[97] J. Liu, M. A. Pennington, and N. Giordano. "Mesoscopic photovoltaic effect". In: *Physical Review B* 45.3 (1992), pp. 1267–1272.

[98] L. DiCarlo, C. M. Marcus, and J. S. Harris. "Photocurrent, rectification, and magnetic field symmetry of induced current through quantum dots". In: *Physical Review Letters* 91.24 (2003), p. 246804.

[99] M. Switkes, C. M. Marcus, K. Campman, and A. C. Gossard. "An Adiabatic Quantum Electron Pump". In: *Science* 283.5409 (1999), pp. 1905–1908.

[100] M. D. Blumenthal, B. Kaestner, L. Li, S. Giblin, T. J. B. M. Janssen, M. Pepper, D. Anderson, G. Jones, and D. A. Ritchie. "Gigahertz quantized charge pumping". In: *Nature Physics* 3.5 (2007), pp. 343–347.

[101] Hume Howe. "Amplitude , temperature , and frequency dependence of quantum pumps in semiconductor heterostructures Hume Howe". PhD thesis. University College London, 2015, pp. 1–172.

[102] L. P. Kouwenhoven, S. Jauhar, K. McCormick, D. Dixon, P. L. McEuen, Yu V. Nazarov, N. C. Van Der Vaart, and C. T. Foxon. "Photon-assisted tunneling through a quantum dot". In: *Physical Review B* 50.3 (1994), pp. 2019–2022.

[103] Enrico Prati, Rossella Latempa, and Marco Fanciulli. "Microwave-assisted transport in a single-donor silicon quantum dot". In: *Physical Review B - Condensed Matter and Materials Physics* 80.16 (2009), pp. 1–6.

[104] Giorgio Ferrari, Laura Fumagalli, Marco Sampietro, Enrico Prati, and Marco Fanciulli. "DC modulation in field-effect transistors operating under microwave irradiation for quantum readout". In: *Journal of Applied Physics* 98.4 (2005).

[105] Giorgio Ferrari, Laura Fumagalli, Marco Sampietro, Enrico Prati, and Marco Fanciulli. "CMOS fully compatible microwave detector based on MOSFET operating in resistive regime". In: *IEEE Microwave and Wireless Components Letters* 15.7 (2005), pp. 445–447.

[106] Enrico Prati, Marco Fanciulli, Alessandro Calderoni, Giorgio Ferrari, and Marco Sampietro. "Microwave irradiation effects on random telegraph signal in a MOSFET". In: *Physics Letters A* 370.5-6 (2007), pp. 491–493.

[107] Jason W. Sidabras, Richard R. Mett, and James S. Hyde. "Aqueous flat-cells perpendicular to the electric field for use in electron paramagnetic resonance spectroscopy, II: Design". In: *Journal of Magnetic Resonance* 172.2 (2005), pp. 333–341.

[108] Wei Cheng Kong, Guang Wei Deng, Shu Xiao Li, Hai Ou Li, Gang Cao, Ming Xiao, and Guo Ping Guo. "Introduction of DC line structures into a superconducting microwave 3D cavity". In: *Review of Scientific Instruments* 86.2 (2015), pp. –5.

[109] Kunito Fukuda and Naoki Asakawa. "Development of multi-frequency ESR/EDMR system using a rectangular cavity equipped with waveguide window". In: *Review of Scientific Instruments* 87.11 (2016), p. 113106.

[110] S. P. Giblin, M. Kataoka, J. D. Fletcher, P. See, T. J B M Janssen, J. P. Griffiths, G. A C Jones, I. Farrer, and D. A. Ritchie. "Rectification in mesoscopic alternating current-gated semiconductor devices". In: *Journal of Applied Physics* 114.16 (2013).

[111] J P Dehollain, J J Pla, E Siew, K Y Tan, a S Dzurak, and A Morello. "Nanoscale broadband transmission lines for spin qubit control". In: *Nanotechnology* 24.1 (2013), p. 015202.

[112] Susanne Pfenninger, J. Forrer, A. Schweiger, and Th Weiland. "Bridged loop-gap resonator: A resonant structure for pulsed ESR transparent to high-frequency radiation". In: *Review of Scientific Instruments* 59.5 (1988), pp. 752–760.

[113] George A Rinard and Gareth R Eaton. *Loop-Gap Resonators*. 2005, pp. 19–52.

[114] James R. Anderson, Ronald A. Venters, Michael K. Bowman, Anne E. True, and Brian M. Hoffman. "ESR and ENDOR applications of loop-gap resonators with distributed circuit coupling". In: *Journal of Magnetic Resonance (1969)* 65.1 (1985), pp. 165–168.

[115] Mitsuhiro Ono, Tateaki Ogata, Kou-Chang Hsieh, Michiya Suzuki, Ekuo Yoshida, and Hitoshi Kamada. "L-Band ESR spectrometer using a loop-gap resonator for in vivo analysis". In: *Chemistry Letters* C (1986), pp. 491–494.

[116] Mehrdad Mehdizadeh, T. Koryu Ishii, James S. Hyde, and Wojciech Froncisz. "Loop-Gap Resonator: A Lumped Mode Microwave Resonant Structure". In: *IEEE Transactions on Microwave Theory and Techniques* 31.12 (1983), pp. 1059–1064.

[117] G. P. Lansbergen, R. Rahman, C. J. Wellard, I. Woo, J. Caro, N. Collaert, S. Biesemans, G. Klimeck, L. C. L. Hollenberg, and S. Rogge. "Gate-induced quantum-confinement transition of a single dopant atom in a silicon FinFET". In: *Nature Physics* 4.8 (June 2008), pp. 656–661.

[118] G. Kawachi, C. F. O. Graeff, Martin S. Brandt, and M. Stutzmann. "Saturation measurements of electrically detected magnetic resonance amorphous silicon based thin-film transistors in hydrogenated". In: *Japanese Journal of Applied Physics* 36 (1997), pp. 121–125.

[119] H Huebl, R P Starrett, D R McCamey, A J Ferguson, and L. H. Willems Van Beveren. "Electrically detected magnetic resonance using radio-frequency reflectometry". In: *Review of Scientific Instruments* 80.11 (Nov. 2009), p. 114705.

[120] V Lang, C C Lo, R E George, S A Lyon, J Bokor, T Schenkel, A Ardavan, and J J L Morton. "Electrically detected magnetic resonance in a W-band microwave cavity." In: *The Review of scientific instruments* 82.3 (Mar. 2011), p. 034704.

[121] T. Teuschler, M. Hundhausen, L. Ley, and R. Arce. "Analysis of random telegraph noise in large-area amorphous double-barrier structures". In: *Physical Review B* 47.19 (1993), pp. 12687–12695.

[122] Benoit Voisin, Viet-Hung Nguyen, Julien Renard, Xavier Jehl, Sylvain Barraud, François Triozon, Maud Vinet, Ivan Duchemin, Yann-Michel Niquet, Silvano de Franceschi, and Marc Sanquer. "Few-electron edge-state quantum dots in a silicon nanowire field-effect transistor." In: *Nano letters* 14.4 (Apr. 2014), pp. 2094–8.

[123] P. W. Brouwer. "Rectification of displacement currents in an adiabatic electron pump". In: *Physical Review B* 63 (2001), p. 121303.

[124] Wolfgang Voesch, Markus Thiemann, Daniel Bothner, Martin Dressel, and Marc Scheffl. "On-Chip ESR Measurements of DPPH at mK Temperatures". In: *Physics Procedia* 75 (2015), pp. 503–510.

[125] S. Stoll and A. Schweiger. "EasySpin, a comprehensive software package for spectral simulation and analysis in EPR". In: *Journal of Magnetic Resonance* 178.1 (2006), pp. 42–55.

[126] Luca A. Pardi, J. Krzystek, Joshua Telser, and Louis Claude Brunel. "Multifrequency EPR Spectra of Molecular Oxygen in Solid Air". In: *Journal of Magnetic Resonance* 146.2 (2000), pp. 375–378.

[127] Hideo. Kon. "Paramagnetic resonance of molecular oxygen in condensed phases". In: *Journal of the American Chemical Society* 95.4 (1973), pp. 1045–1049.

[128] H. G. Grimmeiss, E. Janzén, and B. Skarstam. "Deep sulfur-related centers in silicon". In: *Journal of Applied Physics* 51.8 (1980), pp. 4212–4217.

[129] H. G. Grimmeiss, E. Janzen, H. Ennen, O. Schirmer, J. Schneider, R. W??rner, C. Holm, E. Sirtl, and P. Wagner. "Tellurium donors in silicon". In: *Physical Review B* 24.8 (1981), pp. 4571–4586.

[130] Yina Mo, Martin Bazant, and Efthimios Kaxiras. "Sulfur point defects in crystalline and amorphous silicon". In: *Physical Review B* 70.20 (2004), pp. 1–10.

[131] C. Wu, C. H. Crouch, L. Zhao, J. E. Carey, R. Younkin, J. A. Levinson, E. Mazur, R. M. Farrell, P. Gothoskar, and A. Karger. "Near-unity below-band-gap absorption by microstructured silicon". In: *Applied Physics Letters* 78.13 (2001), pp. 1850–1852.

[132] C. H. Crouch, J. E. Carey, M. Shen, E. Mazur, and F. Y. Génin. "Infrared absorption by sulfur-doped silicon formed by femtosecond laser irradiation". In: *Applied Physics A: Materials Science and Processing* 79.7 (2004), pp. 1635–1641.

[133] Zhihong Huang, James E. Carey, Mingguo Liu, Xiangyi Guo, Eric Mazur, and Joe C. Campbell. "Microstructured silicon photodetector". In: *Applied Physics Letters* 89.3 (2006), pp. 3–6.

[134] T. G. Kim, Jeffrey M. Warrender, and Michael J. Aziz. "Strong sub-band-gap infrared absorption in silicon supersaturated with sulfur". In: *Applied Physics Letters* 88.24 (2006).

[135] Chun-Hao Li, Ji-Hong Zhao, Xin-Yue Yu, Qi-Dai Chen, Jing Feng, Peide Han, and Hong-Bo Sun. "Sulfur-doped silicon photodiode by ion implantation and femtosecond laser annealing". In: *IEEE Sensors Journal* 17.c (2017), pp. 1–1.

[136] Y. Takamura, S. H. Jain, P. B. Griffin, and J. D. Plummer. "Physical processes associated with the deactivation of dopants in laser annealed silicon". In: *Journal of Applied Physics* 92.1 (2002), pp. 235–244.

[137] M. Tabbal, T. Kim, J. M. Warrender, M. J. Aziz, B. L. Cardozo, and R. S. Goldman. "Formation of single crystal sulfur supersaturated silicon based junctions by pulsed laser melting". In: *Journal of Vacuum Science & Technology B* 25.6 (2007), p. 1847.

[138] Stephanie Simmons. "Silicon-based quantum computation". In: *Proceedings of 2013 International Conference on IC Design & Technology (ICICDT)* (May 2013), pp. 109–114.

[139] Ghania Azzouzi and Wahiba Tazibt. "Improving Silicon Solar Cell Efficiency by Using the Impurity Photovoltaic Effect". In: *Energy Procedia* 41 (2013), pp. 40–49.

[140] Ghania Azzouzi and Mohamed Chegaar. "Impurity photovoltaic effect in silicon solar cell doped with sulphur: A numerical simulation". In: *Physica B: Condensed Matter* 406.9 (2011), pp. 1773–1777.

[141] B.E. Kane. "Silicon-based Quantum Computation". In: *Fortschritte der Physik* 48.9-11 (Sept. 2000), pp. 1023–1041.

[142] G. P. Berman, G. D. Doolen, P. C. Hammel, and V. I. Tsifrinovich. "Magnetic resonance force microscopy quantum computer with tellurium donors in silicon". In: *Physical Review Letters* 86.13 (2001), pp. 2894–2896.

[143] Guido Petretto, Andrea Masse, Marco Fanciulli, and Alberto Debernardi. "Analysis of hyperfine structure in chalcogen-doped silicon and germanium nanowires". In: *Physical Review B - Condensed Matter and Materials Physics* 91.12 (2015), p. 125430.

[144] Roberto Lo Nardo, Gary Wolfowicz, Stephanie Simmons, Alexei M. Tyryshkin, Helge Riemann, Nikolai V. Abrosimov, Peter Becker, Hans Joachim Pohl, Michael Steger, Stephen A. Lyon, Mike L W Thewalt, and John J L Morton. "Spin relaxation and donor-acceptor recombination of Se+ in 28-silicon". In: *Physical Review B - Condensed Matter and Materials Physics* 92.16 (2015), pp. 1–6.

[145] X. Mi, J. V. Cady, D. M. Zajac, P. W. Deelman, and J. R. Petta. "Strong coupling of a single electron in silicon to a microwave photon". In: *Science* 355.6321 (2017), pp. 156–158.

[146] Mika A. Sillanpää, Jae I. Park, and Raymond W. Simmonds. "Coherent quantum state storage and transfer between two phase qubits via a resonant cavity". In: *Nature* 449.7161 (2007), pp. 438–442.

[147] J. Majer, J. M. Chow, J. M. Gambetta, Jens Koch, B. R. Johnson, J. A. Schreier, L. Frunzio, D. I. Schuster, A. A. Houck, A. Wallraff, A. Blais, M. H. Devoret, S. M. Girvin, and R. J. Schoelkopf. "Coupling Superconducting Qubits via a Cavity Bus". In: *Nature* 449.September (2007), pp. 443–447.

[148] D. Karaiskaj, J. A. H. Stotz, T. Meyer, M. L. W. Thewalt, and M. Cardona. "Impurity Absorption Spectroscopy in 28Si: The Importance of Inhomogeneous Isotope Broadening". In: *Physical Review Letters* 90.18 (2003), p. 186402.

[149] M. Steger, A. Yang, M. L W Thewalt, M. Cardona, H. Riemann, N. V. Abrosimov, M. F. Churbanov, A. V. Gusev, A. D. Bulanov, I. D. Kovalev, A. K. Kaliteevskii, O. N. Godisov, P. Becker, H. J. Pohl, J. W. Ager, and E. E. Haller. "Impurity absorption spectroscopy of the deep double donor sulfur in isotopically enriched silicon". In: *Physica B: Condensed Matter* 401-402 (2007), pp. 600–603.

[150] A M Tyryshkin, S A Lyon, A Astashkin, and A Raitsimring. "Electron spin relaxation times of phosphorus donors in silicon". In: *Physical Review B* 68.19 (Nov. 2003), p. 193207.

[151] A. Yang, M. Steger, M. L W Thewalt, M. Cardona, H. Riemann, N. V. Abrosimov, M. F. Churbanov, A. V. Gusev, A. D. Bulanov, I. D. Kovalev, A. K. Kaliteevskii, O. N. Godisov, P. Becker, H. J. Pohl, J. W. Ager, and E. E. Haller. "High resolution photoluminescence of sulphur- and copper-related isoelectronic bound excitons in highly enriched 28Si". In: *Physica B: Condensed Matter* 401-402 (2007), pp. 593–596.

[152] M. Steger, A. Yang, M. L W Thewalt, M. Cardona, H. Riemann, N. V. Abrosimov, M. F. Churbanov, A. V. Gusev, A. D. Bulanov, I. D. Kovalev, A. K. Kaliteevskii, O. N. Godisov, P. Becker, H. J. Pohl, E. E. Haller, and J. W. Ager. "High-resolution absorption spectroscopy of the deep impurities S and Se in 28Si revealing the 77Se hyperfine splitting". In: *Physical Review B - Condensed Matter and Materials Physics* 80.11 (2009), pp. 1–8.

[153] M. L.W. Thewalt. *Personal communications*. 2017.

[154] P. T. Greenland, S. A. Lynch, A. F G Van Der Meer, B. N. Murdin, C. R. Pidgeon, B. Redlich, N. Q. Vinh, and G. Aeppli. "Coherent control of Rydberg states in silicon". In: *Nature* 465.7301 (2010), pp. 1057–1061.

[155] Martin Stutzmann, Martin S. Brandt, and Martin W. Bayerl. "Spin-dependent processes in amorphous and microcrystalline silicon: a survey". In: *Journal of Non-Crystalline Solids* 266-269 (May 2000), pp. 1–22.

[156] M W Bayerl, M S Brandt, and M Stutzmann. "Electrically Detected Magnetic Resonance (EDMR) of Defects in GaN Light Emitting Diodes". In: *Phys. Stat. Sol (A)* 159 (1997), R5–R6.

[157] K. Lips, P. Kanschat, and W. Fuhs. "Defects and recombination in microcrystalline silicon". In: *Solar Energy Materials and Solar Cells* 78.1-4 (July 2003), pp. 513–541.

[158] Martin S. Brandt and Martin Stutzmann. "Spin-dependent conductivity in amorphous hydrogenated silicon". In: *Physical Review B* 43.6 (1991), pp. 5184–5187.

[159] J. Behrends, A. Schnegg, C. Boehme, S. Haas, H. Stiebig, F. Finger, B. Rech, and K. Lips. "Recombination and transport in microcrystalline pin solar cells studied with pulsed electrically detected magnetic resonance". In: *Journal of Non-Crystalline Solids* 354.19 (2008), pp. 2411–2415.

[160] J. Behrends, A. Schnegg, K. Lips, E. A. Thomsen, A. K. Pandey, I. D W Samuel, and D. J. Keeble. "Bipolaron formation in organic solar cells observed by pulsed electrically detected magnetic resonance". In: *Physical Review Letters* 105.17 (2010), pp. 12–15.

[161] Alexander Schnegg, Jan Behrends, Matthias Fehr, and Klaus Lips. "Pulsed electrically detected magnetic resonance for thin film silicon and organic solar cells." In: *Physical chemistry chemical physics : PCCP* 14.42 (2012), pp. 14418–38.

[162] Dali Sun, Kipp J. van Schooten, Marzieh Kavand, Hans Malissa, Chuang Zhang, Matthew Groesbeck, Christoph Boehme, and Z. Valy Vardeny. "Inverse spin Hall effect from pulsed spin current in organic semiconductors with tunable spin–orbit coupling". In: *Nature Materials* 15.8 (2016), pp. 863–869.

[163] M. S. Brandt, S. T. B. Goennenwein, T. Graf, H. Huebl, S. Lauterbach, and M. Stutzmann. "Spin-dependent transport in elemental and compound semiconductors and nanostructures". In: *Physica Status Solidi (C)* 1.8 (July 2004), pp. 2056–2093.

[164] K P Homewood, B C Cavenett, W E Spear, and P G LeComber. "Spin effects in p+-i-n+ a-Si:H cells - photovoltaic detected magnetic resonance (PDMR)". In: *J. Phys. C: Solid State Phys.* 16 (1983), pp. L427–L431.

[165] C. Boehme, F. Friedrich, T. Ehara, and K. Lips. "Recombination at silicon dangling bonds". In: *Thin Solid Films* 487.1-2 (2005), pp. 132–136.

[166] D R McCamey, J Van Tol, G W Morley, and C Boehme. "Electronic spin storage in an electrically readable nuclear spin memory with a lifetime >100 seconds." In: *Science (New York, N.Y.)* 330.6011 (Dec. 2010), pp. 1652–6.

[167] David P. Franke, Moritz P D Pflüger, Pierre André Mortemousque, Kohei M. Itoh, and Martin S. Brandt. "Quadrupolar effects on nuclear spins of neutral arsenic donors in silicon". In: *Physical Review B - Condensed Matter and Materials Physics* 93.16 (2016), pp. 1–5.

[168] David P. Franke, Michael Szech, Florian M. Hrubesch, Helge Riemann, Nikolai V. Abrosimov, Peter Becker, Hans Joachim Pohl, Kohei M. Itoh, Michael L.W. Thewalt, and Martin S. Brandt. "Electron nuclear double resonance with donor-bound excitons in silicon". In: *Physical Review B* 235201.23 (2016), pp. 1–6.

[169] T Schenkel, J A Liddle, A Persaud, A M Tyryshkin, S A Lyon, R de Sousa, K B Whaley, J Bokor, J Shangkuan, and I. Chakarov. "Electrical activation and electron spin coherence of ultralow dose antimony implants in silicon". In: *Applied Physics Letters* 88.11 (2006), p. 112101.

[170] Rogerio De Sousa. "Dangling-bond spin relaxation and magnetic 1/f noise from the amorphous-semiconductor/oxide interface: Theory". In: *Physical Review B - Condensed Matter and Materials Physics* 76.24 (2007), pp. 1–15.

[171] G W Morley, D R McCamey, H A Seipel, L -C Brunel, J van Tol, and C Boehme. "Long-Lived Spin Coherence in Silicon with an Electrical Spin Trap Readout". In: *Physical Review Letters* 101.20 (Nov. 2008), p. 207602.

[172] S.-Y. Paik, S.-Y. Lee, W. J. Baker, D. R. McCamey, and C. Boehme. "T1 and T2 spin relaxation time limitations of phosphorous donor electrons near crystalline silicon to silicon dioxide interface defects". In: *Physical Review B* 81.7 (Feb. 2010), p. 075214.

[173] Peter Scherpelz and Giulia Galli. "Optimizing surface defects for atomic-scale electronics: Si dangling bonds". In: *Physical Review Materials* 1 (2017), pp. 1–7.

[174] S. D. Brotherton, M. J. King, and G. J. Parker. "The electrical properties of sulphur in silicon". In: *Journal of Applied Physics* 52.7 (1981), pp. 4649–4658.

[175] E. Janzén, R. Stedman, G. Grossman, and H. G. Grimmeiss. "High-resolution studies of sulfur- and selenium-related donor centers in silicon". In: *Physical Review B* 29.4 (1984), pp. 1907–1918.

[176] S M Sze. *Physics of Semiconductor Devices*. Second. New York: John Wiley & Sons, 1981, p. 849.

[177] Bernard Pajot, Gunter Grossmann, Maurice Astier, and Claude Naud. "Highly Excited States of Donor Centres in Silicon". In: *Solid State Communications* 54.l (1985), pp. 57–60.

[178] David P. Franke. *Personal communications*. 2016.

[179] M Kleverman, H G Grimmeiss, A Litwin, and E Janzén. "Capture processes at double donors in silicon". In: *Physical Review B* 31.6 (1985), pp. 3659–3666.

[180] Håkan Pettersson. *Studies on deep electronic level in silicon and aluminium gallium arsenide alloys*. Lund: Department of Solid State Physics, Lund University, Sweden, 1993.

[181] P Auger. "Sur les rayons β secondaires produits dans un gaz par des rayons X". In: *C.R.A.S.* 177 (1923), pp. 169–171.

[182] G. W. Ludwig. "Paranagnetic Resonance Study of a Deep Donor in Silicon". In: *Physical Review* 137.5A (1965), A1520–A1530.

[183] I. S. Zevenbergen, T. Gregorkiewicz, and C. A J Ammerlaan. "Electron-paramagnetic-resonance identification of hydrogen-passivated sulfur centers in silicon". In: *Physical Review B* 51.23 (1995), pp. 16746–16749.

[184] A.B. van Oosten and C.A.J. Ammerlaan. "Sulfur pair in silicon: 33S electron-nuclear double resonance". In: *Physical Review B* 38.18 (1988), pp. 13291–13296.

[185] John J. L. Morton. *Personal communications*. 2017.

[186] P J Dean. "Inter-impurity recombinations in semiconductors". In: *Progress in Solid State Chemistry* 8.C (1973), pp. 1–126.

[187] P. Dirksen, A. Henstra, and W. T. Wenckebach. "An electron spin echo study of donor-acceptor recombination". In: *Journal of Physics: Condensed Matter* 1.39 (1989), pp. 7085–7092.

[188] CMR-Direct. *4-way female connector - for cryogenic use*. 2017.

[189] Hans Huebl. *Personal communications*. 2014.

[190] M L W Thewalt, U O Ziemells, and R R Parsons. "Enhancement of long lifetime lines in photoluminescence from Si:In". In: *Solid State Communications* 39.1 (1981), pp. 27–30.

[191] T. G. Brown and D. G. Hall. "Optical emission at 1.32 um from sulfur-doped crystalline silicon". In: *Applied Physics Letters* 49.5 (1986), pp. 245–247.

[192] Almath. *CC12 - ALUMINA CYLINDRICAL CRUCIBLE 0.85ML diameter 12MM X I/D9.5MM X 18MM HIGH*. 2016.

[193] S M Sze. *Semiconductor Devices: Physics and Technology*. 2nd. John Wiley & Sons, 2001, p. 568.

[194] C Hu. "Chapter 9 Metal-Semiconductor Contacts". In: *University of Berkeley* (2006), pp. 1–19.

[195] Utah Brigham Young University, Provo. *Diffused Ion Implantation Profile Calculator and Graph*. 2017.

[196] Guildford Surrey Ion Beam Centre University of Surrey. *SUSPRE*. 2017.

[197] F. A. Trumbore. "Solid solubilties of impurity elements in germanium and silicon". In: *Bell System Technical Journal* 39 (1960), pp. 205–233.

[198] C. S. Fuller and J. A. Ditzenberger. "Diffusion of donor and acceptor elements in silicon". In: *Journal of Applied Physics* 27.5 (1956), pp. 544–553.

[199] R. N. Ghoshtagore. "Intrinsic diffusion of boron and phosphorus in silicon free from surface effects". In: *Physical Review B* 3.2 (1971), pp. 389–396.

[200] R. N. Ghoshtagore. "Donor diffusion dynamics in silicon". In: *Physical Review B* 3.2 (1971), pp. 397–403.

[201] Cheuk Chi Lo, Arun Persaud, Scott Dhuey, Deirdre Olynick, Ferenc Borondics, Michael C Martin, Hans a Bechtel, Jeffrey Bokor, and Thomas Schenkel. "Device fabrication and transport measurements of FinFETs built with 28 Si SOI wafers toward donor qubits in silicon". In: *Semiconductor Science and Technology* 24.10 (Oct. 2009), p. 105022.

[202] Naoki Kishimoto and Kazuo Morigaki. "Resistivity Decrease Due to Electron Spin Resonance in the Metallic Region of Heavily Phosphorus-Doped Silicon". In: *Journal of the Physical Society of Japan* 42.1 (1977), pp. 137–145.

[203] B Van Zeghbroeck. *Chapter 3: Metal-Semicond. Junctions*. 2011.

[204] ECE Illinois. *Theory and Fabrication of Integrated Circuits*. 2017.

[205] OxfordNanoSIMSGroup. *NanoSIMS Department of Materials*. 2018.

[206] D R McCamey, J van Tol, G W Morley, and C Boehme. "Fast Nuclear Spin Hyperpolarization of Phosphorus in Silicon". In: *Physical Review Letters* 102.2 (Jan. 2009), p. 027601.

[207] F.M. Hrubesch, G. Braunbeck, a. Voss, M. Stutzmann, and M.S. Brandt. "Broadband electrically detected magnetic resonance using adiabatic pulses". In: *Journal of Magnetic Resonance* 254 (2015), pp. 62–69.

[208] S. O. Kasap. *Principles of Electronic Materials and Devices*. 3rd. McGraw-Hill Education, 2007.

[209] A. J. Szadkowski, A. Kalnitsky, K. B. Ma, and S. Zukotynski. "Implications of the change in work function of chromium by the presence of hydrogen on the properties of electrical contact between chromium and hydrogenated amorphous silicon". In: *Journal of Applied Physics* 53.1 (1982), pp. 557–558.

[210] J P Ponpon and B Bourdon. "OXIDATION OF GLOW DISCHARGE a-Si : H". In: *Solid-State Electronics* 25.9 (1982), pp. 875–876.

[211] X. Zhang, E. Garfunkel, Y. J. Chabal, S. B. Christman, and E. E. Chaban. "Stability of HF-etched Si(100) surfaces in oxygen ambient". In: *Applied Physics Letters* 79.24 (2001), pp. 4051–4053.

[212] G Katsaros, P Spathis, M Stoffel, F Fournel, M Mongillo, V Bouchiat, F Lefloch, a Rastelli, O G Schmidt, and S De Franceschi. "Hybrid superconductor-semiconductor devices made from self-assembled SiGe nanocrystals on silicon." In: *Nature nanotechnology* 5.6 (2010), pp. 458–464.

[213] David M. Pozar. *Microwave Engineering*. 3rd. Danvers: John Wiley & Sons, 2005.

[214] D R McCamey. "Spin and Charge Properties of Si:P Probed using Ion-Implanted Nanostructures". PhD thesis. 2007, pp. 1–202.

[215] M. Vaněček, A. Poruba, Z. Remeš, N. Beck, and M. Nesládek. "Optical properties of microcrystalline materials". In: *Journal of Non-Crystalline Solids* 227-230 (1998), pp. 967–972.

[216] Martin A. Green. *Solar Cells: Operating principles, technology and System Applications*. Ed. by Holonyak. Englewood Cliffs: Prentice-Hall, 1982.

[217] Shiyang Tian, Michael F. Morris, Steven J. Morris, Borna Obradovic, Geng Wang, Al F. Tasch, and Charles M. Snell. "A detailed physical model for ion implant induced damage in silicon". In: *IEEE Transactions on Electron Devices* 45.6 (1998), pp. 1226–1238.

[218] F. F. Morehead Jr. and B. L. Crowder. "A model for the formation of amorphous Si by ion bombardment". In: *Radiation Effects* 6.June (1970), pp. 27–32.

[219] Seiichi Hasegawa, Ryozo Kontani, and Tatsuo Shimizu. "Related content ESR Studies on P + Ion-Implanted Si". In: *Japanese Journal of Applied Physics* 10 (1971), p. 655.

[220] B. L. Crowder, R. S. Title, M. H. Brodsky, and G. D. Pettit. "ESR and optical absorption studies of ion-implanted silicon". In: *Applied Physics Letters* 16.5 (1970), pp. 205–208.

[221] M. H. Brodsky and R. S. Title. "Electron spin resonance in amorphous silicon, germanium, and silicon carbide". In: *Physical Review Letters* 23.11 (1969), pp. 581–585.

[222] M. Fujinami and N. B. Chilton. "Ion implantation induced defects in SiO2: The applicability of the positron probe". In: *Applied Physics Letters* 62.10 (1993), pp. 1131–1133.

[223] K. L. Brower and Wendland Beezhold. "Electron paramagnetic resonance of the lattice damage in oxygen-implanted silicon". In: *Journal of Applied Physics* 43.8 (1972), pp. 3499–3506.

[224] C. D. Weis, C. C. Lo, V. Lang, A. M. Tyryshkin, R. E. George, K. M. Yu, J. Bokor, S. A. Lyon, J. J.L. Morton, and T. Schenkel. "Electrical activation and electron spin resonance measurements of implanted bismuth in isotopically enriched silicon-28". In: *Applied Physics Letters* 100.17 (2012).

[225] B. L. Crowder and F. F. Morehead. "Annealing characteristics of n-type dopants in ion-implanted silicon". In: *Applied Physics Letters* 14.10 (1969), pp. 313–315.

[226] F. F. Morehead, B. L. Crowder, and R. S. Title. "Formation of amorphous silicon by ion bombardment as a function of ion, temperature, and dose". In: *Journal of Applied Physics* 43.3 (1972), pp. 1112–1118.

[227] Friedhelm Finger, Luciano Baia Neto, Reinhard Carius, Thorsten Dylla, and Stefan Klein. "Paramagnetic defects in undoped microcrystalline silicon". In: *physica status solidi (c)* 1.5 (2004), pp. 1248–1254.

[228] A. Stesmans and V. V. Afanas'ev. "Electron spin resonance features of interface defects in thermal (100)Si/SiO[sub 2]". In: *Journal of Applied Physics* 83.5 (1998), p. 2449.

[229] Volker Lang. "Electrically detected magnetic resonance in semiconductor and carbon nanodevices". PhD thesis. 2012, p. 204.

[230] Seo-Young Paik. "Study of spin-dependent transitions and coherence at the (111) oriented phosphorus doped crystalline silicon to silicon dioxide interface using pulsed electrically detected magnetic resonance". PhD thesis. 2011.

[231] J. L. Allain, J. R. Regnard, A Bourret, A Parisini, A Armigliato, G. Tourillon, and S. Pizzini. "Extended x-ray-absorption fine-structure study of the local atomic structure in As+ heavily implanted silicon". In: *Physical Review B* 46.15 (1992), pp. 9434–9445.

[232] G. Feher. "Electron spin resonance experiments on donors in silicon. I. Electronic structure of donors by the electron nuclear double resonance technique". In: *Physical Review* 114.5 (1959), pp. 1219–1244.

[233] B. M. George, J. Behrends, A. Schnegg, T. F. Schulze, M. Fehr, L. Korte, B. Rech, K. Lips, M. Rohrmüller, E. Rauls, W. G. Schmidt, and U. Gerstmann. "Atomic Structure of Interface States in Silicon Heterojunction Solar Cells". In: *Phys. Rev. Lett.* 110 (13 Mar. 2013), p. 136803.

[234] Philip J Caplan, Edward H Poindexter, Bruce E Deal, and Reda R Razouk. "ESR centers , interface states , and oxide fixed charge in thermally oxidized silicon wafers ESR centers , interface states , and oxide fixed charge in thermally oxidized silicon wafers". In: *Journal of Applied Physics* 50.9 (1979), pp. 5847–5854.

[235] Edward H Poindexter, Philip J Caplan, Bruce E Deal, and Reda R Razouk. "Interface states and electron spin resonance centers in thermally oxidized (111) and (100) silicon wafers". In: *Applied Physics Letters* 52.2 (1981), pp. 879–884.

[236] E. H. Poindexter, G. J. Gerardi, M.-E. Rueckel, P. J. Caplan, N. M. Johnson, and D. K. Biegelsen. "Electronic traps and Pb centers at the Si/SiO$_2$ interface: band-gap energy distribution". In: *Journal of Applied Physics* 56.10 (1984), p. 2844.

[237] P. M. Lenahan and P. V. Dressendorfer. "Hole traps and trivalent silicon centers in metal/oxide/silicon devices". In: *Journal of Applied Physics* 55.10 (1984), p. 3495.

[238] H. R. Huff, U. Gosele, and H. Tsuya. "Semiconductor Silicon". In: ed. by Electrochemical Society. Electrochemical Society, 1998, p. 949.

[239] G. Feher, J. C. Hensel, and E. A. Gere. "Paramagnetic resonance absorption from acceptors in silicon". In: *Physical Review Letters* 5.7 (1960), pp. 309–311.

[240] A. Mokhberi, P.B. Griffin, J.D. Plummer, E. Paton, S. McCoy, and K. Elliott. "A comparative study of dopant activation in boron, BF2, arsenic, and phosphorus implanted silicon". In: *IEEE Transactions on Electron Devices* 49.7 (2002), pp. 1183–1191.

[241] Christoph Meier, Jan Behrends, Christian Teutloff, Oleksandr Astakhov, Alexander Schnegg, Klaus Lips, and Robert Bittl. "Multi-frequency EDMR applied to microcrystalline thin-film silicon solar cells". In: *Journal of Magnetic Resonance* 234 (2013), pp. 1–9.

[242] Andre Rainer Stegner. "Shallow dopants in nanostructured and in isotopically engineered silicon". PhD thesis. Technische Universität München, 2010, p. 185.

[243] Christoph Boehme and Klaus Lips. "Time domain measurement of spin-dependent recombination". In: *Applied Physics Letters* 79.26 (2001), pp. 4363–4365.

[244] G. Joshi, R. Miller, L. Ogden, M. Kavand, S. Jamali, K. Ambal, S. Venkatesh, D. Schurig, H. Malissa, J. M. Lupton, and C. Boehme. "Separating hyperfine from spin-orbit interactions in organic semiconductors by multi-octave magnetic resonance using coplanar waveguide microresonators". In: *Applied Physics Letters* 109.10 (2016).

[245] M Steger, K Saeedi, M L W Thewalt, J J L Morton, H Riemann, N V Abrosimov, P Becker, and H-J Pohl. "Quantum information storage for over 180 s using donor spins in a 28Si "semiconductor vacuum"." In: *Science (New York, N.Y.)* 336.6086 (June 2012), pp. 1280–3.

[246] C C Lo, M Urdampilleta, P Ross, M F Gonzalez-Zalba, J Mansir, S A Lyon, M L W Thewalt, and J J L Morton. "Hybrid optical–electrical detection of donor electron spins with bound excitons in silicon". In: *Nature materials* 14.May (2015), pp. 1–5.

[247] A. Yang, M. Steger, D. Karaiskaj, M. L W Thewalt, M. Cardona, K. M. Itoh, H. Riemann, N. V. Abrosimov, M. F. Churbanov, A. V. Gusev, A. D. Bulanov, A. K. Kaliteevskii, O. N. Godisov, P. Becker, H. J. Pohl, J. W. Ager, and E. E. Haller. "Optical detection and ionization of donors in specific electronic and nuclear spin states". In: *Physical Review Letters* 97.22 (2006), pp. 1–4.

[248] Femto. *Variable gain low noise current amplifier DLPCA-200*. 2017.

[249] D. K. Wilson and G. Feher. "Electron spin resonance experiments on donors in silicon. III. investigation of excited states by the application of uniaxial stress and their importance in relaxation processes". In: *Physical Review* 124.4 (1961), pp. 1068–1083.

[250] C. Gemperle, G. Aebli, A. Schweiger, and R. R. Ernst. "Phase cycling in pulse EPR". In: *Journal of Magnetic Resonance (1969)* 88.2 (1990), pp. 241–256.

[251] EL Hahn. "Spin echoes". In: *Physical Review* 297.1946 (1950).

[252] D. R. McCamey, C. Boehme, G. W. Morley, and J. van Tol. "Electrically detected spin echoes of donor nuclei in silicon". In: *Physical Review B* 85.7 (Feb. 2012), p. 073201.

[253] Ralph T. Weber. *Pulsed EPR Primer*. 2000.

[254] V. Rajevac, C. Boehme, C. Michel, A. Gliesche, K. Lips, S. D. Baranovskii, and P. Thomas. "Transport and recombination through weakly coupled localized spin pairs in semiconductors during coherent spin excitation". In: *Physical Review B - Condensed Matter and Materials Physics* 74.24 (2006), pp. 1–5.

[255] Kamyar Saeedi, Stephanie Simmons, Jeff Z Salvail, Phillip Dluhy, Helge Riemann, Nikolai V Abrosimov, Peter Becker, Hans-Joachim Pohl, John J L Morton, and Mike L W Thewalt. "Room-temperature quantum bit storage exceeding 39 minutes using ionized donors in silicon-28." In: *Science (New York, N.Y.)* 342.6160 (Nov. 2013), pp. 830–3.

[256] W. M. Witzel, Rogerio De Sousa, and S. Das Sarma. "Quantum theory of spectral-diffusion-induced electron spin decoherence". In: *Physical Review B - Condensed Matter and Materials Physics* 72.16 (2005), pp. 1–4.

[257] Wen Yang and Ren-Bao Liu. "Quantum many-body theory of qubit decoherence in a finite-size spin bath". In: *Phys. Rev. B* 78 (8 Aug. 2008), p. 085315.

[258] Eisuke Abe, Alexei M. Tyryshkin, Shinichi Tojo, John J.L. Morton, Wayne M. Witzel, Akira Fujimoto, Joel W. Ager, Eugene E. Haller, Junichi Isoya, Stephen A. Lyon, Mike L.W. Thewalt, and Kohei M. Itoh. "Electron spin coherence of phosphorus donors in silicon: Effect of environmental nuclei". In: *Physical Review B - Condensed Matter and Materials Physics* 82.12 (2010), pp. 9–12.

[259] Alexei M Tyryshkin, Shinichi Tojo, John J L Morton, Helge Riemann, Nikolai V Abrosimov, Peter Becker, Hans-Joachim Pohl, Thomas Schenkel, Michael L W Thewalt, Kohei M Itoh, and S A Lyon. "Electron spin coherence exceeding seconds in high-purity silicon." In: *Nature materials* 11.2 (Feb. 2012), pp. 143–7.

[260] JP Gordon and KD Bowers. "Microwave spin echoes from donor electrons in silicon". In: *Physical Review Letters* 1 (1958), pp. 368–371.

[261] H. Y. Carr and E. M. Purcell. "Effects of diffusion on free precession in nuclear magnetic resonance experiments". In: *Physical Review* 94.3 (1954), pp. 630–638.

[262] S. Meiboom and D. Gill. "Modified Spin-Echo Method for Measuring Nuclear Relaxation Times". In: *Review of Scientific Instruments* 29.8 (1958), pp. 688–691.

[263] John J L Morton. "Diamond wedding for spin couple". In: *Nature* 2.June (2006), pp. 365–366.

[264] K. M. Salikhov, S. A. Dzuba, and A. M. Raitsimring. "The theory of electron spin-echo signal decay resulting from dipole-dipole interactions between paramagnetic centers in solids". In: *Journal of Magnetic Resonance (1969)* 42.2 (1981), pp. 255–276.

[265] P. P. Sorokin, G. J. Lasher, and I. L. Gelles. "Cross relaxation studies in diamond". In: *Physical Review* 118.4 (1960), pp. 939–945.

[266] K. D. Bowers and W. B. Mims. "Paramagnetic relaxation in nickel fluosilicate". In: *Physical Review* 115.2 (1959), pp. 285–295.

[267] T Schenkel, C C Lo, C D Weis, J Bokor, A M Tyryshkin, and S A Lyon. "A spin quantum bit architecture with coupled donors and quantum dots in silicon". In: *ArXiv* arXiv:1110 (2011), pp. 1–16.

[268] Juha T Muhonen, Juan P Dehollain, Arne Laucht, Fay E Hudson, Rachpon Kalra, Takeharu Sekiguchi, Kohei M Itoh, David N Jamieson, Jeffrey C McCallum, Andrew S Dzurak, and Andrea Morello. "Storing quantum information for 30 seconds in a nanoelectronic device." In: *Nature nanotechnology* October (Oct. 2014), pp. 1–6.

[269] S. Schofield, N. Curson, M. Simmons, F. Rueß, T. Hallam, L. Oberbeck, and R. Clark. "Atomically Precise Placement of Single Dopants in Si". In: *Physical Review Letters* 91.13 (Sept. 2003), p. 136104.

[270] Martin Fuechsle, Jill A Miwa, Suddhasatta Mahapatra, Hoon Ryu, Sunhee Lee, Oliver Warschkow, Lloyd C L Hollenberg, Gerhard Klimeck, and Michelle Y Simmons. "A single-atom transistor". In: *Nature nanotechnology* 7.4 (Apr. 2012), pp. 242–6.

[271] Michael M Lee, Joël Teuscher, Tsutomu Miyasaka, Takurou N Murakami, and Henry J Snaith. "Efficient hybrid solar cells based on meso-superstructured organometal halide perovskites." In: *Science (New York, N.Y.)* 338.6107 (2012), pp. 643–7.

[272] Akihiro Kojima, Kenjiro Teshima, Yasuo Shirai, and Tsutomu Miyasaka. "Organometal halide perovskites as visible-light sensitizers for photovoltaic cells". In: *Journal of the American Chemical Society* 131.17 (2009), pp. 6050–6051.

[273] Juan-Pablo Correa-Baena, Michael Saliba, Tonio Buonassisi, Michael Grätzel, Antonio Abate, Wolfgang Tress, and Anders Hagfeldt. "Promises and challenges of perovskite solar cells". In: *Science* 358.6364 (2017), pp. 739–744.

[274] Mingzhen Liu, Michael B Johnston, and Henry J Snaith. "Efficient planar heterojunction perovskite solar cells by vapour deposition." In: *Nature* 501.7467 (2013), pp. 395–8.

[275] Mengjin Yang, Yuanyuan Zhou, Yining Zeng, Chun-Sheng Jiang, Nitin P. Padture, and Kai Zhu. "Square-Centimeter Solution-Processed Planar CH3NH3PbI3 Perovskite Solar Cells with Efficiency Exceeding 15%". In: *Advanced Materials* 27.41 (), pp. 6363–6370.

[276] Martin A. Green, Keith Emery, Yoshihiro Hishikawa, Wilhelm Warta, Ewan D. Dunlop, Dean H. Levi, and Anita W. Y. Ho-Baillie. "Solar cell efficiency tables (version 49)". In: *Prog. Photovolt: Res. Appl.* 25.February 2013 (2017), pp. 659–676.

[277] Martin A. Green, Anita Ho-Baillie, and Henry J. Snaith. "The emergence of perovskite solar cells". In: *Nature Photonics* 8.7 (2014), pp. 506–514.

[278] D. B. Mitzi, K. Chondroudis, and C. R. Kagan. "Organic-inorganic electronics". In: *IBM Journal of Research and Development* 45.1 (2001), pp. 29–45.

[279] Xin Yu Chin, Daniele Cortecchia, Jun Yin, Annalisa Bruno, and Cesare Soci. "Lead iodide perovskite light-emitting field-effect transistor". In: *Nature Communications* 6.May (2015), pp. 1–5.

[280] Mohammad Khaja Nazeeruddin and Henry Snaith. "Methylammonium lead triiodide perovskite solar cells: A new paradigm in photovoltaics". In: *MRS Bulletin* 40.08 (2015), pp. 641–645.

[281] Zhi-kuang Tan, Reza Saberi Moghaddam, May Ling Lai, Pablo Docampo, Ruben Higler, Felix Deschler, Michael Price, Aditya Sadhanala, Luis M Pazos, Dan Credgington, Fabian Hanusch, Thomas Bein, Henry J Snaith, and Richard H Friend. "Bright light-emitting diodes based on organometal halide perovskite". In: *Nature Nanotechnology* 9.9 (2014), pp. 687–692.

[282] Shenghao Wang, Yan Jiang, Emilio J. Juarez-Perez, Luis K. Ono, and Yabing Qi. "Accelerated degradation of methylammonium lead iodide perovskites induced by exposure to iodine vapour". In: *Nature Energy* 2.1 (2016), p. 16195.

[283] Zhengguo Xiao, Ross A. Kerner, Lianfeng Zhao, Nhu L. Tran, Kyung Min Lee, Tae-Wook Koh, Gregory D. Scholes, and Barry P. Rand. "Efficient perovskite light-emitting diodes featuring nanometre-sized crystallites". In: *Nature Photonics* 11.2 (2017), pp. 108–115.

[284] William Shockley and Hans J. Queisser. "Detailed balance limit of efficiency of p-n junction solar cells". In: *Journal of Applied Physics* 32.3 (1961), pp. 510–519.

[285] Akshay Rao, Philip C Y Chow, Simon Gélinas, Cody W Schlenker, Chang-Zhi Li, Hin-Lap Yip, Alex K-Y Jen, David S Ginger, and Richard H Friend. "The role of spin in the kinetic control of recombination in organic photovoltaics." In: *Nature* 500.7463 (2013), pp. 435–9.

[286] M Hirasawa, T Ishihara, T Goto, K Uchida, and N Miura. "Magnetoabsorption of the lowest exciton in perovskite-type compound (CH3NH3)PbI3". In: *Physica B* 201 (1994), pp. 427–430.

[287] Wei Geng, Chuan-Jia Tong, Jiang Liu, Wenjun Zhu, Woon-Ming Lau, and Li-Min Liu. "Structures and Electronic Properties of Different CH3NH3PbI3/TiO2 Interface: A First-Principles Study". In: *Scientific Reports* 6.1 (2016), p. 20131.

[288] Yiteng Zhang, Sangchul Oh, Fahhad H. Alharbi, Gregory S. Engel, and Sabre Kais. "Delocalized quantum states enhance photocell efficiency". In: *Phys. Chem. Chem. Phys.* 17.8 (2015), pp. 5743–5750.

[289] Toyoharu Hirota. "Trapped hole center at a Pb++ Vacancy in gamma-Irradiated PbCl2 Crystals". In: *Journal of the Physical Society of Japan* 79.4 (2010), pp. 2–7.

[290] A.V. Patankar and E.E. Schneider. "Electron spin resonance of colour centres in γ-irradiated planar lead halides". In: *Journal of Physics and Chemistry of Solids* 27.3 (1966), pp. 575–579.

[291] W. C. De Gruijter and J. Kerssen. "Luminescence of PbCl2 and PbBr2 single crystals II. Luminescence and EPR of uv irradiated crystals". In: *Journal of Solid State Chemistry* 5.3 (1972), pp. 467–476.

[292] J. Kerssen, W. C. De Gruijter, and J. Volger. "EPR of Pb+ ions and exchange-coupled Pb+ ion pairs in U.V.-irradiated PbCl2 and PbBr2 crystals". In: *Physica* 70.2 (1973), pp. 375–396.

[293] P. G. Baranov and J. Rosa. "The origin of the EPR of U.V. irradiated PbCl2 single crystals". In: *Solid State Communications* 74.7 (1990), pp. 647–648.

[294] I. Heynderickx, E. Goovaerts, and D. Schoemaker. "Electron-spin-resonance study of Pb2 3+ dimer centers in NaCl:PbCl2". In: *Physical Review B* 36.4 (1987), pp. 1843–1852.

[295] S. V. Nistor, E. Goovaerts, and D. Schoemaker. "Direct observation of electron self-trapping in PbCl2 crystals". In: *Physical Review B* 48.13 (1993), pp. 9575–9580.

[296] Guangda Niu, Xudong Guo, and Liduo Wang. "Review of recent progress in chemical stability of perovskite solar cells". In: *J. Mater. Chem. A* 3.17 (2015), pp. 8970–8980.

[297] Taame Abraha Berhe, Wei-Nien Su, Ching-Hsiang Chen, Chun-Jern Pan, Ju-Hsiang Cheng, Hung-Ming Chen, Meng-Che Tsai, Liang-Yih Chen, Amare Aregahegn Dubale, and Bing-Joe Hwang. "Organometal halide perovskite solar cells: degradation and stability". In: *Energy Environ. Sci.* 9.2 (2016), pp. 323–356.

[298] Xiong Li, M. Ibrahim Dar, Chenyi Yi, Jingshan Luo, Manuel Tschumi, Shaik M. Zakeeruddin, Mohammad Khaja Nazeeruddin, Hongwei Han, and Michael Grätzel. "Improved performance and stability of perovskite solar cells by crystal crosslinking with alkylphosphonic acid ω-ammonium chlorides". In: *Nature Chemistry* 7.9 (2015), pp. 703–711.

[299] Namyoung Ahn, Kwisung Kwak, Min Seok Jang, Heetae Yoon, Byung Yang Lee, Jong-Kwon Lee, Peter V. Pikhitsa, Junseop Byun, and Mansoo Choi. "Trapped charge-driven degradation of perovskite solar cells". In: *Nature Communications* 7.May (2016), p. 13422.

[300] Zhengguo Xiao, Yongbo Yuan, Yuchuan Shao, Qi Wang, Qingfeng Dong, Cheng Bi, Pankaj Sharma, Alexei Gruverman, and Jinsong Huang. "Giant switchable photovoltaic effect in organometal trihalide perovskite devices". In: *Nature Materials* 14.2 (2014), pp. 193–198.

[301] Tomas Leijtens, Giles E. Eperon, Nakita K. Noel, Severin N. Habisreutinger, Annamaria Petrozza, and Henry J. Snaith. "Stability of Metal Halide Perovskite Solar Cells". In: *Advanced Energy Materials* (2015), n/a–n/a.

[302] Sang-Won Lee, Seongtak Kim, Soohyun Bae, Kyungjin Cho, Taewon Chung, Laura E. Mundt, Seunghun Lee, Sungeun Park, Hyomin Park, Martin C. Schubert, Stefan W. Glunz, Yohan Ko, Yongseok Jun, Yoonmook Kang, Hae-Seok Lee, and Donghwan Kim. "UV Degradation and Recovery of Perovskite Solar Cells". In: *Scientific Reports* 6.December (2016), p. 38150.

[303] Wenzhe Li, Wei Zhang, Stephan Van Reenen, Rebecca J Sutton, Jiandong Fan, Amir Haghighirad, Michael Johnston, Liduo Wang, and Henry Snaith. "Enhanced UV-light Stability of Planar Heterojunction Perovskite Solar Cells with Caesium Bromide Interface Modification". In: *Energy Environ. Sci.* 9 (2016), pp. 490–498.

[304] Tomas Leijtens, Giles E Eperon, Sandeep Pathak, Antonio Abate, Michael M Lee, and Henry J Snaith. "Overcoming ultraviolet light instability of sensitized TiO2 with meso-superstructured organometal tri-halide perovskite solar cells". In: *Nature Communications* 4 (2013), pp. 28885.1–8.

[305] Duyen H. Cao, Constantinos C. Stoumpos, Christos D. Malliakas, Michael J. Katz, Omar K. Farha, Joseph T. Hupp, and Mercouri G. Kanatzidis. "Remnant PbI2, an unforeseen necessity in high-efficiency hybrid perovskite-based solar cells?" In: *APL Materials* 2.9 (2014), pp. 1–8.

[306] Wan-Jian Yin, Tingting Shi, and Yanfa. Yan. "Unusual defect physics in CH3NH3PbI3 perovskite solar cell absorber." In: *Applied Physics Letters* 104.6 (2014), pp. 063903/1–063903/4.

[307] Xiaoming Wen, Yu Feng, Shujuan Huang, Fuzhi Huang, Yi-Bing Cheng, Martin Green, and Anita Ho-Baillie. "Defect trapping states and charge carrier recombination in organic–inorganic halide perovskites". In: *J. Mater. Chem. C* 4.4 (2016), pp. 793–800.

[308] G. Xing, N. Mathews, S. Sun, S. S. Lim, Y. M. Lam, M. Gratzel, S. Mhaisalkar, and T. C. Sum. "Long-Range Balanced Electron- and Hole-Transport Lengths in Organic-Inorganic CH3NH3PbI3". In: *Science* 342.6156 (2013), pp. 344–347.

[309] D. Shi, V. Adinolfi, R. Comin, M. Yuan, E. Alarousu, A. Buin, Y. Chen, S. Hoogland, A. Rothenberger, K. Katsiev, Y. Losovyj, X. Zhang, P. A. Dowben, O. F. Mohammed, E. H. Sargent, and O. M. Bakr. "Low trap-state density and long carrier diffusion in organolead trihalide perovskite single crystals". In: *Science* 347.6221 (2015), pp. 519–522.

[310] Eran Edri, Saar Kirmayer, Sabyasachi Mukhopadhyay, Konstantin Gartsman, Gary Hodes, and David Cahen. "Elucidating the charge carrier separation and working mechanism of CH3NH3PbI3 - xClx perovskite solar cells". In: *Nature Communications* 5 (2014), pp. 1–8.

[311] Aron Walsh, David O. Scanlon, Shiyou Chen, X. G. Gong, and Su Huai Wei. "Self-regulation mechanism for charged point defects in hybrid halide perovskites". In: *Angewandte Chemie - International Edition* 54.6 (2015), pp. 1791–1794.

[312] Jongseob Kim, Sung-hoon Lee, Jung Hoon Lee, and Ki-ha Hong. "The Role of Intrinsic Defects in Methylammonium Lead Iodide". In: *Journal of Physical Chemistry Letters* 5.8 (2014), pp. 1312–1317.

[313] Andrei Buin, Riccardo Comin, Jixian Xu, Alexander H. Ip, and Edward H. Sargent. "Halide-Dependent Electronic Structure of Organolead Perovskite Materials". In: *Chemistry of Materials* 27.12 (2015), pp. 4405–4412.

[314] Rüdiger-A. Eichel. "Structural and dynamic properties of oxygen vacancies in perovskite oxides—analysis of defect chemistry by modern multi-frequency and pulsed EPR techniques". In: *Phys. Chem. Chem. Phys.* 13.2 (2011), pp. 368–384.

[315] C Boehme, J Behrends, K.V. Maydell, M Schmidt, and K Lips. "Investigation of hopping transport in n-a-Si:H/c-Si solar cells with pulsed electrically detected magnetic resonance". In: *J. Non-Cryst. Solids* 352 (2006), p. 1113.

[316] Felix Kraffert, Robert Steyrleuthner, Christoph Meier, Robert Bittl, and Jan Behrends. "Transient electrically detected magnetic resonance spectroscopy applied to organic solar cells". In: *Applied Physics Letters* 107.4 (2015).

[317] Zhicai He, Biao Xiao, Feng Liu, Hongbin Wu, Yali Yang, Steven Xiao, Cheng Wang, Thomas P. Russell, and Yong Cao. "Single-junction polymer solar cells with high efficiency and photovoltage". In: *Nature Photonics* 9.3 (2015), pp. 174–179.

[318] B. Náfrádi, P Szirmai, M Spina, H Lee, O V Yazyev, A Arakcheeva, D Chernyshov, M Gibert, L. Forró, and E. Horváth. "Optically switched magnetism in photo-

voltaic perovskite CH3NH3(Mn:Pb)I3". In: *Nature Communications* 7 (2016), p. 13406.

[319] B. Náfrádi, P Szirmai, M Spina, H Lee, O V Yazyev, A Arakcheeva, D Chernyshov, M Gibert, L. Forró, and E. Horváth. "Optically switched magnetism in photovoltaic perovskite CH3NH3(Mn:Pb)I3 - Supplementary information". In: *Nature Communications* 7.13406 (2016), p. 13406.

[320] Tomas Leijtens, Giles E. Eperon, Alex J. Barker, Giulia Grancini, Wei Zhang, James M. Ball, Ajay Ram Srimath Kandada, Henry J. Snaith, and Annamaria Petrozza. "Carrier trapping and recombination: the role of defect physics in enhancing the open circuit voltage of metal halide perovskite solar cells". In: *Energy Environ. Sci.* 9.11 (2016), pp. 3472–3481.

[321] Newport. *Liquid Filters for Light Sources*. 2017.

[322] QSIL GmbH Quarzschmelze Ilmenau. *Qsil*. 2018.

[323] Atsushi Wakamiya, Masaru Endo, Takahiro Sasamori, Norihiro Tokitoh, Yuhei Ogomi, Shuzi Hayase, and Yasujiro Murata. "Reproducible Fabrication of Efficient Perovskite-based Solar Cells: X-ray Crystallographic Studies on the Formation of CH3NH3PbI3 Layers". In: *Chemistry Letters* 43.5 (2014), pp. 711–713.

[324] Yasuhiro Yamada, Toru Nakamura, Masaru Endo, Atsushi Wakamiya, and Yoshihiko Kanemitsu. "Photocarrier Recombination Dynamics in Perovskite CH3NH3PbI3 for Solar Cell Applications". In: *Journal of the American Chemical Society* 136.33 (2014), pp. 11610–11613.

[325] J. F. Verwey. "Time and intensity dependence of the photolysis of lead halides". In: *Journal of Physics and Chemistry of Solids* 31.1 (1970), pp. 163–168.

[326] Masanobu Iwanaga, Junpei Azuma, Masanobu Shirai, Koichiro Tanaka, and Tetsusuke Hayashi. "Self-trapped states and related luminescence in PbCl2 crystals". In: *Physical Review B* 65.21 (2002), p. 214306.

[327] Masanobu Iwanaga, Junpei Azuma, Masanobu Shirai, Koichiro Tanaka, and Tetsusuke Hayashi. "Self-trapped electrons and holes in PbBr2 crystals". In: *Physical Review B* 65.21 (2002), p. 214306.

[328] Masanobu Iwanaga and Tetsusuke Hayashi. "Exciton-relaxation dynamics in lead halides". In: *Journal of Luminescence* 102-103.SPEC (2003), pp. 663–668.

[329] M.G. Ormerod and A Charlesby. "The radiation chemistry of some polysiloxanes: An electron spin resonance study". In: *Polymer* 4 (1963), pp. 459–470.

[330] V V Laguta, M Nikl, A Pöppl, J Rosa, D Savchenko, and S Zazubovich. "ESR and TSL study of hole capture in PbWO4 : Mo,La and PbWO4 : Mo,Y scintillator crystals". In: *Journal of Physics D: Applied Physics* 46.7 (2013), p. 075302.

[331] Dane W. DeQuilettes, Wei Zhang, Victor M. Burlakov, Daniel J. Graham, Tomas Leijtens, Anna Osherov, Vladimir Bulović, Henry J. Snaith, David S. Ginger, and Samuel D. Stranks. "Photo-induced halide redistribution in organic–inorganic perovskite films". In: *Nature Communications* 7.May (2016), p. 11683.

[332] S. G. Bishop, U. Strom, and P. C. Taylor. "Optically induced localized paramagnetic states in chalcogenide glasses". In: *Physical Review Letters* 34.21 (1975), pp. 1346–1350.

[333] Dirk Schoemaker. "<111>-Oriented FCl-, FBr-, and FI Centres in Mixed Alkali Halides". In: *Physical Review* 149.2 (1966), pp. 693–704.

[334] Amir Haghighirad. *Personal communications*. 2017.

[335] Matthew T. Klug, Anna Osherov, Amir A. Haghighirad, Samuel D. Stranks, Patrick R. Brown, Sai Bai, Jacob T.-W. Wang, Xiangnan Dang, Vladimir Bulovic, Henry J. Snaith, and Angela M. Belcher. "Tailoring metal halide perovskites through metal substitution: influence on photovoltaic and material properties". In: *Energy Environ. Sci.* 10 (1 2017), pp. 236–246.

[336] Pabitra K. Nayak, Michael Sendner, Bernard Wenger, Zhiping Wang, Kshama Sharma, Alexandra J. Ramadan, Robert Lovrinčić, Annemarie Pucci, P. K. Madhu, and Henry J. Snaith. "Impact of Bi3+ Heterovalent Doping in Organic–Inorganic

Metal Halide Perovskite Crystals". In: *Journal of the American Chemical Society* (). PMID: 29266934, null.

[337] Teledyne microwave solutions. *Teledyne microwave solutions*. 2017.

Appendices

A

Intermodulation products from the microwave amplification

When the microwave amplifiers are driven too hard, they saturate and enter non-linear modes of operation [337]. Non-linearity in the pulse formation in both the AWG and the TWT leads to intermodulation between transmitted frequencies. A sample of some of the effects can be seen in figure A.1. Here it shows the Fourier transform of the cavity's response to a 90 ns sinc pulse from the AWG for various pulse 'transmit power' and 'AWG power' percentage levels. The intermodulation products (and therefore unintended frequencies that exist in the cavity) create noise in our measurements. Ideally only intentionally transmitted frequencies would exist in the cavity. As such the power levels were limited to $P_{trans} < 70\%$ and $P_{AWG} < 40\%$ to avoid the non-linear effects in the pulse preparation that will lead to intermodulation products. The DC is the result of a waveform not perfectly zeroed during the fast Fourier transform process and can be discounted.

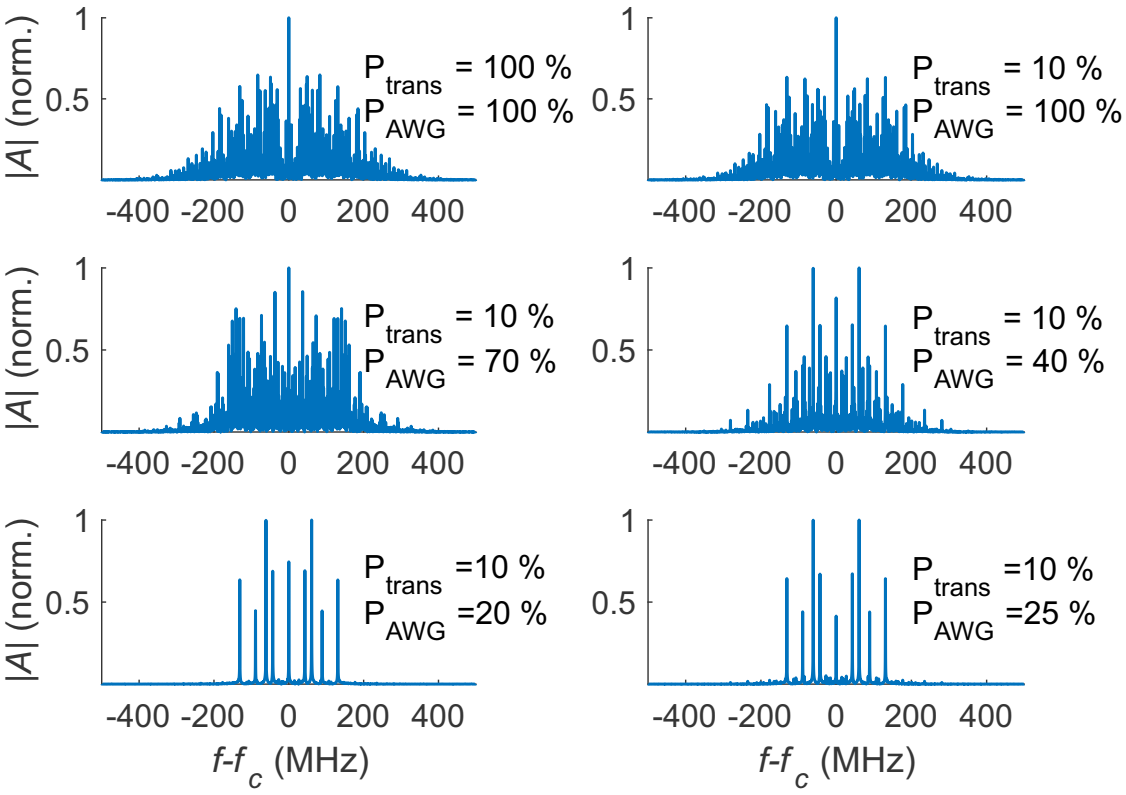


Figure A.1: The Fourier transform of the loaded cavity's microwave response. The figure shows the frequency response of the cavity for various values of 'transmit power' and 'AWG power'.

B

Perovskite single crystal growth

The hybrid perovskite (methylammonium lead trihalide, $MAPbX_3$, where X = Br and I) crystals discussed in Chapter 6 were grown[1] as follows:

1. A 3:1 solution of $MAX:PbX_2$ in the solvent γ-buryrolacton (GBL) was vigorously stirred for one hour on a hotplate at 47° C.

2. Antisolvent vapour-assisted crystallisation was used for nucleation growth; the two solutes were allowed to slowly absorb chloroform. $MAPbX_3$ with cuboid crystal structure grew through a five day period.

3. Single crystal diffraction was used to confirm the space group of the crystals. $MAPbBr_3$ was confirmed as an ideal perovskite with space group Pm-3m, whilst $MAPbI_3$ demonstrated a tetragonal I4/mmm space group. This can be seen in figure B.1.

[1]The crystals used in our experiments were grown by Dr. Amir-Abbas Haghighirad, formerly of Prof Henry Snaith's Photovoltaic and Optoelectronic Device Group. He provided the growth methodology and figure in this appendix for this thesis.

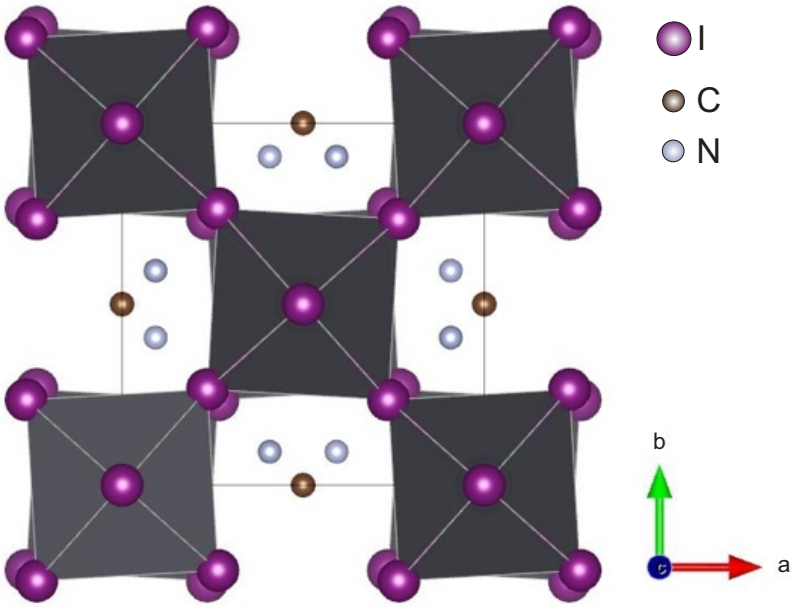


Figure B.1: $MAPbI_3$ crystal structure. Schematic diagram of $MAPbI_3$ crystal structure with the slightly tilted PbI_6^{4-} octahedra. In the figure, purple, brown and grey spheres represent iodine, carbon and nitrogen respectively. Figure created by Dr. Amir-Abbas Haghighirad, 2018.